



Università degli Studi di Cagliari

## **DOTTORATO DI RICERCA**

Scienze e Tecnologie della Terra e dell'Ambiente  
Ciclo XXIX

### **TITOLO TESI**

THREE DIMENSIONAL GEOLOGICAL MAPPING AND  
GROUNDWATER MODEL CALIBRATION FOR MANAGED AQUIFER  
RECHARGE (MAR) TECHNIQUES IN ARID AND SEMI-ARID  
ENVIRONMENTS

Settore scientifico disciplinare di appartenenza  
GEO/05

Presentata da:	Claudio Arras
Coordinatore Dottorato:	Prof. Aldo Muntoni
Tutor:	Prof. Giorgio Ghiglieri Dott.ssa Stefania Da Pelo Dott.ssa Cristina Buttau

Esame finale anno accademico 2015 – 2016  
Tesi discussa nella sessione d'esame marzo – aprile 2017



## Contents

<b>LIST OF FIGURES .....</b>	<b>III</b>
<b>LIST OF TABLES .....</b>	<b>VII</b>
<b>ABSTRACT .....</b>	<b>IX</b>
<b>RIASSUNTO .....</b>	<b>XI</b>
<b>ACKNOWLEDGEMENTS.....</b>	<b>XIII</b>
<b>INTRODUCTION.....</b>	<b>1</b>
<b>1 LITERATURE REVIEW.....</b>	<b>5</b>
1.1 GROUNDWATER RESOURCES MANAGEMENT IN ARID AND SEMI-ARID ENVIRONMENTS.....	5
1.2 3-D GEOLOGICAL MODELLING.....	6
1.3 GROUNDWATER FLOW NUMERICAL MODELLING.....	7
<b>2 STUDY AREA: THE BISKRA AND BATNA REGION .....</b>	<b>9</b>
2.1 GEOGRAPHIC ASSESSMENT .....	9
2.1.1 SURFACE HYDROLOGY.....	9
2.1.2 METEO-CLIMATIC CONTEXT.....	15
2.2 GEOLOGICAL ASSESSMENT.....	18
2.2.1 REVIEW OF THE LITHOSTRATIGRAPHIC SUCCESSION AND STRUCTURES.....	18
2.2.2 TECTONIC SETTING.....	20
2.3 HYDROGEOLOGICAL FEATURES .....	23
<b>3 MATERIALS AND METHODS .....</b>	<b>31</b>
3.1 DATA COLLECTION .....	32
3.1.1 DIGITAL ELEVATION MODEL (DEM).....	32
3.1.2 BOREHOLE REPORTS .....	32
3.1.3 HYDROGEOLOGICAL FIELD SURVEY.....	33
3.1.4 CARTOGRAPHIC DATA .....	35
3.1.5 LANDSAT IMAGERY .....	35
3.1.6 METEO-CLIMATIC DATA .....	37
3.2 DATA HANDLING.....	39
3.2.1 DEMS EVALUATION .....	39
3.2.2 INPUT DATA PRE-PROCESSING PHASE .....	40
3.2.3 GEODATABASE .....	41
3.2.4 IMPLEMENTATION OF 3-D HYDROGEOLOGICAL MODELS .....	43
3.2.4.1 3-D MODEL OF THE BISKRA/BATNA REGION .....	43
3.2.4.2 3-D MODEL OF THE INFERO-FLUX AQUIFER .....	43
3.2.5 HYDROLOGICAL BALANCE CALCULATION .....	47
3.2.5.1 PRECIPITATION .....	47
3.2.5.2 EVAPOTRANSPIRATION .....	47
3.2.5.3 RUNOFF AND INFILTRATION.....	48
3.2.6 GROUND WATER FLOW NUMERICAL MODEL.....	49
3.2.6.1 CONCEPTUAL MODEL .....	49
3.2.6.2 HYDROGEOLOGICAL DATA FOR MODEL CALIBRATION (MAY 1966).....	51

3.2.6.3	HYDROGEOLOGICAL DATA FOR MODEL VERIFICATION (APRIL 2012) .....	53
3.2.6.4	MODEL CONSTRUCTION AND FIRST RUN .....	55
3.2.6.5	MODEL CALIBRATION .....	57
3.2.6.6	MODEL VALIDATION .....	61
<b>4</b>	<b>RESULTS AND DISCUSSION.....</b>	<b>65</b>
4.1	<i>3D HYDRO-GEOLOGICAL MODELS AT REGIONAL SCALE.....</i>	<i>65</i>
4.2	<i>3D HYDRO-GEOLOGICAL MODELS AT LOCAL SCALE .....</i>	<i>68</i>
4.3	<i>HYDROLOGICAL BALANCE.....</i>	<i>71</i>
4.4	<i>GROUNDWATER FLOW NUMERICAL MODEL .....</i>	<i>76</i>
4.4.1	MODEL CALIBRATION.....	76
4.4.2	MODEL VALIDATION.....	79
4.5	<i>MAR SYSTEM DESIGN .....</i>	<i>84</i>
<b>5</b>	<b>CONCLUSION.....</b>	<b>87</b>
	<b>REFERENCES .....</b>	<b>89</b>
	<i>WEBSITES.....</i>	<i>97</i>
	<i>CARTOGRAPHY .....</i>	<i>98</i>
	<b>ANNEX A .....</b>	<b>101</b>
	<b>ANNEX B .....</b>	<b>109</b>
	<b>ANNEX C .....</b>	<b>116</b>

## LIST OF FIGURES

Fig. 1.1 Finite-difference grid and indices. (a) 2D horizontal grid with uniform nodal spacing; the black line represents the model domain and in green the inactive cells. (b) 2D horizontal grid and notation for five nodes. (c) a group of blocks and notation in 3D space (from Anderson et al. 2015).	8
Fig. 2.1 Location of the intervention area in Northern Algeria (blue box).	9
Fig. 2.2 Geographical features of the South-western slope of the Aures Mountains (extracted from the SRTMGL1 DEM) and location of the rain gauge and stream gauge stations described in the text.	10
Fig. 2.3 Panoramic view of the Oued el Hai Biskra (Photograph courtesy of Prof. G. Ghiglieri).	11
Fig. 2.4 The stream gauge station of El Melaga (Photograph courtesy of Prof. G. Ghiglieri).	12
Fig. 2.5 Flow rate records from the El Kantara stream gauge station for the period 1968-1978 (from Haouchine, 2010).	13
Fig. 2.6 Flow rate records from the El Kantara stream gauge station for the period 1988-1993 (from Haouchine, 2010).	13
Fig. 2.7 Flow rate records from the Djemorah stream gauge station for the period 1971-1978 (from Haouchine, 2010).	14
Fig. 2.8 Flow rate records from the Djemorah stream gauge station for the period 1988-1993 (from Haouchine, 2010).	14
Fig. 2.9 Monthly flow rate measured at the El Melaga stream gauge station for the period 1972-1985 (from Haouchine, 2010).	15
Fig. 2.10 Measured cumulative annual rainfall measured at the rain gauge station of Biskra for the period 1974-2011 (ONM).	16
Fig. 2.11 Monthly mean rainfall measured at the rain gauge station of Biskra for the period 1974-2011 (ONM).	16
Fig. 2.12 Monthly mean rainfall and temperatures measured at the Biskra station for the period 1990-2000 (ONM).	17
Fig. 2.13 Structural geological sketch map of northern Algeria (modified from Bracène et al., 2002).	19
Fig. 2.14 Geological sketch map of the Biskra and Batna region showing the lithostratigraphic successions and the main structural features.	21
Fig. 2.15 Structural sketch map of the region of Biskra; the SSF separates the Saharan Atlas-Aures domain, to the North, from the Sahara Platform to the South (modified from Buttau et al. 2013).	22
Fig. 2.16 Gentle open folds in the Cretaceous formations near El Kantara village (Photograph courtesy of Prof. G. Ghiglieri).	22
Fig. 2.17 Hydrogeological map of the Biskra area at 1:200.000 scale (MdH 1980).	23
Fig. 2.18 Summary of the groundwater complexes recognisable in the region of Biskra (modified from MdH 1980).	24
Fig. 2.19 Panoramic view of the Oued el Hai-Biskra riverbed (Photograph courtesy of Prof. G. Ghiglieri).	25
Fig. 2.20 Detail of the deposits constituting the Oued el Hai-Biskra alluvium (Photograph courtesy of Prof. G. Ghiglieri).	25

Fig. 2.21 The red box indicates the location of the productive zone of the Inféro-Flux phreatic aquifer. ....	26
Fig. 2.22 Hydrogeological map of the Infèro-Flux aquifer based on the SCET-COOP field survey conducted in May 1966 (from SCET-COOP 1967). ....	27
Fig. 2.23 Exploitation of groundwater resources for drinking water (AEP), irrigation (IRR), and industry (IND) in the province of Biskra (modified from Benhamida and Fedal 2008). ....	29
Fig. 3.1 Flow chart illustrating the methodological approach used in the present research. .	31
Fig. 3.2 Location of the 155 boreholes dataset. The green and the red dots represent the MdH (1980) and the ANRH boreholes respectively. ....	33
Fig. 3.3 Location of the water points collected during the various field surveys carried out in the frame of the WADIS-MAR Project (modified from WADIS-MAR 2016). ....	34
Fig. 3.4 Piezometric level measurements during WADIS-MAR survey (Photograph courtesy of Prof. G. Ghiglieri). ....	35
Fig. 3.5 Elevation colour ramp over the hill-shaded relief of the A) ASTER GDEM2 and B) SRTMGL1 DEM dataset. ....	39
Fig. 3.6 A) Results of the Model-to-model comparison (SRTMGL1 minus ASTER GDEM2). B) The red dotted lines highlight the stripe effect. Standard Deviations stretching is applied to both the images for contrast enhancing. ....	40
Fig. 3.7 Location of the geological cross sections at 1:200.000 (red lines) and 1:50.000 scale (blue dotted lines). ....	44
Fig. 3.8 Location of the boreholes and cross sections used for the construction of the 3D geological model of the Infèro-Flux aquifer. ....	45
Fig. 3.9 Distribution of the grain size terms of the alluvium described in the borehole reports shown as bar histogram. ....	46
Fig. 3.10 Representation of the topographic surface (SRTMGL1 DEM) and the erosive contact between the alluvium and the Neogene as contour lines. The location of the measured hydraulic conductivities is also shown. ....	50
Fig. 3.11 Scheme representing the parameters required in the computation of the incoming and outcoming flow from the system. ....	51
Fig. 3.12 Cartographic sketch map of the conceptual model showing the piezometric heads and working pumping wells dated back to May 1966 (modified from SCET-COOP, 1967). ....	52
Fig. 3.13 Cartographic sketch map of the conceptual model showing the piezometric heads and working pumping wells dated back to April 2012. ....	54
Fig. 3.14 Cross section roughly oriented N-S showing the measured water table level in May 1966 (cyan line) and April 2012 (dynamic level - blue line) with respect to the SRTMGL1 ground surface (orange line). ....	55
Fig. 3.15 Discretization of the model domain and boundary conditions. ....	56
Fig. 3.16 A) Set of 37 (CT1) and B) 34 (CT2) calibration target (red dots) located on the piezometric heads coming from the SCET-COOP hydrogeological map (blue contourlines). .	58
Fig. 3.17 Location of the pilot points used for the estimation of the hydraulic conductivities using the PEST. A) Scheme n.PP1; B) scheme n.PP2; C) scheme n. PP3. ....	60
Fig. 3.18 Boundary conditions used in the model validation phase. ....	62
Fig. 4.1 Hydrogeological map illustrating the hydrogeological units outcropping in the study area. ....	66
Fig. 4.2 Hydrogeological conceptual model of the Biskra and Batna region illustrating the relationships between the geological framework and the groundwater circulation. ....	67

Fig. 4.3 Geological sketch map showing the A) lithological and B) hydrogeological units outcropping in the Inféro-Flux aquifer area.....	69
Fig. 4.4 Various perspective views of the 3-D geologic surface representing the geometry of the Inféro-Flux aquifer. ....	70
Fig. 4.5 Areal distribution of the calibrated hydraulic conductivities ( $K_x$ ) throughout the model domain as resulted from the PEST execution n.5. The black line cutting the domain from N to S separates the two zones used in the pilot points scheme PP3.....	78
Fig. 4.6 Results of the model run by applying the hydraulic conductivities obtained by the PEST execution n.5: A) scatter plot of simulated to observed fit of water levels; B) plot of residuals at the calibration targets; C) Map view of observed (white) and simulated (black) water tables (shown by contours); D) bar chart illustrating the groundwater budget components.....	80
Fig. 4.7 Scatter plot of simulated to observed fit of water levels for A) May 1966 and C) April 2012 at the same calibration target; plot of residuals for B) May 1966 and D) April 2012 at the same calibration targets. ....	81
Fig. 4.8 History match of water table for both 1966 and 2012 hydrogeological conditions on the error bar related to the georeferencing approximations ( $\pm 2.5$ m) and the SRTMGL1 DEM vertical accuracy ( $\pm 5.6$ m) respectively. ....	82
Fig. 4.9 A) Map view of observed (white) and simulated (black) water table (shown as 1 m contour) and B) bar histogram illustrating the components of the groundwater budget. ....	83
Fig. 4.10 Location of the MAR system designed for the recharge of the Inféro-Flux aquifer. ....	84





## LIST OF TABLES

Table 2.1 Areal extension of the Oued el Hai-Biskra and its tributaries watershed.....	12
Table 2.2 Summary of the stream gauge stations located within the Oued el Hai-Biskra watershed, periods of available flow rate measurements, and extension of the stations drainage area.....	13
Table 2.3 Summary of the pumping wells occurring in the productive zone of the phreatic aquifer (survey date: May 1966 – from SCET-COOP, 1967). Z values were extracted from the SRTMGL1 DEM.....	28
Table 3.1 Summary of the cartographic dataset collected and used for the present research purposes (GCS = Geographic Coordinate System; PCS = Projected Coordinate System).....	36
Table 3.2 Display of the bands and wavelengths of Landsat 8 sensors and descriptions of how each band is best used (modified from USGS 2015).....	37
Table 3.3 Cumulative precipitations and temperatures measured at the ONM and TuTiempo stations. ....	38
Table 3.4 Height statistics for both the ASTER GDEM2 and SRTMGL1 data sets. ....	39
Table 3.5 Statistics of the Model-to-model comparison (SRTMGL1 minus ASTER GDEM2). ..	40
Table 3.6 Geographic transformation used for the projection of the local coordinate systems into the reference system WGS84_UTM_Z31N.....	41
Table 3.7 The structure of the GDB is based on the hierarchy of the collected input data in feature classes contained within thematic feature datasets; the # indicates the feature classes for which a relationship class exists.....	42
Table 3.8 Summary of the grain size term and combination of them derived from the alluvium sediments described in the borehole reports.....	46
Table 3.9 Summary of the measured hydraulic conductivity available for the model area....	50
Table 3.10 Summary of the pumping wells occurring in the productive zone of the phreatic aquifer (survey date: May 1966 – from SCET-COOP (1967). Z values were extracted from the SRTMGL1 DEM.....	52
Table 3.11 Water budget estimation for the Inféro-Flux system at May 1966 using two different values of K. ....	53
Table 3.12 Summary of the pumping wells occurring in the productive zone of the phreatic aquifer (survey date: April 2012 – from WADIS-MAR (2013). Z values were extracted from the SRTMGL1 DEM; daily yields correspond to 20 hours pumping per day.....	54
Table 3.13 Water budget estimation for the Inféro-Flux system at April 2012.....	55
Table 3.14 Combination of calibration target and pilot point schemes used to find the best model fit by using the PEST automated calibration of the hydraulic conductivities.....	59
Table 3.15 Location of the observation points and heads used for model validation. ....	61
Table 4.1 Review of the calculated alluvium volume and the estimated exploitable water volumes for the modeled domain.....	70
Table 4.2 Results of the application of the Hargreaves and Samani equation for the estimation of the reference crop evapotranspiration (ET <sub>o</sub> ).....	72
Table 4.3 Results of the application of the Turc’s equation for the estimation of the actual evapotranspiration (ET <sub>a</sub> ) and the efficient precipitation (P <sub>e</sub> ). The red fields indicate negative P <sub>e</sub> values.....	73

Table 4.4 Results of the application of the Coutagne's (1954) formula to the TuTiempo data set for the estimation of the actual evapotranspiration ( $ET_a$ ) and the efficient precipitation ( $P_e$ ). The red fields indicate values for which the condition $P \leq 1/2 \lambda$ is not respected. ....	74
Table 4.5 Water budget estimation for the wadi alluvium areas. Red values correspond to estimation based on $ET_a$ derived from the Coutagne equation that is out of the validity range of the formula. Averages are provided considering the valid (black) and all the values (red). ....	75
Table 4.6 Summary illustrating the numbers of parameters and observations, and the objective function and correlation coefficient for all the PEST executions.....	77
Table 4.7 Results of the residual analysis using various statistical indicators. ....	79
Table 4.8 Results of the residual analysis using various statistical indicators. ....	81
Table 4.9 Summary of MAR systems designed for the Inféro-Flux aquifer. ....	85

## ABSTRACT

Groundwater is the largest source of liquid fresh water all over the world and represents a fundamental resource for the socio-economic development of drylands, given the context of extended water scarcity. The inherent environmental fragility of drylands and increasing anthropic pressures, which often relate to the unsustainable management of groundwater resources, are leading factors in desertification processes. Natural processes alone could not be enough for the recovery of such fragile environments from degradation, and the corrective interference of local and international communities is necessary.

In this perspective, the European Commission have launched the SWIM Programme to contribute to extensive dissemination and effective implementation of sustainable water management policies and practices in the Southern Mediterranean Region ([www.swim-sm.eu](http://www.swim-sm.eu)). Five Demonstration Projects have been approved, funded, and started implementation in the frame of the SWIM Programme, including the WADIS-MAR Project ([www.wadismar.eu](http://www.wadismar.eu)). The aim of the Project was to enable local communities to manage groundwater resources through the application of sustainable agricultural practices and the implementation of more efficient water harvesting techniques and managed aquifer recharge systems. The Biskra and Batna region (Algeria) and the Jeffara of Medenine (Tunisia) are the two intervention areas selected in the frame of the Project since these are characterised by water scarcity, overexploitation of groundwater resources and are highly exposed to climate change risk and desertification processes.

The main objective of the present research is the development of a comprehensive methodology for the geological, hydrogeological and hydrological characterisation of the Biskra and Batna region aimed at the study of sustainable systems for the management of groundwater resources that could be replicable in similar contexts.

In the study area, as in similar regions in developing countries, adverse environmental conditions and particular political context make a direct in situ investigation difficult and onerous. Therefore, the first phase of the research was focused on the collection of data and available cartography from the literature, free satellite datasets, and field measurements carried out by local authorities. Collected data were verified, digitised, and stored within a geodatabase structure for their easy georeferencing and pre-processing elaboration in the GIS environment.

Subsequently, the pre-processed data were imported into a geo-modeler software and used for the realisation of two three-dimensional hydrogeological models at regional and local scales. The regional scale model extends over the whole south-western slope of the Aures mountains. It was developed to define the thickness and depth of the main aquifer complexes present in the modeled area and to understand the influences of the structural framework on the groundwater circulation. Fourteen and six geological cross sections were realised at 1:200.000 and 1:50.000 scale respectively, and perpendicular to the main geological structures. The geological 3-D model was integrated with the available hydrogeological information to provide the hydrogeological conceptual model of the Biskra and Batna region. From this analysis it emerged that: 1) the interference between the two main fold systems generates geometries such as dome and basins, and therefore wide groundwater storage areas; 2) the groundwater recharge can occur in the mountain domain of the Aures, where most of the recognised hydrogeological units crop out; 3) the

groundwater circulation is influenced by a complex faults' system that allows the communication among the various aquifers and acts as preferred pathway for groundwater rises towards the surface.

The local scale model was developed to define the geometries of a portion of the Inféro-Flux phreatic aquifer, near the city of Biskra. The surface geology was updated using SRTMGL1 DEM and the interpretation of Landsat 8 OLI imageries. Subsequently, nineteen geological cross sections were realised perpendicularly to the groundwater flow direction, at 1:10.000 scale. Due to the poor availability of deep geological data, the sections were realised by integrating surface and deep geological information in a geomorphological interpretation of the river system. The aquifer morphology is characterised by an asymmetric geometry of the confining bed and a maximum deposit depth of 50 metres. The 3-D model has also allowed the estimation of the alluvium volume that corresponds to 83 Mm<sup>3</sup>.

The integration of hydrogeological and hydrological data into the local scale 3-D geological model has allowed the definition of the conceptual model of the Inféro-Flux aquifer. This conceptualisation was used to develop a groundwater flow numerical model using the MODFLOW-2005 code. The numerical model was developed to (1) estimate the hydraulic conductivity parameter and its spatial distribution throughout the model domain, and (2) to obtain quantitative information about the dynamics of the system. A first set of hydrogeological data, which refers to measurements carried out in 1966, was used for the automated calibration of the model through the application of the PEST, and the estimation of the  $K_x$  parameter. The resulting values range between 0.00019 and 0.00869 m/s and are coherent with materials (sands and gravels) that constitute braided channel deposits. The calibration results were validated by using a second set of hydrogeological data, measured in 2012. The analysis of the hydrogeological balance, compared to the information obtained through the hydrological balance, suggests that infiltration during rainy period is not enough to allow the simulated inflow at the northern constant head boundary. Therefore, an additional source of alimentation for the Inféro-Flux aquifer must be considered.

In conclusion, residual analysis confirms the consistency of the groundwater flow numerical model in reproducing the system conceptualisation given that their values were always lower than the maximum error allowed.

## RIASSUNTO

Le acque sotterranee costituiscono la fonte principale di acqua dolce allo stato liquido sulle terre emerse. Esse rappresentano una risorsa fondamentale per lo sviluppo socio-economico delle regioni aride del pianeta, a causa della scarsità di acque superficiali. La fragilità ambientale intrinseca delle zone aride e le crescenti pressioni antropiche, che spesso sono legate a un utilizzo non sostenibile delle risorse idriche sotterranee, sono fattori che hanno una forte influenza sui processi di desertificazione. I processi naturali, da soli, non sono sufficienti per il ripristino di questi ambienti e per questo è necessario un intervento correttivo da parte delle comunità locali e internazionali.

In questa prospettiva la Commissione Europea ha lanciato il Programma SWIM per contribuire alla diffusione ed attuazione di politiche e pratiche di gestione sostenibile delle risorse idriche nelle regioni del Mediterraneo meridionale ([www.swim-sm.eu](http://www.swim-sm.eu)). Nell'ambito del Programma sono stati approvati e finanziati cinque Progetti Dimostrativi, tra cui il Progetto WADIS-MAR ([www.wadismar.eu](http://www.wadismar.eu)). Obiettivo principale del Progetto è quello di aiutare le comunità locali nella gestione delle risorse idriche attraverso l'applicazione di pratiche agricole sostenibili, la realizzazione di sistemi efficienti per la raccolta delle acque superficiali e la progettazione e realizzazione di sistemi di ricarica artificiale degli acquiferi. Le regioni di Biskra e Batna (Algeria) e della Jeffara di Medenine (Tunisia) sono state scelte come aree di intervento nell'ambito del Progetto in quanto caratterizzate da scarsa disponibilità d'acqua superficiale, sovra-sfruttamento delle risorse idriche sotterranee e perché esposte ai rischi connessi con i cambiamenti climatici e i processi di desertificazione.

L'obiettivo generale della presente ricerca è stato lo sviluppo di una metodologia per la caratterizzazione geologica, idrogeologica, e idrologica della regione di Biskra e Batna, finalizzata allo studio di sistemi di gestione integrata e sostenibile della risorsa idrica sotterranea che fosse replicabile in contesti simili.

Nell'area di studio, così come in regioni analoghe in paesi in via di sviluppo, condizioni climatiche avverse e contesti politici particolari rendono i rilievi in situ difficili e onerosi. Pertanto, durante la prima parte della ricerca, è stato svolto un lavoro di ricerca e raccolta dei dati e della cartografia disponibile in letteratura, di dataset satellitari scaricabili gratuitamente dalla rete, e di dati rilevati dalle autorità locali. I dati collezionati sono stati verificati, digitalizzati e organizzati all'interno di un geo-database per poi essere facilmente georeferenziati e pre-processati tramite l'utilizzo di sistemi GIS.

I dati pre-processati sono stati quindi importati su un software di modellazione geologica 3-D e utilizzati per la realizzazione di due modelli idrogeologici tridimensionali a scala regionale e a scala locale. Il modello regionale comprende l'intero versante sud-occidentale del dominio montano dell'Aures. Esso è stato realizzato per definire gli spessori e le profondità dei vari complessi acquiferi presenti nell'area e per capire come il contesto geologico e strutturale influenzi la circolazione idrica sotterranea. Sono state realizzate 14 sezioni geologiche a scala 1:200.000 e sei sezioni a scala 1:50.000, perpendicolari alle strutture geologiche principali. Il modello geologico 3-D ottenuto per interpolazione delle sezioni è stato integrato con le informazioni idrogeologiche disponibili per ottenere il modello idrogeologico concettuale della regione di Biskra e Batna. Dall'analisi del modello è stato possibile definire che: 1) l'interferenza tra i due sistemi di pieghe principali genera geometrie del tipo "duomi e bacini", e quindi vaste aree di accumulo delle acque sotterranee; 2) la ricarica degli acquiferi

può avvenire nel dominio montano dell'Aures, dove affiorano la maggior parte delle unità idrogeologiche; 3) la circolazione idrica sotterranea è influenzata da un complesso sistema di faglie, il quale permette la comunicazione idrica tra i vari acquiferi e costituisce un percorso preferenziale per la risalita delle acque verso la superficie.

Il modello 3-D a scala locale è stato sviluppato per definire la morfologia di una porzione dell'acquifero freatico Inféro-Flux, ubicato nei pressi della città di Biskra. La geologia di superficie è stata aggiornata attraverso l'utilizzo del DEM SRTMGL1 e l'interpretazione delle immagini LANDSAT 8 OLI. Sono state poi realizzate 19 sezioni geologiche a scala 1:10.000, perpendicolari alla direzione del flusso sotterraneo. Data la scarsità di dati geologici profondi, le sezioni sono state realizzate integrando tutte le informazioni geologiche disponibili in una interpretazione geomorfologica del sistema fluviale. Il modello 3-D così ottenuto ha permesso: 1) la definizione della geometria della superficie geologica che separa il *bedrock* neogenico dalle alluvioni quaternarie; 2) la stima dei volumi dei depositi alluvionali, pari a 83 Mm<sup>3</sup>.

Il modello geologico 3-D è stato integrato con i dati idrogeologici e quelli relativi al bilancio idrologico per la definizione del modello concettuale dell'acquifero freatico Inféro-Flux. Tale concettualizzazione è stata utilizzata per la costruzione di un modello numerico di flusso in stato stazionario utilizzando il codice MODFLOW. Il modello numerico è stato costruito per stimare la conducibilità idraulica e la sua distribuzione spaziale all'interno del dominio di interesse in quanto parametro idrodinamico fondamentale, e in secondo luogo per ottenere delle informazioni quantitative circa il funzionamento del sistema idrogeologico. Un primo set di dati idrogeologici, misurati nel maggio 1966, è stato utilizzato per la calibrazione del modello numerico attraverso l'applicazione del codice PEST per la stima automatica della conducibilità idraulica. I valori ottenuti variano tra 0.00019 e 0.00869 m/s e sono compatibili con le granulometrie dei materiali (sabbie e ghiaie) che costituiscono i depositi originati da sistemi fluviali del tipo a canali intrecciati, o braided channel, così come la loro distribuzione spaziale all'interno del dominio. Il risultato della calibrazione è stato quindi validato attraverso l'utilizzo di un secondo set di dati idrogeologici, misurati nell'Aprile 2012. L'analisi del bilancio idrogeologico, rapportato alle informazioni ricavate dal bilancio idrologico, suggerisce che le acque di infiltrazione durante i periodi piovosi non sono sufficienti a giustificare le portate simulate e di conseguenza è necessario considerare un'ulteriore fonte di alimentazione per l'acquifero freatico Inféro-Flux. Tale sorgente di alimentazione può essere rappresentata dalle acque sotterranee che risalgono verso la superficie attraverso i sistemi di faglia, come dimostrato dal modello idrogeologico concettuale a scala regionale.

L'analisi dei residui conferma l'attendibilità e la solidità del modello in quanto i valori sono sempre al di sotto dell'errore massimo ammesso legato all'accuratezza verticale del DEM, dimostrando che il modello numerico è in grado di simulare con buona approssimazione la concettualizzazione del sistema.

## ACKNOWLEDGEMENTS

Firstly, I would like to express my sincere gratitude to my supervisor Prof Giorgio Ghiglieri to give me the opportunity to join the WADIS-MAR Project and to conduct my PhD research in a multi-disciplinary and international cooperative environment, for the continuous support of my PhD study and related research, and for giving me invaluable guidance and expertise.

Besides my supervisor, I would like to thank Prof Stefania Da Pelo and all the researchers and Professors of the Chemical and Geological Department of the University of Cagliari for their insightful comments and encouragement, and for widening my research from various perspectives among which Prof Antonio Funedda, Dr Maria Teresa Melis, and Prof Alfredo Loi.

I am deeply thankful to the NRD Centre (Desertification Research Centre) of the University of Sassari and the WADIS-MAR Project for the amazing possibility of conducting the present research. My sincere gratitude goes to Prof Giuseppe Enne, Prof Pier Paolo Roggero and Prof Luciano Gutierrez who provided me the opportunity to join the NRD team and participating in this project. Special thanks go to the NRD colleagues and fellows for all their support, collaboration and friendship, among which Alberto Carletti, Nadia Maio, Pietro Arras, Francesca Demuro, Anna Paola Dessena, Matteo Funaro, Ileana Iocola, and Alessandra Paulotto.

A special thank must be addressed to Dr Pier Luigi Cau of CRS4 (Centre for Advanced Studies, Research and Development in Sardinia) for his patience, the invaluable support, and the hard question which motivated me in sharpening skills and knowledge about a completely new world such as the numerical modelling.

Thank you so much to my dear TeleGIS labmates Dr Cristina Buttau, Dr Gabriela-Mihaela Afrasinei, PhD student Sonia Aldana Martinez and Patrizia Fenza for the stimulating discussions, for the rainy and sunny days we were working together in the field, and for sharing all the funny and stressful situations we have faced in the last three years ("*Entusiamo*" is the word of the year!!). I would also like to thank Dr Fabrizio Cocco and the new entry in the attic team Dr Marco Pistis for their helpfulness and friendship.

I would also like to thank the Algerian and Tunisian WADIS-MAR partners, Institut Technique de Développement de l'Agronomie Saharienne, Biskra (ITDAS, Algeria), Agence Nationale des Ressources Hydrauliques (ANRH, Algeria), institute des regions Arides (IRA, Tunisia), and Observatoire du Sahara et du Sahel (OSS, Tunisia) for the provided data and collaboration. Special thanks go to the OSS team and staff for their hospitality, support and guidance throughout the three months research internship at OSS headquarter among which BabaSy, AbdoulKarim Bello, Habiba Khiari, Moez Labiadh, Leila Dridi, Mustapha Mimouni and Wafa Jouini.

Thanks go to Mr Mohamed Ouessar, Mr Kamel Nagaz, Mongi Ben Zaid, Mr Amar Zerrim, Mr Messaoud Guied, Amor Jlali, Bouajila Essifi and LAZHAR of IRA for the warm welcome and support during various field surveys and meetings in wonderful Tunisia.

I would like to thank my family: my parents, my brothers, uncles and cousins for supporting and encouraging me throughout these years. My sincere and hearty gratitude to the Calia and Demurtas families for all their support, affection, and tasty meals, I have found a second family in you!

Last but not the least, to my best friend, lover and colleague, Mara, for the incredible passion and sweetness in living this life together.

Cagliari, Sardinia, April 2017

Claudio Arras



## INTRODUCTION

Chapter 12 of Agenda 21, as approved by the United Nations Conference on Environment and Development (UNCED 1992), defines desertification as *“land degradation in arid, semi-arid and dry sub-humid areas resulting from various factors, including climatic variations and human activities”*. For Verheye (2006), desertification is *“the process of degradation of the environment, being the result of either natural conditions (decrease or extreme variability of rainfall) or adverse human interventions, but always leading to a critical shortage of water for the vegetation”*. From these definitions, three key concepts could be identified that required a deeper evaluation and understanding (Kassas 1995): (1) the menace (land degradation); (2) the menaced territories (drylands); (3) the causes (natural and anthropogenic).

As defined by the United Nations Conventions to Combat Desertification (UNCCD 1994), land degradation is regarded as *“the reduction or loss, in arid, semi-arid and dry sub-humid areas, of the biological or economic productivity and complexity of rainfed cropland, irrigated cropland, or range, pasture, forest and woodlands, resulting either from excessive land use or from human activities and habitation patterns, such as: (1) soil erosion caused by wind and/or water; (2) deterioration of the physical, chemical, biological or economic properties of the soil; and (3) long-term loss of natural vegetation”*.

Drylands are those regions of the world where precipitation rate is less than the amount of potential water consumption from evapotranspiration and plant growth (Kassas 1995). The magnitude of this deficit is commonly expressed by the aridity index (Ai) parameter that is also used for classifying drylands into four main categories (UNEP 1992): hyper-arid ( $A_i < 0.03$ ), arid ( $0.03 < A_i < 0.02$ ), semi-arid ( $0.02 < A_i < 0.5$ ), and dry sub-humid ( $0.5 < A_i < 0.75$ ). Hyper-arid regions refer to actual desert zones where precipitations are very low and irregular, and agriculture and grazing are not possible. Instead, arid, semi-arid, and dry sub-humid regions are fragile environments that are prone to desertification processes. Approximately 41% of land surfaces worldwide are occupied by drylands, extending over six million hectares (De Pauw 2004). Africa and Asia are the continents that most suffer from these climatic conditions and drylands cover approximately 2000 million hectares in both cases representing the 65% and 44% of total continental lands respectively.

The inherent ecological fragility of dryland systems and increasing anthropic pressures are leading factors in desertification processes. The inherent environmental vulnerability of drylands is strongly related to the extreme rainfall variability over time and space resulting in a long period of drought followed by intense precipitation events and floods. Anthropic pressures are related to rapid population growth and internal migration of people from rural to urban areas looking for easy access to goods and services, including clean drinking water. Moreover, changing from subsistence to commercial economy often results in increasing exploitation of natural resources and environmental pollution.

The combination of such natural and anthropic factors can seriously damage the system and natural processes alone could not be enough for such fragile environments recovery, thus the corrective interference of local and international communities is necessary (UNCCD 1994; Kassas 1995).

The management of dryland areas should primarily focus on the best and most economical and sustainable use of available water, either from rainfall or groundwater (Verheye 2006). In past decades, traditional approaches have focused on the realisation of large infrastructure projects to limit desertification phenomena. However, as pointed out by a series of international conferences in 1992 (the Rio-Dublin Principles) and non-governmental organisation as the Global-Water Partnership, it is necessary to *“promote the coordinated development and management of water, land and related resources, to maximise the resultant economic and social welfare in an equitable manner without compromising the sustainability of vital ecosystems”*. This is the definition of Integrated Water Resources Management (IWRM).

In this perspective, the European Commission have launched the SWIM (Sustainable Water Integrated Management) Programme to contribute to the extensive dissemination and effective implementation of sustainable water management policies and practices in the Southern Mediterranean Region ([www.swim-sm.eu](http://www.swim-sm.eu)). Five Demonstration Projects have been approved, funded, and started implementation at the beginning of 2012 in the frame of the SWIM Programme, including the WADIS-MAR Project (Water harvesting and Agricultural techniques in Drylands: an Integrated and Sustainable model in MAghreb Regions – [www.wadismar.eu](http://www.wadismar.eu)). It is based on a participative and bottom-up approach and takes into account local and traditional experience. The aim is to enable local communities to manage groundwater resources through the application of sustainable agricultural practices and the implementation of more efficient Water Harvesting Techniques (WHT), including the design of Managed Aquifer Recharge (MAR) systems. The partnership is composed of five international institutions, which is led by the Desertification Research Centre (NRD) of the University of Sassari (Italy) and includes the University of Barcelona (UBI; Spain), the Sahara and Sahel Observatory (OSS; Tunisia), the Arid Regions Institute (IRA; Tunisia), and the National Agency for the Hydraulic Resources (ANRH; Algeria). The Biskra and Batna region (Algeria) and the Jeffara of Medenine (Tunisia) are the two intervention sites selected in the frame of the Project. Those areas are characterised by water scarcity, overexploitation of groundwater resources and are highly exposed to climate change risk and desertification processes (Ghiglieri et al. 2014), as demonstrated by increasing phenomena of soil salinization and sand encroachment (Afrasinei et al. 2017a; Afrasinei et al. 2017b).

In the present research, a comprehensive study on the geological, hydrological, and hydrogeological features and dynamics characterising the Biskra and Batna region, in Algeria is presented, being compulsory for the design of a Managed Aquifer Recharge (MAR) system. The aim is to provide a consistent methodology that could be replicable in similar environmental systems, where data are not easily accessible and direct field survey is often difficult. In particular, the developed methodology is based on the collection and validation of existing bibliographic and free satellite data to be used as input data in the development of two 3-D hydrogeological models at regional and local scale. The regional scale model was developed to understand the relationships between the various aquifer occurring in the study area, while the local scale model was built to define the geometry of a portion of the Inféro-Flux aquifer and, consequently, to provide useful indications about the best site for the design of a MAR system. Moreover, the local scale 3-D model was used to constrain the geometry of the aquifer in the development of a groundwater flow numerical model used for the quantitative characterisation of the hydrodynamic conditions of the aquifer.

The present research contributes to the literature through the application of three-dimensional geological models for the investigation of groundwater systems at regional-scale. In fact, despite the increased attention given to such themes in the last decades, there are still only a rather small number of published case studies (Raiber et al. 2012). Moreover, case studies regarding the integration of 3-D geological models and groundwater flow numerical models applied to arid and semi-arid environments are in their early infancy, especially because of the lack of adequate field measurements and data.



# 1 LITERATURE REVIEW

## 1.1 GROUNDWATER RESOURCES MANAGEMENT IN ARID AND SEMI-ARID ENVIRONMENTS

Groundwater represents the largest source of liquid fresh water all over the world (Bouwer 2000), playing a fundamental role in the development of drylands, given the current context surface water scarcity. Increasing population growth and rural exodus reflect in increasing water demand for municipal and irrigation purposes. However, this resource is often not adequately managed to ensure its long-term sustainability (Sophocleous 2005) and, in arid and semi-arid regions, its depletion is emphasised by the imbalance between natural recharge and overexploitation.

Managed Aquifer Recharge (MAR) systems are commonly identified as a robust groundwater management tool in arid and semi-arid regions (Dillon 2005; Alraggad and Jasem 2010). They contribute, particularly if practised as part of a wider approach to water resource management, to re-pressuring aquifers subject to declining yields (Gale 2005) and to improve water quality through soil-aquifer treatment or geo-purification (Bouwer 2002). With a MAR system, surface water is intentionally injected into the ground, where it is not vulnerable anymore to evaporation losses and it is relatively safe from contamination (Shaeri Karimi et al. 2014), for subsequent recovery or environmental benefit (Dillon et al. 2009). This aspect is of particular interest in arid and semi-arid regions where there is the need to store in an efficient way excess runoff during rainy periods to prepare for drought and secure supplies (Dillon 2005).

MAR applications include a wide variety of techniques and schemes, but are generally classified into five main groups depending on the methods used to either catch the water or to getting the water infiltrated (Gale 2005; IGRAC and Acacia Institute 2007):

- 1) spreading methods are used to infiltrate water through permeable surface into the unsaturated zone. These methods were applied in South-Africa where infiltration ponds were realised to infiltrate urban stormwater and wastewater into unconsolidated sediments for augmenting freshwater supplies and improve water quality (Department of Water Affairs 2010)
- 2) induced bank infiltration covers infiltration of surface water through river, lake or dune sediments caused by well pumping;
- 3) recharge by well, shaft and borehole is generally used where there is the need to pass across a low permeability surface structures to recharge confined aquifers;
- 4) in-channel modifications are barriers realised directly in the stream network to temporarily store stormwater and improve infiltration into river deposits.
- 5) rainwater and runoff harvesting comprises the gathering and infiltration of surface or roof runoff by barriers, bunds and trenches. Sand-filled trenches were realised in agricultural areas in Jordan to intercept surface runoff for deeper infiltration into the vadose zone (Abu-Zreig et al. 2000).

Despite the wide variety of MAR techniques and schemes, the design and management of the best technical solution for a particular case study requires the evaluation of several aspects, such as geological, geochemical, hydrological, biological and engineering (Bouwer

2002). Geological, hydrogeological, and hydrological aspects, in particular, are essential in the development of the conceptual hydrogeological model and significant benefits are gained by the current rapid developments in 3D geological and groundwater flow modelling software and techniques, as well as the increasing availability of digital geological data (Royse et al. 2010).

## **1.2 3-D GEOLOGICAL MODELLING**

Conventional geological maps are no longer adequate for storing, representing, and transmitting geological information (Xue et al. 2004). In their infancy, three-dimensional geological models were developed for hydrocarbon exploration and production (Chilès et al. 2004), allowing a complete geometrical representation of subsurface geology. Rapid development of computer hardware and software and increasing availability of digital geological data have enabled the diffusion of 3-D modelling techniques and there is a continuous research for developing new techniques and methodologies for building more complex 3-D geological models (Wu and Xu 2003; Borracini et al. 2004; McCaffrey et al. 2005; Zhu et al. 2012). Moreover, these models represent powerful tools for sharing scientific results to a wide range of stakeholders, such as government authorities (Raiber et al. 2012).

The general methodology used for developing 3-D geological models is well documented. It is mainly based on the use of seismic data (Duvinage and Mallet 2000; Zehnder and Allmendinger 2000), borehole data implemented with cross sections (Lemon and Jones 2003; Kaufmann and Martin 2008; Zhu et al. 2012), or multi-source data integration (Wu et al. 2005). 3-D geological modelling range to a variety of applications, of which one of the most distinctive is predictive process modelling of geologic, tectonic, and hydrologic processes necessary for land-use planning, hazard mitigation, resource management, contaminant dispersion, among others (Xue et al. 2004).

3-D geological modelling aimed at the representation of aquifer systems is of particular interest for the purposes of the present research study. 3-D models were proven to be useful instruments in: understanding the relationships and connections between shallow and deep aquifer, particularly if integrated with hydrogeochemical data (White and Reeves 1999; Raiber et al. 2012; Da Pelo et al. 2017); evaluating aquifer extents and influences of geologic structures on hydrologic properties (Artimo et al. 2003a; Ferril et al. 2004; Saraperä and Artimo 2004); identifying areas of potential recharge (Di Salvo et al. 2012).

Moreover, 3-D geological models represent one of the primary input data required in the development of a groundwater flow and transport numerical model (Artimo et al. 2003b). The integration of 3-D geological and numerical modelling approaches has become increasingly commonplace in the last decade and several studies have been conducted on the development of new methods for the interpretation, description and characterization of aquifers using 3D geological modelling. Berg and Thorleifson (2001) have collected a series of experiences carried out in the United States and Canada about the characterisation of Quaternary and pre-Quaternary unconsolidated deposits to enhance strategies for sustainable use of groundwater and its protection. It includes 1) acquiring, evaluating, and compiling geologic data, 2) constructing 3-D maps, and 3) employment of 3-D maps and data for groundwater numerical modelling. Other applications targeted at the management of

groundwater resources come from case studies carried out in Europe (Artimo et al. 2003b; Turner et al. 2015).

### 1.3 GROUNDWATER FLOW NUMERICAL MODELLING

Groundwater flow numerical models are physically based mathematical models derived from Darcy's law and the law of conservation of mass. The general governing equation (differential equation) representing the three-dimensional transient groundwater flow for heterogeneous and anisotropic conditions is:

$$\frac{\partial}{\partial x} \left( K_x \frac{\partial h}{\partial x} \right) + \frac{\partial}{\partial y} \left( K_y \frac{\partial h}{\partial y} \right) + \frac{\partial}{\partial z} \left( K_z \frac{\partial h}{\partial z} \right) + W = S_s \frac{\partial h}{\partial t}$$

Where:

- $K_x, K_y, K_z$  are values of hydraulic conductivity along the x, y, and z coordinate axes, which are assumed to be parallel to the major axes of hydraulic conductivity [L/T];
- $h$  is the potentiometric head [L];
- $W$  is a volumetric flux per unit of volume representing sources and/or sinks of water, with  $W < 0.0$  for flow out of the ground-water system, and  $W > 0.0$  for flow into the system [ $T^{-1}$ ];
- $S_s$  is the specific storage of the porous material [ $L^{-1}$ ]; and
- $t$  is time [T].

Two different numerical methods are mostly used in groundwater flow modelling to solve the governing equation: the finite-difference (FD) and the finite-element (FE) methods. Two- and three-dimensional finite-difference models for the simulation of groundwater flow has become to be widely diffused in the seventies (*Prickett and Lonquist, 1971; Trescott et al., 1976*). In the first years of the eighties, the United States Geological Survey (USGS) developed the Modular Three-Dimensional Finite-Difference Ground-Water Flow Model (*McDonald and Harbaugh, 1984*), also known as MODFLOW. Several improvement and integration have been made to it (*McDonald and Harbaugh, 1988; Harbaugh and McDonald, 1996a and 1996b; Harbaugh et al., 2000*) and the last code update was released in 2005 as the MODFLOW-2005 (*Harbaugh, 2005*). The finite-difference method (*Remson et al. 1971; Wang and Anderson 1995*) approximates the model domain to a rectangular grid, in which nodes are located in the centre of the FD cells or blocks. The set of indices i, j, k is used to indicate the relative location of the node within a 3D space and represent the column, row, and layer, respectively (Fig. 1.1). Heads are defined only at nodes, and values represent the average heads in the FD cell/block.

In the finite-element method, the model domain is subdivided into a mesh of triangular or quadrilateral elements defined by nodes. In this approach, the heads (dependent variable) are defined as a continuous solution within elements. The method is discussed in detail in *Istok (1989), Wang and Anderson (1995), Diersch (2013), and Pinder and Gray (2013)*.

The methodology describing how to design, calibrate, and perform forecast simulations has been improved throughout the years and it is well documented by the scientific literature (*Todd and Mays 2005; Anderson et al. 2015*). It mainly includes the following steps:

1. Definition of the purpose of the model;
2. Development of the conceptual model;
3. Selection of the mathematical model and computer code;
4. Model design;
5. Calibration process;
6. Forecasting simulations;
7. Forecast sensitivity analysis;
8. Results presentation and post-audit model performance.

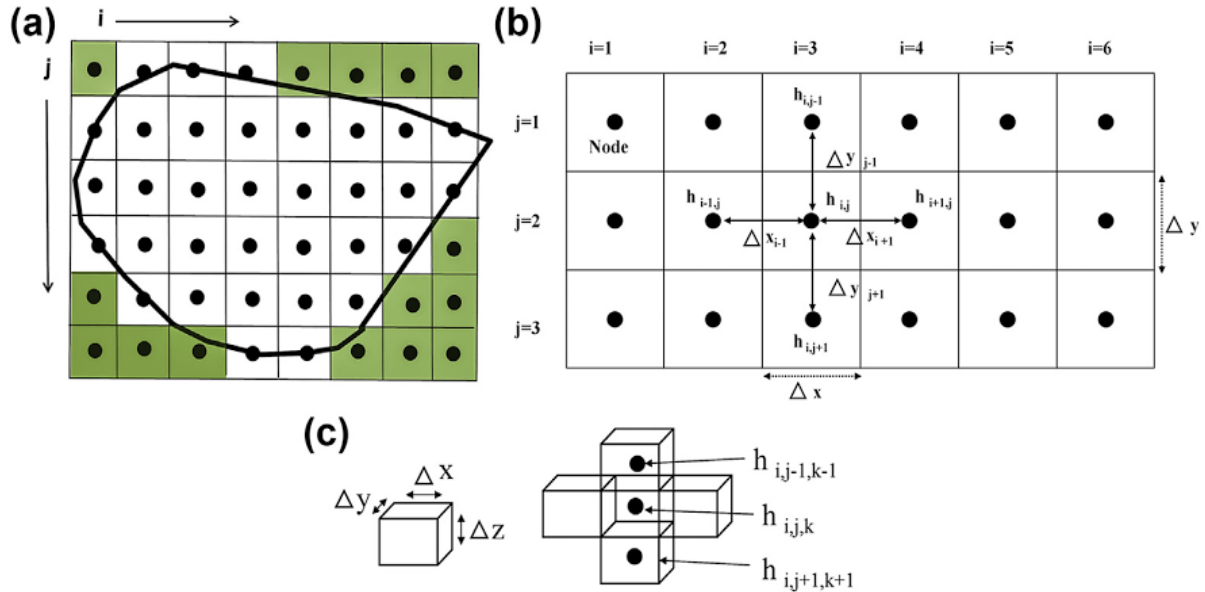


Fig. 1.1 Finite-difference grid and indices. (a) 2D horizontal grid with uniform nodal spacing; the black line represents the model domain and in green the inactive cells. (b) 2D horizontal grid and notation for five nodes. (c) a group of blocks and notation in 3D space (from Anderson et al. 2015).

Furthermore, due to the significance of model results and forecast in political decision, standard procedures have been developed to document a groundwater flow model application and provide quality assurance measures of the modelling effort (ASTM 2006).

Applications of groundwater flow numerical models are continuously increasing as tools for the analysis of hydrogeological systems and the management of groundwater resources (Singh 2014). In particular, a recent literature review (Ringleb et al. 2016) has pointed out the increasing application of numerical models (more than 200 case studies) targeted at the planning of MAR schemes, identification and quantification of geochemical processes during the injection, storage and recovery phases, and to the evaluation of MAR performance and efficiency.



## 2 STUDY AREA: THE BISKRA AND BATNA REGION

The target area selected in the frame of the present research is located in the provinces of Biskra and Batna, in North-Eastern Algeria. Geographically, it mainly extends over the South-Western slope of the Aures Mountains, at the boundary with the Sahara Platform (Fig. 2.1, Fig. 2.2).



Fig. 2.1 Location of the intervention area in Northern Algeria (blue box).

### 2.1 GEOGRAPHIC ASSESSMENT

The Aures represents the eastern continuation of the Saharan Atlas chain. An alternation of mountain ridges and fluvial valleys dipping toward SW (Fig. 2.2) characterises the South-western slope of the Aures Mountains. Streams emerging from the mountain domain to the adjoining plains, such as the El Outaya and the Zibane lowland, produce extensive alluvial fan deposits that define the morphology of the Aures piedmont. This domain constitutes a spreading area where surface runoff and most floods are subjected to quick infiltration processes (SCET-COOP 1967; Haouchine 2010). The El Outaya plain, in particular, represents a little endorheic basin surrounded by the Atlas reliefs to the East and by the Saharan Atlas ranges of Djebel Mekrizane, Monts du Zab, and Djebel bou Rhezal (519 m a.m.s.l.) to the North, West, and South respectively. The Zibane lowland is characterised by a flat south-eastern dipping surface that reaches negative elevation values corresponding to the endorheic basin of Chott Melhrir (-70 m a.m.s.l.).

#### 2.1.1 SURFACE HYDROLOGY

The Oued el Hai Biskra is the main drainage system of the study region (Fig. 2.2). It has its headwaters in the Belezma Mountains (2100 m a.m.s.l.) where precipitation rate is comprised between 400 and 500 mm/year. It flows through the Aures domain for approximately 60 km with an NE-SW direction, receiving waters from few tributaries, and emerges from a morphological sluice on the Djebel Mekrizane to the El Outaya Plain. Since the year 2000, this portion of the watershed drains into the *Barrage Fontaine des Gazelles*. It is an earth-filled dam with a clayey core and a total capacity of  $55.491 \cdot 10^6 \text{ m}^3$ , built to provide irrigation water for the region ([http://www.cobagroup.com/NOTICIAS/arg\\_ago2015/news\\_EN\\_05.html](http://www.cobagroup.com/NOTICIAS/arg_ago2015/news_EN_05.html)). Successively, the Oued el Hai-Biskra flows for 23 km with an N-S direction crossing the alluvial fan originated

from the Southwestern slope of the Aures. Here, it receives the contribution of the Oued bou Gatou tributary, which drains a basin of 269 km<sup>2</sup> comprised between the Aures ranges of Djebel Haouidja and Djebel el Fedj. Once it reaches the Djebel bou Rhezal range, the el Hai-Biskra stream flows along the slope towards East for 5 km, the last which running through 40 m wide passage into rocky outcrops. Subsequently, it receives the contribution of three tributaries: the Oued Branis, the Oued Lefrah, and the Oued el Besbas. The Oued Branis (called Oued Abdi in the source area) represents the main tributary of the Oued el-Hai Biskra system. It drains the Aures ranges of Djebel Bous, Djebel Mahmel (2300 m a.m.s.l.), and Djebel el Azreg extending over an area of 699 km<sup>2</sup>.

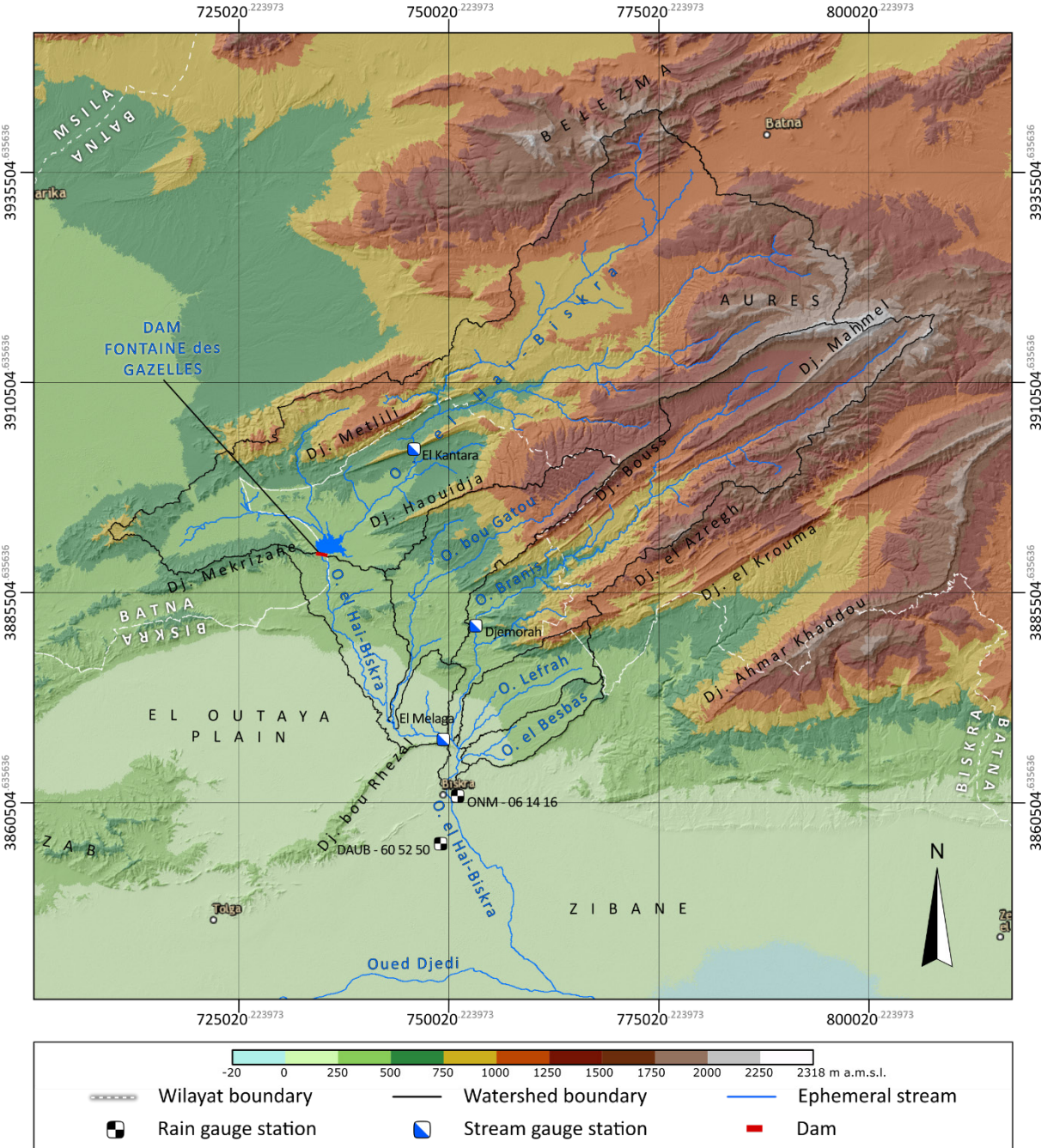


Fig. 2.2 Geographical features of the South-western slope of the Aures Mountains (extracted from the SRTMGL1 DEM) and location of the rain gauge and stream gauge stations described in the text.

The Oued Lefrah and Oued el Besbas drain an area of 113 and 64 km<sup>2</sup> respectively, being mostly characterised by hilly reliefs and maximum elevations of 1162 m a.m.sl. at Djebel Fouchi. The confluence of the main stream and its tributaries leads to an increasing extension of the alluvial area that reaches a width of 1,4 km just downstream the confluence with the Oued el Besbas. Afterwards, the alluvium width progressively reduces to 400 m because forced in a morphological sluice. After the sluice, where the city of Biskra is set, the Oued el-hai Biskra flows through a vast alluvial fan with a North-South direction for 30 km and then flows into the Oued Djedi.

The Oued el Hai-Biskra and all its tributaries are characterised by several interconnected flow channels that are divided by longitudinal bars constituted by sand and gravel deposits, which can be often submerged during flood events (Fig. 2.3). These geomorphological features, called braided channel, are common alluvial stream forms in drylands (Slatyer and Mabbutt 1964; Mabbutt 1977).

The Oued Djedi represents the largest drainage system of the whole region draining a total surface of 9130 km<sup>2</sup> that extends over the southern slope of the Saharan Atlas and flows into the Chott Melhir. Given the purposes of the present research, the portion of the watershed upstream the city of Biskra was considered. It extends over an area of about 3100 km<sup>2</sup> (Table 2.1).



*Fig. 2.3 Panoramic view of the Oued el Hai Biskra (Photograph courtesy of Prof. G. Ghiglieri).*

SUB-BASIN	AREA [km <sup>2</sup> ]
Oued el Hai-Biskra (dam)	1730
Oued el Hai-Biskra (whole system)	1948
Oued bou Gatou	269
Oued Branis	699
Oued Lefrah	113
Oued el Besbas	64
<b>TOTAL</b>	<b>3093</b>

*Table 2.1 Areal extension of the Oued el Hai-Biskra and its tributaries watershed.*

The quantitative characterization of the surface waters flowing within the Oued el Hai-Biskra watershed is difficult because of their ephemeral regime and the few stream gauge stations located in the region. The available flow rate measurements come from the stations of El Kantara, Djemorah, and El Melaga but datasets are irregular and discontinuous in time (Table 2.2). The El Kantara stream gauge station is located near the El Kantara village and drained the Northern part of the Oued el Hai-Biskra watershed extending over an area of 1170 km<sup>2</sup>. Two datasets are available for the station including monthly flow rate for the period 1968-1978 and 1988-1993. The Djemorah station drains an area of 620 km<sup>2</sup> in the Aures ranges. It mostly comprised the mountain domain of the Oued Abdi-Branis watershed. Records are available for the period 1971-1978 and 1988-1993. Stream gauge records from the El Melaga station are available for a thirteen years period, from 1972 to 1985. The station is located at the base slope of Djebel bou Rhezal (Fig. 2.4), before the confluence of the Oued el Hai-Biskra and the Oued branis. Original records for all the stations were not available. Therefore, in the text will be provided a brief description of the summary graphs reported in Haouchine (2010).



*Fig. 2.4 The stream gauge station of El Melaga (Photograph courtesy of Prof. G. Ghiglieri).*

STATION	PERIOD	WATERSHED AREA [km <sup>2</sup> ]
El Kantara	1968-1978 / 1988-1993	1170
Djemorah	1971-1978 / 1988-1993	620
El Melaga	1972-1985	3080

Table 2.2 Summary of the stream gauge stations located within the Oued el Hai-Biskra watershed, periods of available flow rate measurements, and extension of the stations drainage area.

Records from the El Kantara stream gauge station for the first period dataset (Fig. 2.5) show an average flow rate of 0.62 m<sup>3</sup>/s, corresponding to 20 hm<sup>3</sup>/year. The maximum flow rates were registered in October 1969 (4.6 m<sup>3</sup>/s) and January 1977 (4.1 m<sup>3</sup>/s), while the minimum ones were measured in September 1977 and August 1978 (0.01 m<sup>3</sup>/s).

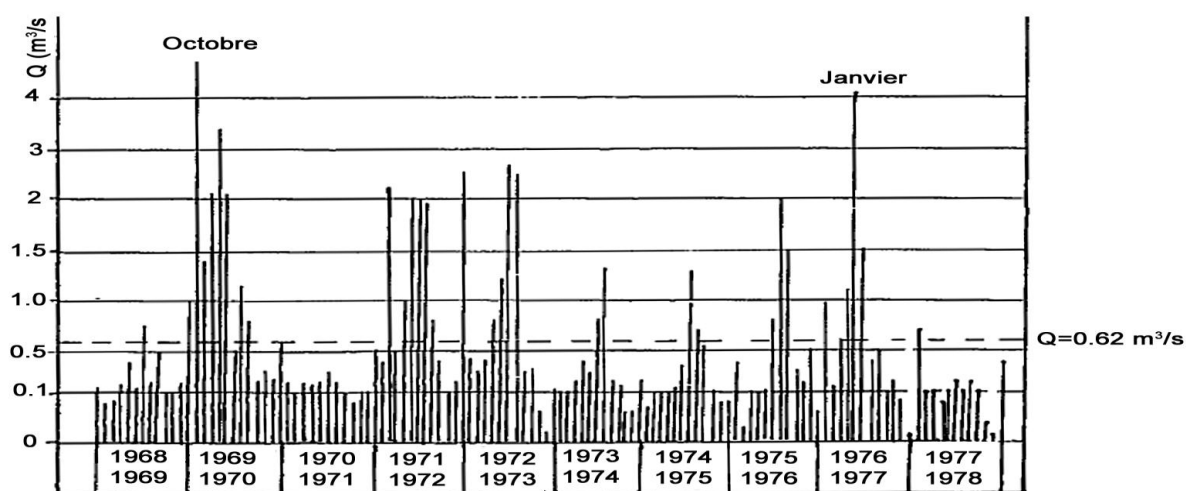


Fig. 2.5 Flow rate records from the El Kantara stream gauge station for the period 1968-1978 (from Haouchine, 2010).

Records from the 1988-1993 dataset (Fig. 2.6) show a drier situation with respect to the first dataset. Flow rates were lower than 0.5 m<sup>3</sup>/s, except for the months of March 1989 and November 1990 when maximum flow rates of 2.17 m<sup>3</sup>/s and 1.69 m<sup>3</sup>/s were measured, respectively.

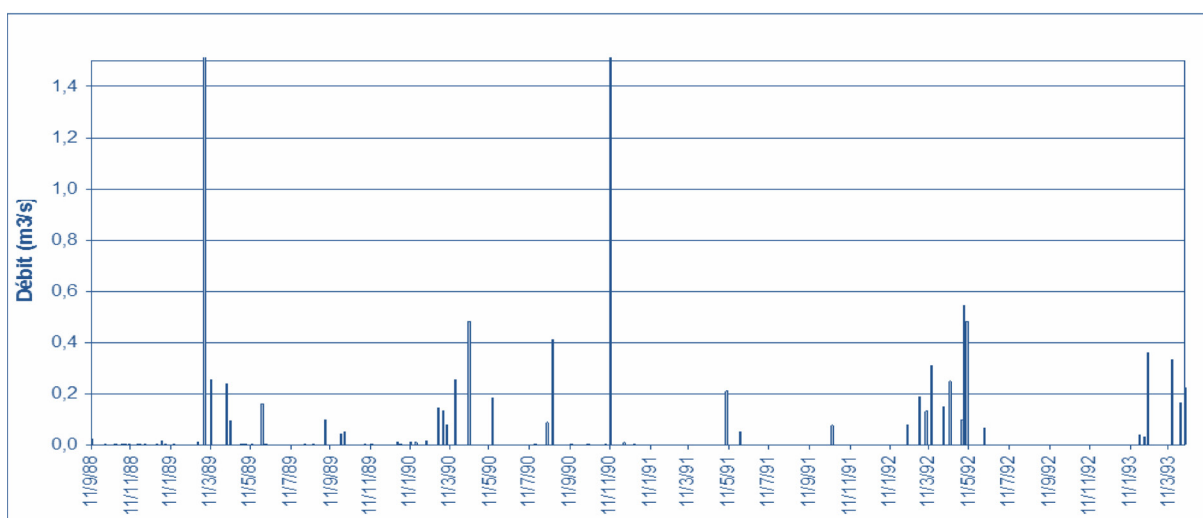


Fig. 2.6 Flow rate records from the El Kantara stream gauge station for the period 1988-1993 (from Haouchine, 2010).

Records from the Djemorah station for the period 1971-1978 indicate an average flow rate of 0.68 m<sup>3</sup>/s with exceptional flow rates of 55.8 m<sup>3</sup>/s and 15.1 m<sup>3</sup>/s measured the 04/11/1972 and 30/11/1972, respectively (Fig. 2.7) (Haouchine 2010).

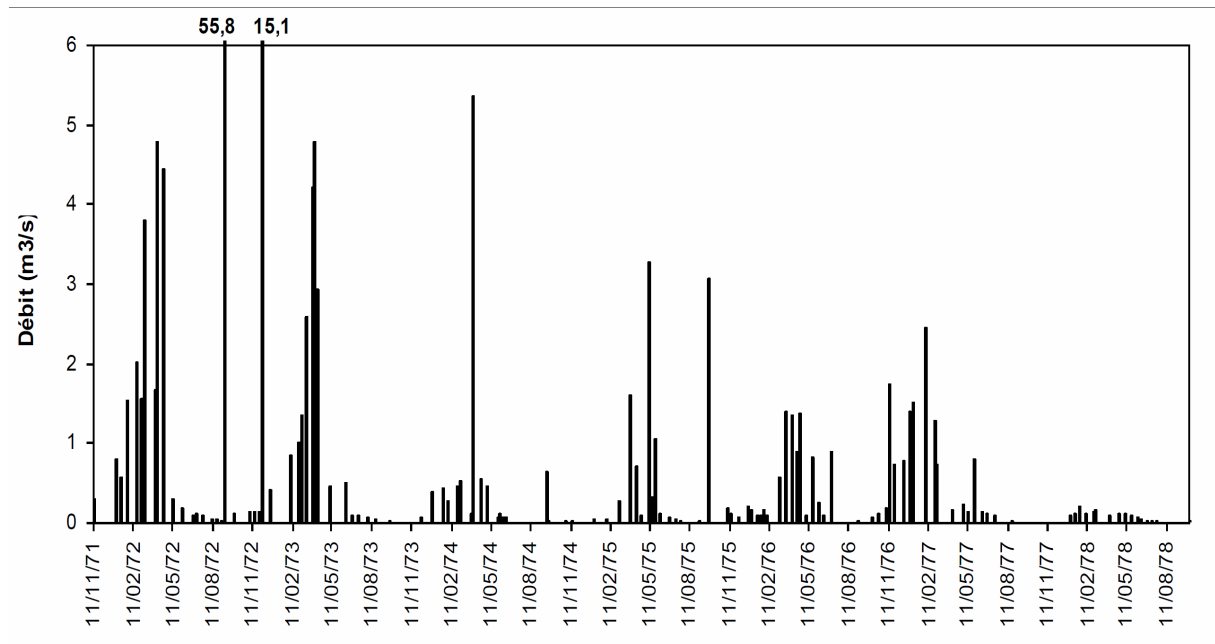


Fig. 2.7 Flow rate records from the Djemorah stream gauge station for the period 1971-1978 (from Haouchine, 2010).

The set of measurements for the period 1988-1993 (Fig. 2.8) indicate a dry period with flow rates lower than 1 m<sup>3</sup>/s. More intense floods, with flow rates of 3.12, 2.77, and 5.69 m<sup>3</sup>/s, were registered the 25/05/1989, 11/11/1990, and 07/11/1992, respectively.

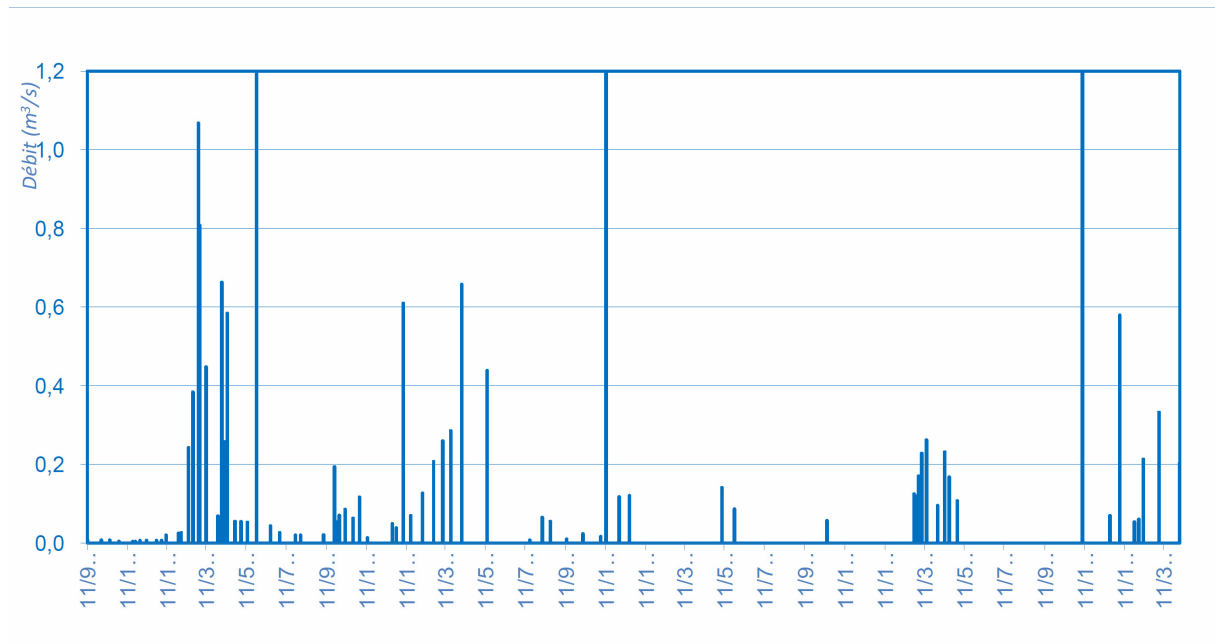


Fig. 2.8 Flow rate records from the Djemorah stream gauge station for the period 1988-1993 (from Haouchine, 2010).

For the El Melaga station, only one set of records is available and covers the period 1972-1985 (Fig. 2.9). The flow rate is variable and ranges from 0.042 to 5.92 m<sup>3</sup>/s, with an average of 1.12 m<sup>3</sup>/s. No exceptional events were registered in this time series.

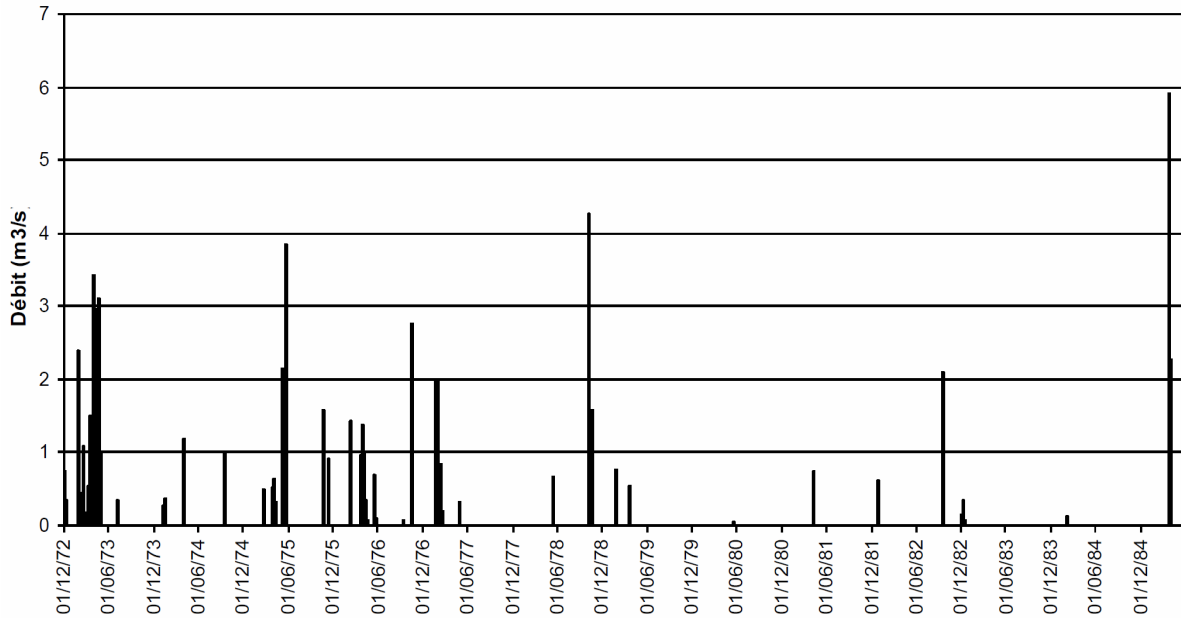


Fig. 2.9 Monthly flow rate measured at the El Melaga stream gauge station for the period 1972-1985 (from Haouchine, 2010).

### 2.1.2 METEO-CLIMATIC CONTEXT

The Biskra and Batna region is characterised by hot and dry climate, stretching over the semiarid, arid, and pre-desertic zones. The analysis of the annual cumulative precipitation measured at the Biskra rain gauge station (ONM – Office National de la Meteorologie) for the period 1974-2011 shows that precipitations are extremely variable and range from 31.9 mm in 1993 to 407.1 mm in 2009. The average for the whole period is 131.1 mm. The bar chart (Fig. 2.10) shows an increasing precipitation trend which is mostly related to the high rainfall rate of the last decade of measurements. In fact, cumulative rainfall measured in 1999 (222,3 mm), 2004 (237.6), 2009 (407.1), and 2011 (296.5) are higher than the average calculated for the same period 1999-2011 (168.7 mm).

Monthly mean rainfall analysis (Fig. 2.11) shows that summer is the driest season with the minimum rainfall occurring in July (0.59 mm). During the other seasons, precipitations are rather well distributed even if they do not exceed 20 mm/month. The rainiest months are January (18.9 mm), April (17.6 mm), and November (15.9 mm).

The monthly means of the maximum, average, and minimum temperatures, measured at the Biskra station for the period 1990-2000, are illustrated in Fig. 2.12. Monthly mean precipitations for the same period are also illustrated. Max temperatures of 44 °C are registered in July and August and are always higher than 20 °C during the whole year. Min temperatures occur in the winter months reaching 3 °C in December, January, and February while in summer minimum temperatures reaches 23 °C. The 1990-2000 monthly mean precipitations have roughly the same pattern of the 1974-2011 period.

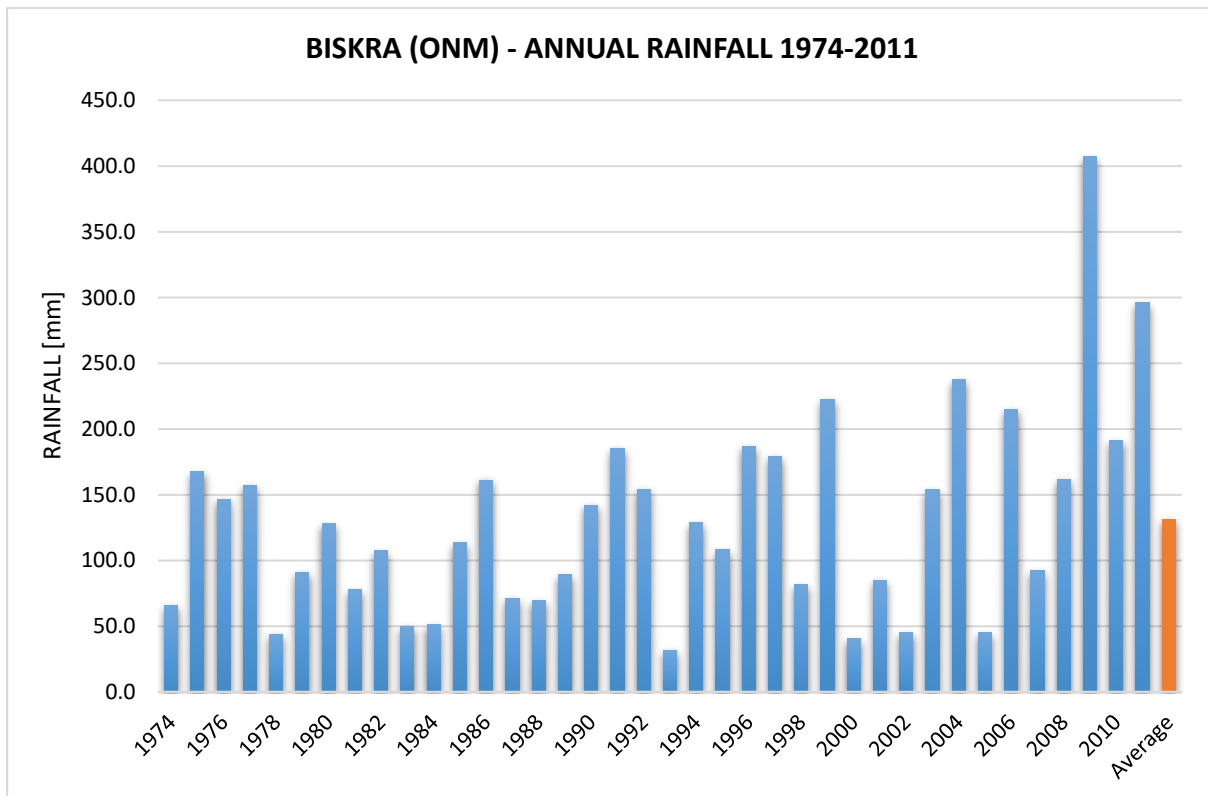


Fig. 2.10 Measured cumulative annual rainfall measured at the rain gauge station of Biskra for the period 1974-2011 (ONM).

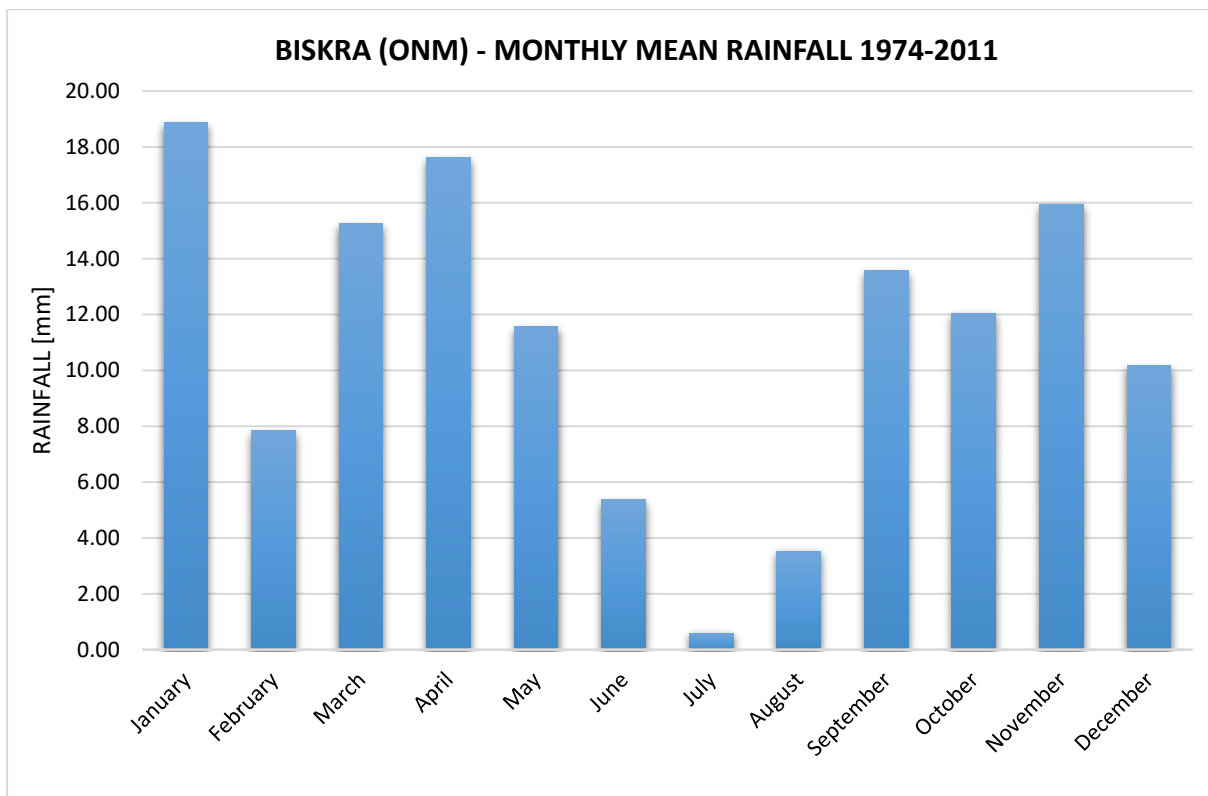


Fig. 2.11 Monthly mean rainfall measured at the rain gauge station of Biskra for the period 1974-2011 (ONM).



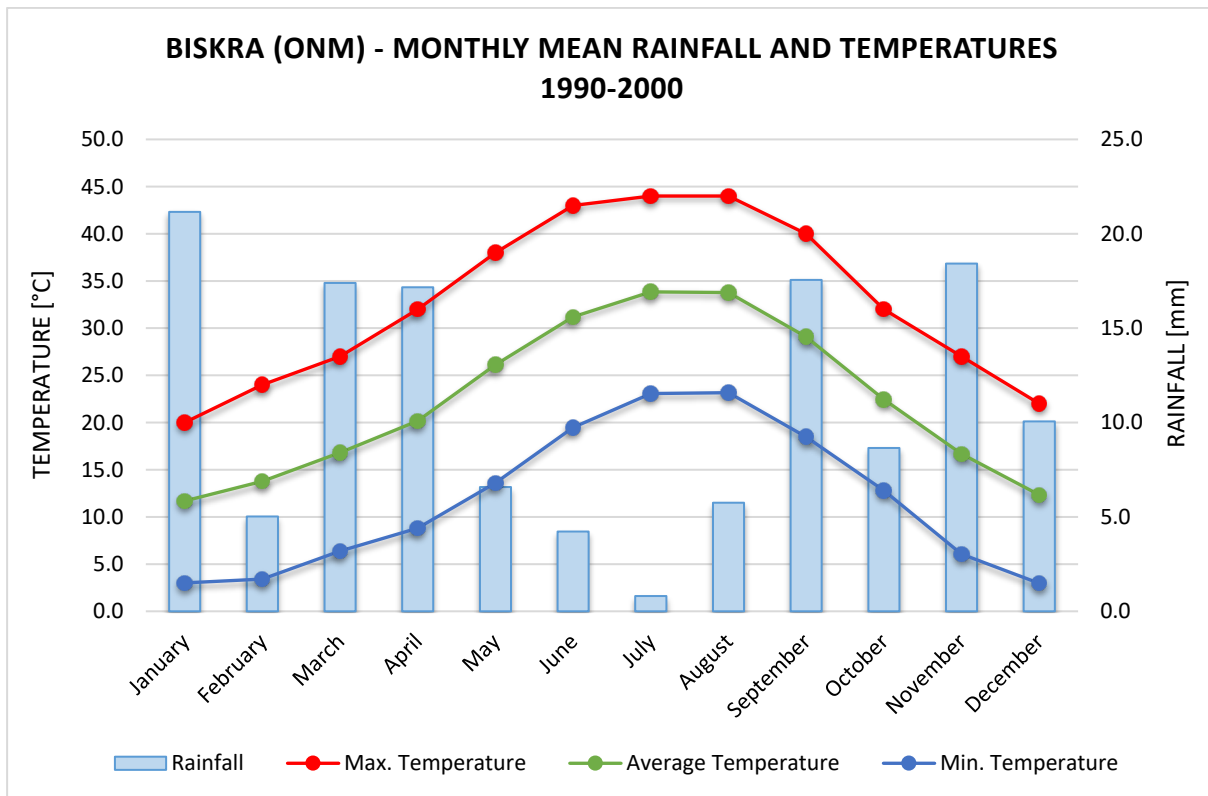


Fig. 2.12 Monthly mean rainfall and temperatures measured at the Biskra station for the period 1990-2000 (ONM).

## 2.2 GEOLOGICAL ASSESSMENT

Three main geological domains characterise the Northern Algeria, namely the Sahara Platform, the Atlas Mountains, and the Tell-Rif orogenic system (Frizon de Lamotte et al. 2000) (Fig. 2.13). The Sahara Platform is a relatively stable region where the Alpine tectonics produced just local and marginal effects. Here, weakly deformed sedimentary deposits of Paleozoic to Mesozoic Era cover the Precambrian basement, which was deformed during the Pan-African orogeny (Ziegler 1988; Boote et al. 1998). A wide structural lineation known as South Atlantic Front (SAF) (Askri et al. 1995) divides the Sahara Platform from the Atlas Mountains domains.

In Northern Algeria, the Atlas Mountains include the Saharan Atlas and the Aures. These constitute a fold-thrust belt (Bracène and Frizon de Lamotte 2002) developed along zones of crustal weakness inherited from rifting extension. The rifting phase is associated with the opening of both Atlantic and Tethyan oceans during Late Triassic to Liassic (Mattauer et al. 1977; Stets and Wurster 1977; Laville and Petit 1984; Winterer and Hinz 1984; Andrieux et al. 1989; Ait Ouali 1991; Stets 1992). Then, the convergence between the Eurasian and African plates led to the tectonic inversion of the Mesozoic basins and the building of the Atlas Mountains domain (Mattauer et al. 1977; Giese and Jacobshagen 1992; Guiraud and Bosworth 1997) through two main compressional events:

- ATLAS EVENT (Lower Eocene–Lutetian) (Laffitte 1939; Guiraud 1975) is characterised by an NW-SE shortening trend, with the development of several structures with an NE-SW orientation and a contemporaneous uplift. A phase of relative inactivity follows in the Miocene (Bracène et al. 2003) with the deposition of molasse deposits that covered the oldest formations.
- VILLAFRANCIAN EVENT (Miocene) (Boudjema 1987; Frizon de Lamotte et al. 1990) is characterised by an N-S shortening trend and produced the tilting of the Miocene formations and the development of fold structures with an E-W axial trend.

The Algerian High Plateaux is a rigid core located between the Atlas and the Tell-Rif system. It is constituted by a thin or even absent Meso-Cenozoic cover overlying more or less metamorphosed Paleozoic rocks (Frizon de Lamotte et al. 2000). The Tell-Rif system is considered the former southern margin of the Tethys Ocean that roughly underwent the same tectonic history as the Atlas system (Frizon de Lamotte et al. 2000). It includes the remnant of the ocean floor deposits ("flysch" domain) that covers the remains of the northern Tethys margin (internal zones domain) (Durand-Delga and Fontboté 1980; Bouillin 1986; Cattaneo et al. 1999).

The study area mostly extends over the Southwestern slope of the Aures Mountains, at the boundary with the Saharan Platform (Fig. 2.13).

### 2.2.1 REVIEW OF THE LITHOSTRATIGRAPHIC SUCCESSION AND STRUCTURES

This section provides the lithostratigraphic review of the Mesozoic and Cenozoic formations cropping out in the study area, and the description of the main geological structures recognisable at cartographic scale (Fig. 2.14).

An alternation of Triassic evaporitic gypsum and terrigenous clastic rocks of represent the oldest formations cropping out in the study area. They occur for diapirism phenomena and constitute isolated reliefs, such as Djebel el Melah. The permeability of such formation is high, and it plays a major role in conditioning the salinity of surface and ground waters.

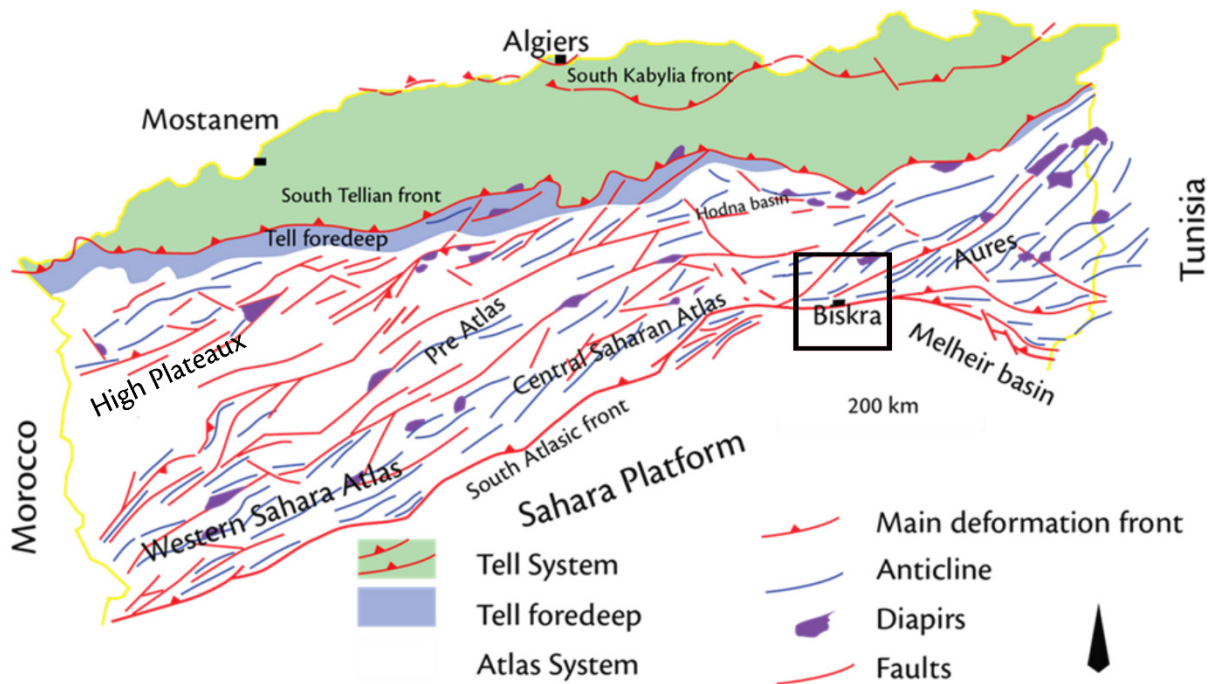


Fig. 2.13 Structural geological sketch map of northern Algeria (modified from Bracène et al., 2002).

A succession of marls, dolostones, and limestones of internal platform environment constitute the Jurassic formations. The most extended outcrop occurs at Djebel el Azreg location, as the core of a broad anticline. Other outcrops occur at Djebel Kahla but with minor extension.

Cretaceous formations widely crop out in the study area, being well known and well described in the literature. The Lower Cretaceous consists of a succession of Barremian to Albian Age formations. In particular, terrigenous clastic rocks of continental environment (Laffitte 1939; Vila 1980; Wildi 1983; Bureau 1986; Kazi Tani 1986) constitute the Barremian Stage, followed in the succession by the Orbitulina limestones of Aptian Age (Sn Repal 1970). Cross-bedded sandstones make up the base of the Albian formation, and an alternation of clay and marls followed by limestones rocks close the sequence (Bracène and Frizon de Lamotte 2002). The Upper Cretaceous (Kieken 1974; Guiraud 1975; Bureau 1986; Kazi Tani 1986) consists of an alternation of marls and gypsum of Cenomanian Age. Limestones and marls intercalation of Turonian and Senonian Age complete the succession that, for the whole Upper Cretaceous, reaches a total thickness of about 2000 m.

The Paleogene succession lies over the Mesozoic sequence. It is composed of a series of marls, massive limestones, dolostones, and gypsum of Eocene Epoch (Sn Repal 1970; Kieken 1974; Guiraud 1975) and arenaceous facies with alternation of clays, siltstones, and gypsum of Oligocene Epoch (Bracène and Frizon de Lamotte 2002).

The Neogene succession overlies the above-described formation in stratigraphic discordance. It is constituted by conglomerates with sandstones intercalation, clays, and limestones levels of Miocene Epoch, and by the alternation of Pliocene sandstones and marly gypsum.

The Quaternary deposits consist of aeolian sands and loose sediments of the wadi alluvium and alluvial fan deposits. They occur in the plains and depressed zones, but also at the

piedmont slope and within the alluvial valleys as filling materials. Thickness ranges from a few to tens of metres.

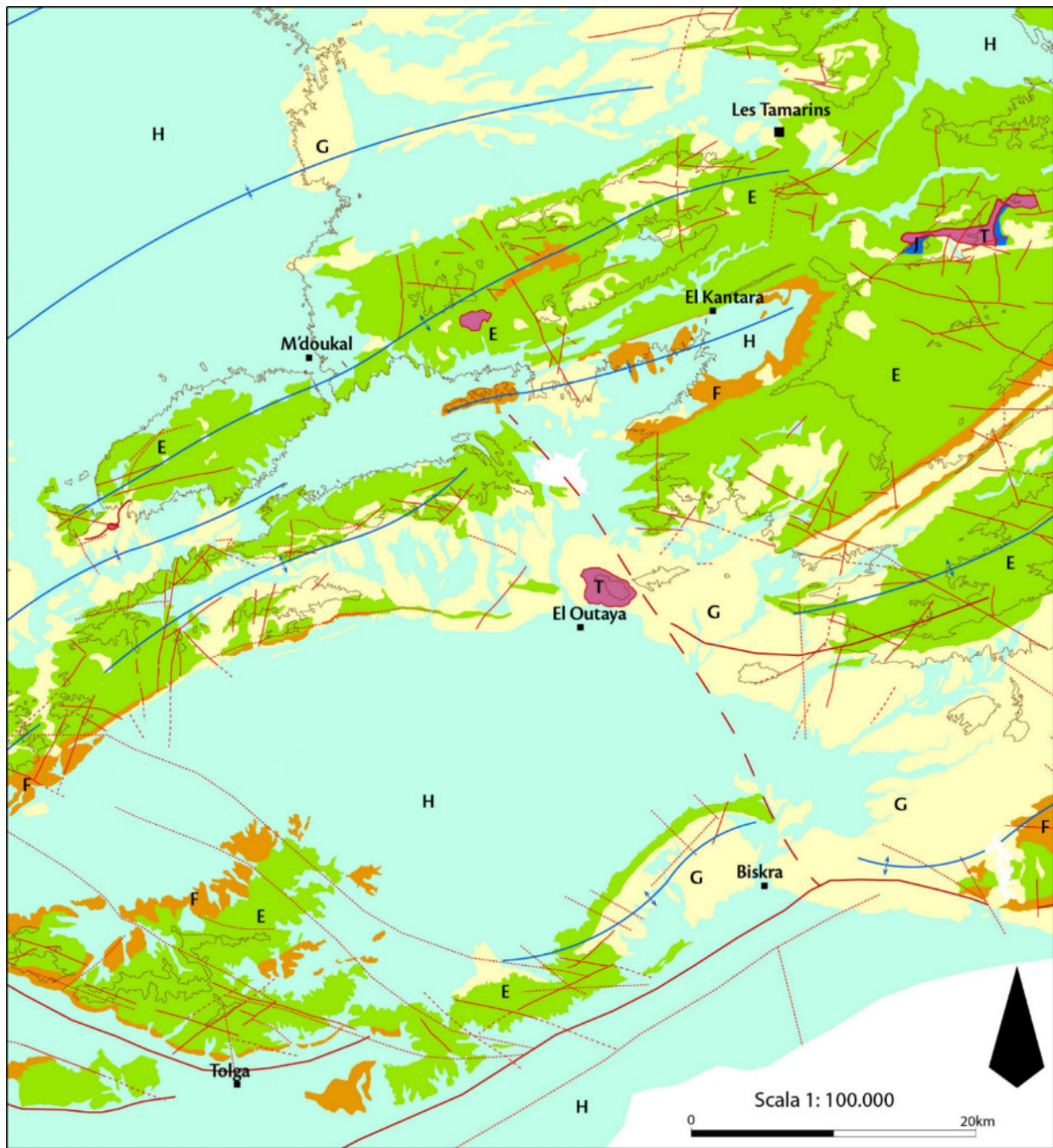
### 2.2.2 TECTONIC SETTING

The characterisation of the tectonic framework was developed through the interpretation of the available cartography and literature. The study area is characterised by a complex interference of two different system of folds, displaced by numerous strike-slip faults and thrusts (Fig. 2.14, Fig. 2.15) (Buttau et al. 2013). The oldest recognizable structures are a set of folds NE-trending that involved the formations of Triassic Age to Eocene Epoch: Dovar Sefiane anticline (ADS), Douar Seggana syncline (SDS), Djebel Metlil anticline (ADM), El Kantara syncline (SEK), Mechtat ez Zmale anticline (AMZ), El Outaya syncline (SEO), Amentane anticline (AA), Branis syncline (SB), and Biskra anticline (AB) (Fig. 2.15, Fig. 2.16). At cartographic scale, these folds can be considered almost cylindrical, with axes dipping towards SW and NE; these features give the folds the typical "whale back" geometry. The open folds are slightly asymmetric, SE-verging, with sub-vertical NE-trending axial planes; the wavelength is about 10 km and the amplitude 1.5 km. Lower order folds are visible in a discontinuous way at cartographic scale, depending on the involved lithotype, and the wavelength ranges from 10 m to 100 m.

Fold and fault accidents related to the Villafranchian phase are characterised by NW-trending axes and have deformed the first set of folds. They are discontinuous along the axis trend due to the interference with the older NE-trending folds and are recognisable at cartographic scale only in the NE sector respect to Biskra (Fig. 2.14, Fig. 2.15). These open folds can be considered almost cylindrical, symmetric, and with sub-vertical axial planes.

Wavelength and amplitude are 5 km and 500 m, respectively. At cartographic scale, the Sefiane synform (ss) and the El Kantara antiform (ak) are the best observable NW-trending folds. More folds with those trending features can occur in the region, but they are not well exposed because hidden by younger deposits.

Several normal and reverse faults of variable orientation were mapped (Fig. 2.14, Fig. 2.15) and they predate the oldest fold systems. The reverse faults are the most important for along-strike continuity (Guiraud et al. 2001). They are located in the flanks of the NE-trending antiforms affecting the Mesozoic formations and, in some cases, are buried by Cenozoic deposits (Fig. 2.14). The above-described folds and reverse faults are dislocated by right lateral strike-slip faults NNE-striking, well recognisable in the eastern part of the study area (Bouhmama village), that interrupt the axial continuity of the NE-trending folds (Fig. 2.14, Fig. 2.15). Even if these faults do not always outcrop because overlain by recent Quaternary sediments, they are recognisable throughout the deformations induced in the structures. The Biskra fault (FB) is a vertical strike-slip (dextral) fault that deforms the great Biskra anticline (AB), the Amentane anticline (AA), and the Mechtal ez Zmala anticline (AMZ). It represents the most important structure that crosses the region of Biskra, whereas the displacement produced is at least 700 m.



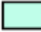








<b>Geologic legend</b>		<b>Simbology</b>	
	<b>H Holocene:</b> Evolving alluvium, colluvial, and aeolian deposits.		Axial plane trace of synform
	<b>G Neogene:</b> Clays, marls, and arenaceous marls.		Axial plane trace of antiform
	<b>F Paleogene:</b> Sandstones, marls, clays, and conglomerates.		Undefined, certain, and uncertain fault
	<b>E Cretaceous:</b> Limestones, marls, and sandstones.		
	<b>J Jurassic:</b> Limestones, crystalline dolomia, and marls.		
	<b>T Triassic:</b> Gypsum, clays, and dolomia.		

Fig. 2.14 Geological sketch map of the Biskra and Batna region showing the lithostratigraphic successions and the main structural features.

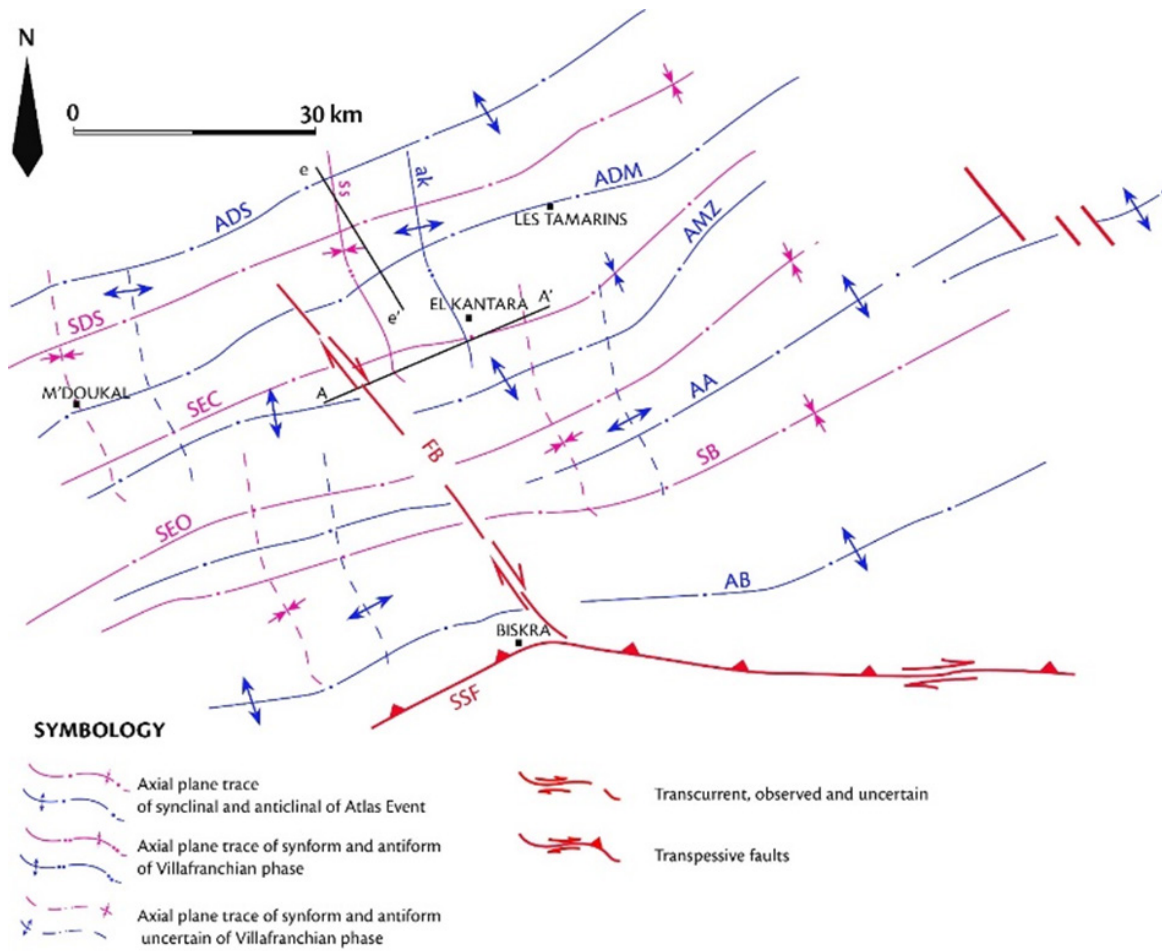


Fig. 2.15 Structural sketch map of the region of Biskra; the SSF separates the Saharan Atlas-Aures domain, to the North, from the Sahara Platform to the South (modified from Buttau et al. 2013).



Fig. 2.16 Gentle open folds in the Cretaceous formations near El Kantara village (Photograph courtesy of Prof. G. Ghiglieri).

## 2.3 HYDROGEOLOGICAL FEATURES

The above-described geological succession hosts several groundwater complexes (Fig. 2.17, Fig. 2.18). In particular, aquifers hosted by the Cretaceous to Neogene formations are commonly grouped into two aquifer systems (MdH 1980): the Complex Terminal aquifer (CT) and the Continental Intercalary aquifer (CI). Some impermeable levels interrupt the succession and are responsible for hydraulic discontinuity between aquifers. In the present section, the various groundwater systems occurring in the Biskra and Batna region will be described, including additional information about the amount and intended use of exploited water in the Biskra Province. The latter data comes from a census carried out by the Algerian National Agency for the Hydraulic Resources (ANRH) in 2008 (Benhamida and Fedal 2008) (Fig. 2.23).

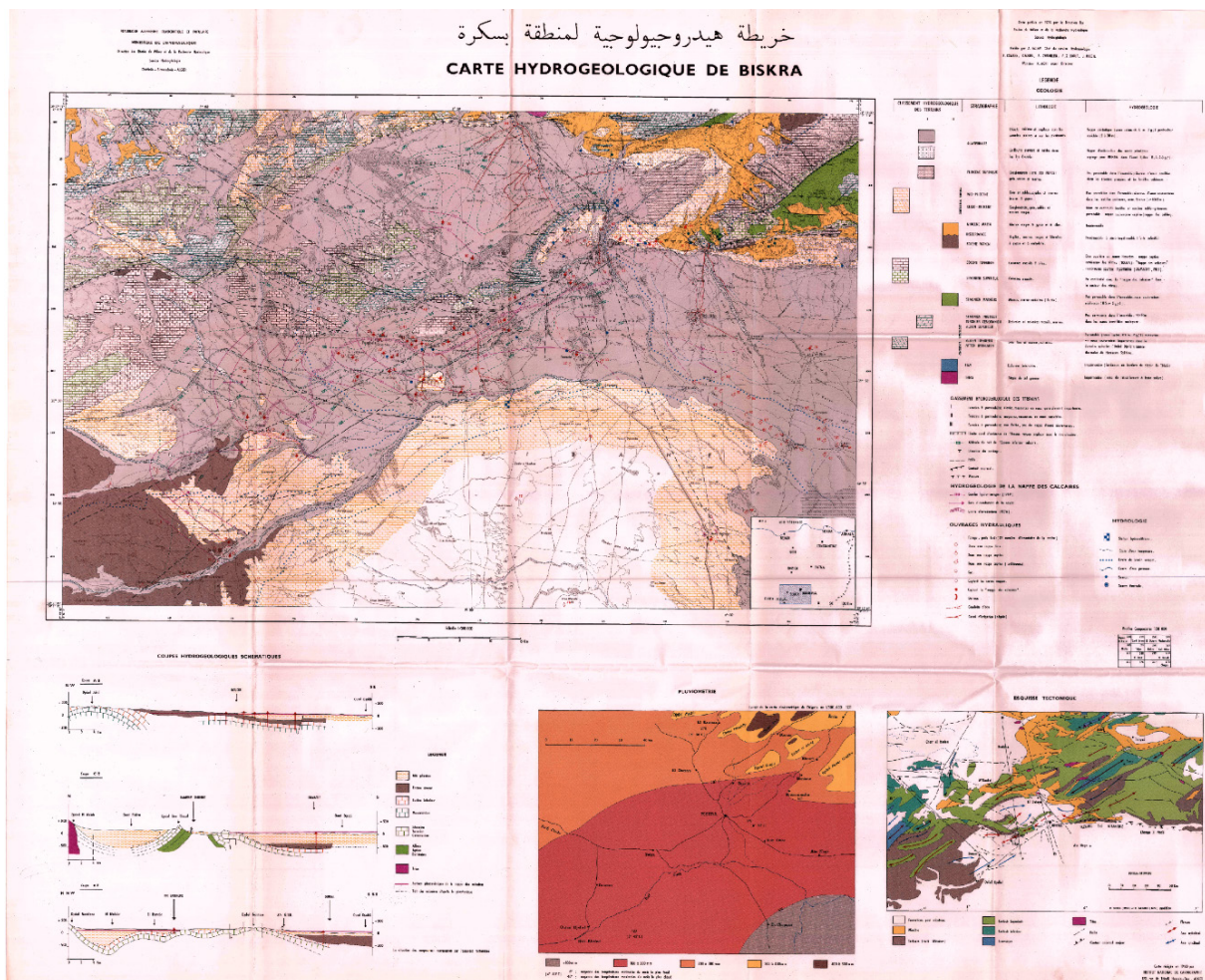


Fig. 2.17 Hydrogeological map of the Biskra area at 1:200.000 scale (MdH 1980).

**Quaternary aquifer:** Alluvial deposits within the *wadi* valleys (Fig. 2.19, Fig. 2.20) or loose sediments in the piedmont areas host the Quaternary phreatic aquifer. The thickness ranges from a few metres to tens of metres and withdrawal occurs at 1422 pumping wells extracting 60 hm<sup>3</sup>/year. Waters are generally of good quality, but exploitation for drinking water purposes (AEP) occur at only 39 wells, thus most of the wells (1383) withdraw water for irrigation (IRR).

	STRATIGRAPHIC UNIT	LITHOLOGIC DESCRIPTION	HYDROGEOLOGICAL UNIT	
H	Quaternary	Sand, clay	Phreatic aquifer	Qa
G	Mio-Pliocene	Sand, clay	Mio-Pliocene aquifer Sand aquifer	MPa As
F	Middle Eocene	Clay, gypsum	Impermeable	mEi
	Lower Eocene	Limestone	Tolga aquifer	AT
E	Maastrichtian Campanian	Limestone	Maastrichtian Campanian aquifer	MCa
	Santonian Coniacian	Clay, gypsum, salt	Impermeable	CSi
	Turonian	Limestone, dolomia	Turonian aquifer	Ta
	Cenomanian	Clay, marl, marly limestone, gypsum	Impermeable	Ci
	Albian	Limestone, marl, sandstone	Continental Intercalary aquifer	Cla
	Aptian	Sandstone, dolomia		

Complex Terminal aquifer CTA

| 100 m

Fig. 2.18 Summary of the groundwater complexes recognisable in the region of Biskra (modified from MdH 1980).





*Fig. 2.19 Panoramic view of the Oued el Hai-Biskra riverbed (Photograph courtesy of Prof. G. Ghiglieri).*



*Fig. 2.20 Detail of the deposits constituting the Oued el Hai-Biskra alluvium (Photograph courtesy of Prof. G. Ghiglieri).*

In the area of Biskra, the phreatic aquifer hosted by the alluvium of the Oued el Hai-Biskra, which is known as Inféro-Flux, is exploited for drinking water purposes. This segment is located between the Oued el Besbas confluence to the North and the morphological sluice upstream the city of Biskra to the South (Fig. 2.21).

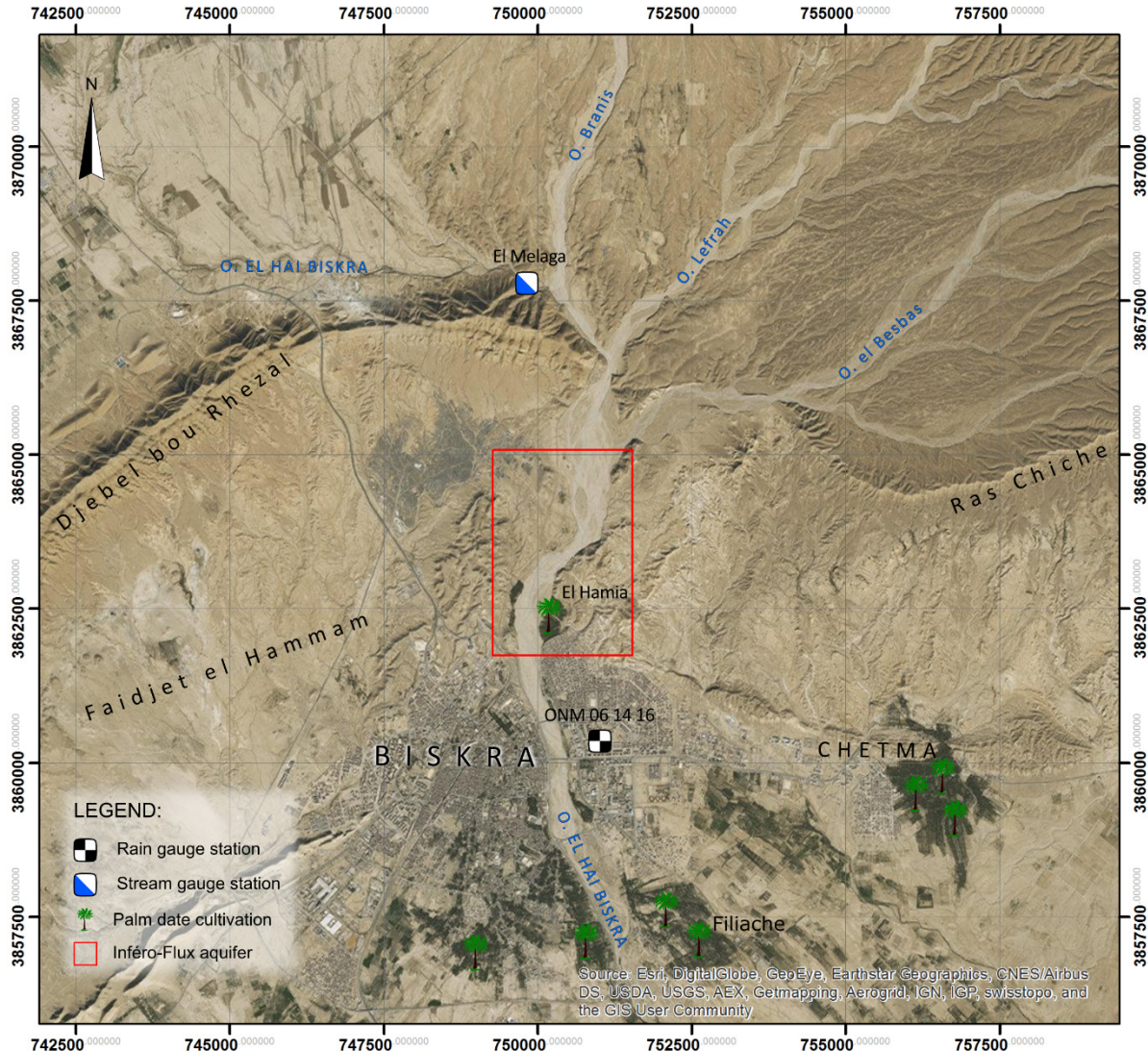


Fig. 2.21 The red box indicates the location of the productive zone of the Inféro-Flux phreatic aquifer.

From the analysis of the literature, and in particular from the SCET-COOP report compiled in 1967, emerged that the first observations conducted to understand the natural conditions of the groundwater resource in this area date back to 1861, when the aquifer yield was estimated at 300 L/s. Subsequently, in 1914 a drain was realised on the right riverside (Ain el Hamia locality), and in 1925 a yield of 200 L/s was estimated for this section of the aquifer. Other measurements at the sources of Ras el Ma (average 90,4 L/s) and Filiache (average 42,5 L/s) followed in 1952/1953 and 1951/1953, respectively. The intensive exploitation of the aquifer for irrigation and drinking water usages occurs since 1954 with the realisation of the first pumping well Benoto1 (B1). Other five pumping wells were realised from 1954 to 1960 giving a total production of 300 L/s (Table 2.3). In May 1966 the SCET-COOP carried out a piezometric survey for the characterization of the aquifer, from which the hydrogeological map illustrated in Fig. 2.22.

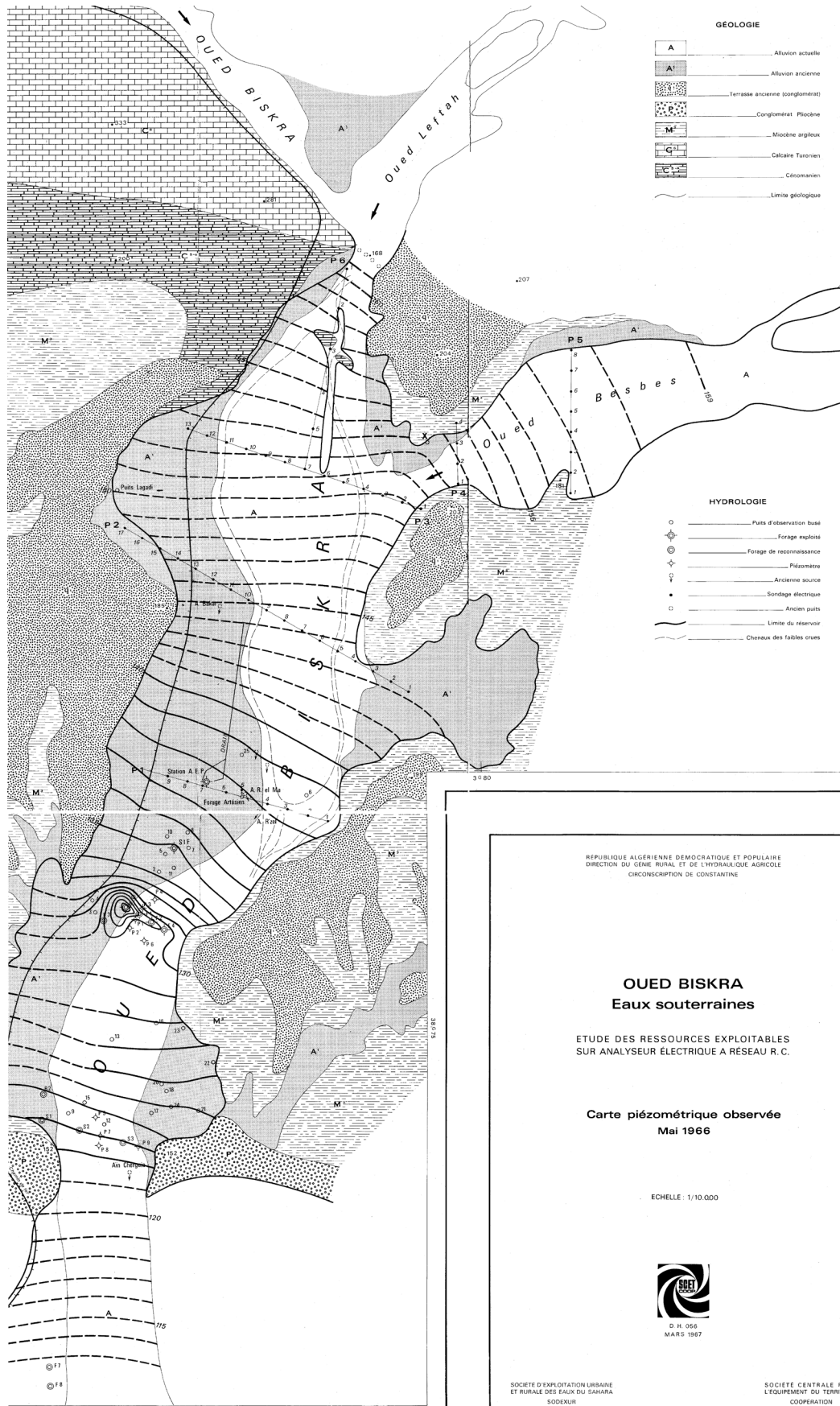


Fig. 2.22 Hydrogeological map of the Infèro-Flux aquifer based on the SCET-COOP field survey conducted in May 1966 (from SCET-COOP 1967).

WELL	UTM Z31N_X [m]	UTM Z31N_Y [m]	Z [m a.m.s.l.]	YIELD [L/s]	YIELD [m <sup>3</sup> /d]
B01	750008	3863189	133	90	7776
SIF	750246	3863483	141	40	3456
F01	750008	3863189	132	45	3888
F02	750073	3863157	132	45	3888
F04	750135	3863114	134	45	3888
AEP Stat.	750412	3863807	113	40	3456
<b>TOTAL</b>				<b>305</b>	<b>26352</b>

Table 2.3 Summary of the pumping wells occurring in the productive zone of the phreatic aquifer (survey date: May 1966 – from SCET-COOP, 1967). Z values were extracted from the SRTMGL1 DEM.

The recharge of phreatic aquifers takes place through direct infiltration of precipitations or floods waters. However, due to the small amount of efficient precipitation waters (Pe) resulting from the high evapotranspiration rate that characterises the intervention area, it is necessary to consider other sources for the aquifer alimentation. Proofs about the hypothesis of recharge from deeper groundwater systems are related to the higher temperature (31-32 °C) of springs and exploited waters with respect to the mean annual air temperature measured at Biskra (21.7 °C: SCET-COOP 1967; 26 and 29 °C: MdH 1980). Moreover, the Inféro-Flux and Maastrichtian groundwater have a similar chemical composition (SCET-COOP 1967). Indeed, the hypothesis on direct infiltration from floods is not excluded and was based on piezometric head variations corresponding to floods events during two years observations (SCET-COOP 1967).

The Complex Terminal aquifer (CT) represents a large groundwater system composed of several minor aquifers hosted by the Upper Cretaceous to Mio-Pliocene formations. Those aquifers are generally unconfined, and direct recharge could occur in the region of the Saharan Atlas, where the hydrogeological units crop out. Uncertainties on the erosion intensity that took place during the Cenozoic do not allow an estimation of the thickness of the whole CT aquifer. The Complex Terminal system includes the following aquifers (MdH 1980; Benhamida and Fedal 2008):

Mio-Pliocene sands aquifer: in the region of Biskra and Batna this aquifer has a wide areal extension and is characterised by a succession of sand and gravel levels with local clay lenses. The heterogeneity of the deposit influences the hydraulic conductivity of the aquifer that is highly variable depending on location. Its thickness ranges from 100 to 300 m and the average yield is about 15 L/s. Groundwater flow direction is toward the endorheic basin of Chott Melrhir. The Sands aquifer is the most exploited and withdrawal occurs at 5905 pumping wells. A large number of wells (5780) withdraw water for irrigation while drinking water exploitation occurs at 101 wells. Only ten wells withdraw water for industrial usages (IND). In 2008, the total exploited water was 265 hm<sup>3</sup>/year.

Middle Eocene aquitard: is represented by evaporitic and marly deposits of lagoon environment that constitute the impermeable bottom of the Mio-Pliocene aquifer and confine the Upper Cretaceous aquifers.

Limestones aquifer: limestones of Upper Cretaceous (Campanian-Maastrichtian) to Lower Eocene Epoch host this karst aquifer that has a total thickness ranging from 400 to 500 m. The exploitation of the Eocene aquifer (also known as Tolga aquifer) occurs at 2370 wells. Pumping tests done in the Tolga area show good transmissivity values ranging from 5 10<sup>-2</sup> to

20 10<sup>-2</sup> m<sup>2</sup>/s. Most of the withdrawal is used for irrigation (1341 wells), while drinking water is withdrawn from 64 wells, and only three wells extract water for industrial usages. The annual exploitation rate is 166 hm<sup>3</sup>. On the contrary, just 11 hm<sup>3</sup>/year of groundwater were withdrawn from the Maastrichtian aquifer at 65 wells. In this case, most of the wells (37) exploited water for domestic usages, while irrigation and industry water are exploited at 26 and one well, respectively.

**Coniacian-Santonian aquiclude:** the intercalation of evaporitic deposits, ranging in thickness from 100 to 300 metres, separates the Limestones from the Turonian aquifer.

**Turonian aquifer:** limestones and dolomia deposits host the Turonian karst aquifer that locally could be in hydraulic communication with the Limestones aquifer. Withdrawal for drinking water and irrigation occurs at twelve and seven wells, respectively, for a total exploitation rate of 0,5 hm<sup>3</sup>/year.

An aquiclude level constituted by an alternation of marls and gypsum deposits of Cenomanian Age separates the CT from the CI. The **Continental Intercalary aquifer (CI)** extends over the whole North Africa region. It represents one of the largest confined aquifers in the world covering a surface of about 600,000 km<sup>2</sup> and has a potential reservoir thickness that ranges from 120 to 1000 m (Castany 1982). The CI consists of several horizons with strong artesian pressure (5–25 bars) and temperatures ranging from 65 to 75 °C (ERESS 1972). The CI, in the region of interest, is identified at variable depths ranging from 1600 to 2500 m, and it is hosted by the Lower Cretaceous formations (Barremian to Albian). The annual withdrawal is 39 hm<sup>3</sup> and occurs at 19 wells. Twelve of them exploit water for domestic usages while the remaining seven wells withdrew water for irrigation.

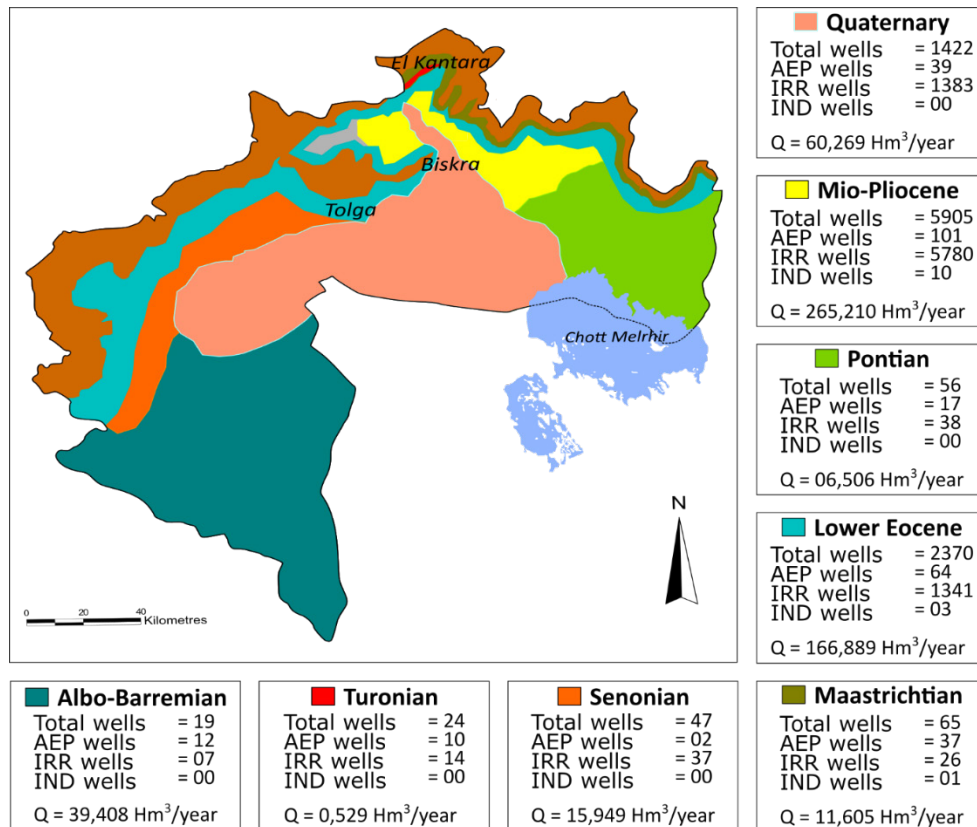


Fig. 2.23 Exploitation of groundwater resources for drinking water (AEP), irrigation (IRR), and industry (IND) in the province of Biskra (modified from Benhamida and Fedal 2008).



### 3 MATERIALS AND METHODS

Bibliographic research and direct field survey in the intervention areas represent the largest source of input data for scientific research and applications (Kaufmann and Martin 2008). In this case, adverse environmental conditions and particular political context made a direct investigation in situ difficult and onerous. Therefore, the methodology developed in the frame of the present research (Fig. 3.1) is based on the collection of data and cartography available from the literature, freely released satellite datasets, and field measurements carried out by local authorities. The aim was the reconstruction of two 3-D hydrogeological models of the study area at regional and local scale, which are fundamental in the conceptualisation of the framework affecting the groundwater circulation. The conceptualisation provides the basis of knowledge required for the design, calibration and validation of the groundwater flow numerical model developed for the productive zone of the Inféro-Flux aquifer.

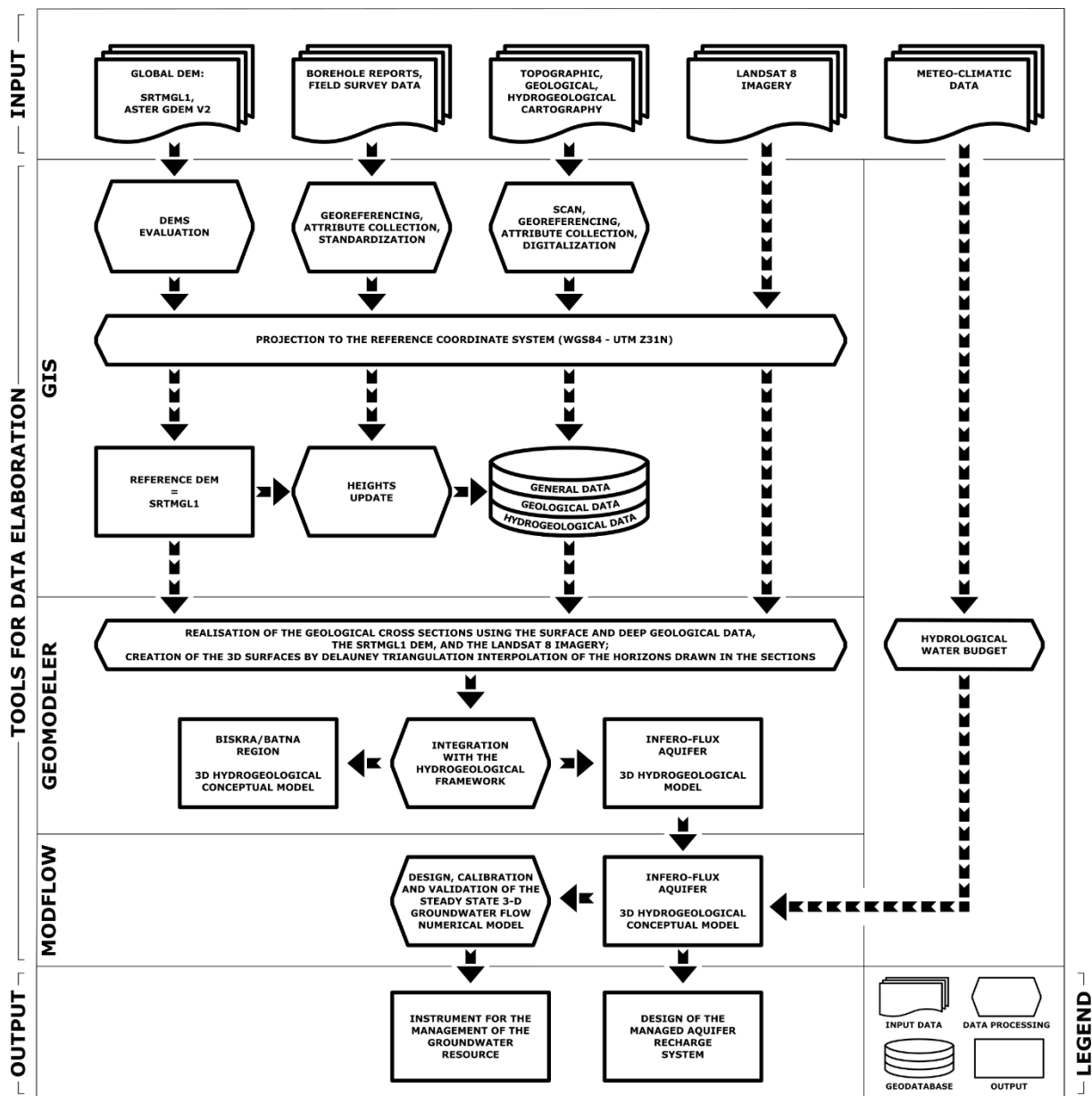


Fig. 3.1 Flow chart illustrating the methodological approach used in the present research.

## 3.1 DATA COLLECTION

### 3.1.1 DIGITAL ELEVATION MODEL (DEM)

“Digital Elevation Model (DEM) is a computational representation of the continuous variation of relief over space from which topographic parameters can be digitally generated” (Jing et al. 2014). Several methods can be used to produce DEMs including airborne and satellite-borne stereoscopic photogrammetry, RADAR/SAR interferometry, Light Detection and Ranging (LIDAR) and other traditional approaches (e.g. GPS, levelled benchmarks) (Athmania and Achour 2014). The release of the space-born Advanced Spaceborne Thermal Emission and Reflection Radiometer-Global Digital Elevation Model Version 2 (ASTER GDEM2) and the Shuttle Radar Topography Mission Version 3.0 Global 1 Arc-Second (SRTMGL1) elevation datasets provided significant advances in elevation modelling. These DEM data are Global, so they are available for most of the inhabited world areas and are free of charge (download from <http://www.earthexplorer.usgs.gov/>). Both datasets have a spatial resolution of one arc-second (about 30 m).

ASTER GDEM was built up by METI (Ministry of Economy, Trade and Industry) of Japan together with NASA (National Aeronautics and Space Administration) of United States (US). It is freely accessible starting with the 29th June 2009 (ASTER GDEM Validation Team 2009). The absolute vertical accuracy of the elevation data is 20 m (at 95% confidence). A new data set, ASTER GDEM2, was released in 2011 with 260.000 overlapping images added to the original one. The aim was to enhance the spatial resolution and the coverage accuracy of the water bodies and to reduce the occurrence of data artefacts (ASTER GDEM Validation Team 2011).

The SRTMGL1 dataset is the result of the cooperative work between the National Imagery and Mapping Agency (NIMA) and NASA. Elevation data were collected during an 11-day mission in February 2000, and the measurements were undergone using the X-band and C-band Interferometric Synthetic Aperture Radar (InSAR) sensor (5.6 and 5.3 cm wavelengths, respectively). SRTM C-band data are available over Africa at 1° X 1° tiles at one arc-second resolution (about 30 m) since the 8th October 2014. Africa is the first continent to be released after the US and its territories as the global one arc second data. The absolute height error is 5.6 m (at 90% confidence) on the African continent (Farr et al. 2007).

Global DEMs provide a good representation of the topographic surface and are widely used in studies requiring topographic data (Gesch et al. 2006a; Gesch et al. 2006b; Farr et al. 2007). Fields of application range from geomorphology to hydrology, and many others.

### 3.1.2 BOREHOLE REPORTS

Results of drilling operations undergone for geological exploration or groundwater exploitation (pumping wells) and monitoring (piezometers) are described within borehole reports, representing a primary source for underground geological information. For the present research one hundred and fifty-five (155) borehole paper reports were collected. The dataset is composed of 105 borehole descriptions published in the explanatory notes of the hydrogeological map of Biskra (MdH 1980), and of 50 reports provided by the ANRH (Fig. 3.2). In those reports, underground deposits and rocks were identified and described. Their chronostratigraphic interpretation was also provided based on the geological framework of the region. When boreholes were realised for groundwaters exploitation or monitoring, several hydrogeological and hydrogeochemical parameters were also measured and



described within the reports. Hydrogeological data included piezometric level, hydraulic conductivity (if aquifer pumping test were done) and well coating; hydrogeochemical parameters resulted from in situ and laboratory analysis on groundwaters samples included chemical and physical parameters, namely total dissolved salts concentration (TDS), temperature, pH, and concentration of major cations and anions. The boreholes location was mostly provided using the projected coordinate system “Voirol 1879 Nord Algerie Ancienne”, but sometimes the geographic coordinate system “Nord Sahara 1959 (Paris)” was used.

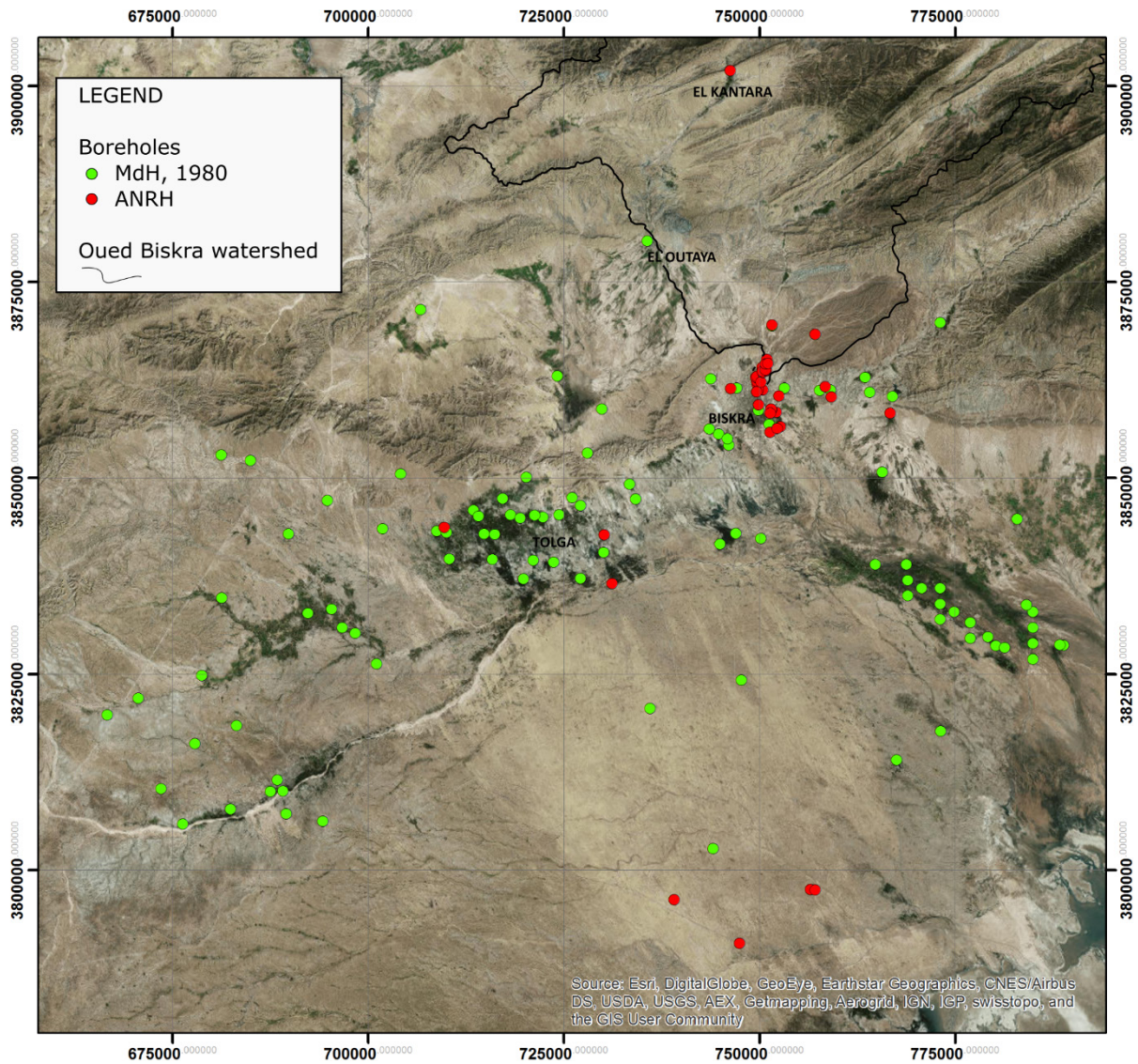


Fig. 3.2 Location of the 155 boreholes dataset. The green and the red dots represent the MdH (1980) and the ANRH boreholes respectively.

### 3.1.3 HYDROGEOLOGICAL FIELD SURVEY

In April and June 2012, May 2013, and March 2014 the WADIS-MAR team have conducted various field surveys in the Oued el Hai Biskra watershed (WADIS-MAR 2016) (Fig. 3.3). In April 2012 the census of the working pumping wells exploiting the Quaternary phreatic aquifer around the city of Biskra was undertaken. It included the determination of the water levels at 18 wells location by using an *Ejkelkamp* sounding device with acoustic and light

signal (Fig. 3.4), and the measurement of water Eh, pH, conductivity, temperature, and dissolved oxygen using the *WTW Multi3410* multi-parameter sensor. A total of 96 water samples were collected for chemical and multi-isotopic characterisation in June 2012, May 2013 and March 2014 at 73 control points. The control points included 64 wells for groundwaters, two thermal springs, one freshwater spring, five streams for surface water, and one rainwater sample. Springs and surface water samples were directly collected whereas groundwater samples were collected from previously installed pumps. Physico-chemical parameters (pH, temperature, electrical conductivity - EC, dissolved oxygen - O<sub>2</sub>, redox potential – Eh, and TDS) were measured in situ, directly in the springs or streams water flow whereas in the wells a flow cell was used to avoid contact with the atmosphere. Water samples were stored in plastic bottles and completely filled to avoid oxidation of species in contact with atmosphere.

Additionally, 12 solid samples of sulphates and saline soils were collected for the characterisation of their isotopic composition and mineralisation. All the operations were conducted according to the “*WADIS-MAR quick guide for groundwater sampling*” (WADIS-MAR 2013).

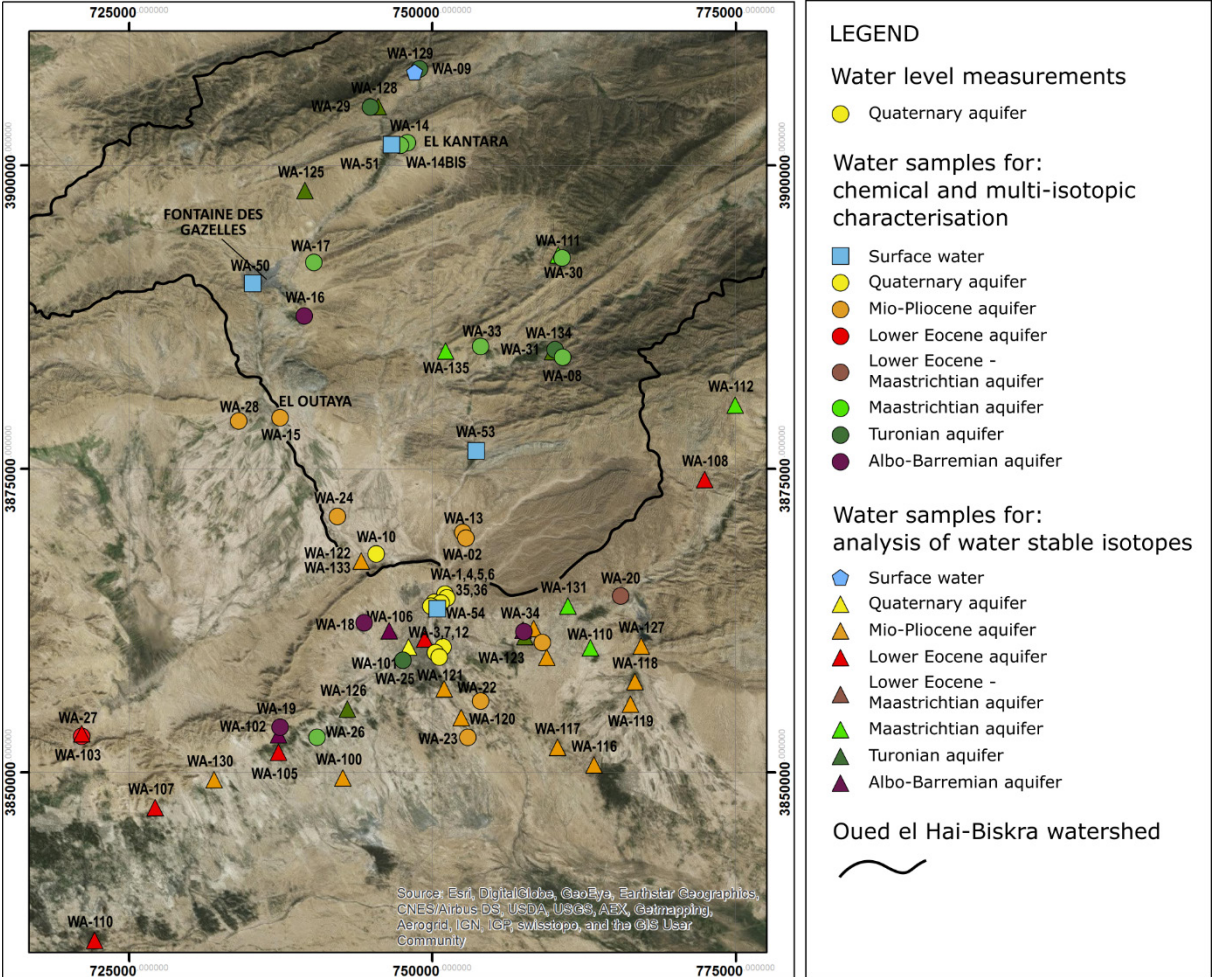


Fig. 3.3 Location of the water points collected during the various field surveys carried out in the frame of the WADIS-MAR Project (modified from WADIS-MAR 2016).



Fig. 3.4 Piezometric level measurements during WADIS-MAR survey (Photograph courtesy of Prof. G. Ghiglieri).

#### 3.1.4 CARTOGRAPHIC DATA

Cartographic data is a common input data easily collectable from the literature. Several topographic (n.18), geological (n.09), and hydrogeological (n.02) maps were collected at different scales, ranging from 1:10.000 to 1:200.000. Various spatial referencing systems were used to geographically locate the maps' areas. They included the "WGS\_1984" and "Nord\_Sahara\_1959\_(Paris)" geographic coordinate system (GCS), and the "Nord\_Sahara\_1959\_UTM\_Zone\_31N" and "Voirol\_1879\_Nord\_Algerie\_Ancienne" as projected coordinate systems (PCS). A summary of the collected cartographies and their characteristics is reported in Table 3.1.

#### 3.1.5 LANDSAT IMAGERY

Landsat is a joint effort of USGS and the NASA. Since the launch of the Earth Resources Technology Satellite (ERTS-1, which was later renamed Landsat1) in 1972, Landsat satellites provide continuous space-based images of the Earth's land surface. After Landsat1, the launches of Landsat2, Landsat3, Landsat4, and Landsat5 followed in 1975, 1978, 1982, and 1984, respectively. The launch of Landsat6, in 1993, ends unsuccessfully. At the moment, Landsat7 and Landsat8, which were launched in 1999 and 2013, respectively, continue to provide global data. Landsat8, in particular, is equipped with the push-broom Operational Land Imager (OLI) and the Thermal Infrared Sensor (TIRS). The OLI sensor collects data with a spatial resolution of 30 m in the visible, near Infrared (near-IR), and Short Wave Infrared (SWIR) wavelengths regions, and a 15 m resolution data for the panchromatic band. It also contains a deep blue band for coastal-aerosol studies and a band for cirrus cloud detection.

N°	MAP NAME	SCALE	SOURCE	COORDINATE SYSTEM
<b>TOPOGRAPHIC CARTOGRAPHY</b>				
01	Feuille L-M-07-08 – Ain Rich	1:200.000	IGN, 1966	
02	Feuille L-M-09-10 – Messaad	1:200.000	IGN, 1965	
03	Feuille N-O-07-08 – Biskra	1:200.000	IGN, 1964	
04	Feuille N-O-09-10 – Ourir	1:200.000	IGN, 1966	GCS: WGS 1984
05	Feuille P-Q-07-08 – Zeribet el Oued	1:200.000	IGN, 1964	GCS: Nord Sahara 1959 (Paris) PCS: Nord Sahara 1959 UTM Zone 31N
06	Feuille P-Q-09-10 – Bordj el Hamraia	1:200.000	IGN, 1961	
07	Feuille N°257 – Djebel Sahbana	1:50.000	IGN, 1956	
08	Feuille N°258 – M'Doukal	1:50.000	IGN, 1956	GCS: WGS 1984
09	Feuille N°259 – El Kantara	1:50.000	IGN, 1960	GCS: Nord Sahara 1959 (Paris)
10	Feuille N°260 – Menaâ	1:50.000	IGN, 1953	PCS: Voirol 1879 Nord Algerie Ancienne
11	Feuille N°288 – Djebel Dokhane	1:50.000	SAG, 1961	GCS: Nord Sahara 1959 (Paris)
12	Feuille N°289 – Oued Salsou	1:50.000	SAG, 1960	PCS: Voirol 1879 Nord Algerie Ancienne
13	Feuille N°290 – El Outaya	1:50.000	IGN, 1952	GCS: WGS 1984
14	Feuille N°291 – Mchounech	1:50.000	IGN, 1955	GCS: Nord Sahara 1959 (Paris) PCS: Voirol 1879 Nord Algerie Ancienne
15	Feuille N°318 – Chaiba	1:50.000	SAG, 1960	GCS: Nord Sahara 1959 (Paris)
16	Feuille N°319 – Tolga	1:50.000	SAG, 1961	PCS: Voirol 1879 Nord Algerie Ancienne
17	Feuille N°320 – Biskra	1:50.000	IGN, 1957	GCS: WGS 1984
18	Feuille N°321 – Sidi Okba	1:50.000	IGN, 1957	GCS: Nord Sahara 1959 (Paris) PCS: Voirol 1879 Nord Algerie Ancienne
<b>GEOLOGICAL CARTOGRAPHY</b>				
01	Aures	1:200.000	Laffitte, 1939	GCS: Nord Sahara 1959 (Paris)
02	Feuille NI-31_XVIII – Biskra	1:200.000	Unknown, ---	GCS: WGS 1984
03	Feuille NI-31_XXIV – Barika	1:200.000	Unknown, ---	PCS: Nord Sahara 1959 UTM Zone 31N
04	Feuille N°48 – Biskra	1:200.000	SGA, 1962	GCS: Nord Sahara 1959 (Paris)
05	Feuille L-M_07-08 – Ain Rich (N°47)	1:200.000	SGA, 1972	GCS: WGS 1984 GCS: Nord Sahara 1959 (Paris) PCS: Nord Sahara 1959 UTM Zone 31N
06	Biskra	1:200.000	Unknown, ---	PCS: Voirol 1879 Nord Algerie Ancienne
07	Feuille N°228 – Les Tamarins	1:50.000	SGA, 1998	GCS: WGS 1984
08	Feuille N°258 – M'Doukal	1:50.000	SGA, 1998	GCS: Nord Sahara 1959 (Paris)
09	Feuille N°259 – El Kantara	1:50.000	SGA, 1981	PCS: Voirol 1879 Nord Algerie Ancienne
<b>HYDROGEOLOGICAL CARTOGRAPHY</b>				
01	Biskra	1:200.000	MdH, 1979	GCS: WGS 1984 GCS: Nord Sahara 1959 (Paris) PCS: Nord Sahara 1959 UTM Zone 31N
02	Oued Biskra	1:10.000	SCET-COOP, 1967	GCS: Nord Sahara 1959 (Paris)

Table 3.1 Summary of the cartographic dataset collected and used for the present research purposes (GCS = Geographic Coordinate System; PCS = Projected Coordinate System).

The TIRS contains two thermal bands, which were designed to allow the use of split-window surface temperature retrieval algorithms; however, users are refrained from using the band 11 data due to larger calibration uncertainty (USGS 2015).

Landsat data is employed in a broad range of applications including geology, agriculture, forestry, land cover mapping, resource management, water, and coastal research (Table 3.2).

BAND NAME	L8 OLI/TIRS	WAVELENGTH	DESCRIPTION OF USE
<b>Coastal/Aerosol</b>	Band 1	0.43–0.45	Coastal areas and shallow water observations; aerosol, dust, smoke detection studies.
<b>Blue (B)</b>	Band 2	0.45–0.51	Bathymetric mapping; soil/vegetation discrimination, forest type mapping, and identifying human-made features.
<b>Green (G)</b>	Band 3	0.53–0.59	Peak vegetation; plant vigor assessments.
<b>Red (R)</b>	Band 4	0.64–0.67	Vegetation type identification; soils and urban features.
<b>Near-Infrared (NIR)</b>	Band 5	0.85–0.88	Vegetation detection and analysis; shoreline mapping and biomass content.
<b>Shortwave Infrared-1 (SWIR-1)</b>	Band 6	1.57–1.65	Vegetation moisture content/drought analysis; burned and fire-affected areas; detection of active fires.
<b>Shortwave Infrared-2 (SWIR-2)</b>	Band 7	2.11–2.29	Additional detection of active fires (especially at night); plant moisture/drought analysis.
<b>Panchromatic (PAN)</b>	Band 8	0.50–0.68	Sharpening multispectral imagery to higher resolution.
<b>Cirrus</b>	Band 9	1.36–1.38	Cirrus cloud detection.
<b>Thermal (T)</b>	Band 10	10.60–11.19	Ground temperature mapping and soil moisture estimations.
	Band 11	11.50–12.51	

Table 3.2 Display of the bands and wavelengths of Landsat 8 sensors and descriptions of how each band is best used (modified from USGS 2015).

Landsat level-1 data products are available for download at no charge, and with no restrictions from EarthExplorer (<http://earthexplorer.usgs.gov>), GloVis (<http://glovis.usgs.gov>), or the LandsatLook Viewer (<http://landsatlook.usgs.gov>) as a Georeferenced Tagged Image File Format (GeoTIFF). This product is processed to standard parameters including cubic convolution resampling, north-up (map) orientation, Universal Transverse Mercator (UTM) map projection, and World Geodetic System (WGS) 1984 datum.

### 3.1.6 METEO-CLIMATIC DATA

Meteo-climatic data are difficult to collect in regions as the one here described because of the poor number of weather stations and discontinuities of measurements. The National Meteorological Office (*Office National de Météorologie* – ONM) is in charge with weather measurements within the national boundaries. Currently, active weather stations located in the target area are the Biskra and Batna stations, but ONM measured data are only available for the Biskra station (ONM 06 14 16). The dataset includes monthly precipitation for the period 1974–2011, and average and minimum temperature for the period 1990–2000 (Table 3.3).

The TuTiempo web database provides measured weather data for many locations all over the world and was already used in similar context studies (Rödiger et al. 2014; Azooz and Talal 2015). The TuTiempo station (DUAB 60 52 50) is located in the area of the Biskra Airport, at about six km S-SW from the ONM station. It provides an almost complete set of

daily parameters including precipitations and temperatures for the period 1982-2015 (<http://en.tutiempo.net/climate/ws-605250.html>) (Table 3.3).

SOURCE: ONM		TUTIEMPO						
STATION: BISKRA – 06 14 16		BISKRA – DUAB 60 52 50						
UTM_Z31N: X: 750757 m – Y: 3860364 m		X: 749754 m – Y: 3854261 m						
ELEVATION: Z: 117 m a.m.s.l.		Z: 87 m a.m.s.l.						
YEAR	P [mm]	T [°C]	TM [°C]	Tm [°C]	P [mm]	T [°C]	TM [°C]	Tm [°C]
1974	65.8	-	-	-	-	-	-	-
1975	167.7	-	-	-	-	-	-	-
1976	146.7	-	-	-	-	-	-	-
1977	157.3	-	-	-	-	-	-	-
1978	43.5	-	-	-	-	-	-	-
1979	90.7	-	-	-	-	-	-	-
1980	128.0	-	-	-	-	-	-	-
1981	78.0	-	-	-	-	-	-	-
1982	107.5	-	-	-	119.1	22.4	27.8	17.3
1983	49.9	-	-	-	44.7	22.3	27.8	16.5
1984	51.1	-	-	-	56.9	21.5	27.0	16.2
1985	113.9	-	-	-	116.6	22.2	27.7	17.0
1986	161.2	-	-	-	126.5	22.1	27.5	16.9
1987	71.0	-	-	-	91.0	22.8	28.3	17.4
1988	69.8	-	-	-	182.6	22.9	28.4	17.6
1989	89.3	-	-	-	72.9	22.6	27.8	17.4
1990	142.1	22.7	-	12.69	144.6	22.6	27.6	17.8
1991	185.4	21.7	-	11.60	138.4	21.7	27.0	16.6
1992	154.3	21.7	-	11.68	192.5	21.8	27.2	16.6
1993	31.9	22.4	-	11.70	297.2	22.4	27.9	16.9
1994	128.9	23.0	-	12.36	342.7	23.1	28.8	17.5
1995	108.4	22.3	-	11.47	286.2	22.3	27.9	16.7
1996	186.4	21.6	-	10.68	292.6	21.6	27.1	16.2
1997	178.8	22.2	-	12.17	192.1	22.7	28.4	17.2
1998	81.8	22.1	-	11.46	101.1	22.2	28.0	16.5
1999	222.3	23.2	-	11.78	88.9	23.2	28.8	17.7
2000	40.6	22.5	-	11.86	73.2	22.7	28.5	16.6
2001	84.5	-	-	-	80.5	23.5	29.2	17.6
2002	45.4	-	-	-	60.7	22.9	28.8	16.8
2003	154.0	-	-	-	204.5	23.1	28.5	17.2
2004	237.6	-	-	-	304.1	22.3	28.1	16.5
2005	45.2	-	-	-	73.2	23.1	28.9	17.1
2006	215.0	-	-	-	144.8	22.9	28.7	16.9
2007	92.2	-	-	-	69.1	22.9	28.7	17.0
2008	161.8	-	-	-	100.1	22.7	28.6	16.9
2009	407.1	-	-	-	133.6	22.4	28.5	16.2
2010	191.3	-	-	-	198.9	22.7	28.6	16.9
2011	296.5	-	-	-	252.7	22.5	28.5	16.6
2012	-	-	-	-	126.0	23.4	29.5	17.1
2013	-	-	-	-	204.5	22.8	28.7	16.9
2014	-	-	-	-	63.8	23.5	29.5	17.3
2015	-	-	-	-	109.7	22.9	28.9	16.8
<b>AVERAGE</b>	<b>131.1</b>	<b>22.3</b>	<b>-</b>	<b>11.8</b>	<b>149.6</b>	<b>22.6</b>	<b>28.3</b>	<b>17.0</b>

Table 3.3 Cumulative precipitations and temperatures measured at the ONM and TuTiempo stations.

## 3.2 DATA HANDLING

### 3.2.1 DEMS EVALUATION

When multiple datasets are available for the same study area it is fundamental to understand their potential limitations related to particular purposes and applications through the assessment of their accuracy at local and regional scales (Jing et al. 2014). Two ASTER GDEM2 and SRTMGL1 DEM tiles were downloaded for the assessment of their appropriateness for this study. Both tiles extend over 34°00'N to 35°00'N and 5°00'E to 6°00'E (geographic projection) and cover an area of about 10200 km<sup>2</sup> (Fig. 3.5 A-B). The ASTER GDEM2 (Fig. 3.5 A) shows a minimum elevation value of -77 m and a maximum elevation value of 1096 m, the mean elevation is 150,76 m, and the standard deviation is 118,77 m. The SRTMGL1 (Fig. 3.5 B) shows a minimum and a maximum elevation value of -50 m and 1070 m respectively, the mean is 154,4 m, and the standard deviation is 116,55 m. Height statistics for both the datasets are summarised in Table 3.4.

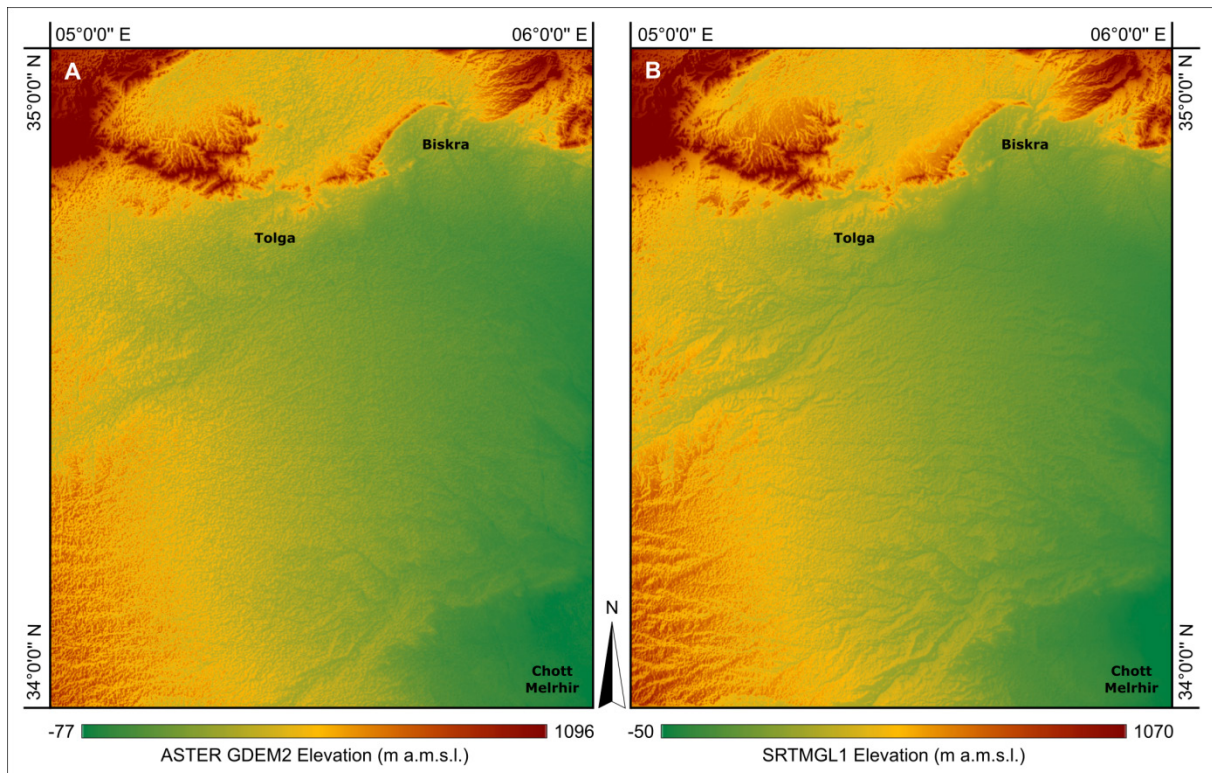


Fig. 3.5 Elevation colour ramp over the hill-shaded relief of the A) ASTER GDEM2 and B) SRTMGL1 DEM dataset.

MODEL	MIN [m]	MAX [m]	MEAN [m]	STD DEV. [m]
<b>ASTER GDEM2</b>	-77	1096	150,76	118,77
<b>SRTMGL1</b>	-50	1070	154,40	116,55

Table 3.4 Height statistics for both the ASTER GDEM2 and SRTMGL1 data sets.

Previous investigations have shown that DEMs are subjected to systematic horizontal shifts (Denker 2005; ASTER GDEM Validation Team 2009) and correct georeferencing and co-registration are necessary to ensure that corresponding pixels on image pairs represent the same geographic location. The datasets were checked for correct overlay and results showed that no horizontal shifts exist between them. Therefore, the possibility of differences caused by shifts of unchanged object boundaries is excluded (Aleksandrowicz et al. 2014). The visual

comparison between DEMs is based on the production of relative difference map (Jing et al. 2014). The aim is to locate areas of significant vertical displacement between the two data sets and to identify large-scale systematic effect and artefacts such as stripe effects (Hilton et al. 2003). The pixel-to-pixel comparison was performed using the ArcGis “raster calculator tool”. The resulting image is characterised by a slight stripe effect oriented NNE-SSW (Fig. 3.6 A-B), which Hirt et al. (2010) ascribed to the ASTER model. The statistics summary for the pixel-to-pixel comparison is shown in Table 3.5. Further visual analysis of the images and statistics performed over the endorheic area of the Chott Melrhir have shown that the ASTER GDEM2 results in sparse and sporadic negative values within it. On the contrary, the SRTMGL1 best fits the depression area with a uniform distribution of the negative values. This demonstrates that the SRTMGL1 has a higher sensitivity towards endorheic flat depression areas than the ASTER GDEM2 (Arras et al. 2017).

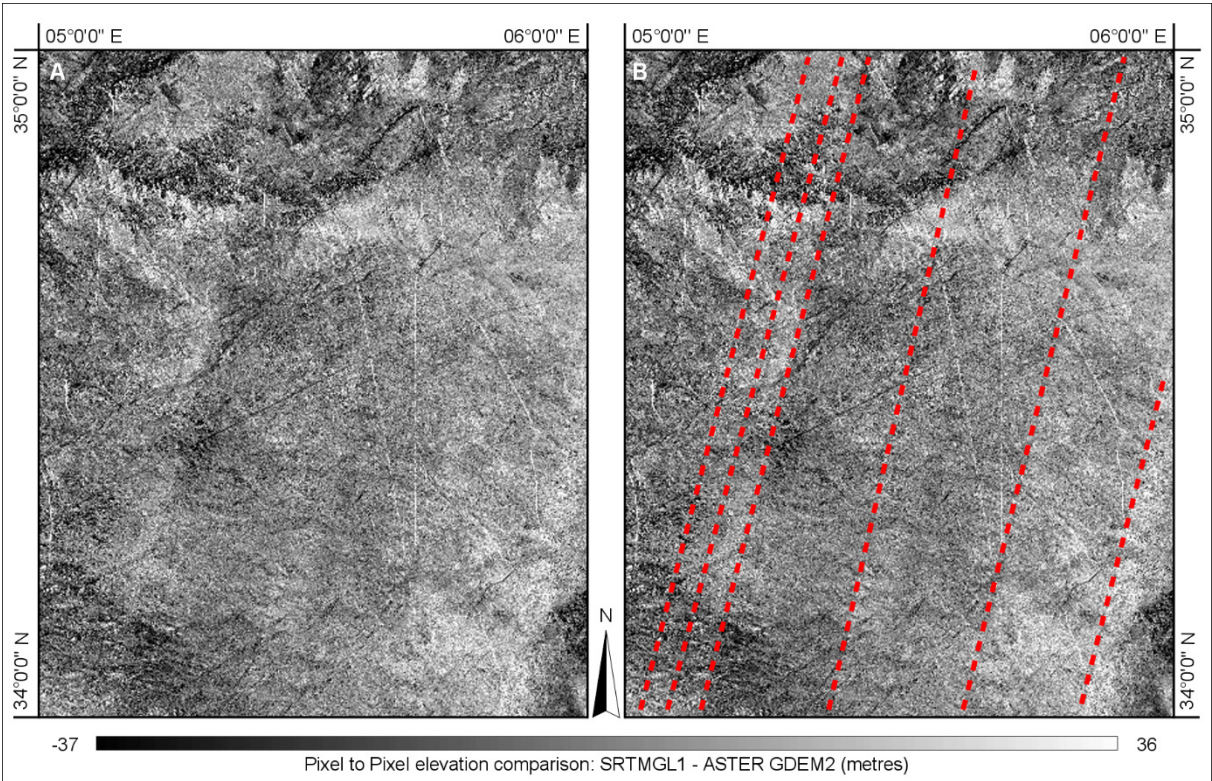


Fig. 3.6 A) Results of the Model-to-model comparison (SRTMGL1 minus ASTER GDEM2). B) The red dotted lines highlight the stripe effect. Standard Deviations stretching is applied to both the images for contrast enhancing.

MAX NEGATIVE SHIFT [m]	MAX POSITIVE SHIFT [m]	MEAN [m]	STD DEV. [m]
-108	116	3,64	6,67

Table 3.5 Statistics of the Model-to-model comparison (SRTMGL1 minus ASTER GDEM2).

The results of the DEMs evaluation demonstrate that, in the investigated area, the SRTMGL1 dataset is more accurate than the ASTER GDEM2 and therefore it was selected as reference topographic surface for subsequent elaborations.

### 3.2.2 INPUT DATA PRE-PROCESSING PHASE

The projected coordinate system WGS84 (World Geodetic System 1984) UTM (Universal Transverse of Mercator) Zone 31 North was selected as the reference coordinate system to overcome the issues related to the various local coordinate systems used for locating the



input data. The WGS84\_UTM\_Z31N is valid for regions of the world located within the 0° E to 6° E meridian of the northern hemisphere, including Northern Algeria. The ArcGIS “Projections and Transformations Tool (Data Management)” was used to change the projection of spatial data from the original coordinate systems to the reference one. The geographic transformations used to perform the task are summarised in Table 3.6.

ORIGINAL CS	REFERENCE CS	TRANSFORMATION
Nord Sahara 1959 UTM Zone 31N		Nord_Sahara_1959_To_WGS_1984_2
Nord Sahara 1959 (Paris)	WGS84_UTM_Z31N	Nord_Sahara_1959_Paris_To_Nord_Sahara_1959+_Nord_Sahara_1959_To_WGS_1984_2
Voirol 1879 Nord Algerie Ancienne		Voirol_1879_Grad_To_Voirol_1879

Table 3.6 Geographic transformation used for the projection of the local coordinate systems into the reference system WGS84\_UTM\_Z31N.

Hydrological features, such as the stream network and watershed of the Oued el Hai-Biskra system were automatically extracted from the SRTMGL1 using the ArcGIS “Hydrology tools” from the “Spatial Analyst toolbox”. The outputs were verified by comparing the extracted data with the available topographic cartography at 1:50.000 scale. Incongruences were identified in the delimitation of sub-watersheds in the area located to the east of the *Fontaine des Gazelles* dam. In this case, boundaries were manually corrected by redrawing them using the topographic map contours.

The whole cartography was scanned to obtain a digital image and then georeferenced using the ArcGIS “Georeferencing toolbar” by assigning the map coordinates to the digital image. At least four ground control points, homogeneously distributed, must be used for georeferencing a layer (Fantozzi 2013). Subsequently, the raster was then projected to the reference coordinate system using the ArcGIS “Project raster (Data Management) Tool”. The projected cartography was used as a static base map or their content was digitised to overcome the lack of native digital base maps, as described in the next section.

### 3.2.3 GEODATABASE

All the collected or newly obtained input data were evaluated and structured within an ArcGIS geodatabase (.gdb). A database (DB) within GIS environments is commonly used for storage and management of large amount of hydrogeological data (Gogu et al. 2001; Murray et al. 2003; Bonomi 2009) because of their rapid georeferencing and spatial visualisation (Chesnaux et al. 2011) and the integration of various types of datasets (Strassberg et al. 2007). Moreover, DB could be continuously updated and already organised information will be helpful in the planning of future hydrogeological investigations (Chesnaux et al. 2011) contributing in efficiency maximisation and increasing research productivity (McCarthy and Graniero 2006).

The boreholes dataset was located in the GIS environment as point shapefile using their local coordinate system and then re-projected to the reference one. General information on the wells (well name, locality, coordinates, field elevation, and depth) were inserted in the attribute table. Afterwards, through the analysis of the whole dataset, the remaining information was organised by themes (lithology, chronostratigraphic interpretation, hydrogeology, chemical analysis, and well coating), homogenised, and compiled within tables of attributes. A new progressive alphanumeric code WA000 (WadisAlgeria000) was assigned to each borehole representing the common field in the main point feature class

and related tables. The creation of relationship classes with cardinality one-to-many guaranteed the connection between the feature classes and the tables.

The various objects composing the cartographic rasters were interpreted according to their geometries and managed as polygons, polylines or points feature classes using the ArcGIS “Editing Tools”. The legend contents were also preserved through the compilation of the attributes table for each feature.

The structure of the GDB is based on three feature datasets, each one representing and hosting a particular set of thematic data (Table 3.7):

- General Input Data: general geographic and topographic data collected from topographic maps or extracted from the SRTMGL1.
- Geological Data: geological data were digitised from the available geological cartography and derived from the borehole reports.
- Hydrogeological Data: hydrogeological data were digitised from the available hydrogeological cartography or acquired from the field survey reports.

A large number of feature classes can be hosted within a feature dataset, the only limitation being that feature classes must be projected into the same coordinate system chosen as a reference for the feature dataset. New elevation values were extracted from the SRTMGL1 and used to update all the points data, since original information was sometimes missing, incomplete, or based on old topographic maps with scarce accuracy.

FEATURE DATASET	FEATURE CLASS	TYPE
<b>GENERAL INPUT DATA</b>	Province boundaries	Polygon
	Urban centres	Point
	Gauge stations	Point
	Oued el Hai-Biskra watershed	Polygon
	Oued el Hai-Biskra stream network	Polyline
<b>GEOLOGICAL DATA</b>	Biskra region Geological attitudes	Point
	Biskra region Geological structures	Polyline
	Biskra region Geological contacts	Polygon
	# Boreholes	Point
	# Boreholes: Chemical Analysis	Table
	# Boreholes: Chrono-stratigraphy	Table
	# Boreholes: Coating	Table
	# Boreholes: Hydrogeological data	Table
# Boreholes: Lithology	Table	
<b>HYDROGEOLOGICAL DATA</b>	Scet-coop_Piezometric heads	Polyline
	Scet-coop_Points	Point
	Scet-coop_lines	Polyline
	WM_Survey_Samples	Point
	WM_Piezometric heads 2012	Polyline

*Table 3.7 The structure of the GDB is based on the hierarchy of the collected input data in feature classes contained within thematic feature datasets; the # indicates the feature classes for which a relationship class exists.*

### 3.2.4 IMPLEMENTATION OF 3-D HYDROGEOLOGICAL MODELS

Two 3-D hydrogeological models undergone at regional and local scales, respectively, were realised through the interpretation of surface and deep geological data, previously structured in the GDB, and the SRTMGL1 using the geo-modelling software MOVE (Midland Valley exploration Ltd). MOVE allows the extraction of topographic profiles from DEMs and the visualisation of geological contacts and structures as intersection points along the profile. The boreholes and the associated stratigraphy were also projected to the nearest geological sections and used to calibrate the subsurface configuration of the geological contacts. A set of one (local-scale) or more horizons (regional-scale) were delineated for each section, based on a valid geometrical and consistent geological configuration of the homologous surface and deep contacts. The horizons representing the same contacts in the various sections were then interpolated to produce 3-D geological surfaces. The “point-based Delaunay triangulation” was used as interpolation method because of its efficacy in the visualisation and reconstruction of geological objects (Xue et al. 2004).

#### 3.2.4.1 3-D MODEL OF THE BISKRA/BATNA REGION

The stratigraphic succession and structures of the region derived from the available geological cartography and literature were interpreted through overlay on the hydrogeological units described in Chapter 2.3. The aim was to define the thickness and depth of the main aquifer complexes occurring in the modelled area and understand the influences of the structural framework on the groundwater circulation (Buttau et al. 2013). Fourteen geological cross sections at 1:200.000 scale were located and realised based on these interpretations (Fig. 3.7). The sections are 380 km long and perpendicular to the main geological structures. Twelve of them have NW-SE orientation, and the remaining two are oriented NE-SW. Six geological sections, with 25 km of length and variable orientations (Fig. 3.7), were realised at 1:50.000 scale to better understand and describe the structure geometries.

In practice, the geological cross-sections were manually performed and then imported, georeferenced, and digitised within the geo-modeler. All the 1:50.000 sections realised for the regional scale 3-D model are illustrated in the Annex A of the present work.

#### 3.2.4.2 3-D MODEL OF THE INFÉRO-FLUX AQUIFER

A local-scale 3D geological model of a tract of the Inféro-Flux aquifer was built to obtain an accurate geometrical representation of the confining bed separating the Inféro-Flux aquifer from the Neogene rocky basement (Arras et al. 2014). The geological map of this area was updated by integrating the SCET-COOP hydrogeological map with the LANDSAT8 imagery and elevation information referred to the SRTMGL1. For the local-scale 3-D model 19 sections at 1:10.000 scale were realised in the productive zone of the aquifer and perpendicular to the flow direction of the Oued el Hai-Biskra (Fig. 3.8).

Twenty-five borehole reports were collected for the modelled area, but description of the subsurface geology was reported only at twenty borehole locations, which were used to constrain the shape of the geological contacts in the sections. Most of the wells were realised for water supply purposes, thus they are roughly located in the alluvium and reach a maximum depth of 50 m. The erosional contact is intercepted at six well locations, and depth ranges from 20 m to 40 m, depending on their locations with respect to the riverbed. Those wells were built for geological survey purposes, and some of them are deeper than 200 m.

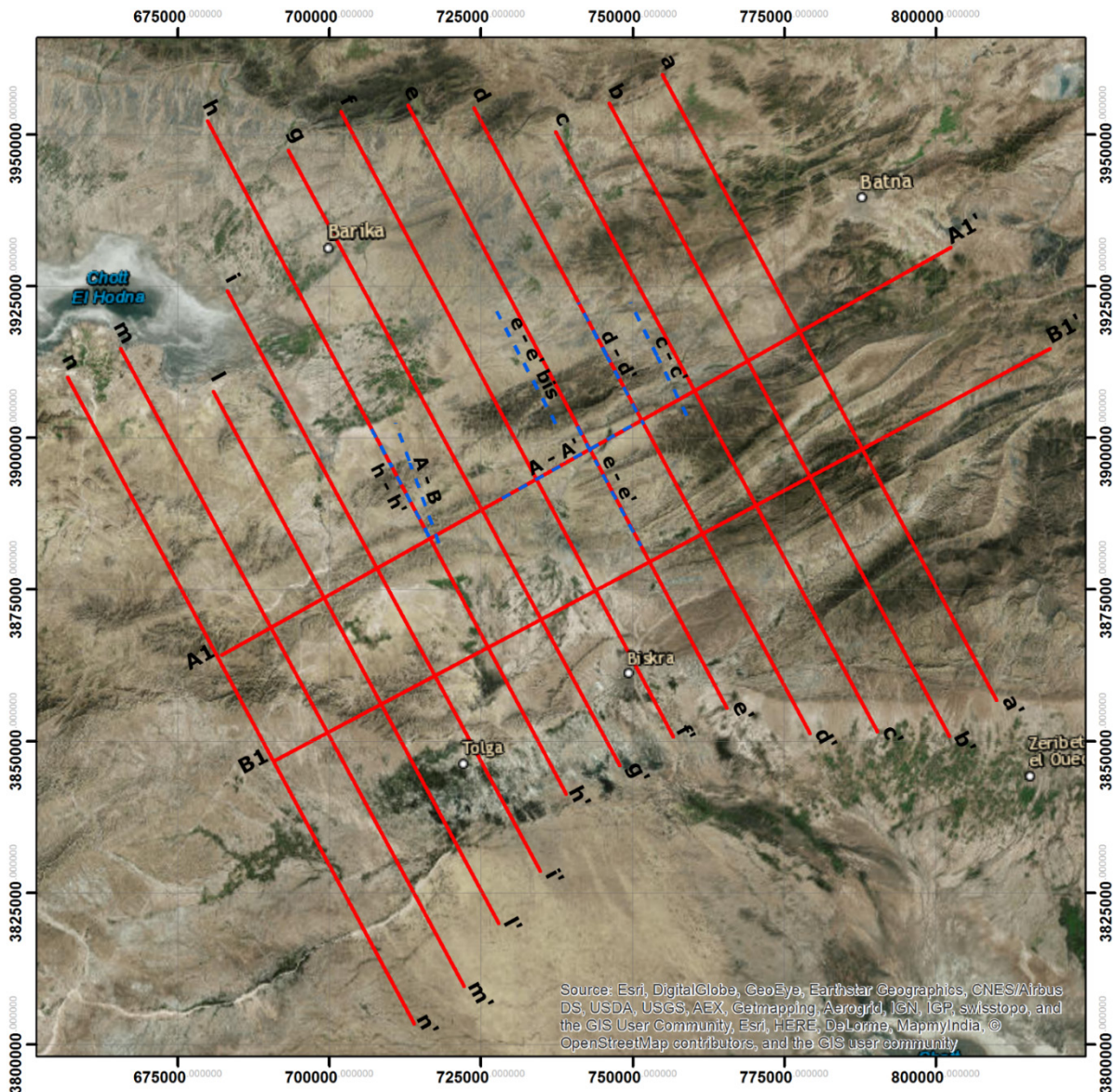


Fig. 3.7 Location of the geological cross sections at 1:200.000 (red lines) and 1:50.000 scale (blue dotted lines).

Due to the small length of the section traces (1.5 km), the geological cross sections were directly drawn within the geo-modeller. The horizons representing the confining bed were drawn through a geomorphological interpretation of the outcropping geology and topography and honouring the Quaternary-Neogene contact matched in the boreholes. All the sections realised for the local scale 3-D model are illustrated in the Annex B of the present work.

The geo-modeller allows the computation of the volume comprised between the SRTMGL1 and the geological 3D surface by defining them as upper and lower boundaries, respectively. The “Create TetraVolume between horizons” tool was used using a regular grid of cubic cells of 10 m.

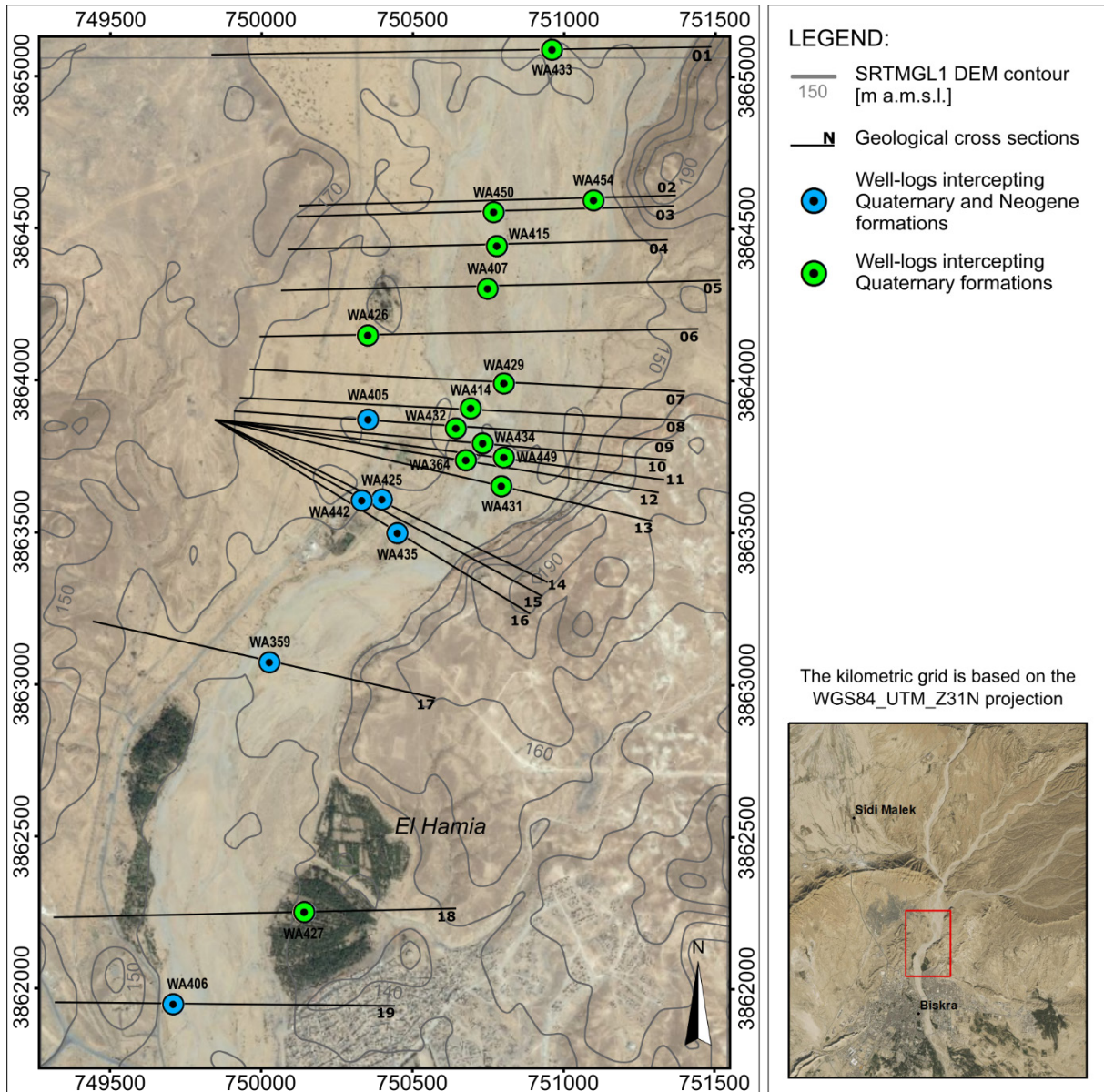


Fig. 3.8 Location of the boreholes and cross sections used for the construction of the 3D geological model of the Inféro-Flux aquifer.

Once the alluvium volume was computed, the amount of exploitable water can be estimated through the application of the specific yield ( $S_y$ ) parameter. This is defined as “the ratio of the volume of water that, after saturation, can be drained by gravity to its own volume” (Todd and Mays 2005):

$$S_y = W_y/V_t$$

Where  $W_y$  is the volume of drained water (in this case, the volume of exploitable water), and  $V_t$  is the bulk volume of the media (in this case, the volume of the alluvium deposits).

A variety of techniques could be used to measure specific yield, but methods based on well-pumping tests give the most reliable results (Todd and Mays 2005). Some direct measurements were obtained from pumping tests at three well locations in the study area, but results are extremely variable and range from 6% to 47% (SCET-COOP 1967). An attempt

for the estimation of the parameter is here reported and it is based on the analysis of the Quaternary deposits description retrieved from the borehole reports. In the modelled area, the wadi alluvium is intercepted at 20 boreholes for a total deposit description of 755 m. Alluvium materials were organised in 14 classes based on four granulometries (gravel, sand, silt, and clay) and their combination (Table 3.8, Fig. 3.9). Subsequently, the specific yield was estimated for each granulometry and combinations using values reported in the literature (Johnson 1963; Todd and Mays 2005) and the weighted mean computed.

ALLUVIUM TYPE	THICKNESS [m]	PERCENTAGE [%]	SPECIFIC YIELD
Gravel (Gr)	274	36.3	24
Gravel (Gr) + Sand (Sn)	149	19.7	19
Gravel (Gr) + Clay (Cl)	105	13.9	8
Sand (Sn)	45	6.0	23
Sand (Sn) + Gravel (Gr)	55	7.3	21
Sand (Sn) + Silt (Sl)	1	0.1	13
Sand (Sn) + Clay (Cl)	14	1.9	10
Silt (Sl)	6	0.8	4
Silt + Gravel (Gr)	7	0.9	8
Silt + Sand (Sn)	4	0.5	2
Clay (Cl)	43	5.7	3
Clay (Cl) + Gravel (Gr)	29	3.8	7
Clay (Cl) + Sand (Sn)	16	2.1	5
Clay (Cl) + Silt (Sl)	7	0.9	3
<b>TOTAL</b>	<b>755</b>	<b>100</b>	<b>-</b>

Table 3.8 Summary of the grain size term and combination of them derived from the alluvium sediments described in the borehole reports.

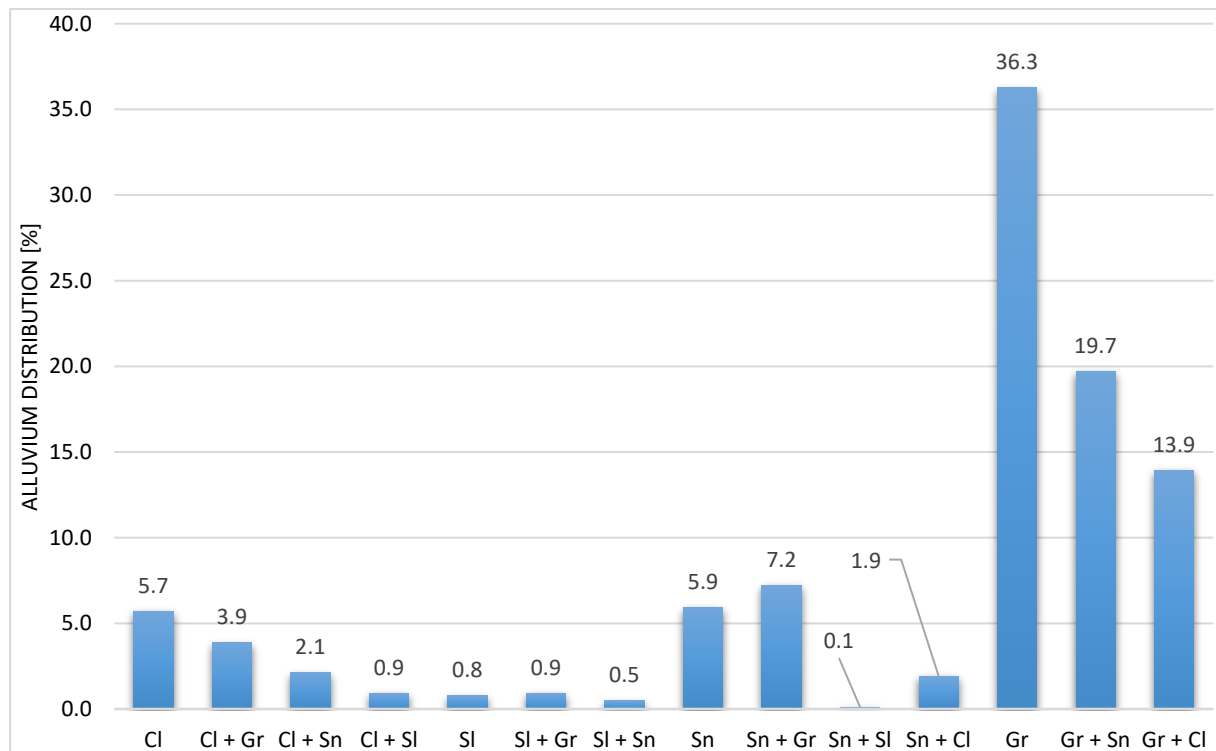


Fig. 3.9 Distribution of the grain size terms of the alluvium described in the borehole reports shown as bar histogram.

### 3.2.5 HYDROLOGICAL BALANCE CALCULATION

The water balance calculation was performed at local scale to enhance the conceptualization of the natural hydrologic dynamics affecting the Inféro-Flux aquifer. The lack of complete series of measured data, the poor distribution of measurement stations, and complications related to the collection of original record made the computation of the water budget difficult and problematic. However, an attempt for their estimation was performed by applying the following simplified equation:

$$P = ET_a + R + I$$

Where  $P$  is the amount of rainfall water,  $ET_a$  is the actual evapotranspiration,  $R$  is the surface runoff, and  $I$  is the effective infiltration.

#### 3.2.5.1 PRECIPITATION

Two precipitation dataset were available for the study area, as described in the Chapter 3.1.6. The ONM dataset has the longer precipitation series but temperatures cover only a ten years' period. The last ones are required in the evaluation of the evapotranspiration parameter. On the contrary, the TuTiempo dataset includes precipitation and temperature records covering a 32-years period. Therefore, the TuTiempo dataset was selected as the reference set of rainfall data.

#### 3.2.5.2 EVAPOTRANSPIRATION

The Food and Agriculture Organization of the United Nations (FAO; Allen et al. 1998) recommends the Penman-Monteith method for the estimation of the reference crop evapotranspiration ( $ET_o$ ).  $ET_o$  is defined (Allen et al. 1998) as the "evapotranspiration rate from a hypothetical grass reference crop with an assumed crop height of 0.12 m, a fixed surface resistance of 70 s/m and an albedo of 0.23". The only factors affecting the  $ET_o$  are climatic parameters, and consequently, it represents a climatic parameter that can be computed from weather data.  $ET_o$  expresses the evaporating power of the atmosphere at a specific location and time of the year and does not consider the crop characteristics and soil factors. However, the Penman-Monteith method requires the availability of several parameters as the net radiance at the crop surface, soil heat flux density, mean daily air temperature at 2 m height, and others. When these data are not available, the FAO (Allen et al. 1998) suggests to using the Hargreaves and Samani (1985) equation:

$$ET_o = 0.408 * 0.0023 (T_{mean} + 17.8)(T_{max} - T_{min})^{0.5} R_a$$

Where

0.408	is the conversion factor from [ $\text{MJ m}^{-2} \text{d}^{-1}$ ] to [ $\text{mm/d}$ ],
0.0023	is an empirical constant,
$T_{mean}$	is the daily average air temperature at 2 m height [ $^{\circ}\text{C}$ ],
$T_{max}$	is the daily maximum air temperature [ $^{\circ}\text{C}$ ],
$T_{min}$	is the daily minimum air temperature [ $^{\circ}\text{C}$ ],
$R_a$	is the extra-terrestrial radiation [ $\text{MJ m}^{-2} \text{d}^{-1}$ ].

The extra-terrestrial radiation for each day of the year and different latitudes can be estimated by knowing the solar constant, solar declination, and time of the year using the equation:

$$R_a = \frac{24 (60)}{\pi} G_{sc} d_r [\omega_s \sin(\varphi) \sin(\delta) + \cos(\varphi) \cos(\delta) \sin(\omega_s)]$$

Where

$G_{sc}$	solar constant	=	0.0820 MJ m <sup>-2</sup> min <sup>-1</sup> ,
$d_r$	inverse relative distance Earth-Sun	=	$1 + 0.033 \cos(\frac{2\pi}{365} J)$ ,
$\omega_s$	sunset hour angle [rad]	=	$\arccos[-\tan(\varphi) \tan(\delta)]$ ,
$\varphi$	latitude [rad]	=	$\frac{\pi}{180}$ (decimal degrees),
$\delta$	solar declination [rad]	=	$0.409 \sin(\frac{2\pi}{365} J - 1.39)$ ,
J	day in the year between 1 (1 January) and 365 or 366 (31 December).		

Er-Raki et al. (2010) have evaluated the Hargreaves and Samani equation over arid climatic conditions of Morocco and Mexico by comparing it against the FAO Penman-Monteith method. The result shows that the equation works quite well under moderate wind conditions (< 3 m/s).

Estimation of actual evapotranspiration ( $ET_a$ ) can be performed using several approaches and equations. Turc (1951) proposed an annual estimation of  $ET_a$  based on annual cumulative precipitations and average temperatures through the following equation:

$$ET_a (Turc) = \frac{P}{\sqrt{0,9 + \frac{P^2}{L^2}}}$$

Where

P	annual cumulative precipitation [mm],		
L	thermal indicator	=	$300 + 25 T_c + 0.05 T_c^3$ ,
$T_c$	corrected temperature parameter [°C]	=	$\frac{P_1 \times T_1 + P_2 \times T_2 \dots + P_{12} \times T_{12}}{P_1 + P_2 \dots + P_{12}}$

Another method used for the estimation of the  $ET_a$  is the Coutagne (1954) formula:

$$ET_a (Coutagne) = P - \lambda P^2$$

Where

P	annual cumulative precipitation [m],		
$\lambda$	thermal indicator	=	$1/(0.8 + 0.14 T)$ ,
T	mean annual temperature [°C].		

The consistency of the equation is verified if  $1/8 \lambda \leq P \leq 1/2 \lambda$ .

### 3.2.5.3 RUNOFF AND INFILTRATION

Effective precipitation ( $P_e$ ) is defined as the difference between precipitation and actual evapotranspiration. The  $P_e$  term corresponds to the amount of water available for the occurrence of surface runoff and infiltration.

$$P_e = P - ET_a = R + I$$



In the study area, surface runoff was measured at daily and monthly scale at the stream gauge station of El Melaga, Djemorah, and El Kantara but in a discontinuous way and for short periods (Section 2.1.1, Table 2.2). Moreover, measured records were not available.

Infiltration is a parameter not commonly measured, and no values were available for the study area. However, several estimations were conducted in the frame of PhD researches at local universities (Mimeche 2003; Haouchine 2010). Haouchine (2010) estimated the infiltration capacity for the area extending over El Outaya plain, which also includes the present study area, through the application of an overlay mapping method within a GIS environment. Results showed that five classes of infiltration capacity ( $I_c$ ) were identified in the plain area. The classes are: 32.5% for the plain area, 25% for the talweg and oued alluvium, 15% for fissured limestones, 7.5% for less fissured limestones and dolostones, and 0.5% for the Triassic salt outcrop. For the present research, the 25% infiltration capacity estimated for the talweg and oued area is considered. The amount of infiltration water is obtained by multiplying the coefficient for the effective precipitation. Afterwards, runoff is computed as final parameter of the water budget by subtracting the infiltration term from the  $P_e$ .

$$I = P_e \times I_c \quad \text{and} \quad R = P_e - I$$

### 3.2.6 GROUND WATER FLOW NUMERICAL MODEL

The lack of continuous and detailed hydrogeological data, as the impossibility to carry out new field surveys, did not allow a comprehensive understanding of the characteristics and dynamics affecting the productive zone of the Inféro-Flux aquifer. The development and calibration of a groundwater flow model was performed to estimate the spatial distribution of the hydraulic conductivities, which is one of the main parameter required in the definition of the hydraulic characteristics of the porous media, over the whole domain (Arras et al. 2016). Successively, results provided by the calibrated model were interpreted to provide quantitative indications on how the aquifer system works.

#### 3.2.6.1 CONCEPTUAL MODEL

Before designing the numerical model, a preliminary phase was dedicated to the conceptualisation of the system by integrating all the geological, hydrogeological, and hydrologic data and interpretation.

The whole model domain extends over a surface of 7.6 km<sup>2</sup>. It includes the two main hydrogeological units recognised in the area (Fig. 3.10): the Quaternary alluvium, which hosts the phreatic aquifer, and the Neogene formations, which constitute the confining bed of the aquifer (a detailed explanation of how the geological sketch map was obtained will be provided in Chapter 4.4.2). The alluvium deposits cover an area of 2.9 km<sup>2</sup>. The SRTMGL1, which has one arc-second horizontal resolution (about 30 meters) and an absolute height error of 5.6 m, was used as the reference surface for the ground heights while the local-scale 3-D hydrogeological model was used for defining the aquifer confining bed.

From the analysis of the borehole reports and literature, five hydraulic conductivity values ( $K$ ) were collected for the modelled area (Fig. 3.10, Table 3.9), with values ranging from 0.00015 to 0.0025 m/s.

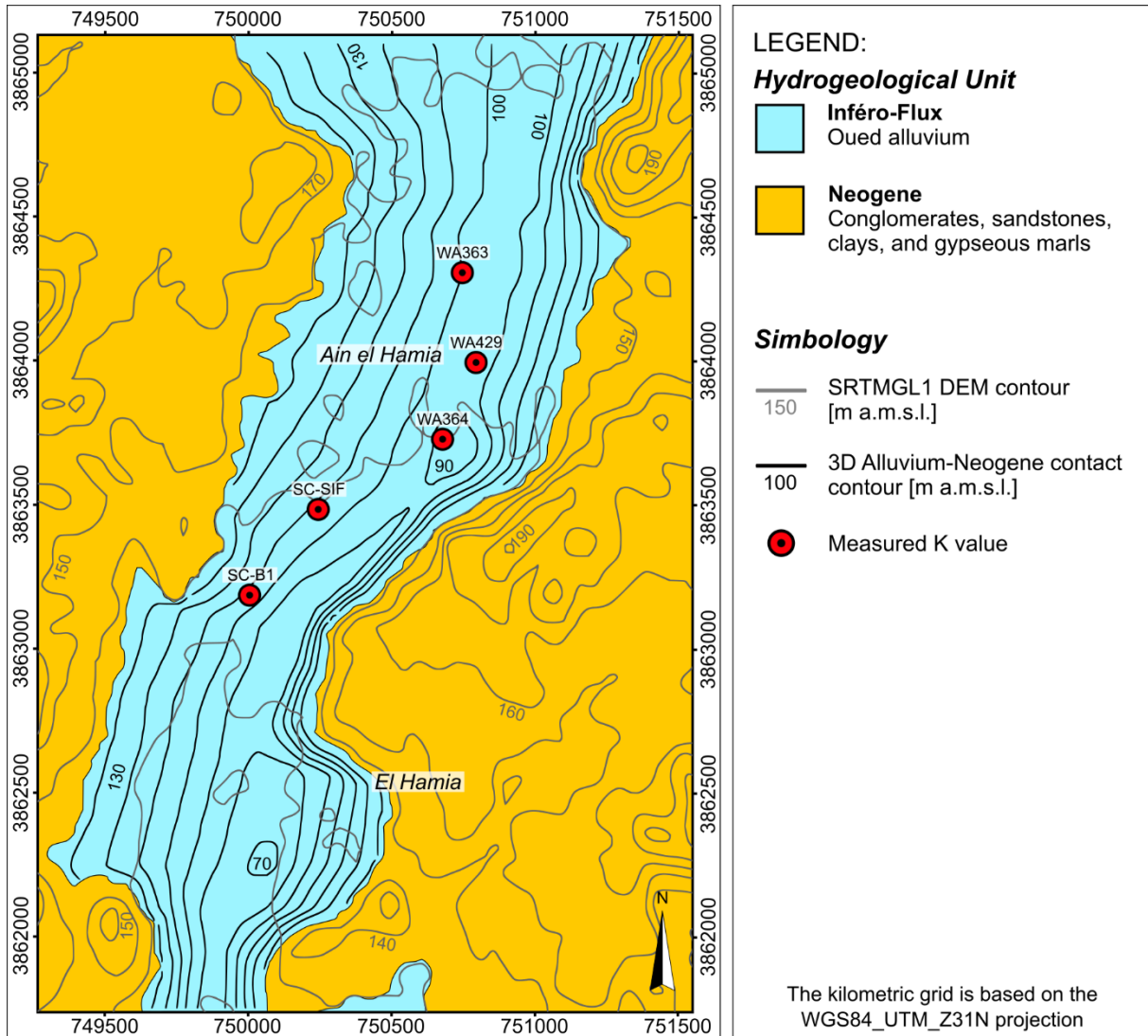


Fig. 3.10 Representation of the topographic surface (SRTMGL1 DEM) and the erosive contact between the alluvium and the Neogene as contour lines. The location of the measured hydraulic conductivities is also shown.

WELL NAME	X_UTM Z31N [m]	Y_UTM Z31N [m]	K [m/s]
WA363	750747	3864307	0.0012
WA364	750680	3863737	0.0025
WA429	750797	3863997	0.00055
SCETCOOP_B1	750008	3863189	0.00015
SCETCOOP_SIF	750246	3863482	0.00044

Table 3.9 Summary of the measured hydraulic conductivity available for the model area.

Two set of hydrogeological data were collected and employed. They referred to the field measurements carried out in May 1966 (SCET-COOP 1967) and April 2012. For both periods, the water budget was manually computed by integrating all the hydrological and hydrogeological information. The quantification of the incoming and outcoming flow to and from the system was estimated at the northern and southern boundary of the domain by defining the flow nets and applying Darcy's law through the following equation:

$$Q = ST/Z$$

Where  $Q$  is the groundwater flow,  $S$  is the distance between adjoining flow nets,  $T$  is the transmissivity, and  $Z$  is the distance between two piezometric heads with hydraulic gradient of one metre (Fig. 3.11). The transmissivity parameter was estimated as the product of the saturation zone thickness (comprised between the water table and the confining bed surface) and an average value of the hydraulic conductivity.

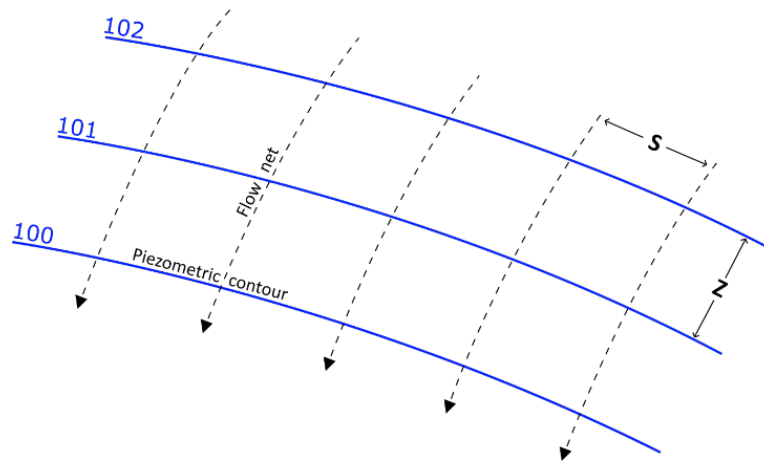


Fig. 3.11 Scheme representing the parameters required in the computation of the incoming and outgoing flow from the system.

The hydrogeological data referring to the 1966 and 2012 dataset were used for calibrating and validating the groundwater flow numerical model, respectively.

A direct recharge of the aquifer was considered. It corresponds to the annual amount of direct infiltration of meteoric water in the alluvium surface. Withdrawal from the aquifer occurs at the pumping well locations.

### 3.2.6.2 HYDROGEOLOGICAL DATA FOR MODEL CALIBRATION (MAY 1966)

Hydrogeological data used for the model calibration referred to the hydrogeological map published by SCET-COOP (1967) (Fig. 3.12). Piezometric heads have an almost equidistant distribution, except for the central area of the domain where an asymmetrical cone of influence coincide with the alignment of the B1, F1, F2, and F4 pumping wells. The direction of groundwater flow is from North to South. As a whole, exploitation occurred at six pumping wells (Fig. 3.12) with yields ranging from 40 and 90 L/s for a total withdrawal of 305 L/s and 26352 m<sup>3</sup>/d (Table 3.10). In the report, original yield rates were provided in litre per second, thus daily exploitation were computed considering a withdrawal frequency of 24 hours per day.

Groundwater inflow to the system was computed at the northern boundary using the piezometric contours 148 and 147 m a.m.s.l., while for groundwater outflow at the southern boundary, the piezometric heads 122 and 121 m a.m.s.l. were used. The direct infiltration from precipitation over the upper aquifer surface was 4.4 m<sup>3</sup>/d and it was obtained by multiplying the average infiltration with the alluvium area (see Table 4.5, Section 4.2). Two estimations were done using an average hydraulic conductivity value coherent with the lithological characteristics of the alluvium, namely 10<sup>-4</sup> and 10<sup>-3</sup> m/s.

A summary of the water budget components is shown in Table 3.11.

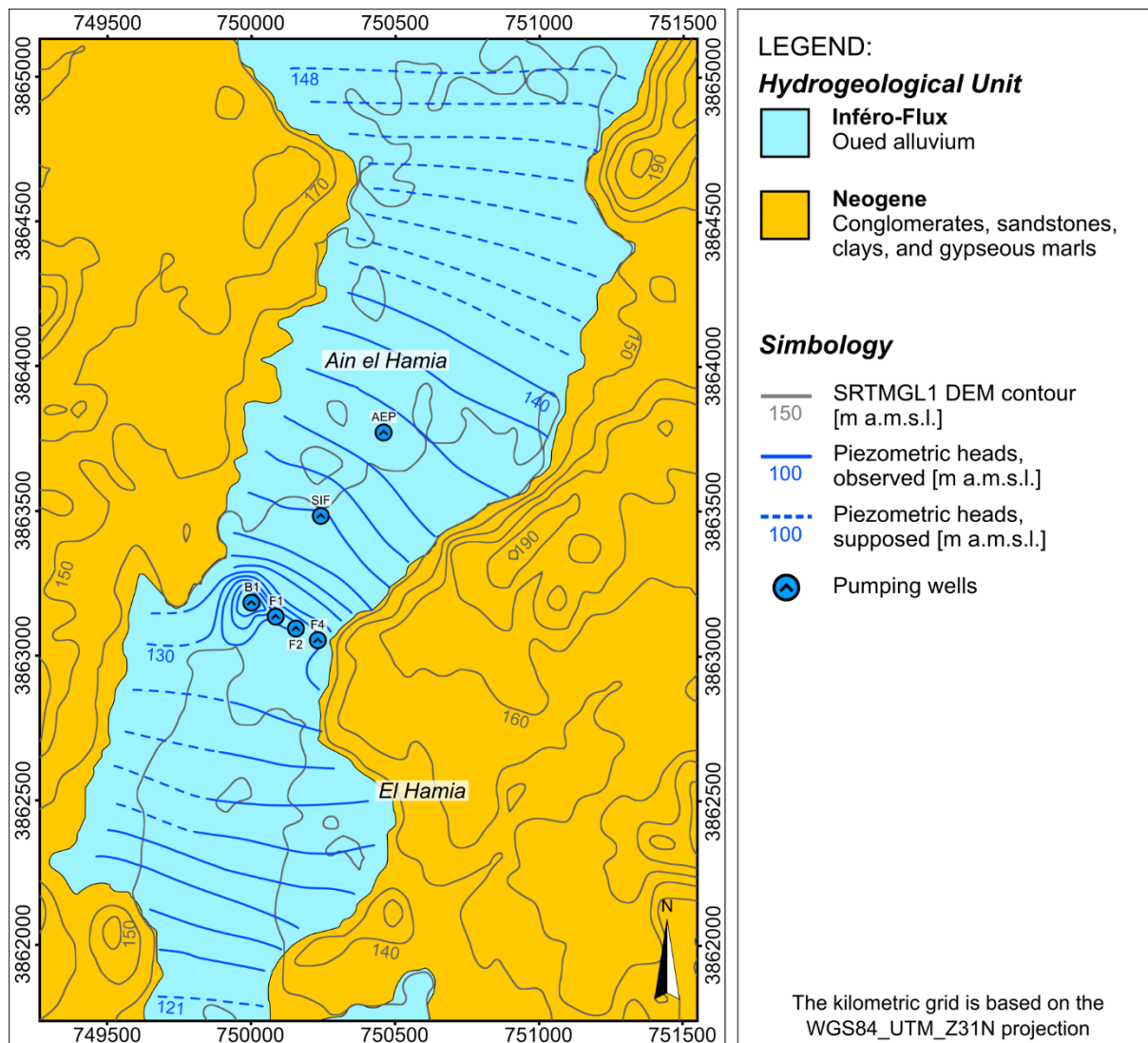


Fig. 3.12 Cartographic sketch map of the conceptual model showing the piezometric heads and working pumping wells dated back to May 1966 (modified from SCET-COOP, 1967).

WELL	UTM Z31N_X [m]	UTM Z31N_Y [m]	Z [m a.m.s.l.]	YIELD [L/s]	YIELD [m <sup>3</sup> /d]
<b>B01</b>	750008	3863189	133	90	7776
<b>SIF</b>	750246	3863483	141	40	3456
<b>F01</b>	750008	3863189	132	45	3888
<b>F02</b>	750073	3863157	132	45	3888
<b>F04</b>	750135	3863114	134	45	3888
<b>AEP Stat.</b>	750412	3863807	113	40	3456
<b>TOTAL</b>				<b>305</b>	<b>26352</b>

Table 3.10 Summary of the pumping wells occurring in the productive zone of the phreatic aquifer (survey date: May 1966 – from SCET-COOP (1967). Z values were extracted from the SRTMGL1 DEM.

WATER BUDGET – MAY 1966						
	INPUT [m <sup>3</sup> /d]		OUTPUT [m <sup>3</sup> /d]		IN – OUT [m <sup>3</sup> /d]	
FLOW IN	2759	27599				
FLOW OUT			612	6125		
INFILTRATION	4.4					
WITHDRAWAL				26352		
<b>TOTAL</b>	<b>2763.4</b>	<b>27603.4</b>	<b>26964</b>	<b>32477</b>	<b>-24200.6</b>	<b>-4873.6</b>
K [m/s]	10 <sup>-4</sup>	10 <sup>-3</sup>	10 <sup>-4</sup>	10 <sup>-3</sup>	10 <sup>-4</sup>	10 <sup>-3</sup>

Table 3.11 Water budget estimation for the Inféro-Flux system at May 1966 using two different values of K.

### 3.2.6.3 HYDROGEOLOGICAL DATA FOR MODEL VERIFICATION (APRIL 2012)

The census of the pumping wells located in the area of Biskra performed in April 2012 (ANRH 2013) included measurements of dynamic water levels at 12 pumping well locations within the modelled domain. These water depth measurements were used for the estimation of the piezometric level using the SRTMGL1 as reference ground surface. Then, the reconstruction of the groundwater contourlines was done using a one-metre interval (Fig. 3.13). However, the resulting contourlines did not have a real hydrogeological meaning since it was based on dynamic piezometric levels.

The groundwater flow direction is roughly North-South. Exploitation occurred at the same twelve wells where water levels were measured; the pumping rate is comprised between 15 and 30 L/s for a total production of 273 L/s and 19656 m<sup>3</sup>/d (frequency of 20 h/d) (Table 3.12).

The groundwater inflow was computed at the northern boundary using the piezometric contours 128 and 127 m a.m.s.l., while for the outflow at the southern boundary the piezometric contours 113 and 112 m a.m.s.l. were used. Two estimations were done using both 10<sup>-4</sup> and 10<sup>-3</sup> m/s  $K_x$  values.

The direct infiltration from precipitation over the upper aquifer surface was 4.4 m<sup>3</sup>/d, and it was obtained by multiplying the average infiltration with the alluvium area (see Tab.4.5, Section 4.2). A summary of the water budget components is shown in Table 3.13.

Fig. 3.14 shows the depth of the water level for both periods (May 1966 and April 2012) on the topographic profile derived from the SRTMGL1 DEM. The cross section is realised in the productive zone of the aquifer and is parallel to the groundwater flow direction (roughly N-S in this tract). The cross section shows that the piezometric level in May 1966 was slightly below the ground surface and locally could be also above it, while in April 2012 the water level is 10-15 m lower than the level recorded in 1966. However, it must be considered that the piezometric map referred to the 2012 is strongly influenced by the pumping wells and thus it is difficult to quantify the magnitude of the overexploitation.

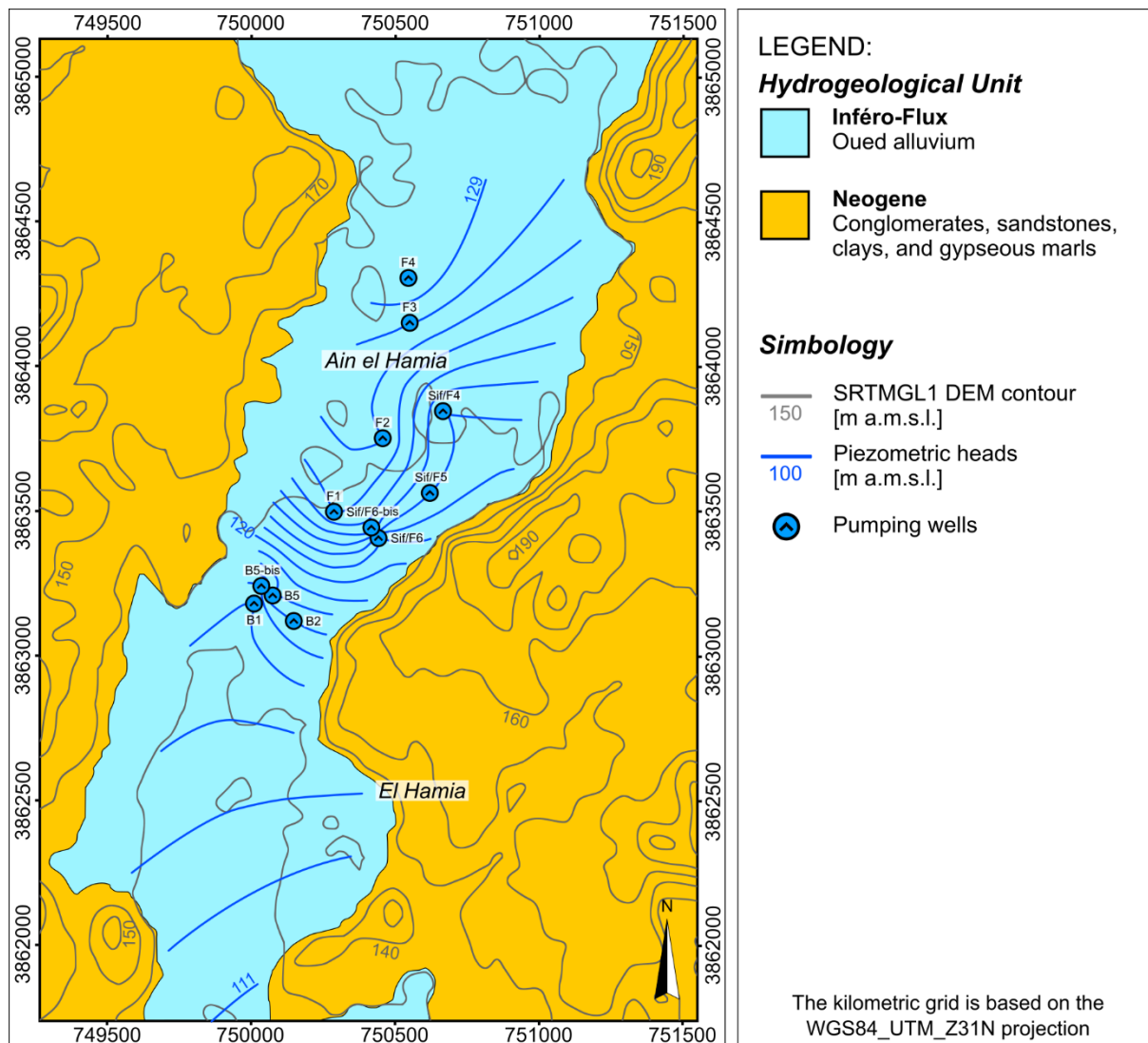


Fig. 3.13 Cartographic sketch map of the conceptual model showing the piezometric heads and working pumping wells dated back to April 2012.

WELL	X [m]	Y [m]	Z [m a.m.s.l.]	YIELD [L/s]	YIELD [m <sup>3</sup> /d]
F03	750553	3864152	146	20	1440
F04	750548	3864306	145	20	1440
F02	750462	3863748	142	20	1440
Sif/F04	750663	3863846	141	18	1296
F01	750291	3863497	139	25	1800
Sif/F05	750619	3863568	137	30	2160
Sif/F06	750446	3863409	137	25	1800
Sif/F06-bis	750420	3863439	136	30	2160
B05-bis	750044	3863243	133	20	1440
B05	750070	3863213	132	15	1080
B01	750020	3863181	132	25	1800
B02	750149	3863123	132	25	1800
<b>TOTAL</b>				<b>273</b>	<b>19656</b>

Table 3.12 Summary of the pumping wells occurring in the productive zone of the phreatic aquifer (survey date: April 2012 – from WADIS-MAR (2013)). Z values were extracted from the SRTMGL1 DEM; daily yields correspond to 20 hours pumping per day.

WATER BUDGET – APRIL 2012						
	INPUT [m <sup>3</sup> /d]		OUTPUT [m <sup>3</sup> /d]		IN – OUT [m <sup>3</sup> /d]	
FLOW IN	1699	16987				
FLOW OUT			660	6584		
INFILTRATION	4.4					
WITHDRAWAL			19656			
<b>TOTAL</b>	<b>1703.4</b>	<b>16991.4</b>	<b>20316</b>	<b>26240</b>	<b>-18612.6</b>	<b>-9248.6</b>
K [m/s]	10 <sup>-4</sup>	10 <sup>-3</sup>	10 <sup>-4</sup>	10 <sup>-3</sup>	10 <sup>-4</sup>	10 <sup>-3</sup>

Table 3.13 Water budget estimation for the Inféro-Flux system at April 2012.

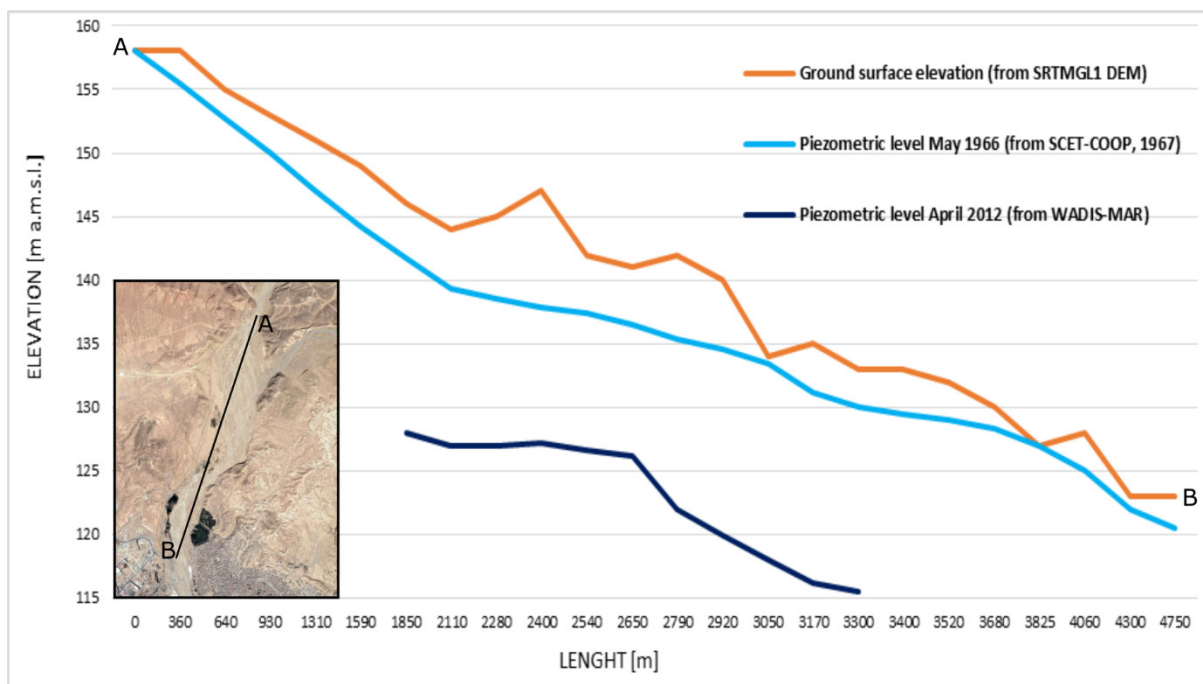


Fig. 3.14 Cross section roughly oriented N-S showing the measured water table level in May 1966 (cyan line) and April 2012 (dynamic level - blue line) with respect to the SRTMGL1 ground surface (orange line).

### 3.2.6.4 MODEL CONSTRUCTION AND FIRST RUN

A three-dimensional groundwater flow numerical model of the Inféro-Flux aquifer was realised using the Graphical User Interface (GUI) Visual Modflow Flex 2015.1. A standard structured Finite-Difference grid was used for the discretization of the model domain (Fig. 3.15). The block centred grid was composed of 17368 cells with a nodal spacing of 20 m organised in 167 rows and 104 columns. The phreatic aquifer was modelled as a single unconfined layer and is composed by 7460 active cells, while the remaining 9908 cells represented the Neogene bedrock and were set as inactive. The top and bottom elevations of the layer referred to the SRTMGL1 DEM and 3-D confining bed surface, respectively. Aquifer thickness ranged from a minimum of 0.1 m in the riversides to 58 m in the deepest area, with an average of 28 m. Horizontal hydraulic conductivity  $K_x$  was set to the average value of 0.001 m/s and applied to the whole layer.

The following perimeter boundary conditions were defined (Fig. 3.15):

- Type 1 specified head boundary conditions (Dirichlet conditions) were set to simulate the northern and southern limits of the modelled domain; they corresponded to the piezometric levels reported in the SCET-COOP hydrogeological map and the head values

of 148 and 121 m a.m.s.l. were assigned to all the cells, representing the northern and southern boundary, respectively.

- No flow boundary conditions (special case of type 2 specified flow boundary – Neumann conditions) were set on both left and right riverbanks, corresponding to the contacts between the Neogene and the phreatic aquifer.
- Specified flow boundaries were applied to the nodes where pumping wells were located; details about wells coordinates and pumping rates (m<sup>3</sup>/d) used for the simulation are already illustrated in Table 3.10.

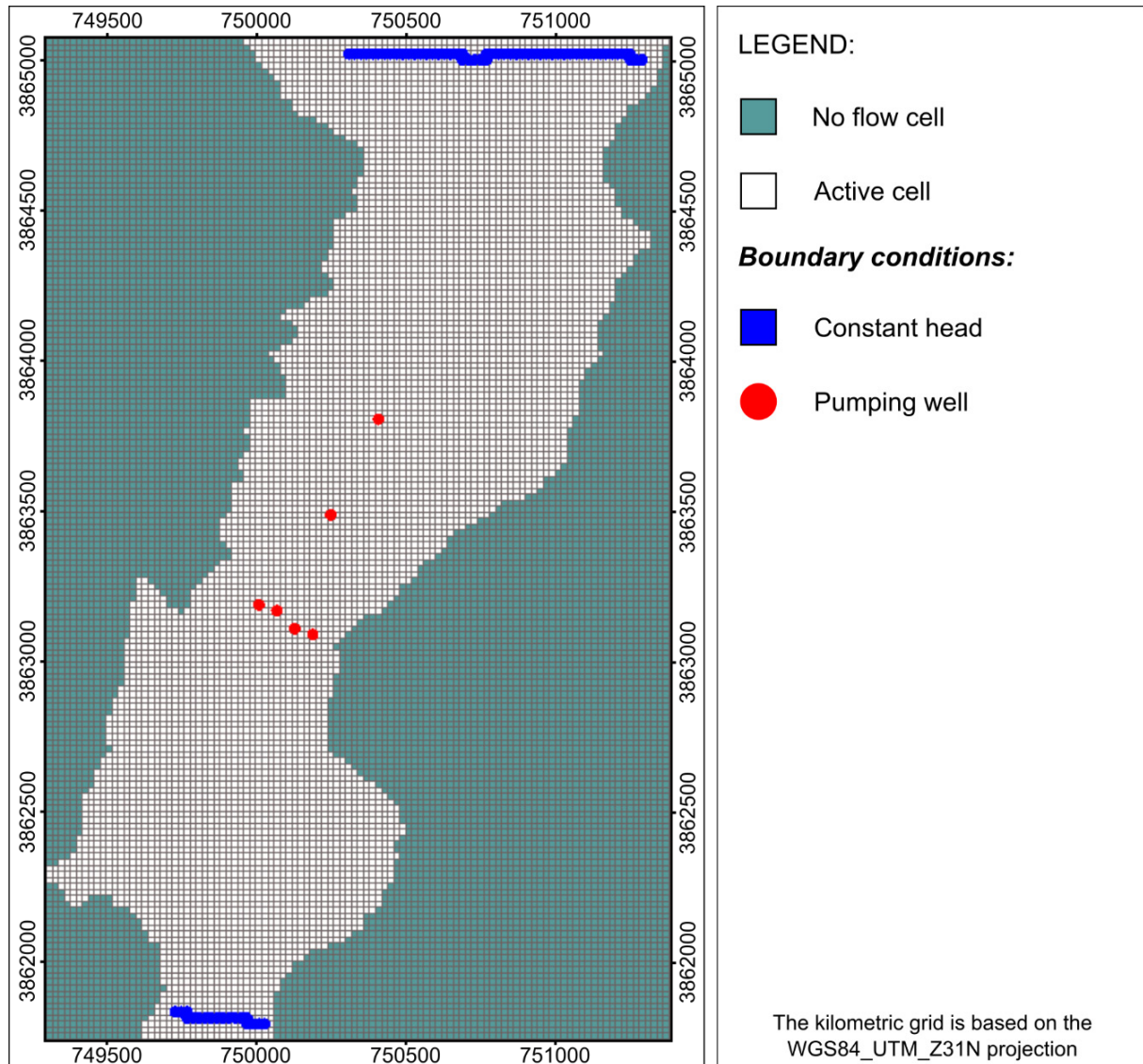


Fig. 3.15 Discretization of the model domain and boundary conditions.

The packages used for the model simulation are the following:

- The Preconditioned Conjugate Gradient (PCG) solver package was used to solve iteratively the governing equation and to obtain hydraulic heads and groundwater flows at each cell nodes.
- The Layer Property Flow Package (LPF) was used to perform the cell-by-cell flow. Setting the layer type as unconfined (1), the package computes the transmissivity value at each



iteration as the product of hydraulic conductivity and saturated thickness for each cell (Harbaugh, Arlen 2005).

### 3.2.6.5 MODEL CALIBRATION

Calibration of groundwater flow model aims at the calculation of hydrogeological parameters from field-measured values of heads. In this sense, the groundwater model is posed as an inverse problem since head observations constitute the dependent variable in the governing equation and are used to solve for parameter values (Anderson et al. 2015). Hydraulic conductivity represents a fundamental hydrogeological parameter required in the hydrodynamic characterisation of aquifers. However, the poor number of measured K values did not allow a reasonable parametrization and therefore, the calibration process was performed to estimate the spatial distribution of the parameter.

The lack of continuous hydrogeological data imposed the application of steady state conditions in the calibration process. To perform it, calibration targets must be defined. They generally consist of head observations measured at piezometers or wells located within the study area that are subsequently compared with simulated values during calibration to describe the model fit. In this case, original head measurements used for the reconstruction of the SCET-COOP piezometric map (SCET-COOP 1967) were unknown. Heads values were then estimated from the piezometric map by manually locating the calibration targets. A first set of 37 calibration targets (CT1), using two points per piezometric head, were defined using the scheme illustrated in Fig. 3.16 A. The second set (CT2) was composed of 34 calibration targets comprising only head observations located where the influence of the pumping wells could be neglected (Fig. 3.16 B). The default weight (1) was assigned to all the calibration targets.

Once the calibration targets were selected, the automated calibration of the hydraulic conductivity was done using the PEST code. With the PEST, available measurements of the parameters were used to estimate values at a definite number of discrete locations, or pilot points, distributed all over the model domain. These values were adjusted in an automated trial-and-error process in order to minimise the sum of squared weighted residuals (the difference between measured and observed head at each calibration target), which is referred to as the “objective function” ( $\phi = \Phi$ ). If the targets include only head observations, the objective function is (Doherty 2010):

$$\phi = \sum_{i=1}^n [W_{hi}(h_m - h_s)_i]^2$$

Where

$W_{hi}$  is the weight for the  $i$ th head observation;

$h_m$  is the measured (observed) head target;

$h_s$  is the simulated head.

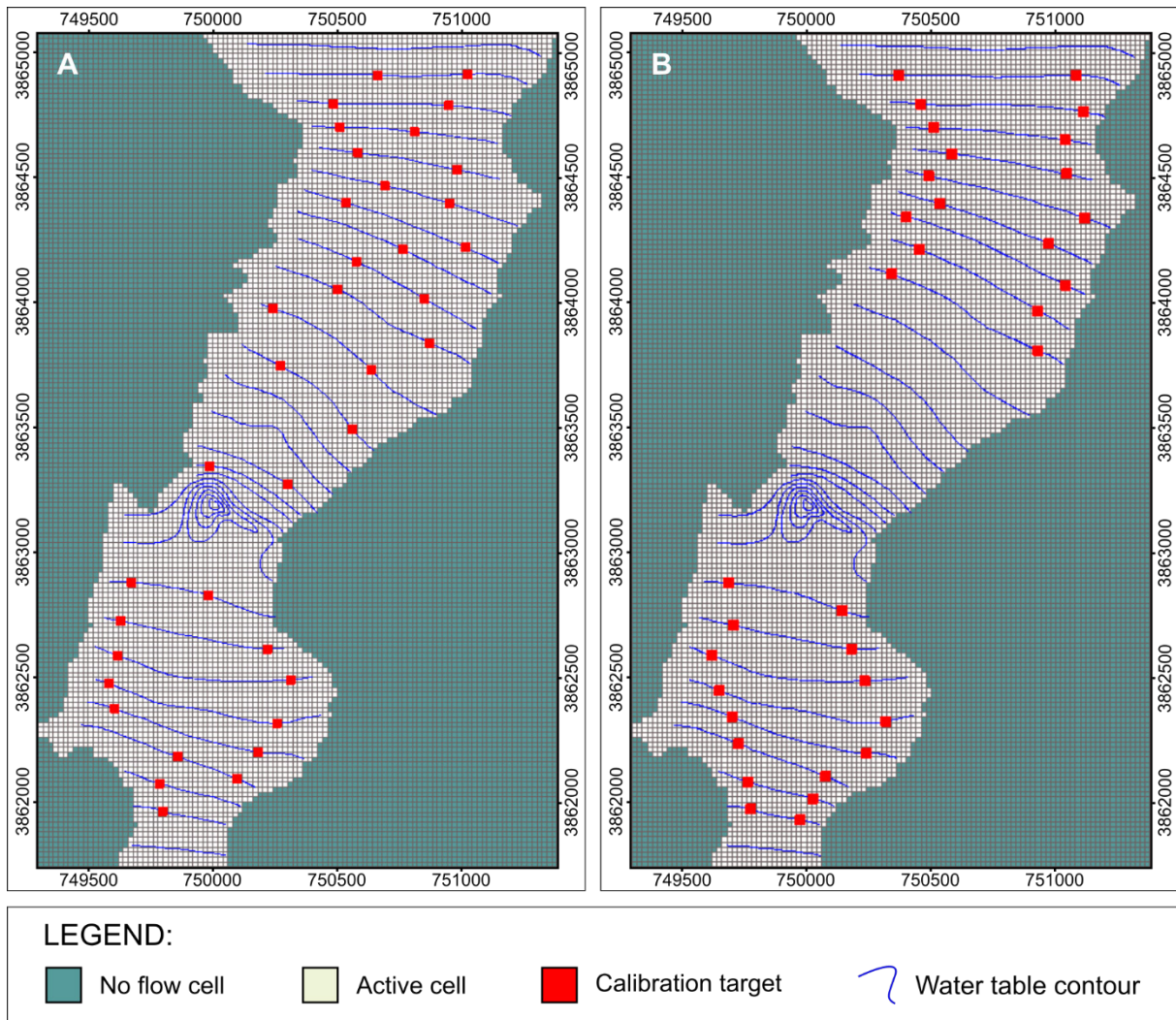


Fig. 3.16 A) Set of 37 (CT1) and B) 34 (CT2) calibration target (red dots) located on the piezometric heads coming from the SCET-COOP hydrogeological map (blue contourlines).

The correlation coefficient  $R$  provides a further measurement of goodness of fit, allowing the direct comparison of the results of different parameter estimation exercises (Doherty 2010). The correlation coefficient  $R$  is calculated as:

$$R = \frac{\sum(w_i c_i - m)(w_i c_{0i} - m_o)}{[\sum(w_i c_i - m)(w_i c_i - m) \sum(w_i c_{0i} - m_o)(w_i c_{0i} - m_o)]^{1/2}}$$

Where

$c_i$  is the  $i$ 'th observation value,

$c_{0i}$  is the model-generated counterpart to the  $i$ 'th observation value,

$m$  is the mean value of weighted observations,

$m_o$  is the mean of weighted model-generated counterparts to observations, and

$w_i$  is the weight associated with the  $i$ 'th observation (or "rotated observation" if a covariance matrix is used to specify observation uncertainty instead of individual observation weights).

The fit between modelled outputs and observations is generally considered acceptable when R is above 0.9 (Hill 1998; Doherty 2010).

In the parameterisation scheme of the pilot points, the measured hydraulic conductivities (see Fig. 3.10 and Table 3.9) were set as hard pilot points, meaning that values remain unchanged during the iterative process. For the distribution of the soft pilot points three different strategies were adopted. In the first scheme (PP1), 15 soft points were set corresponding to the boreholes location already used in the construction of the local scale 3-D model (Fig. 3.17 A). The second scheme (PP2) was based on the regular distribution of 304 soft points using a grid of 100 m (Fig. 3.17 B). In the latter scheme (PP3), the same pattern of scheme n.2 was used, but soft and hard pilot points were grouped into two different zones based on the local geological information, namely the relict braided channel (Zone01) and active braided channel (Zone02). In particular, 2 hard pilot points (WA364; SCETCOOP\_SIF) and 107 soft pilot points composed the Zone01, while the Zone02 included 3 hard pilot points (WA363; WA429; SCETCOOP\_B1) and 197 soft pilot points (Fig. 3.17 C).

The variability range used for the estimation of the  $K_x$  at the soft pilot points was set to  $1E-15$  m/s and  $1E+30$  m/s for the lower and upper limits respectively.

PEST uses geostatistical interpolation via Kriging to assign parameter values to all the nodes. The poor number of measured data did not allow a reasonable geostatistical study of the dataset by the mean of the variogram. However, some kriging parameters were defined according to literature results in similar conditions (Neuman 1982; Bjerg et al. 1992; Belcher et al. 2002):

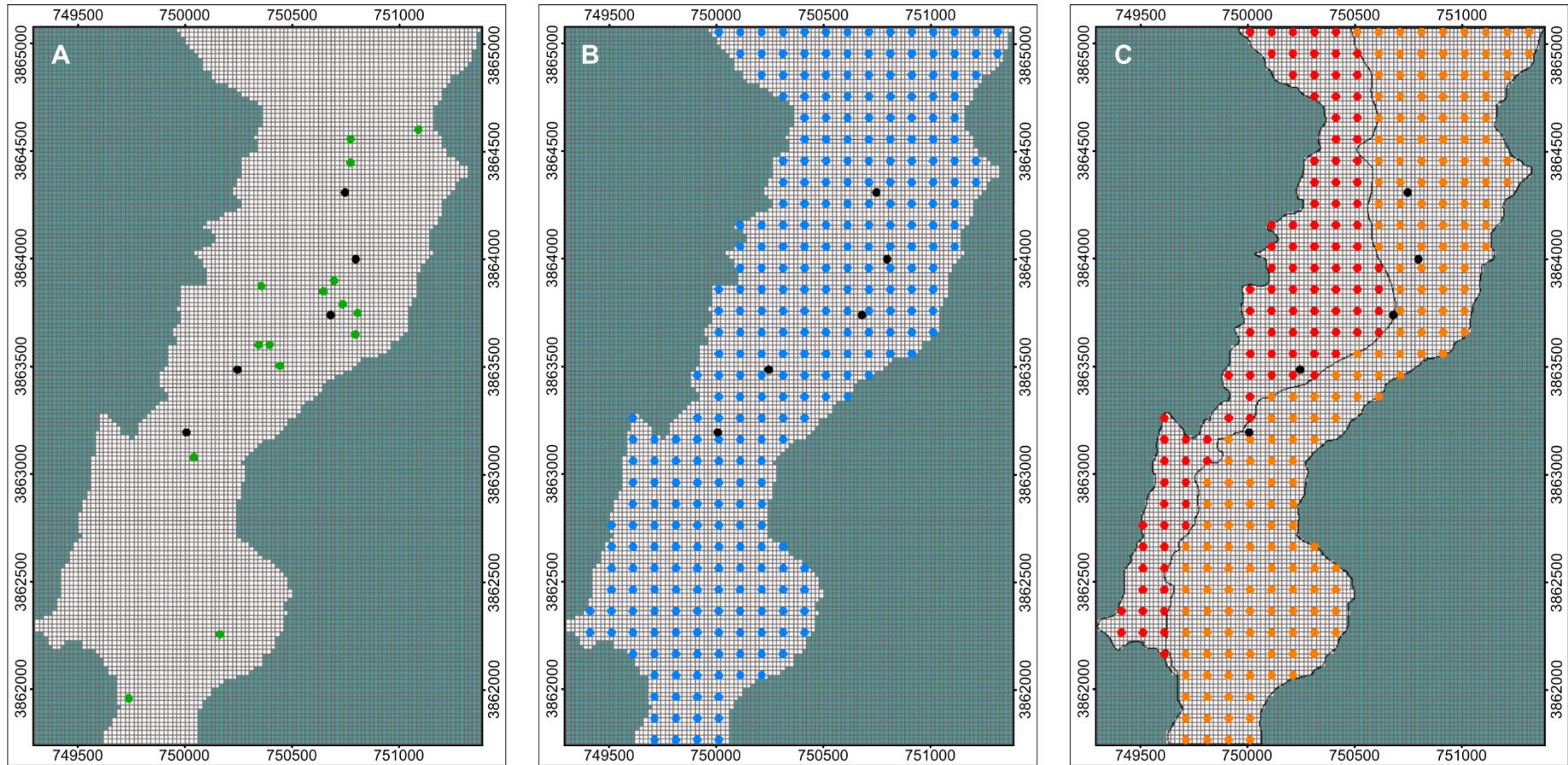
- log-transformation was selected to obtain the normal distribution of the hydraulic conductivity data set, which allowed the production of a more interpretable variogram;
- Exponential function was used to fit the empirical semivariogram.

Default values were used for other required parameters as nugget (0), bearing (0), and Alpha (500).

The automated calibration of the hydraulic conductivity parameter was performed through several PEST executions (Table 3.14), in which the two sets of calibration targets were combined with the various pilot point schemes to find the most consistent geological distribution of hydraulic conductivities and obtain the best model fit in terms of minimisation of the objective function and correlation coefficient.

PEST EXEC.	CALIBR. TARGET	OBSERVATION N.	PILOT POINTS SCHEME	PARAMETERS N.
<b>Pe1</b>	CT1 (Fig. 3.16 A)	37	PP1 (Fig. 3.17 A)	15 + 5
<b>Pe2</b>	CT2 (Fig. 3.16 B)	34	PP1 (Fig. 3.17 A)	15 + 5
<b>Pe3</b>	CT1 (Fig. 3.16 A)	37	PP2 (Fig. 3.17 B)	304 + 5
<b>Pe4</b>	CT2 (Fig. 3.16 B)	34	PP2 (Fig. 3.17 B)	304 + 5
<b>Pe5</b>	CT2 (Fig. 3.16 B)	34	PP3 (Fig. 3.17 C)	Zone01 = 107 + 2 Zone02 = 197 + 3

Table 3.14 Combination of calibration target and pilot point schemes used to find the best model fit by using the PEST automated calibration of the hydraulic conductivities.



**LEGEND:** Soft Pilot Point  
 No flow cell Active cell Hard Pilot Point Irregular distrib. Regular distrib. Regular distrib. (Zone 1) Regular distrib. (Zone 2)

Fig. 3.17 Location of the pilot points used for the estimation of the hydraulic conductivities using the PEST. A) Scheme n.PP1; B) scheme n.PP2; C) scheme n. PP3.

### 3.2.6.6 MODEL VALIDATION

The unicity of the solution is not guaranteed by the model calibration because it is based on only one set of hydrogeological data. To provide more consistent results, it is necessary to validate the model using the parameters values obtained from the calibration with a different dataset that, in this case, corresponded to the hydrogeological conditions observed in April 2012. Hydraulic conductivities estimated from Pe5 were used in the model validation phase, as the following perimeter boundary conditions (Fig. 3.18):

- Type 1 specified head boundary conditions (Dirichlet conditions) were set to simulate the northern and southern limits of the model domain; they corresponds to the piezometric levels obtained through interpolation of dynamic levels measured in 2012. Head values of 128 and 112 m a.m.s.l. were assigned to all the cells representing the northern and southern boundary respectively.
- No flow boundary conditions (special case of type 2 specified flow boundary – Neumann conditions) were set on both left and right riverbanks, corresponding to the contacts between the Neogene and the phreatic aquifer.
- Specified flow boundaries were applied to the nodes where pumping wells were located; details about wells coordinates and pumping rates (m<sup>3</sup>/d) used for the simulation are already illustrated in Table 3.12.

The model validation was performed at different calibration target with respect to those used for the calibration process. They referred to twelve head targets corresponding to the water table measured in April 2012 at the pumping well locations (Fig. 3.18). Validation was also performed at the same calibration target using heads estimated from the SCET-COOP (1967) water table, to provide comparable results. Head values at the target point locations for both periods are summarised in Table 3.15.

HEAD TARGETS	X [m]	Y [m]	1966 HEADs [m a.m.s.l.]	2012 HEADs [m a.m.s.l.]
<b>F:04 – Ob.01</b>	750548	3864305	141.1	130
<b>F:03 – Ob.02</b>	750552	3864151	139.8	128
<b>Sif/F:04 – Ob.03</b>	750662	3863846	138.5	123
<b>F:02 – Ob.04</b>	750462	3863748	137.5	127
<b>Sif/F:05 – Ob.05</b>	750619	3863567	137.4	123
<b>F:01 – Ob.06</b>	750291	3863496	135.2	126
<b>Sif/F:06-bis – Ob.07</b>	750419	3863438	136.9	124,5
<b>Sif/F:06 – Ob.08</b>	750445	3863408	136.9	121
<b>B:05-bis – Ob.09</b>	750043	3863243	129.9	116
<b>B:05 – Ob.10</b>	750070	3863213	130.1	118
<b>B:01 – Ob.11</b>	750008	3863189	125.5	115
<b>B:02 – Ob.12</b>	750148	3863123	129.2	117

*Table 3.15 Location of the observation points and heads used for model validation.*

Results of model calibration and validation is documented by reporting summary statistics of the residuals, scatter plots of observed versus simulated values and residuals, a map of observed and simulated water level contours, and the evaluation of the simulated water budget. In particular, summary statistics of the residuals include:

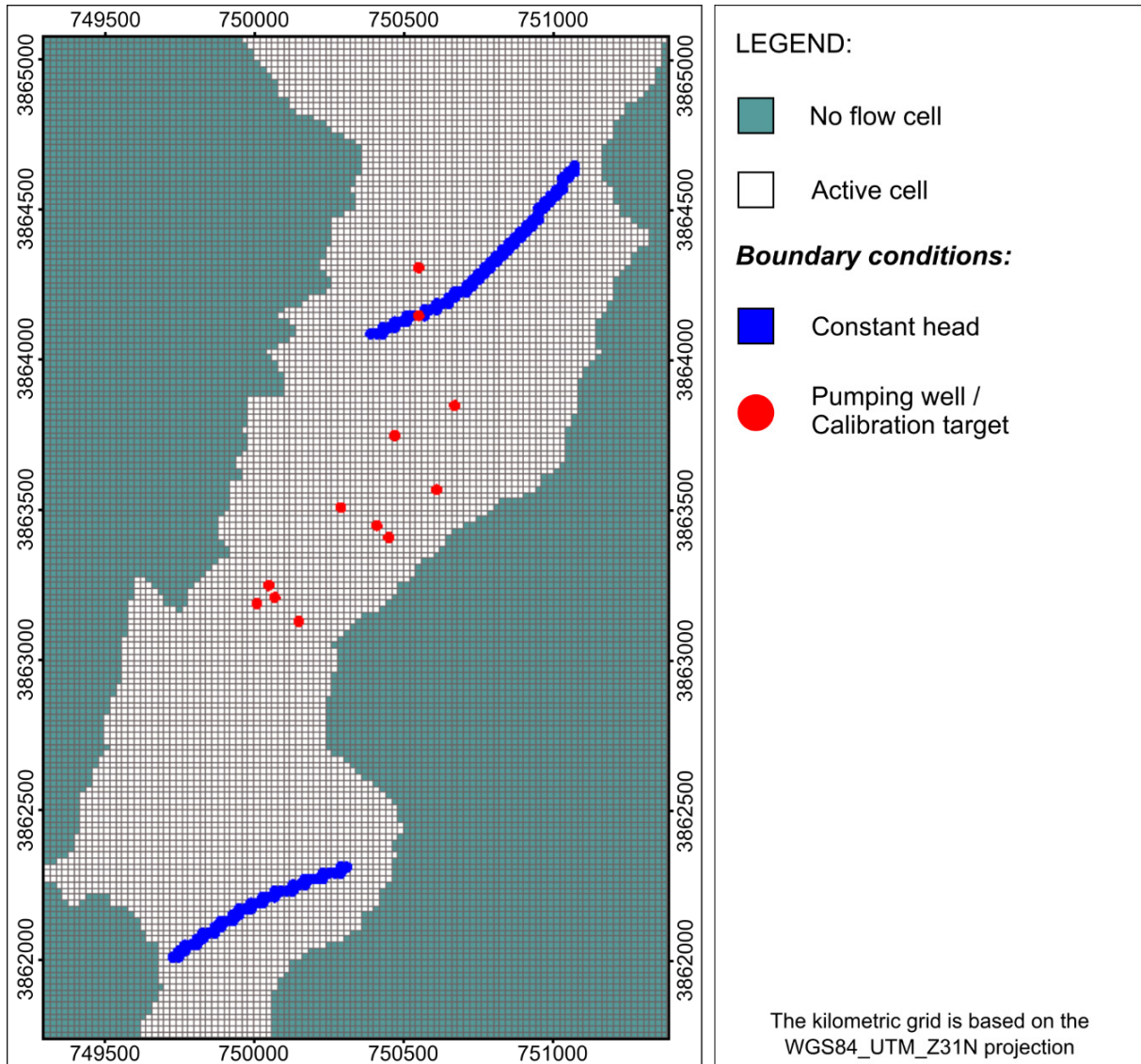


Fig. 3.18 Boundary conditions used in the model validation phase.

Mean Error (ME) is the mean difference of the residual errors:

$$ME = \frac{1}{n} \sum_{i=1}^n (h_m - h_s)_i$$

Mean Absolute Error (MAE) is the mean of the absolute value of the residuals:

$$MAE = \frac{1}{n} \sum_{i=1}^n |(h_m - h_s)_i|$$

Root Mean Squared Error (RMSE) is the average of the squared residuals:

$$MAE = \left[ \frac{1}{n} \sum_{i=1}^n (h_m - h_s)_i^2 \right]^{0.5}$$

Where  $n$  is the number of targets,  $h_m$  is the measured heads, and  $h_s$  is the simulated heads.

The maximum allowed residual error for the hydraulic heads derived from the SCET-COOP hydrogeological map refers to the error related to the georeferencing phase of the original hardcopy map, corresponding to  $\pm 2.5$  metres. In the case of the head values measured in 2012, the maximum allowed residual error is related to the absolute height error of the SRTMGL1 DEM, which was used for calculating the piezometric heads from water level measurements, and corresponds to  $\pm 5.6$  m.





## 4 RESULTS AND DISCUSSION

### 4.1 3D HYDRO-GEOLOGICAL MODELS AT REGIONAL SCALE

Geometries of the aquifer complexes identified in the region of Biskra and Batna are strongly influenced by the deformation history undergone by the Mesozoic and Eocene rocks related to the building of the Atlas Mountains domain.

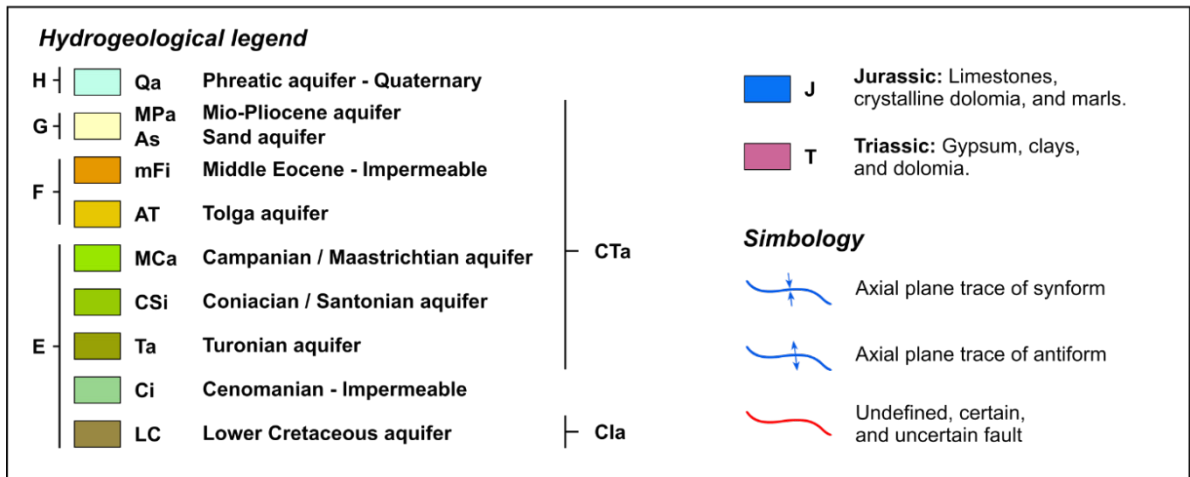
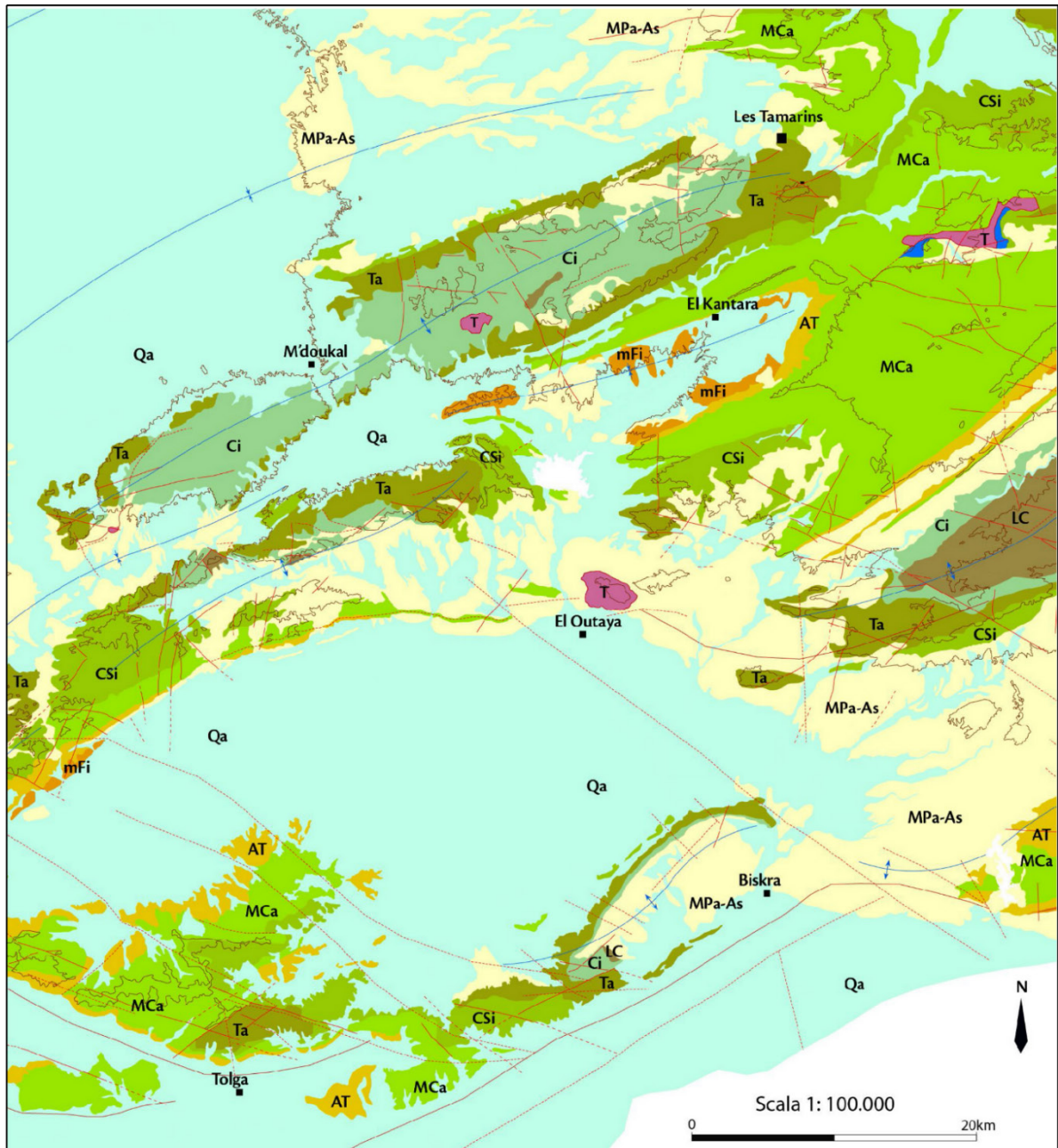
Shortening related to the Upper Cretaceous deformation was accommodated by folds causing the thickening of the cover and, consequently, of the aquifers. These folds constitute structural highs that play a very important role in recharging or dispersing surface water flows. Moreover, crests of the major antiforms often set up the watershed boundaries and, in the northern part of the study area, these highs constitute recharge areas for the Cretaceous and Eocene aquifers. Antiforms strongly influence the groundwater flow direction by forcing the flow towards the synformal axis, as confirmed by numerical modelling applied in similar geometrical contexts (Ben-Itzhak and Gvirtzman 2005). The most prominent synforms are the ones of El Seggana (SDS), El Kantara (SEK), Outaya (SEO) and Branisn (SB) (Fig. 4.1, Fig. 4.2). They act as storage areas allowing the accumulation of huge reserves of groundwater. Locally, synform geometries involving marl strata, can allow the formation of perched aquifers.

In the area of El Kantara (Fig. 4.1, Fig. 4.2), the Seggana synform (ss) and the El Kantara antiform (ak) are superimposed on the Djebel Metlil antiform (ADM) and El Kantara synform (SEC). The superimposition of folds with different trends can lead to very complex structure. In this specific case, the type of interference is known as dome and basins (Type I, Ramsay 1967) and such pattern produces zones of accumulation that heavily impact in the groundwater contributions.

The carbonate rocks constituting the Mesozoic and Eocene aquifers have a geometry related to the NE-trending fold systems and a regional dipping that force groundwater to flow toward SSW (Fig. 4.2).

NW-SE trending faults like the strike-slip Fault of Biskra complicate the model of the groundwater circulation (Fig. 4.2), in particular:

1. Fault displacement allows groundwater communication between aquifers separated by impermeable formations as in the case of the connection between the Turonian aquifer and the Maastrichtian one, separated by impermeable formations of Coniacian-Santonian Age;
2. Fault structure diverts part of the SSW groundwater flows toward NW-SE direction;
3. Fault plane acts as the preferred path for deep groundwater rises that supplies shallow aquifers like the Miocene and Quaternary ones. It also allow the rise of hydrothermal water (40 °C) from deep aquifers as observed in the El Kantara area.



4.

Fig. 4.1 Hydrogeological map illustrating the hydrogeological units outcropping in the study area.

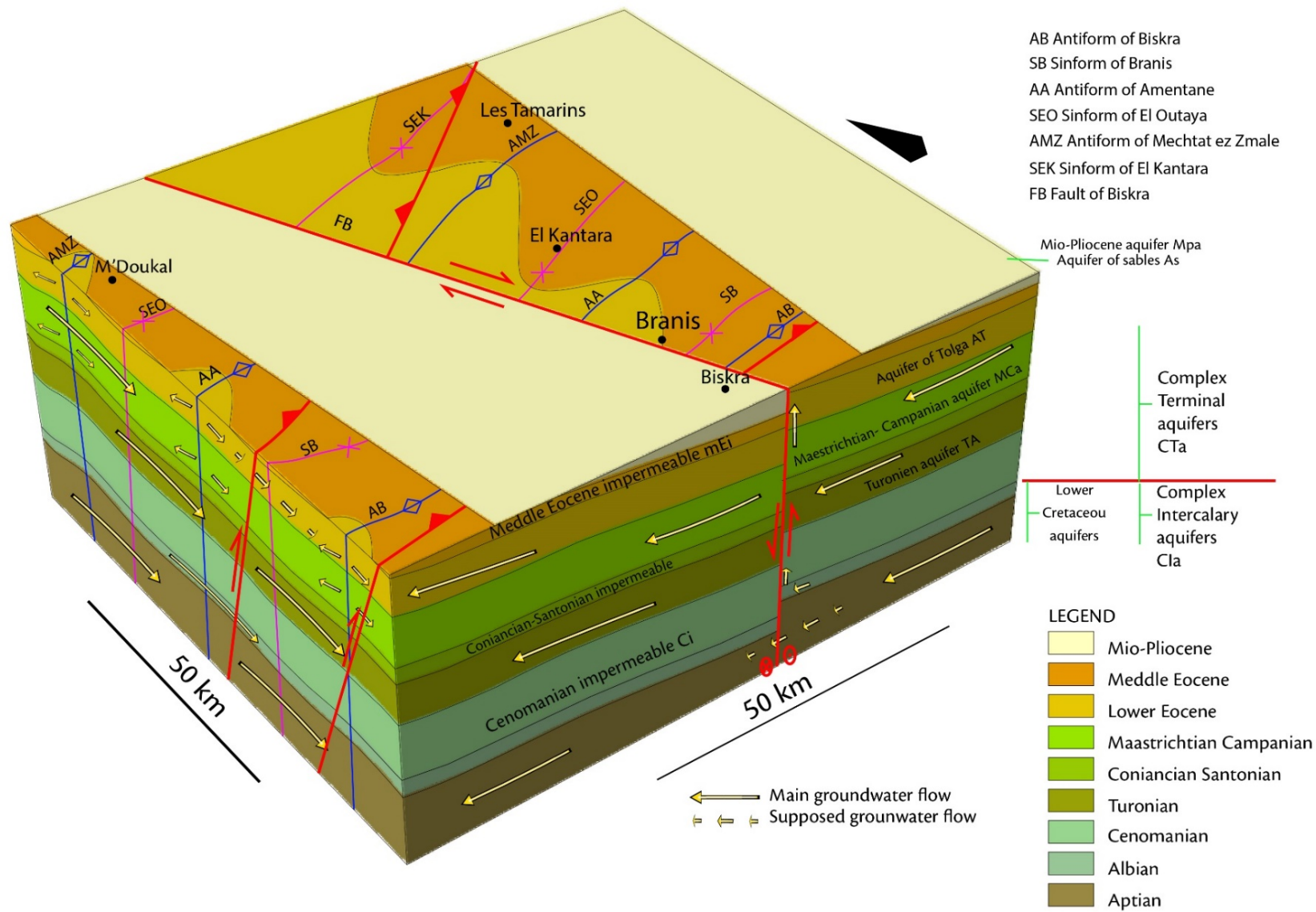


Fig. 4.2 Hydrogeological conceptual model of the Biskra and Batna region illustrating the relationships between the geological framework and the groundwater circulation.

## 4.2 3D HYDRO-GEOLOGICAL MODELS AT LOCAL SCALE

The update of the available cartography is based on the delimitation of geological boundaries observed in the hydrogeological map produced by the SCET-COOP on the contours extracted from the SRTMGL1 DEM (Fig. 4.3 A). The results allowed a better understanding of the whole river system in the study area. Its geomorphological interpretation has strongly influenced the shape of the horizons in the geological cross sections and therefore, the shape of the final surface.

In this area, a succession of marine to continental deposits of Mio-Pliocene to Upper Pliocene age crop out on the wadi riversides. The left bank is characterised by little hills stretched along the NE-SW direction and steep slopes, while the right riverside has a gentle slope morphology. Elevations range from 150 to 190 m a.m.s.l. and in the southern part of the area the Upper Pliocene rocks constitute a morphological sluice from which the Oued el Hai Biskra emerges to the Zibane lowland on a wide alluvial fan. The wide alluvial valley, which includes the relict and active braided channel alluvium, extends over a surface of 3 km<sup>2</sup> and its extension ranges in width from 1.4 km, at the confluence between the Oued el Hai Biskra and the Oued el Besbas, to 0.4 km at the morphological sluice. The flow direction is roughly N-S, except for the central zone of the area where it is turned off according to the NE-SW direction of the Pliocene hills. On the right riverside and the El Hamia locality, the boundary between the active and relict braided stream was delineated according to slope variations observed on the DEM surface in the plain topography. Sometimes this interpretation was not easily because of the DEM undulation related to the morphology of the braided channel.

Regarding the hydrogeological characteristics of the described geological bodies, the Neogene formations are characterised by a low permeability and water could be hosted only within coarse levels and sandy lenses (MdH 1980). The whole Quaternary alluvium, on the contrary, is mainly composed of coarse deposits constituting a productive phreatic aquifer. Given this information, the lithological units were grouped into two hydrogeological units as shown in Fig. 4.3 B.

The 3-D geological model obtained by interpolating the horizons delineated on the geological sections constitutes the natural continuation of the eroded Neogene rocks beneath the Quaternary deposits. In this frame, the final surface is characterised by a geomorphological continuity with the Neogene outcrops. The result is an asymmetric shape surface with a steep slope on the left bank that reaches a maximum depth of 50 m, while on the right bank it gently rises towards the topographic level (Fig. 4.4). This morphological pattern could be related to heavy flood erosion that affected the Neogene rocks when the base level was lower than the present day situation.

The surface obtained through the interpolation of the geological boundaries provides the geometrical configuration of the confining bed of the Inféro-Flux phreatic aquifer. The accuracy of the surface is strongly influenced by the reduced number of deep geological information and their discontinuous distribution within the study area. However, the integration between deep and surface geological data and the SRTMGL1 DEM into a geomorphological interpretation of the stream system has allowed the delimitation of the horizons even where the boreholes were entirely included in the alluvium and did not intercept the Neogene bedrock.

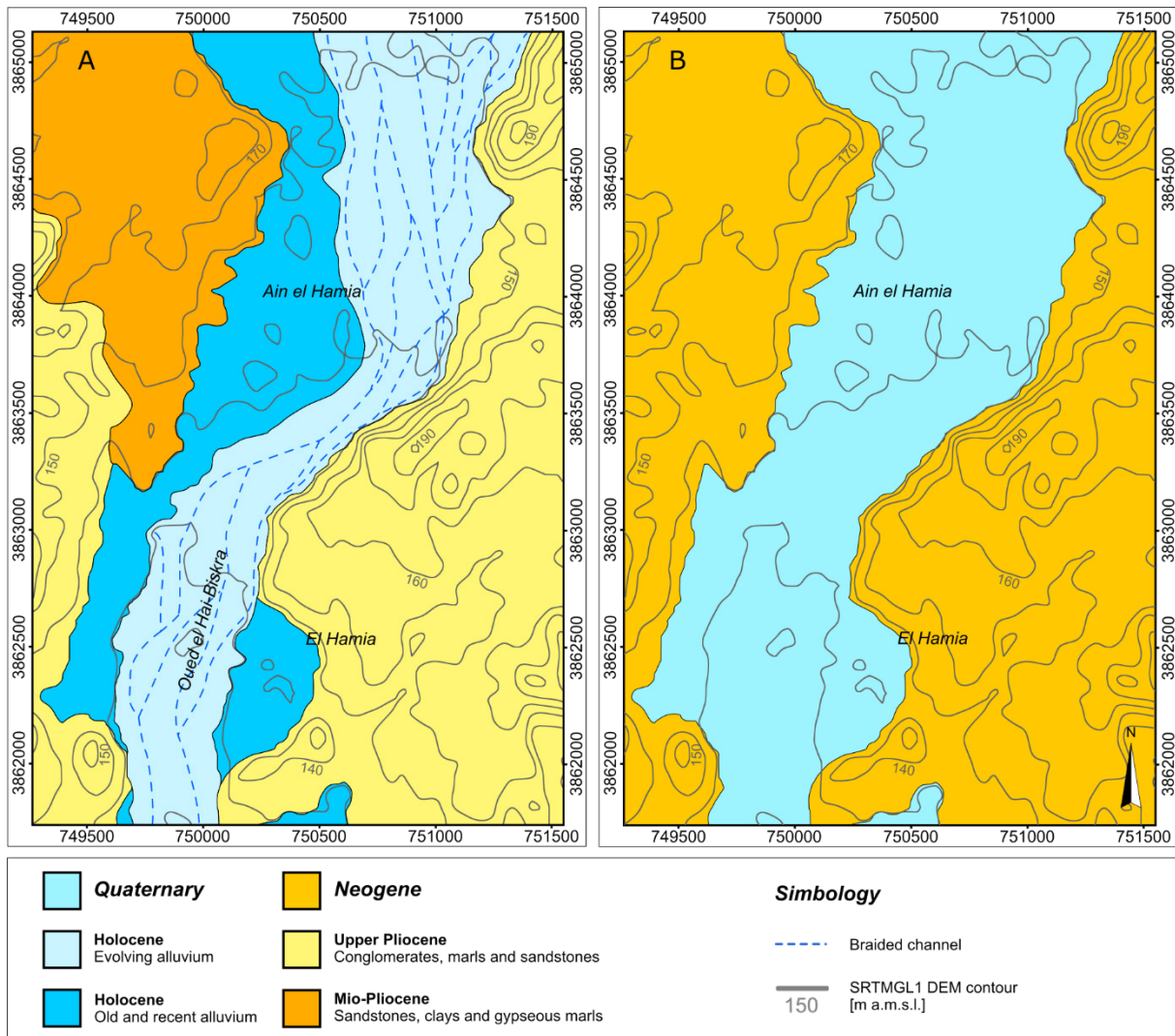


Fig. 4.3 Geological sketch map showing the A) lithological and B) hydrogeological units outcropping in the Inféro-Flux aquifer area.

The 3-D model is based on a consistent geological and geomorphological interpretation and could be used for a quantitative computation of the volume of the Quaternary deposits, even if approximative. The application of the Tetravolume tool, with a grid size of 10 m, provides a volume of 83 Mm<sup>3</sup>, in good agreement with the value of 100 Mm<sup>3</sup> estimated by SCET-COOP (1967) for the same area. Analysis of the alluvium description contained within the borehole reports has allowed the estimation of an average specific yield for the study area that corresponds to  $S_y = 17.4$ . This value is strongly influenced by the coarsest granulometries (gravel/sands) that constitute the larger amount of the alluvium deposits (69%). The volume of exploitable groundwater resources was obtained by multiplying the  $S_y$  with the alluvium volume, and the result gave back a value of 14.5 billion m<sup>3</sup> (Table 4.1).

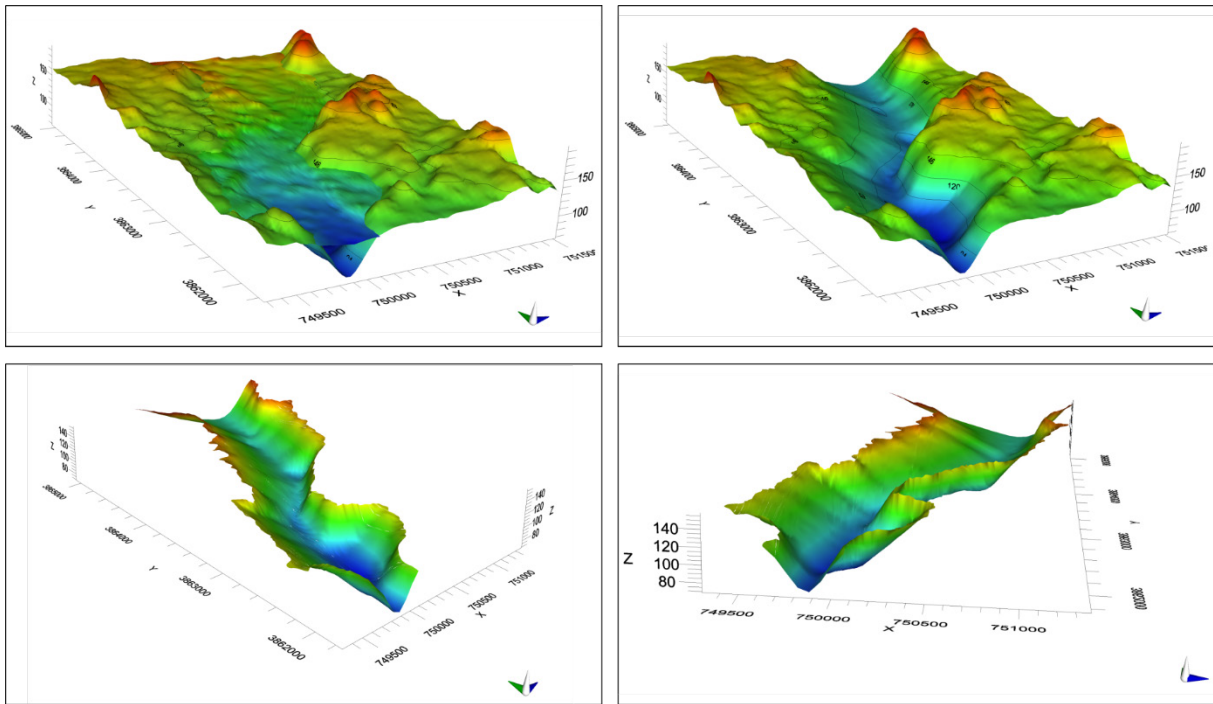


Fig. 4.4 Various perspective views of the 3-D geologic surface representing the geometry of the Inféro-Flux aquifer.

ALLUVIUM VOLUME [m <sup>3</sup> ]	SPECIFIC YIELD (S <sub>y</sub> )	EXPLOITABLE VOLUME [m <sup>3</sup> ]
<b>83 337 302</b>	<b>17.4</b>	<b>14 471 992</b>

Table 4.1 Review of the calculated alluvium volume and the estimated exploitable water volumes for the modeled domain.

### 4.3 HYDROLOGICAL BALANCE

For the estimation of the crop reference evapotranspiration (ET<sub>o</sub>) using the Hargreaves and Samani equation, the extra-terrestrial radiation was firstly estimated. For the Biskra latitude (34.875°N decimal degrees = 0.61 rad), Ra ranges from 15.9 to 17.0 MJ m<sup>-2</sup> d<sup>-1</sup>. Subsequently, the ET<sub>o</sub> was computed at daily scale and yearly cumulative ranges from 675 mm/year in 1990 to 814 mm/year in 2012, while the average ET<sub>o</sub> for the whole period is 751 mm/year (Table 4.2).

The application of the Turc equation using the corrected temperature factor ( $T_c$ ) resulted in  $ET_a$  values greater than the annual precipitations (Table 4.3). It means that the efficient precipitation ( $P_e$ ), i.e. annual precipitation minus actual evapotranspiration, is always negative. The only exception is for 1993, when  $P=297.2$  mm,  $ET_a =297.1$  mm, and therefore  $P_e=0.1$  mm.

The Coutagne formula provides correct  $ET_a$  results for the period 1982-1987, 1989, 1998-2002, 2005, 2007-2008, and 2014-2015 that range from 1 to 4 mm/year. For the other periods and years,  $P$  is bigger than  $1/2 \lambda$ , and therefore  $ET_a$  values are out of the validity range (red highlighted values in Table 4.4).

Potential evapotranspiration estimated by using the Hargreaves and Samani equation significantly exceed the amount of annual precipitation. It demonstrates that the atmosphere, at the latitude of the intervention area, has a high evaporation power as expectable for the study area, which is characterised by arid climatic conditions. The application of the Turc equation for the estimation of actual evapotranspiration at annual scale shows that this method is not applicable in such area. In fact, effective precipitations are always negative, and it means that no water should be available for runoff and infiltration. The Coutagne method gives  $ET_a$  values that fall very close to the annual rainfall providing very little amount of water for effective precipitation. Moreover, nearly 50% of the results are out of the validity range of the equation. The amount of infiltration and runoff water occurring in the wadi surfaces that was computed using the infiltration capacity index proposed by Haouchine (2010) is reported in the water budget summary table (Table 4.5). Valid results are illustrated in black and range from 0.1 to 1.3 and 0.4 to 3.9 mm/year for infiltration and runoff, respectively.

<b>ET<sub>o</sub> – CROP REFERENCE EVAPOTRANSPIRATION: HARGREAVES AND SAMANI EQUATION</b>					
<b>Year</b>	<b>P [mm]</b>	<b>ET<sub>o</sub> [mm]</b>	<b>Year</b>	<b>P [mm]</b>	<b>ET<sub>o</sub> [mm]</b>
1982	119.1	709	2000	73.2	779
1983	44.7	740	2001	80.5	774
1984	56.9	708	2002	60.7	762
1985	116.6	728	2003	204.5	769
1986	126.5	729	2004	304.1	766
1987	91.0	753	2005	73.2	735
1988	182.6	751	2006	144.8	785
1989	72.9	694	2007	69.1	766
1990	144.6	675	2008	100.1	769
1991	138.4	695	2009	133.6	787
1992	192.5	723	2010	198.9	780
1993	297.2	746	2011	252.7	779
1994	342.7	758	2012	126.0	814
1995	286.2	734	2013	204.5	781
1996	292.6	716	2014	63.8	806
1997	192.1	755	2015	109.7	792
1998	101.1	749			
1999	88.9	734	<b>AVERAGE</b>	<b>149.6</b>	<b>751</b>

*Table 4.2 Results of the application of the Hargreaves and Samani equation for the estimation of the reference crop evapotranspiration (ET<sub>o</sub>).*



ET <sub>a</sub> – ACTUAL EVAPOTRANSPIRATION: TURC EQUATION						
Year	P [mm]	T [°C]	T <sub>c</sub> [°C]	L (T <sub>c</sub> )	ET <sub>a</sub> [mm]	P <sub>e</sub> [mm]
1982	119.1	22.4	18.0	1044.1	124.7	-5.5
1983	44.7	22.3	22.0	1386.1	47.1	-2.4
1984	56.9	21.5	20.8	1272.2	59.9	-3.0
1985	116.6	22.2	19.2	1130.1	122.1	-5.6
1986	126.5	22.1	21.4	1321.3	132.7	-6.2
1987	91.0	22.8	16.7	951.7	95.4	-4.4
1988	182.6	22.9	22.0	1386.1	190.7	-8.0
1989	72.9	22.6	23.7	1556.6	76.7	-3.8
1990	144.6	22.6	21.7	1355.6	151.4	-6.9
1991	138.4	21.7	19.5	1155.3	144.8	-6.3
1992	192.5	21.8	19.2	1134.3	199.8	-7.2
1993	297.2	22.4	16.5	936.9	297.1	+0.1
1994	342.7	23.1	24.9	1693.7	353.3	-10.6
1995	286.2	22.3	25.4	1751.6	297.3	-11.1
1996	292.6	21.6	21.8	1360.1	300.8	-8.2
1997	192.1	22.7	18.5	1081.1	199.0	-6.9
1998	101.1	22.2	22.1	1394.1	106.3	-5.2
1999	88.9	23.2	15.4	866.7	93.2	-4.3
2000	73.2	22.7	25.0	1711.8	77.0	-3.9
2001	80.5	23.5	16.1	909.1	84.5	-4.0
2002	60.7	22.9	24.6	1657.8	63.9	-3.2
2003	204.5	23.1	17.4	1001.1	210.7	-6.2
2004	304.1	22.3	19.1	1128.1	308.3	-4.2
2005	73.2	23.1	21.2	1306.4	77.0	-3.8
2006	144.8	22.9	17.9	1034.0	151.0	-6.2
2007	69.1	22.9	24.4	1632.5	72.7	-3.7
2008	100.1	22.7	19.4	1148.8	105.1	-5.0
2009	133.6	22.4	18.9	1111.3	139.7	-6.1
2010	198.9	22.7	20.9	1279.3	206.9	-8.0
2011	252.7	22.5	22.7	1452.4	262.0	-9.3
2012	126.0	23.4	22.7	1447.8	132.2	-6.3
2013	204.5	22.8	20.4	1236.0	212.3	-7.9
2014	63.8	23.5	23.1	1497.1	67.1	-3.4
2015	109.7	22.9	21.0	1289.1	115.2	-5.5
<b>AVERAGE</b>	<b>149.6</b>	<b>22.6</b>	<b>20.7</b>	<b>1282.9</b>	<b>155.2</b>	<b>-5.7</b>

Table 4.3 Results of the application of the Turc's equation for the estimation of the actual evapotranspiration (ET<sub>a</sub>) and the efficient precipitation (P<sub>e</sub>). The red fields indicate negative P<sub>e</sub> values.

ET <sub>a</sub> - ACTUAL EVAPOTRANSPIRATION: COUTAGNE EQUATION								
Year	P [m]	T [°C]	$\lambda$	$1/8 \lambda$	$1/2 \lambda$	ET <sub>a</sub> [m]	ET <sub>a</sub> [mm]	P <sub>e</sub> [mm]
1982	0.119	22.4	0.254	0.032	0.127	0.116	116	4
1983	0.045	22.3	0.255	0.032	0.128	0.044	44	1
1984	0.057	21.5	0.263	0.033	0.131	0.056	56	1
1985	0.117	22.2	0.255	0.032	0.128	0.113	113	3
1986	0.127	22.1	0.257	0.032	0.128	0.122	122	4
1987	0.091	22.8	0.251	0.031	0.125	0.089	89	2
1988	0.183	22.9	0.249	0.031	0.125	0.174	174	8
1989	0.073	22.6	0.253	0.032	0.126	0.072	72	1
1990	0.145	22.6	0.252	0.032	0.126	0.139	139	5
1991	0.138	21.7	0.261	0.033	0.130	0.133	133	5
1992	0.193	21.8	0.260	0.032	0.130	0.183	183	10
1993	0.297	22.4	0.254	0.032	0.127	0.275	275	22
1994	0.343	23.1	0.248	0.031	0.124	0.314	314	29
1995	0.286	22.3	0.255	0.032	0.128	0.265	265	21
1996	0.293	21.6	0.262	0.033	0.131	0.270	270	22
1997	0.192	22.7	0.251	0.031	0.126	0.183	183	9
1998	0.101	22.2	0.256	0.032	0.128	0.099	99	3
1999	0.089	23.2	0.247	0.031	0.124	0.087	87	2
2000	0.073	22.7	0.252	0.031	0.126	0.072	72	1
2001	0.080	23.5	0.245	0.031	0.122	0.079	79	2
2002	0.061	22.9	0.249	0.031	0.125	0.060	60	1
2003	0.204	23.1	0.248	0.031	0.124	0.194	194	10
2004	0.304	22.3	0.255	0.032	0.127	0.280	280	24
2005	0.073	23.1	0.248	0.031	0.124	0.072	72	1
2006	0.145	22.9	0.250	0.031	0.125	0.140	140	5
2007	0.069	22.9	0.250	0.031	0.125	0.068	68	1
2008	0.100	22.7	0.251	0.031	0.126	0.098	98	3
2009	0.134	22.4	0.254	0.032	0.127	0.129	129	5
2010	0.199	22.7	0.251	0.031	0.125	0.189	189	10
2011	0.253	22.5	0.253	0.032	0.126	0.237	237	16
2012	0.126	23.4	0.246	0.031	0.123	0.122	122	4
2013	0.204	22.8	0.250	0.031	0.125	0.194	194	10
2014	0.064	23.5	0.245	0.031	0.122	0.063	63	1
2015	0.110	22.9	0.250	0.031	0.125	0.107	107	3
<b>AVERAGE</b>	<b>0.150</b>	<b>22.6</b>				<b>0.142</b>	<b>142</b>	<b>7</b>

Table 4.4 Results of the application of the Coutagne's (1954) formula to the TuTiempo data set for the estimation of the actual evapotranspiration (ET<sub>a</sub>) and the efficient precipitation (P<sub>e</sub>). The red fields indicate values for which the condition  $P \leq 1/2 \lambda$  is not respected.

WATER BUDGET						
Year	P [mm]	ET <sub>a</sub> [mm] Coutagne	P <sub>e</sub> [mm]	I [mm]	R [mm]	
1982	119.1	116	4	0.90	2.70	
1983	44.7	44	1	0.13	0.38	
1984	56.9	56	1	0.21	0.64	
1985	116.6	113	3	0.87	2.60	
1986	126.5	122	4	1.03	3.08	
1987	91.0	89	2	0.52	1.55	
1988	182.6	174	8	2.08	6.23	
1989	72.9	72	1	0.34	1.01	
1990	144.6	139	5	1.32	3.95	
1991	138.4	133	5	1.25	3.75	
1992	192.5	183	10	2.41	7.23	
1993	297.2	275	22	5.61	16.82	
1994	342.7	314	29	7.27	21.82	
1995	286.2	265	21	5.23	15.69	
1996	292.6	270	22	5.61	16.83	
1997	192.1	183	9	2.32	6.95	
1998	101.1	99	3	0.65	1.96	
1999	88.9	87	2	0.49	1.47	
2000	73.2	72	1	0.34	1.01	
2001	80.5	79	2	0.40	1.19	
2002	60.7	60	1	0.23	0.69	
2003	204.5	194	10	2.59	7.77	
2004	304.1	280	24	5.89	17.68	
2005	73.2	72	1	0.33	1.00	
2006	144.8	140	5	1.31	3.93	
2007	69.1	68	1	0.30	0.89	
2008	100.1	98	3	0.63	1.89	
2009	133.6	129	5	1.13	3.40	
2010	198.9	189	10	2.48	7.44	
2011	252.7	237	16	4.04	12.11	
2012	126.0	122	4	0.97	2.92	
2013	204.5	194	10	2.61	7.84	
2014	63.8	63	1	0.25	0.75	
2015	109.7	107	3	0.75	2.26	
<b>AVERAGE</b>	<b>149.6 – 88.49</b>	<b>142.2 – 86.3</b>	<b>7.4 – 2.1</b>	<b>1.8 – 0.54</b>	<b>5.5 – 1.61</b>	

Table 4.5 Water budget estimation for the wadi alluvium areas. Red values correspond to estimation based on ET<sub>a</sub> derived from the Coutagne equation that is out of the validity range of the formula. Averages are provided considering the valid (black) and all the values (red).

#### 4.4 GROUNDWATER FLOW NUMERICAL MODEL

The conceptualisation of the groundwater system used for the development of the flow numerical model presents a few shortcomings regarding the quantification of recharge water from at least two main sources. The 3-D hydrogeological conceptual model realised at regional scale confirms that groundwater could rise to the surface from the deep hydrogeological systems along preferred pathways as the Biskra fault. However, the quantification of such deep contribution to the Inféro-Flux aquifer is not easy to estimate. The second recharge source, not considered in the conceptualisation is the infiltration during flood events. In fact, it is known that direct infiltration recharge to the phreatic aquifer could occur during flood events (SCET-COOP 1967), but its quantification was difficult to estimate because of the poor number of stream gauge stations in the study area, the lack of continuous stream flow measurements, and the poorly consistent results obtained from the hydrological balance calculation.

##### 4.4.1 MODEL CALIBRATION

First and second PEST execution (Pe1, Pe2) are characterised by relatively high objective functions ( $\phi = 1.555$  and  $0.904$ , respectively) but acceptable correlation coefficient ( $R = 0.99969$  and  $0.99985$ , respectively). In both cases, the distribution of the calibrated hydraulic conductivities is characterised by “bull’s-eye” patterns, where the parameter values vary among several orders of magnitude in a restricted space; in particular, Pe1 resulted in parameter values ranging from  $2.893E-05$  to  $0.01236$  m/s, while for Pe2, parameter values range from  $9.956E-06$  to  $0.07073$  m/s. “Bull’s-eye” patterns do not have a real geological meaning but represent a geometrical effect related to the irregular distribution of the pilot points throughout the model domain. In fact, these PEST executions were performed by using the same pilot points (PP1) scheme but changing the calibration target configuration. Moreover, running the model using the hydraulic conductivities obtained through Pe1 and Pe2, in both cases the B1 pumping well needs to be deactivated in order to reach water budget closure.

The Pe3 was performed by using the pilot point scheme PP2 to avoid geometrical issues in the distribution of the calibrated parameter. However, the very high objective function ( $\phi = 530.8$ ) indicates an anomalous termination of the PEST. Hydraulic conductivities range from  $0.00019$  to  $0.00434$  m/s and also in this case, running the model with the obtained parameters, the B1 pumping well must be deactivated to reach water budget closure.

Pe4 and Pe5 have very low and similar objective function ( $\phi = 8.01E-04$  and  $2.20E-02$ , respectively) and maximum correlation coefficient ( $R = 1$  in both cases). The resulting parameters are also characterised by very similar patterns and values, which range from  $0.00015$  to  $0.00933$  m/s and from  $0.00019$  to  $0.00869$  m/s, for Pe4 and Pe5 respectively.

Results of the Pe5 were selected as the best solution in representing the hydrodynamic characteristics of the aquifer and therefore it will be discussed in detail. Distribution of the hydraulic conductivities obtained by the previous PEST executions and model runs using those parameters are illustrated in the ANNEX C of the present work.

A summary of the PEST executions parameters and results in terms of objective function and correlation coefficient is reported in Table 4.6.

PEST EXEC.	PARAMETERS N	ADJ. PARAMETERS N.	OBSERVATIONS N.	$\phi$	R
Pe1	20	15	37	1.555	0.99969
Pe2	20	15	34	0.9046	0.99985
Pe3	309	304	37	530.8	0.97602
Pe4	309	304	34	8.01E-04	1.00000
Pe5	309	304	34	2.20E-02	1.00000

Table 4.6 Summary illustrating the numbers of parameters and observations, and the objective function and correlation coefficient for all the PEST executions.

#### PEST execution n.5 (Pe5)

The variability of the  $K_x$  parameter throughout the whole modelled domain roughly falls within two orders of magnitude, with values ranging from 0.00019 to 0.00869 m/s (Fig. 4.5). Its spatial distribution could be summarised as follows:

1. The central and northern sectors, where the highest values occur, increasing from 0.0006 m/s in both domain sides (cyan-green colour shades), to the maximum value of 0.0087 m/s roughly in its central axis (yellow-orange colour shades); areas where values are lower than 0.0005 m/s constitute local spots in the north-western and central eastern part of the sector (cyan-blue color shades).
2. The southern sector, where values decrease from 0.0006 – 0.0009 m/s in both domain sides (cyan-green colour shades) to 0.0002 m/s in the central and eastern area of the domain (cyan-blue colour shades).

The lowest  $K_x$  values are located in the central part of the domain constituting a little isolated spot surrounded by higher values. This particular feature does not have a real geological meaning but its occurrence is related to the measured hydraulic conductivity value at the B1 well location that was set as hard pilot point.

Values obtained from the Pe5 are typical of coarse materials like sands and gravels (Todd and Mays 2005). These granulometry terms are coherent with the typology of deposits originated from braided stream systems, where channel bars are built up from coarse material deposition during high-energy fluxes such as flood events (Slatyer and Mabbutt 1964). The spatial distribution of the parameter within the modelled domain does not seem to be influenced by the zonation imposed by the pilot point scheme used for this calibration effort, on the contrary, it is roughly continuous. It is reasonable to consider it related to the evolving mechanism of braided stream, which is characterised by lateral migration. The abandoned stream area constitutes the relict braided that could be submerged again, when exceptional floods occur.

Local increase of the parameter values can be explained by the occurrence of coarser deposits in those areas. In particular, in the central region of the domain the deposition of coarse grain size materials can be related to floods energy reduction in correspondence of the bend created by the Neogene rocky outcrops, which redirects the flux from a N-S direction to a NE-SW one. Deposition of coarser materials in the second high parameter values area, which is located just upstream the first one and mostly comprised within the relict braided stream zone, can be related to ancient events when the braided channel extended over the relict zone, before migrating to the present flowing area.

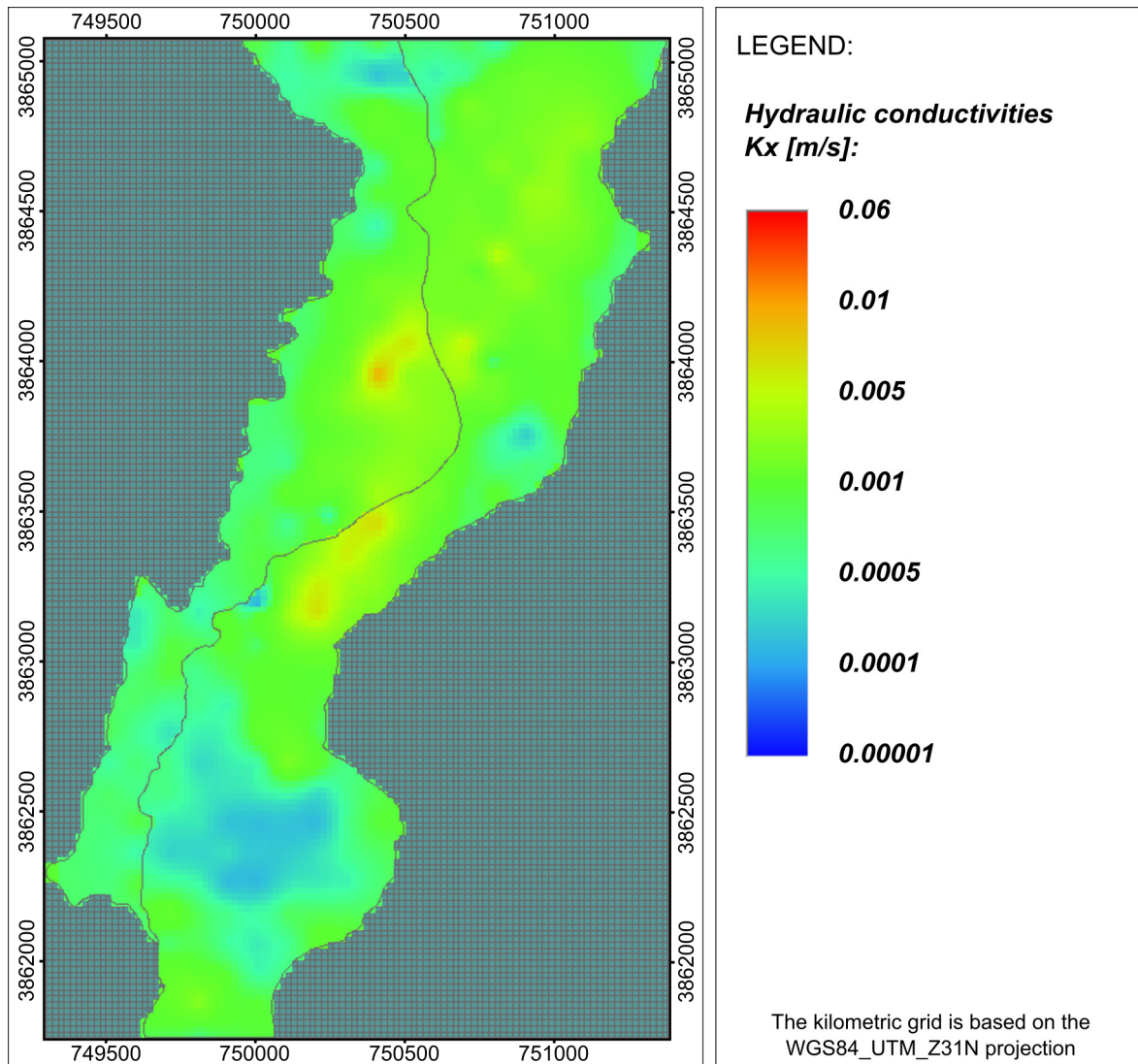


Fig. 4.5 Areal distribution of the calibrated hydraulic conductivities ( $K_x$ ) throughout the model domain as resulted from the PEST execution n.5. The black line cutting the domain from N to S separates the two zones used in the pilot points scheme PP3.

On the contrary, the low hydraulic conductivities values occurring in the southern sector of the domain are most probably related to the deposition of finer deposits that could be the results of further floods energy reduction after the bend.

Hydraulic conductivities estimated through the last PEST execution (Pe5) were used for running the model and evaluate accuracy and precision of the simulation in reproducing measured piezometric heads. Summary statistics (Table 4.7) illustrates that residuals range from a maximum of 0.094 to a minimum of -0.0024 m; the mean residual value is 0.018 m, the absolute residual mean is 0.044m, and the root mean squared is 0.052 m.

Scatter plots were also realised for a quick assessment of model fit. Fig. 4.6 A represents the scatter plot of calibration target vs. simulated head values; it shows that all the points are well distributed along the zero residual line indicating a one-to-one correspondence between simulated and observed values.

RESIDUAL ANALYSIS	VALUE [m]
Min. Residual	-0.0024 m
Max. Residual	0,094 m
Residual Mean	0,018 m
Absolute Residual Mean	0,044 m
Root Mean Squared	0,052 m
Correlation Coefficient	1

Table 4.7 Results of the residual analysis using various statistical indicators.

Fig. 4.6 B represents the scatter plot of residual errors (measured value  $h_m$  minus simulated values  $h_s$ ) at calibration targets; residuals fall very close to the zero residual line and are comprised between +0.094 and -0.085 m.

One-to-one correspondence between measured and simulated heads and low residual values, which are below the 10% of the allowed maximum residual error, prove the good performance of the numerical model in reproducing the measured heads and therefore, the consistency of the hydraulic conductivities estimated by the PEST by applying the CT2 configuration and the PP3 scheme.

A map of observed and simulated water levels is illustrated in Fig. 4.6 C, using 1-metre contour lines. The visual comparison shows that contourlines of simulated piezometric heads are in good agreement with the piezometric heads measured in 1966, especially in the northern and southern part of the domain, from the piezometric heads 148 to 139 m a.m.s.l. and 129 to 121 m a.m.s.l., respectively. In the central domain area, where no calibration targets were used to perform the PEST, the match is rather low, and it is possible to observe a slight displacement. Simulated heads resulted in a more regular spatial distribution with respect to the measured heads, which are characterised by a larger spacing that decrease towards pumping wells alignment and their corresponding cones of influence.

The last figure (Fig. 4.6 D) illustrates the groundwater budget. Simulated groundwater budget assumes that total inflow must be equal to total outflow. The inflow from the northern constant head boundary is 33501 m<sup>3</sup>/d while the outflow at the southern constant head boundary is 7199 m<sup>3</sup>/d. The sink occurs at the six pumping wells described by the SCET-COOP (1967). The model was able to simulate a total withdrawal of 26352 m<sup>3</sup>/d allowing the closure of the water budget.

#### 4.4.2 MODEL VALIDATION

Scatter and residual plot graphs are shown for both 1966 (Fig. 4.7 A,B) and 2012 (Fig. 4.7 C,D) hydrogeological conditions and refer to the second set of calibration targets used for the model validation. The scatter plot of calculated to observed heads for the period 1966 (Fig. 4.7 A) shows a general good distribution of values along the line of zero residuals except for the calibration target Sif/F:06, Sif/F:06-bis, and B:02. The plot of the residuals (Fig. 4.7 B), for the same period, shows that errors are distributed within the range 2.17 m (B:02) to -2.74 m (Sif/F:06). The Residual mean is 0.024 m, the absolute residual mean is 1.16 m, and the root mean squared is 1.5 m (Table 4.8). For 2012, the scatter plot graph (Fig. 4.7 C) shows that biases are larger than the previous dataset. The plot of residuals illustrates that errors are comprised between 2.76 m (B:05-bis) and -4.74 m (F:01) with just two zero residuals at F:03 and Sif/F:05 calibration target (Fig. 4.7 D).

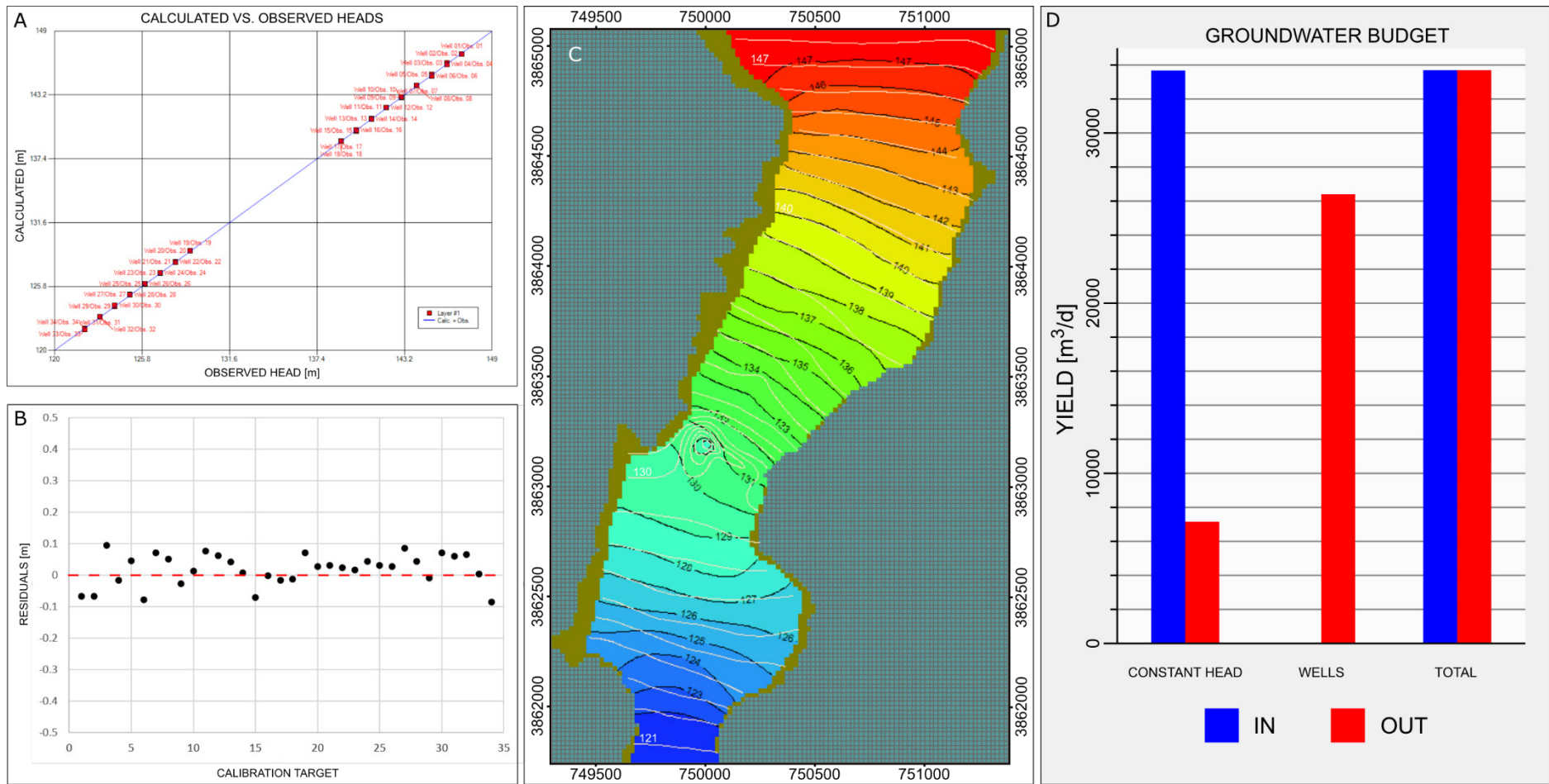


Fig. 4.6 Results of the model run by applying the hydraulic conductivities obtained by the PEST execution n.5: A) scatter plot of simulated to observed fit of water levels; B) plot of residuals at the calibration targets; C) Map view of observed (white) and simulated (black) water tables (shown by contours); D) bar chart illustrating the groundwater budget components.



The residual mean is -0.13 m, the absolute residual mean is 2.047 m, and the root mean squared is 2.44 m (Table 4.8).

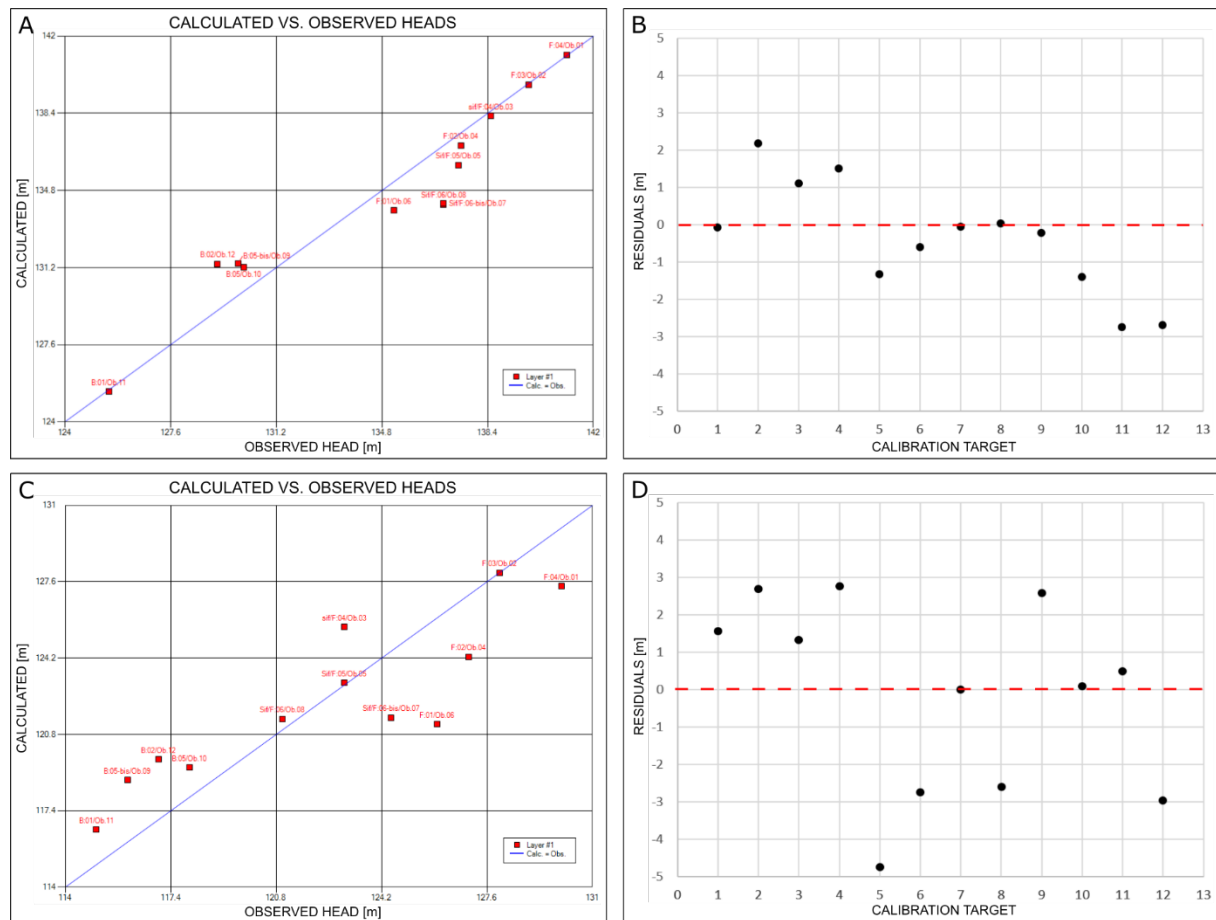


Fig. 4.7 Scatter plot of simulated to observed fit of water levels for A) May 1966 and C) April 2012 at the same calibration target; plot of residuals for B) May 1966 and D) April 2012 at the same calibration targets.

RESIDUAL ANALYSIS	1966 VALUES	2012 VALUES
Min. Residual	0.024 m	0.00 m
Max. Residual	-2.7 m	-4.7 m
Residual Mean	-0.36 m	-0.13 m
Absolute Residual Mean	1.16 m	2.047 m
Root Mean Squared	1.5 m	2.44 m
Correlation Coefficient	0.95	0.88

Table 4.8 Results of the residual analysis using various statistical indicators.

A further graphic analysis of residuals is illustrated in Fig. 4.8. The graph shows measured and simulated heads at each calibration target on the error bar defining the maximum error allowed for both datasets (circles for 1966 and squares for 2012). For the 1966 dataset, the error is related to the georeferenced/projection residual error of the hard copy map, which, in this case, is equal to  $\pm 2.5$  metres. For the 2012 dataset, the error is related to the vertical accuracy of the SRTMGL1 DEM ( $\pm 5.6$  metres) that was used for the calculation of the piezometric heads using the measurements of water table depth. In both cases, the magnitude of the residual errors is comprised within the range of the allowed maximum

error and therefore results of model calibration and validation could be considered acceptable, as well as the consistency of the model simulations.

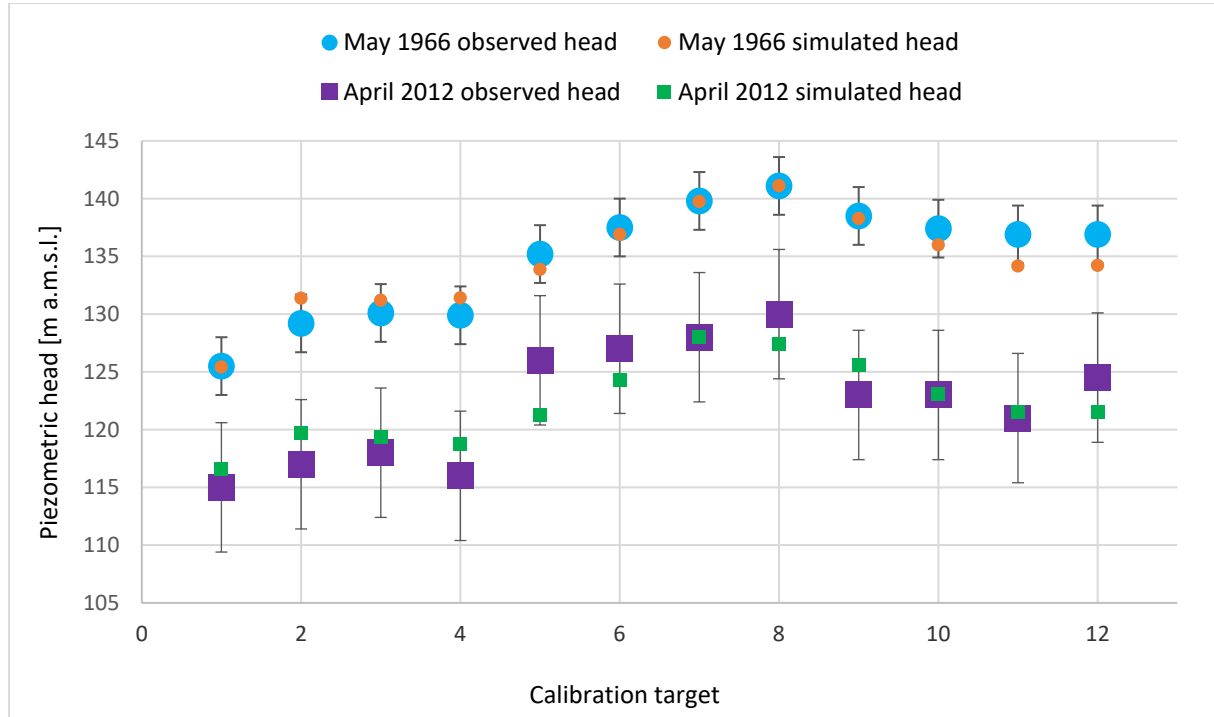


Fig. 4.8 History match of water table for both 1966 and 2012 hydrogeological conditions on the error bar related to the georeferencing approximations ( $\pm 2.5$  m) and the SRTMGL1 DEM vertical accuracy ( $\pm 5.6$  m) respectively.

Visual comparison of measured and simulated heads contours (Fig. 4.9 A) shows that there is no match between them. This result is understandable as it can be related to the fact that the piezometric contours were realised using dynamic water levels measured at pumping wells locations that were strongly influenced by the withdrawal effects on the water table. Therefore, it represents just a geometrical interpolation without an actual hydrogeological meaning.

Fig. 4.9 (B) illustrates the components of the groundwater budget. The computed inflow at the constant head is  $23499 \text{ m}^3/\text{d}$  while the outflow and sink computed at the southern constant head and wells boundary conditions are  $5283$  and  $18216 \text{ m}^3/\text{d}$ , respectively. The model was able to simulate all the boundary conditions allowing the closure of the groundwater budget.

Groundwater budgets resulting from the model runs using the two different hydrogeological conditions show that the inflow at the northern boundary is  $33501 \text{ m}^3/\text{d}$  and  $23499 \text{ m}^3/\text{d}$ , respectively. These values are comparable and are characterised by the same order of magnitude. One question arises about the origin of such groundwater inflow that can relate to the analysis of the hydrological balance. Despite the poor consistency of the computed hydrological balance using empirical formulas at annual scales, average infiltration rates can be used to estimate the amount of rainwater that could potentially infiltrate into the Quaternary alluvium deposits upstream the modelled domain and evaluate the magnitude of such contribution to the inflow.

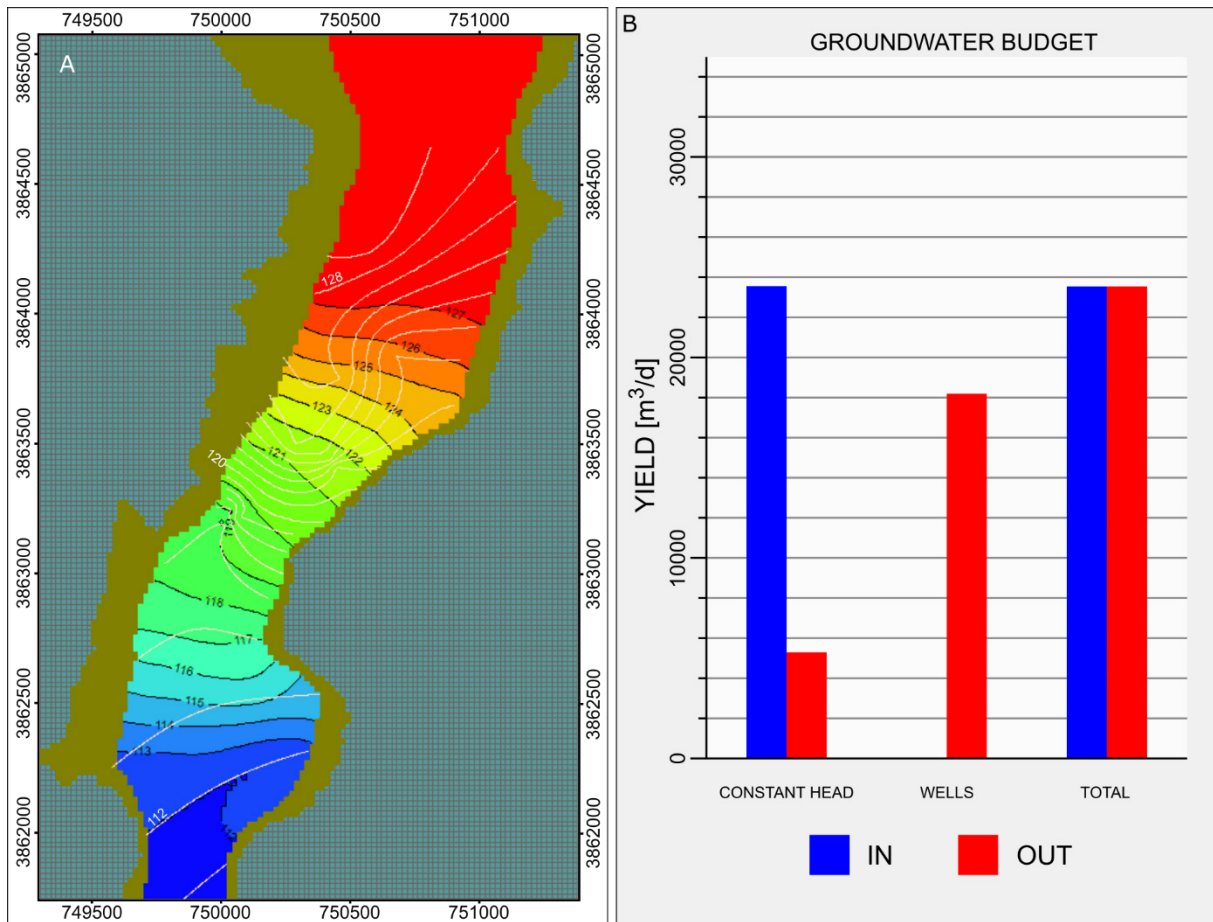


Fig. 4.9 A) Map view of observed (white) and simulated (black) water table (shown as 1 m contour) and B) bar histogram illustrating the components of the groundwater budget.

Quaternary alluvium that can be considered continuous extends over 18.66 km<sup>2</sup> in the sub-watershed of the Oued Branis, Oued Lefrah, and Oued el Besbas. The product of the alluvium surface and the average infiltration value of 0.54 mm/year was estimated using the Haouchine (2010) method and resulted in an amount of infiltrated water of 10079 m<sup>3</sup>/year, and therefore 27.6 m<sup>3</sup>/d.

Given that the infiltration rate (as a result of the hydrological balance) computed in this research can be underestimated and there is the need to perform a more accurate estimation, it is clear that a total infiltration rate of 27.6 m<sup>3</sup>/d is greatly below the total inflow simulated by the model to satisfy the groundwater budget. It means that to compensate for the small contribution of direct alimentation of the aquifer by rainwater infiltration there is the need to consider a further source of alimentation that can be related to the alimentation from the deep groundwater systems as illustrated by the results of the hydrogeological conceptual model at regional scale.

## 4.5 MAR SYSTEM DESIGN

The definition of the geometry of the Inféro-Flux aquifer through the realisation of the 3-D geological model at local-scale provided strong indications about the best location of the MAR system design in the frame of the concomitant PhD research of the colleague Engineer Alberto Carletti. The northern area of the model domain is characterised by the maximum extension of the alluvium deposits in width (about 1,5 km) representing the largest storage area of the modelled domain (Fig. 4.10). The designed MAR system would be located into an active braided channel to collect surface water during floods or normal runoff, and it is constituted by the following components:

- four temporary barriers;
- three recharge trenches;
- four dry star recharge wells with draining pipes;
- two dry recharge wells with buried pipes;
- one recharge basin;
- six piezometers.

For this MAR system, the potential recharge yield was estimated at 1,665 Mm<sup>3</sup>/year. The estimation assumed that source water is represented by flooding water crossing the Oued el Hai-Biskra during twenty days per year, an infiltration capacity of 0,15 L/s m<sup>2</sup> and an average hydraulic conductivity of 10<sup>-3</sup> m/s (Table 4.9).

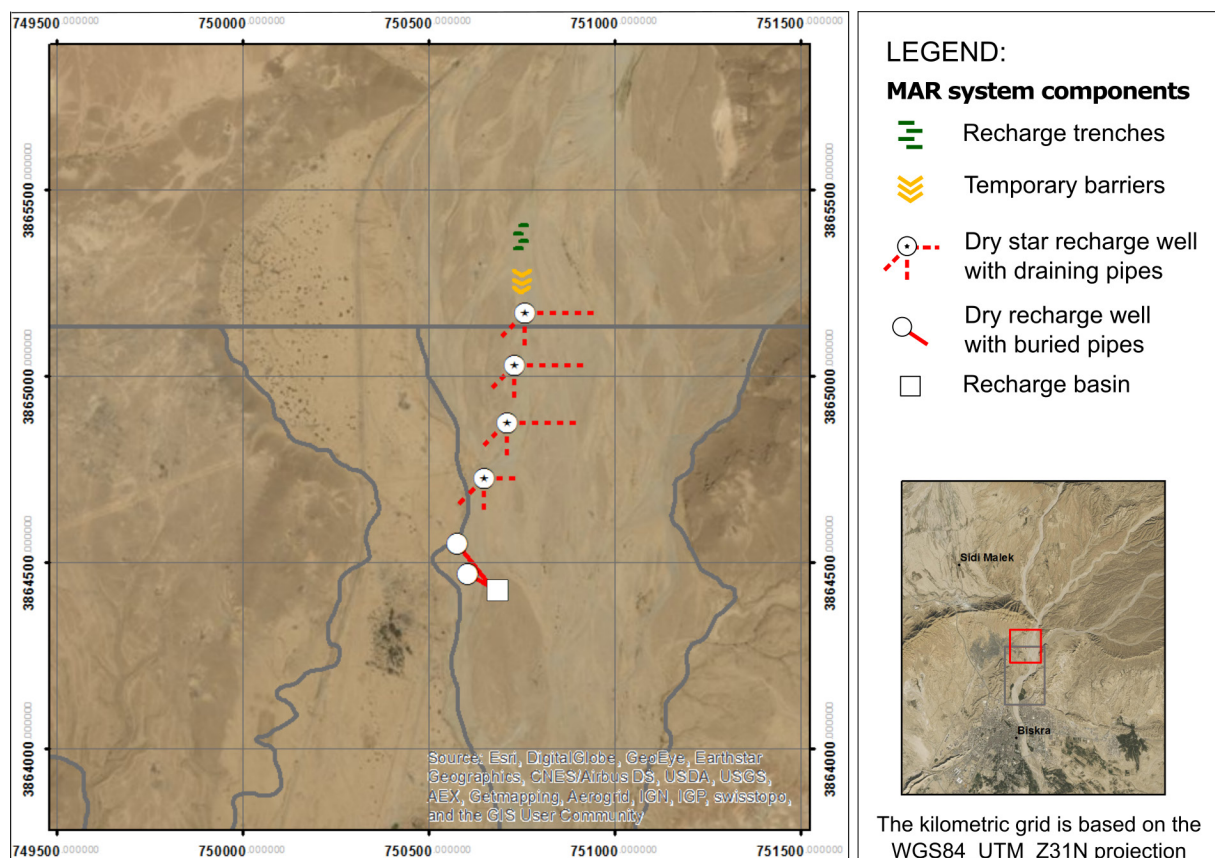


Fig. 4.10 Location of the MAR system designed for the recharge of the Inféro-Flux aquifer.

RECHARGE SYSTEM	YIELD (m3/year per unit)	UNIT N.	TOTAL YIELD (m3/year)
Recharge trenches	66 526	3	199 578
Recharge wells (dry star well)	166 467	4	665 869
Drainage pipes (Recharge well)	97 667	4 (3 per well)	390 666
Recharge well (dry well)	166 467	2	332 934
Recharge basin	76 723	1	76 723

*Table 4.9 Summary of MAR systems designed for the Inféro-Flux aquifer.*



## 5 CONCLUSION

A sustainable and integrated management of the groundwater resources requires a thorough knowledge of the investigated system, in order to understand the complex dynamics related to the geological and meteo-climatic context of the investigated area. The Biskra and Batna region, in Northern Algeria, is characterized by an arid and semi-arid climate and groundwater resources are subjected to overexploitation.

In these areas, the local political context makes the in situ investigation difficult and onerous. Therefore, a methodological approach to address the lack of direct field measurement has been developed. A large amount of data were collected from literature and processed. These input data were integrated with free satellite SRTMGL1 Digital Elevation Model and Landsat8 imagery, and elaborated for the development of 3D hydrogeological models at both regional and local scales. Geological contacts delineated on several geological cross sections were interpolated to obtain the geometrical configuration of the geological bodies identified in the area as three-dimension surfaces. The 3D geological model, integrated with hydrogeological information, allowed to define the geometry of the main groundwater complexes occurring in the region and to understand how the geological and structural framework affects the groundwater circulation. Groundwater recharge occurs in the Aures Mountains, where most of the hydrogeological units are well exposed and precipitations are larger than those measured in the area of Biskra. The interference of two main fold systems creates dome and basin geometries that result in wide storage areas. Several faults induce complications to the groundwater circulation, connecting the various aquifers and acting as preferred pathway for its rise towards the surface. These interpretations were validated by integrating the results of the hydrogeochemical and isotopic survey carried out on groundwater samples of Biskra in 2012, 2013, and 2014 in the frame of the WADIS-MAR Project. The University of Barcelona, which is one of the WADIS-MAR Project partners, have performed these analyses. Coupled hydrochemical and isotopic results confirmed previous hypotheses based mainly on structural geology evidences, showing that the tertiary aquifers are inter-connected, acting as a whole. Moreover, the faults affecting the area connect the tertiary aquifers with the deeper cretaceous aquifers. Among other results, contamination by nitrate was identified near the city of Biskra, affecting the Quaternary and the Mio-Pliocene aquifers. The use of nitrate isotopes evidenced the origin of contamination to be probably related with wastewater, animal manure and fertilizers. Three main sources of sulphate were identified: sewage, fertilizers, and geogenic sulphate from Triassic lithology (Barbieri et al. 2016).

The development of the local scale 3D geological model of the inféro-Flux aquifer required the integration of several geological and topographic data into a geomorphological interpretation to overcome the issues related to the poor number of deep geological data. The final surface, even if approximate, provided quantitative information about the geometrical configuration of the aquifer. The volumes of alluvium and exploitable water were estimated through the average specific yield inferred from the analysis of more than 700 metres of Quaternary deposits qualitatively described in the borehole reports. The assessed 3D model of the Inféro-Flux also allowed the identification of the appropriate locations for the Managed Aquifer Recharge (MAR) system implementation, designed in the frame of the PhD thesis of Alberto Carletti. The northern area of the model domain was selected as the best site for the MAR design, representing the most transmissive area of the

aquifer. For the designed MAR system, the potential recharge yield was estimated in 1,665 Mm<sup>3</sup>/year.

For the purposes of this research, the 3D model reproducing the Inféro-Flux aquifer confining bed represented one of the main input data used for the development of a steady state groundwater flow numerical model of the aquifer. A first conceptualisation phase allowed the definition of the hydrogeological and hydrological dynamics affecting the modelled domain. Piezometric observations were available for two periods, May 1966 and April 2012, and were used in the model calibration and validation phase, respectively. However, uncertainties in the quantification of the aquifer recharge from direct infiltration during precipitations and floods still remains due to the difficulties in the collection of consistent climatic data and the elaboration of the hydrological budget in a region characterised by arid and semi-arid climatic conditions.

The hydrogeological model at the regional scale indicates that the recharge of the phreatic aquifer could occur for rise up of deep groundwater; nevertheless, it was difficult to locate the areas of deep recharge and its quantification. The model calibration using the best configuration of calibration targets and pilot points has provided consistent hydraulic conductivity values that are coherent with the typology of deposits built up by braided stream systems. The model runs performed under two different set of hydrogeological data in the calibration and validation phases provided good results in terms of residuals. They are included in the allowed maximum error that is related to the georeferencing process for the 1966 dataset, and to the vertical accuracy of the digital elevation model for the 2012 dataset. These results demonstrate the consistency of the calibration effort and the ability of the model to simulate the conceptualisation of the aquifer system.

The characterisation and quantification of recharges to the aquifer from the various sources will enable a comprehensive conceptualization of the system. Those integrations implemented in the numerical model will provide a valuable tool for the management of the groundwater resource, its quality assessment, and the simulation of the effects of the designed MAR system in re-pressuring the phreatic aquifer.



## REFERENCES

- Abu-Zreig M, Attom M, Hamasha N (2000) Rainfall harvesting using sand ditches in Jordan. *Agric Water Manag* 46:183–192. doi: 10.1016/S0378-3774(00)00082-2
- Afrasinei G-M, Melis MT, Buttau C, Arras C, Zerrim A, Guied M, Ouessar M, Essifi B, Zaied MB, Jlali A, Jarray H, Ghiglieri G (2017a) Classification Methods for Detecting and Evaluating Changes in Desertification-Related Features in Arid and Semi-arid Environments. In: et al O (ed) *Water and Land Security in Drylands*, in press. Springer,
- Afrasinei G-M, Melis MT, Buttau C, Bradd JM, Arras C, Ghiglieri G (2017b) Assessment of remote sensing-based classification methods for change detection of salt-affected areas (Biskra area, Algeria). *J Appl Remote Sens* 11:29. doi: 10.1117/1.JRS.11.016025
- Ait Ouali R (1991) *Le rifting des Monts des Ksour au Lias: Organisation du bassin, diagénèse des assises carbonatées, place dans les ouvertures mésozoïques au Maghreb*. Université d'Algerie
- Aleksandrowicz S, Turlej K, Lewiński S, Bochenek Z (2014) Change detection algorithm for the production of land cover change maps over the European union countries. *Remote Sens* 6:5976–5994. doi: 10.3390/rs6075976
- Allen RG, Pereira LS, Raes D, Smith M (1998) *Crop evapotranspiration: Guidelines for computing crop requirements*. Irrig Drain Pap No 56, FAO 300. doi: 10.1016/j.eja.2010.12.001
- Alraggad M, Jasem H (2010) Managed Aquifer Recharge (MAR) through Surface Infiltration in the Azraq Basin / Jordan. *J Water Resour Prot* 2:1057–1070. doi: 10.4236/jwarp.2010.212125
- Anderson MP, Woessner WW, Hunt RJ (2015) *Applied groundwater modeling, Simulation of flow and advective transport*, Second Edi. Elsevier
- Andrieux J, Frizon de Lamotte D, Braud J (1989) A structural scheme for the western Mediterranean area in Jurassic and Early Cretaceous times. *Geodin Acta* 3:5–15.
- ANRH (2013) Recharge artificielle de la nappe d'Infero-Flux de la ville de Biskra (Algerie). Dans le but de securiser l'alimentation en eau potable d'une part et d'autre part l'irrigation.
- Arras C, Baba Sy M, Buttau C, Carletti A, Afrasinei G-M, Ghiglieri G (2016) Preliminary results of a 3-D groundwater flow model in an arid region of NE Algeria using PMWin: the Inféro-flux phreatic aquifer (Biskra). *Rend Online Soc Geol Ital* 41:18–21. doi: 10.3301/ROL.2016.82
- Arras C, Buttau C, Carletti A, Funedda A, Ghiglieri G (2014) Geological 3D model for the design of artificial recharge facilities into the Oued Biskra inféro-flux aquifer (NE Algeria). In: *Rendiconti Online Societa Geologica Italiana*. p 542
- Arras C, Melis MT, Afrasinei G-M, Buttau C, Carletti A, Ghiglieri G (2017) Evaluation and validation of SRTMGL1 and ASTER GDEM2 for two Maghreb regions (Biskra, Algeria and Medenine, Tunisia). In: *Water and Land Security in Drylands*, in press. Springer,

- Artimo A, Berg RC, Abert CC, Makinen J (2003a) Constructing a three-dimensional geologic model of the Virttaankangas aquifer, Southwestern Finland: methods applicable to Illinois.
- Artimo A, Mäkinen J, Berg RC, Abert CC, Salonen V-P (2003b) Three-dimensional geologic modeling and visualization of the Virttaankangas aquifer, southwestern Finland. *Hydrogeol J* 11:378–386. doi: 10.1007/s10040-003-0256-6
- Askri H, Belmecheri A, Benrabah B, Boudjema A, Boumendjel K, Daoudi M, Drid M, Ghalem T, Docca AM, Ghandriche H, Ghomari A, Guellati N, Khennous M, Lounici R, Naili H, Takherist D, Terkmani M (1995) Geology of Algeria. In: Well Evaluation Conference Algeria. pp 1–93
- ASTER GDEM Validation Team (2009) ASTER Global DEM Validation - Summary Report.
- ASTER GDEM Validation Team (2011) ASTER Global Digital Elevation Model Version 2 – Summary of Validation Results.
- ASTM (2006) D 5718 - 95 (Reapproved 2006) - Standard guide for documenting a ground-water flow model application.
- Athmania D, Achour H (2014) External validation of the ASTER GDEM2, GMTED2010 and CGIAR-CSI- SRTM v4.1 free access digital elevation models (DEMs) in Tunisia and Algeria. *Remote Sens* 6:4600–4620. doi: 10.3390/rs6054600
- Azooz AA, Talal SK (2015) Evidence of climate change in Iraq. *J Environ Prot Sustain Dev* 1:66–73.
- Barbieri M, Otero N, Carrey R, Domenech C, Arras C, Buttau C, Carletti A, Da Pelo S, Torrentò C, Meftah E, Zahrouna A, Soler A, Ghiglieri G (2016) Isotopic tools applied to the hydrogeochemical characterization and the identification of contamination sources in the Oued Biskra watershed (Algeria). In: *Rendiconti Online Societa Geologica Italiana. Società Geologica Italiana, Roma*, p 709
- Belcher W, Sweetkind D, Elliott P (2002) Probability Distributions of Hydraulic Conductivity for the Hydrogeologic Units of the Death Valley Regional Ground-Water Flow System , Nevada and California. *Water-Resources Investig Rep* 02-4212 18.
- Ben-Itzhak LL, Gvirtzman H (2005) Groundwater flow along and across structural folding: an example from the Judean Desert, Israel. *J Hydrol* 312:51–69. doi: <http://dx.doi.org/10.1016/j.jhydrol.2005.02.009>
- Benhamida S, Fedal M (2008) Inventaire des points d'eau et enquete sur les debits extratits de la wilaya de biskra.
- Berg RC, Thorleifson H (2001) Geological Models for Groundwater Flow. In: *Open File Ser 2001-1, Worksh Extended Abstr, North North-Central Section, Geological Society of America 35th Annu Meeting, Normal, Illinois*,.
- Bjerg PL, Hinsby K, Christensen TH, Gravesen P (1992) Spatial variability of hydraulic conductivity of an unconfined sandy aquifer determined by a mini slug test. *J Hydrol* 136:107–122. doi: 10.1016/0022-1694(92)90007-I

- Bonomi T (2009) Database development and 3D modeling of textural variations in heterogeneous, unconsolidated aquifer media: Application to the Milan plain. *Comput Geosci* 35:134–145. doi: 10.1016/j.cageo.2007.09.006
- Boote DRD, Clark-Lowes DD, Traut MW (1998) Palaeozoic petroleum systems of North Africa, in *Petroleum Geology of North Africa*. *Geol Soc Spec Publ* 133:7–68.
- Borracini F, De Donatis M, D'Ambrogi C, Pantaloni M (2004) Il Foglio 280-Fossombrone 3D: un progetto pilota per la cartografia geologica nazionale alla scala 1:50.000 in tre dimensioni. 123:319–331.
- Boudjema A (1987) Evolution structurale du bassin pétrolier «triasique» du Sahara Nord-Oriental (Algérie). Université Paris-Sud
- Bouillin JP (1986) Le “bassin Maghrébin”: Une ancienne limite entre l'Europe et l'Afrique fi l'ouest des Alpes. *Bull la Société géologique Fr* 2:547–558.
- Bouwer H (2000) Integrated water management: emerging issues and challenges. *Agric Water Manag* 45:217–228. doi: 10.1016/S0378-3774(00)00092-5
- Bouwer H (2002) Artificial recharge of groundwater: hydrogeology and engineering. *Hydrogeol J* 10:121–142. doi: 10.1007/s10040-001-0182-4
- Bracène R, Frizon de Lamotte D (2002) The origin of intraplate deformation in the Atlas system of western and central Algeria: From Jurassic rifting to Cenozoic-Quaternary inversion. *Tectonophysics* 357:207–226. doi: 10.1016/S0040-1951(02)00369-4
- Bracène R, Patriat M, Ellouz N, Gaulier J-M (2003) Subsidence history in basins of northern Algeria. *Sediment Geol* 156:213–239.
- Bureau D (1986) Approche sédimentaire de la dynamique structurale: évolution mésozoïque et devenir tertiaire de la partie septentrionale du fossé présaharien(sud-ouest constantinois et Aurès, Algérie). Université Paris IV
- Buttau C, Funedda A, Carletti A, Viridis S, Ghiglieri G (2013) Studio geologico strutturale per indagini idrogeologiche dell'area compresa tra le regioni di Batna e Biskra (NE Algeria). *Rend Online Soc Geol Ital* 29:13–16.
- Castany G (1982) Bassin sédimentaire du Sahara septentrional (Algérie-Tunisie)—Aquifères du continental intercalaire et du complexe terminal. *Bull Bur Rech Géologiques Minières* 2:127–147.
- Cattaneo G, Gelard J-P, Aite MO, Mouterde rene (1999) La marge septentrionale de la Téthys maghrébine au Jurassique (Djurdjura et Chellata, Grande Kabylie, Algérie). *Bull la Société géologique Fr* 170:173–188.
- Chesnaux R, Lambert M, Walter J, Fillastre U, Hay M, Rouleau A, Daigneault R, Moisan A, Germaneau D (2011) Building a geodatabase for mapping hydrogeological features and 3D modeling of groundwater systems: Application to the Saguenay-Lac-St.-Jean region, Canada. *Comput Geosci* 37:1870–1882. doi: 10.1016/j.cageo.2011.04.013
- Chilès JP, Aug C, Guillen A, Lees T (2004) Modelling the Geometry of Geological Units and its Uncertainty in 3D From Structural Data : The Potential-Field Method. *Orebody Model*

Strateg Mine Plan - Spectr 14 22–24.

Coutagne A (1954) Quelques considérations sur le pouvoir évaporant de l'atmosphère, le déficit d'écoulement effectif et le déficit d'écoulement maximum. *La Houille Blanche* 360–374. doi: 10.1051/lhb/1954036

Da Pelo S, Ghiglieri G, Buttau C, Biddau R, Cuzzocrea C, Funedda A, Carletti A, Vacca S, Cidu R (2017) Coupling 3D hydrogeological modelling and geochemical mapping for an innovative approach to support management of aquifers. *Ital J Eng Geol Environ* 41–51. doi: 10.4408/IJEGE.2017-01.S-04

De Pauw EF (2004) Management of Dryland and Desert Areas. In: *Land Use, Land Cover and Soil Sciences*.

Denker H (2005) Evaluation of SRTM3 and GTOPO30 Terrain Data in Germany. *Gravity, Geoid Sp Mission* 218–223. doi: 10.1007/3-540-26932-0\_38

Department of Water Affairs (2010) Strategy and Guideline Development for National Groundwater Planning Requirements. The Atlantis Water Resource Management Scheme: 30 years of Artificial Groundwater Recharge. PRSA 000/00/11609/10 - Activity 17 (AR5.1).

Di Salvo C, Di Luzio E, Mancini M, Moscatelli M, Capelli G, Cavinato GP, Mazza R (2012) GIS-based hydrostratigraphic modeling of the city of Rome (Italy): analysis of the geometric relationships between a buried aquifer in the Tiber Valley and the confining hydrostratigraphic complexes. *Hydrogeol J* 20:1549–1567. doi: 10.1007/s10040-012-0899-2

Diersch H-J (2013) FEFLOW: finite element modeling of flow, mass and heat transport in porous and fractured media.

Dillon P (2005) Future management of aquifer recharge. *Hydrogeol J* 13:313–316. doi: 10.1007/s10040-004-0413-6

Dillon P, Pavelic P, Page D, Beringen H, Ward J (2009) Managed aquifer recharge: An introduction. Australian Government - National Water Commission, Canberra, A.C.T.

Doherty J (2010) PEST Model-Independent Parameter Estimation, 5th edn.

Durand-Delga M, Fontboté JM (1980) Le cadre structural de la Méditerranée occidentale. *Mémoire du BRGM* 15:677–685.

Duvinage I, Mallet JL (2000) Faulted horizon construction.

Er-Raki S, Chehbouni A, Khabba S, Simonneaux V, Jarlan L, Ouldbba A, Rodriguez JC, Allen R (2010) Assessment of reference evapotranspiration methods in semi-arid regions: Can weather forecast data be used as alternate of ground meteorological parameters? *J Arid Environ* 74:1587–1596. doi: 10.1016/j.jaridenv.2010.07.002

ERESS (1972) Etude des Ressources en Eau de Sahara Septentrional (7 Vols. and Annexes). Paris

Fantozzi PL (2013) Georeferenziare i dati geografici con ArcGIS.

- Farr TG, Rosen PA, Caro E, Crippen R, Duren R, Hensley S, Kobrick M, Paller M, Rodriguez E, Roth L, Seal D, Shaffer S, Shimada J, Umland J, Werner M, Oskin M, Burbank D, Alsdorf D (2007) The Shuttle Radar Topography Mission. *Rev Geophys.* doi: 10.1029/2005RG000183
- Ferril DA, Sims DW, Waiting DJ, Morris AP, Franklin NM, Schultz AL (2004) Structural framework of the Edwards Aquifer recharge zone in south-central Texas. *Geol Soc Am Bull* 116:407–418. doi: 10.1130/B25174.1
- Frizon de Lamotte D, Ghandriche H, Moretti I (1990) La flexure Saharienne: trace d'un chevauchement aveugle post-Pliocène de flèche plurikilométrique au Nord du Sahara (Aurès, Algérie). *Comptes rendus l'Académie des Sci Série 2, Mécanique, Phys Chim Sci l'univers, Sci la Terre* 310:1527–1532.
- Frizon de Lamotte D, Saint bezar B, Bracène R, Mercier E (2000) The two main steps of the Atlas building and geodynamics of the western Mediterranean. *Tectonics* 19:740–761.
- Gale I (2005) Strategies for Managed Aquifer Recharge (MAR) in semi-arid areas.
- Gesch B, Muller J, Farr TG (2006a) The shuttle radar topography mission-Data validation and applications. *Photogramm Eng Remote Sensing* 72:233.
- Gesch D, Farr TG, Slater J, Muller JP, Cook S (2006b) New products from the shuttle radar topography mission. *Eos, Trans Am Geophys Union* 87:174–174.
- Ghiglieri G, Afrasinei G-M, Arras C, Baba Sy M, Barbieri M, Belkheiri O, Ben Zaid M, Buttau C, Carletti A, Dodo A, Enne G, Funedda A, Ioccola I, Ledda L, Lobina R, Meftah E, Melis MT, Messaudane A, Nagaz K, Ouldamura A, Ouessar M, Pittalis D, Roggero PP, Said M, Sghaier M, Soler A, Taibi R, Torrentò C, Viridis S, Zanolla C, Yahyaoui H, Zahrouna A (2014) WADIS-MAR - Water harvesting and Agricultural techniques in Dry lands: an Integrated and Sustainable model in Maghreb Regions. In: *Flowpath*. pp 55–56
- Giese P, Jacobshagen V (1992) Inversion tectonics of intracontinental ranges: High and Middle Atlas, Morocco. *Geol Rundwh* 8:249–259.
- Gogu RC, Carabin G, Hallet V, Peters V, Dassargues A (2001) GIS-based hydrogeological databases and groundwater modelling. *Hydrogeol J* 9:555–569. doi: 10.1007/s10040-001-0167-3
- Guiraud R (1975) L'évolution post-triasique de l'avant-pays de la chaîne alpine en Algérie, d'après l'étude du bassin du Hodna et des régions voisines. *Rev Geogr Phys Geol Dyn* 17:427–446.
- Guiraud R, Bellion Y, Ballais L (2001) Notice Explicative de la Carte Géologique à 1\50.000, LES TAMARINS-Feuille 228.
- Guiraud R, Bosworth W (1997) Senonian basin inversion and rejuvenation of rifting in Africa and Arabia: synthesis and implications to plate-scale tectonics. *Tectonophysics* 282:39–82. doi: [http://dx.doi.org/10.1016/S0040-1951\(97\)00212-6](http://dx.doi.org/10.1016/S0040-1951(97)00212-6)
- Haouchine A (2010) Hydrogéologie en zone semi aride et aride: région de Biskra. Université des Sciences et de la Technologie Houari Boumediene

- Harbaugh, Arlen W (2005) MODFLOW-2005 , The U . S . Geological Survey Modular Ground-Water Model — the Ground-Water Flow Process. US Geol Surv Tech Methods 253.
- Hargreaves GH, Samani ZA (1985) Reference crop evapotranspiration from temperature. *Appl Eng Agric* 1:96–99.
- Hill MC (1998) Methods and guidelines for effective model calibration.
- Hilton RD, Featherstone WE, Berry PAM, Johnston CPD, Kirby JF (2003) Comparison of digital elevation models over Australia and external validation using ERS-1 satellite radar altimetry. *Aust J Earth Sci* 50:157–168. doi: 10.1046/j.1440-0952.2003.00982.x.
- Hirt C, Filmer MS, Featherstone WE (2010) Comparison and validation of the recent freely available ASTER-GDEM ver1, SRTM ver4.1 and GEODATA DEM-9S ver3 digital elevation models over Australia. *Aust J Earth Sci* 57:337–347. doi: 10.1080/08120091003677553
- IGRAC, Acacia Institute (2007) Artificial Recharge of Groundwater in the World.
- Istok J (1989) Groundwater modeling by the finite element method, *Water Reso.* 2000 Florida avenue, NW, Washington, DC 20009
- Jing C, Shortridge A, Lin S, Wu J (2014) Comparison and validation of SRTM and ASTER GDEM for a subtropical landscape in Southeastern China. *Int J Digit Earth* 7:969–992. doi: 10.1080/17538947.2013.807307
- Johnson AI (1963) Specific Yield - Compilation of Specific Yields for Various Materials. USGS Open-File Rep 119. doi: 10.1017/CBO9781107415324.004
- Kassas M (1995) Desertification: a general review. *J Arid Environ* 30:115–128. doi: 10.1016/S0140-1963(05)80063-1
- Kaufmann O, Martin T (2008) 3D geological modelling from boreholes, cross-sections and geological maps, application over former natural gas storages in coal mines. *Comput Geosci* 34:278–290. doi: 10.1016/j.cageo.2007.09.005
- Kazi Tani N (1986) Evolution géodynamique de la bordure nord-africaine: le domaine intraplaque nord-algérien, approche mégaséquentielle.
- Kieken M (1974) Etude géologique du Hodna, du Titteri et de la partie occidentale des Biban. *Publ Serv Cart Géol, Algérie* 46:1–217.
- Laffitte R (1939) Etude géologique de l'Aurès [Algérie].
- Laville E, Petit JP (1984) Role of synsedimentary strike-slip faults in the formation of Moroccan Triassic basins. *Geology* 12:424–427.
- Lemon AM, Jones NL (2003) Building solid models from boreholes and user-defined cross-sections. *Comput Geosci* 29:547–555. doi: 10.1016/S0098-3004(03)00051-7
- Mabbutt JA (1977) Desert Landforms. Canberra
- Mattauer M, Tapponier P, Proust F (1977) Sur les mecanismes de formation des chaines intracontinentales; l'exemple des chaines atlasiques du Maroc. *Bull la Société géologique Fr* 7:521–526.

- McCaffrey K, Jones R, Holdsworth R, Wilson R, Clegg P, Imber J, Holliman N, Trinks I (2005) Unlocking the spatial dimension: digital technologies and the future of geoscience fieldwork. *J Geol Soc London* 162:927–938. doi: 10.1144/0016-764905-017
- McCarthy JD, Graniero PA (2006) A GIS-based borehole data management and 3D visualization system. *Comput Geosci* 32:1699–1708. doi: 10.1016/j.cageo.2006.03.006
- MdH (1980) Carte hydrogéologique de Biskra au 1:200.000.
- Mimeche L (2003) Evaluation et cartographie de la vulnérabilité à la pollution des eaux souterraines de la région de Biskra (sud-est algérien). université de Batna, Algérie
- Murray J, O'Geen AT, McDaniel PA (2003) DEVELOPMENT OF A GIS DATABASE FOR GROUND-WATER RECHARGE ASSESSMENT OF THE PALOUSE BASIN. *Soil Sci* 168:759–768. doi: 10.1097/01.ss.0000100474.96182.5f
- Neuman SP (1982) Statistical Characterization of Aquifer Heterogeneities: An Overview. *Geol Soc Am Spec Pap* 189:81–102. doi: 10.1130/SPE189-p81
- Pinder GF, Gray WG (2013) Finite element simulation in surface and subsurface hydrology.
- Raiber M, White PA, Daughney CJ, Tschirter C, Davidson P, Bainbridge SE (2012) Three-dimensional geological modelling and multivariate statistical analysis of water chemistry data to analyse and visualise aquifer structure and groundwater composition in the Wairau Plain, Marlborough District, New Zealand. *J Hydrol* 436–437:13–34. doi: 10.1016/j.jhydrol.2012.01.045
- Ramsay JG (1967) Folding and Fracturing of Rocks. In: *Folding and Fracturing of Rocks*. p 568
- Remson I, Hornberger GM, Molz FJ (1971) *Numerical Methods in Subsurface Hydrology*: Wiley Interscience. New York
- Ringleb J, Sallwey J, Stefan C (2016) Assessment of Managed Aquifer Recharge through Modeling—A Review. *Water* 2016, Vol 8, Page 579 8:579. doi: 10.3390/W8120579
- Rödiger T, Geyer S, Mallast U, Merz R, Krause P, Fischer C, Siebert C (2014) Multi-response calibration of a conceptual hydrological model in the semiarid catchment of Wadi al Arab, Jordan. *J Hydrol* 509:193–206. doi: 10.1016/j.jhydrol.2013.11.026
- Royse KR, Kessler H, Robins NS, Hughes AG, Mathers SJ (2010) The use of 3D geological models in the development of the conceptual groundwater model [Die Anwendung geologischer 3D-Modelle bei der Entwicklung eines konzeptionellen Grundwassermodells]. *Zeitschrift der Dtsch Gesellschaft für Geowissenschaften* 161:237–249.
- Saraperä S, Artimo A (2004) Updating of the three-dimensional hydrogeological model of the Virttaankangas area, Southwestern Finland. In: Berg RC, Russel H, Thorleifson LH (eds) *Three-dimensional geologic mapping for groundwater applications. Workshop Extended Abstracts - IGS Open-File Series 2004-8*. Illinois State Geological Survey,
- SCET-COOP (1967) Oued Biskra: Eaux souterraines - Etude des ressources exploitables sur analyseur électrique a réseau r.c.

- Shaeri Karimi S, Yasi M, Cox JP, Eslamian S (2014) Handbook of Engineering Hydrology, Vol.3: Environmental Hydrology and Water Management.
- Singh A (2014) Groundwater resources management through the applications of simulation modeling: A review. *Sci Total Environ* 499:414–423. doi: 10.1016/j.scitotenv.2014.05.048
- Slatyer RO, Mabbutt JA (1964) Hydrology of arid and semi- arid regions. In: Chow VT (ed) Handbook of Applied Hydrology. McGraw-Hill, New York, pp 24-1-46
- Sn Repal (1970) Synthèse géologique du Nord de l'Algérie. Sonatrach, unpublished report.
- Sophocleous M (2005) Groundwater recharge and sustainability in the High Plains aquifer in Kansas, USA. *Hydrogeol J* 13:351–365. doi: 10.1007/s10040-004-0385-6
- Stets J (1992) Mid-Jurassic events in the western high Atlas (Morocco). *Geol Rundschau* 81:69–84.
- Stets J, Wurster P (1977) Atlas and Atlantic-structural relations. *Trans Geophysical Union* 58:908–908.
- Strassberg G, Maidment DR, Jones NL (2007) A Geographic Data Model for Representing Ground Water Systems. *Ground Water* 45:515–518. doi: 10.1111/j.1745-6584.2007.00324.x
- Todd D Keith, Mays LW (2005) Groundwater Hydrology, Third Edit.
- Turc L (1951) Nouvelles formale pour le bilan de Peau en fonction des valeurs moyennes annuelles des précipitations et de la température. *Comptes Rendus l'Académie Sci* 233:633–635.
- Turner RJ, Mansour MM, Dearden R, Ó Dochartaigh B, Hughes AG (2015) Improved understanding of groundwater flow in complex superficial deposits using three-dimensional geological-framework and groundwater models: an example from Glasgow, Scotland (UK). *Hydrogeol J* 23:493–506. doi: 10.1007/s10040-014-1207-0
- UNCCD (1994) United Nations Convention to combat desertification in countries experiencing serious drought and/or desertification, particularly in Africa. Paris
- UNCED (1992) Managing Fragile Ecosystems: Combating Desertification and Drought.
- UNEP (1992) World Atlas of Desertification. London
- USGS (2015) Landsat—Earth observation satellites. Reston, VA
- Verheye W (2006) Dry lands and desertification. In: Land Use, Land Cover and Soil Sciences.
- Vila J (1980) La chaîne Alpine d'Algérie orientale et des confins tunisiens. Université Paris IV
- WADIS-MAR (2016) Hydrochemical and isotopic characterization of the WADIS-MAR study watersheds: Oued Biskra (Algeria) and Oum Zessar (Tunisia).
- WADIS-MAR (2013) Quick Guide - WADIS-MAR: Guide for groundwater sampling.
- Wang HF, Anderson MP (1995) Introduction to groundwater modeling: finite difference and



finite element methods.

- White PA, Reeves RR (1999) Waimea Plains aquifer structure as determined by three-dimensional computer modelling. *J Hydrol* 38:49–75.
- Wildi W (1983) La chaîne tello-rifaine (Algérie, Maroc, Tunisie): structure, stratigraphie et évolution du Trias au Miocène. *Rev Geogr Phys Geol Dyn* 24:201–297.
- Winterer EL, Hinz K (1984) The evolution of the Mazagan Continental Margin: a synthesis of geophysical and geological data with results of drilling during DSDP leg. 79. In: King K, Winterer EL (eds) *DSDP Initial Reports*, vol. 79. U.S. Government Printing Office, Washington, pp 893–919
- Wu Q, Xu H (2003) An approach to computer modeling and visualization of geological faults in 3D. *Comput Geosci* 29:503–509. doi: [http://dx.doi.org/10.1016/S0098-3004\(03\)00018-9](http://dx.doi.org/10.1016/S0098-3004(03)00018-9)
- Wu Q, Xu H, Zou X (2005) An effective method for 3D geological modeling with multi-source data integration. *Comput Geosci* 31:35–43. doi: [10.1016/j.cageo.2004.09.005](https://doi.org/10.1016/j.cageo.2004.09.005)
- Xue Y, Sun M, Ma A (2004) On the reconstruction of three-dimensional complex geological objects using Delaunay triangulation. *Futur Gener Comput Syst* 20:1227–1234. doi: [10.1016/j.future.2003.11.012](https://doi.org/10.1016/j.future.2003.11.012)
- Zehnder AT, Allmendinger RW (2000) Velocity field for the trishear model. *J Struct Geol* 22:1009–1014. doi: [10.1016/S0191-8141\(00\)00037-7](https://doi.org/10.1016/S0191-8141(00)00037-7)
- Zhu L, Zhang C, Li M, Pan X, Sun J (2012) Building 3D solid models of sedimentary stratigraphic systems from borehole data: An automatic method and case studies. *Eng Geol* 127:1–13. doi: [10.1016/j.enggeo.2011.12.001](https://doi.org/10.1016/j.enggeo.2011.12.001)
- Ziegler PA (1988) Evolution of the Arctic-North Atlantic and Western Tethys. *AAPG Mem* 43:1–198.

## **WEBSITES**

[http://www.cobagroup.com/NOTICIAS/arq\\_ago2015/news\\_EN\\_05.html](http://www.cobagroup.com/NOTICIAS/arq_ago2015/news_EN_05.html)

<http://www.earthexplorer.usgs.gov/>

<http://www.ons.dz/>

<http://www.stratigraphy.org/>

<http://www.swim-sm.eu/>

<http://www.wadismar.eu/>

## **CARTOGRAPHY**

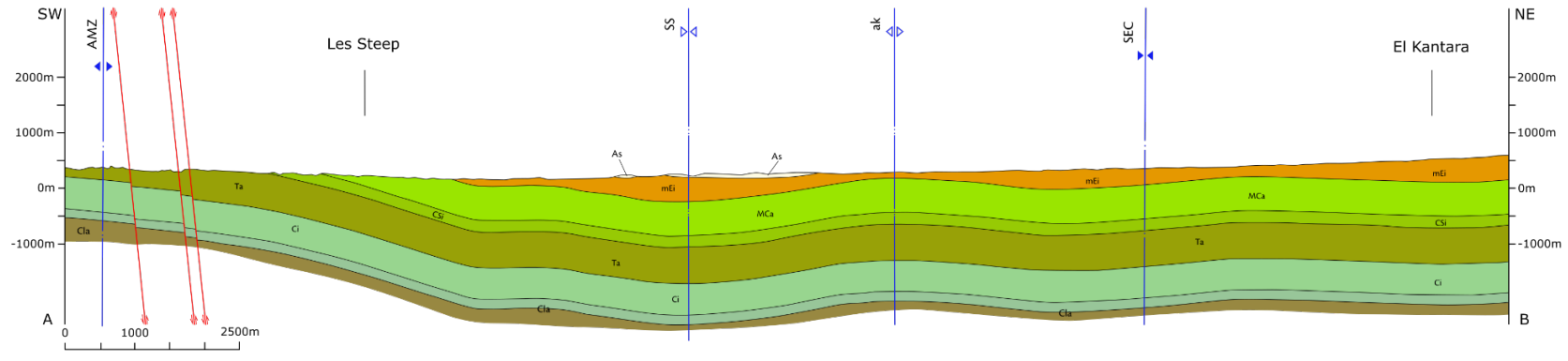
- IGN (1952). EL OUTAYA, Feuille N° 290. Carte d'Algérie – 1:50.000 – Type 1922 – Ministère des Travaux Publics et des Transports, Institut Géographique National (IGN): 136 bis, Rue de Grenelle – Paris (VIIe); Edition 2 – IGNF – Aout 1957.
- IGN (1953). MENAA, Feuille N° 260. Carte d'Algérie – 1:50.000 – Edition Provisoire – Ministère des Travaux Publics et des Transports, Institut Géographique National (IGN): 136 bis, Rue de Grenelle – Paris (VIIe).
- IGN (1955). MCHOUNECH, Feuille N° 291. Carte d'Algérie – 1:50.000 – Edition Provisoire – Ministère des Travaux Publics et des Transports, Institut Géographique National (IGN): 136 bis, Rue de Grenelle – Paris (VIIe).
- IGN (1956). DJEBEL SAHBANA, Feuille N° 257. Carte d'Algérie – 1:50.000 – Edition Provisoire – Ministère des Travaux Publics et des Transports, Institut Géographique National (IGN): 136 bis, Rue de Grenelle – Paris (VIIe).
- IGN (1956). M'DOUKAL, Feuille N° 258. Carte d'Algérie – 1:50.000 – Edition Provisoire – Ministère des Travaux Publics et des Transports, Institut Géographique National (IGN): 136 bis, Rue de Grenelle – Paris (VIIe).
- IGN (1957). BISKRA, Feuille N° 320. Carte d'Algérie – 1:50.000 – Type 1922 – Ministère des Travaux Publics et des Transports, Institut Géographique National (IGN): 136 bis, Rue de Grenelle – Paris (VIIe).
- IGN (1957). SIDI OKBA, Feuille N° 321. Carte d'Algérie – 1:50.000 – Type 1922 – Ministère des Travaux Publics et des Transports, Institut Géographique National (IGN): 136 bis, Rue de Grenelle – Paris (VIIe); Edition 2 – IGNF – Aout 1957.
- IGN (1960). EL KANTARA, Feuille N° 259. Carte d'Algérie – 1:50.000 – Edition Provisoire – Ministère des Travaux Publics et des Transports, Institut Géographique National (IGN): 136 bis, Rue de Grenelle – Paris (VIIe).
- IGN (1961). BORDJ EL HARAIA, Feuille P-Q\_9-10. Carte d'Algérie – 1:200.000 – Type 1960, Ministère des Travaux Publics et des Transports, Institut Géographique National (IGN): 136 bis, Rue de Grenelle – Paris (VIIe).
- IGN (1964). BISKRA, Feuille N-O\_7-8. Carte d'Algérie – 1:200.000 – Type 1960, Ministère des Travaux Publics et des Transports, Institut Géographique National (IGN): 136 bis, Rue de Grenelle – Paris (VIIe).
- IGN (1964). ZERIBET EL OUED, Feuille P-Q\_7-8. Carte d'Algérie – 1:200.000 – Type 1960, Ministère des Travaux Publics et des Transports, Institut Géographique National (IGN): 136 bis, Rue de Grenelle – Paris (VIIe).
- IGN (1965). MESSAAD, Feuille L-M\_9-10. Carte d'Algérie – 1:200.000 – Type 1960, Ministère des Travaux Publics et des Transports, Institut Géographique National (IGN): 136 bis, Rue de Grenelle – Paris (VIIe).
- IGN (1966). AIN RICH, Feuille L-M\_7-8. Carte d'Algérie – 1:200.000 – Type 1960; Ministère des Travaux Publics et des Transports, Institut Géographique National (IGN): 136 bis, Rue de Grenelle – Paris (VIIe).

- IGN (1966). OURIR, Feuille N-O\_9-10. Carte d'Algérie – 1:200.000 – Type 1960, Ministère des Travaux Publics et des Transports, Institut Géographique National (IGN): 136 bis, Rue de Grenelle – Paris (VIIe).
- INCT (2003). TKOUKT, Feuille NI-32-XIX-7 Ouest. Edition N°01 Visa N°163 L1 2614 2003; Ministère de la Défense Nationale, Institut National de Cartographie et de Télédétection (INCT): 123, Rue de Tripoli Hussein-Dey – Algier.
- Laffitte R. (1939). Etude géologique de l'Aurès [Algérie]. Service de la carte géologique de l'Algérie.
- SAG (1960). CHAIBA, Feuille N° 318. Carte d'Algérie – 1:50.000, Section Géographique de l'Armée (SAG); G.G.F.3. P.741, Edition I Novembre 1960.
- SAG (1960). OUED SALSOU, Feuille N° 289. Carte d'Algérie – 1:50.000, Section Géographique de l'Armée (SAG); G.G.F.3. P.741, Edition I Novembre 1960.
- SAG (1961). DJEBEL DOKHANE, Feuille N° 288. Carte d'Algérie – 1:50.000, Section Géographique de l'Armée (SAG); G.G.F.3. P.741, Edition I Mars 1961.
- SAG (1961). TOLGA, Feuille N° 319. Carte d'Algérie – 1:50.000, Section Géographique de l'Armée (SAG); G.G.F.3. P.741, Edition I Février 1961.
- SGA (1962). BISKRA, Feuille N°48. Carte Géologique de l'Algérie – 1:200.000, Service de la Carte Géologique de l'Algérie (SGA).
- SGA (1972). AIN RICH, Feuille L-M\_7-8 (N°47). Carte Géologique de l'Algérie – 1:200.000, Ministère de l'Industrie et de l'Énergie, Direction des Mines et de la Géologie, Service Géologique de l'Algérie (SGA).
- SDG (1981). EL KANTARA, Feuille N°259. Carte Géologique de l'Algérie – 1:50.000, Ministère de l'Industrie Lourde, Direction des Mines et de la Géologie, Sous-Direction de la Géologie (SDG).
- SGA (1998). LES TAMARINS, Feuille N°228. Carte Géologique de l'Algérie – 1:50.000, Ministère de l'Énergie et de Mines, Office National de la Recherche Géologique et Minière, Service Géologique de l'Algérie (SGA): B.P. 102, Boumerdès.
- SGA (1998). M'DOUKAL, Feuille N°258. Carte Géologique de l'Algérie – 1:50.000, Ministère de l'Énergie et de Mines, Office National de la Recherche Géologique et Minière, Service Géologique de l'Algérie (SGA): B.P. 102, Boumerdès.
- Unknown (----). BISKRA, Feuille N° NI-31\_XVIII. Carte Géologique Interpretative 1:200.000.
- Unknown (----). BARIKA, Feuille N° NI-31\_XXIV. Carte Géologique Interpretative 1:200.000.
- Unknown (----). Carte Géologique de la Région de BISKRA. 1:200.000.

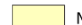

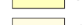
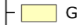












**ANNEX A**  
REGIONAL SCALE 3-D MODEL:  
Geological cross sections at 1:50.000 scale


# Balanced geological section A-A'





## LEGEND

	MPa	Mio-Pliocene		G	Continental deposits, clay, marls, arenaceous marls (Neogene)
	As	Upper Miocene (Tortonian - Langhian)		F	Sandstones, marls, clays and conglomerates (Paleogene)
	mEi	Middle Eocene		E	Limestones, marls, sandstones (Cretaceous)
	MuEla	Upper Cretaceous (Late Maastrichtian) - Lower Eocene			
	MCa	Upper Cretaceous (Early Maastrichtian - Campanian)			
	CSi	Upper Cretaceous (Early Santonian - Coniacian)			
	Ta	Upper Cretaceous (Turonian)			
	Ci	Upper Cretaceous (Early Turonian - Cenomanian)			
	Cla	Early Cretaceous (Albian)			
		Early Cretaceous (Aptian)			

 Axial plane trace of antiform related to the "Atlas Event"

 Axial plane trace of synform related to the "Atlas Event"

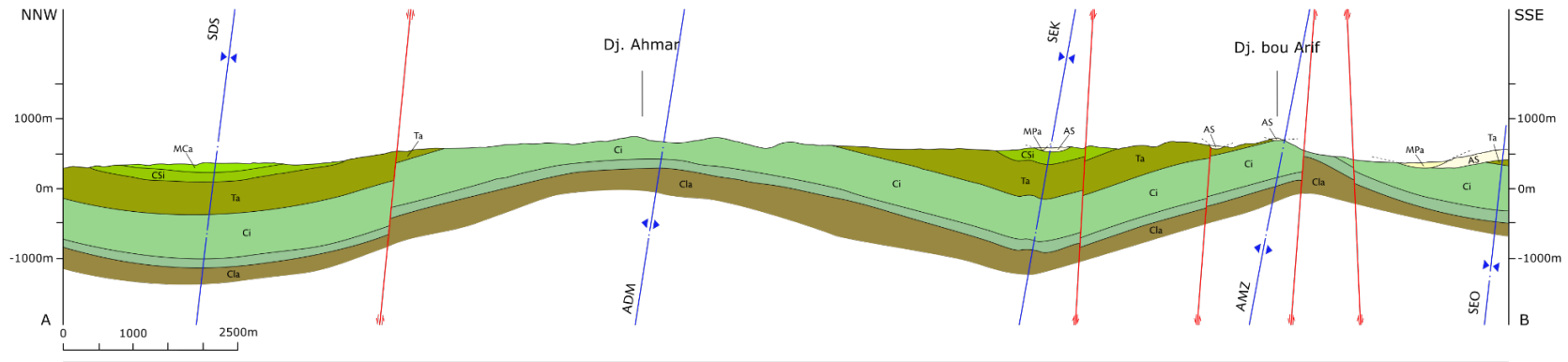
 Axial plane trace of synform related to the "Villafranchian phase"

 Axial plane trace of antiform related to the "Villafranchian phase"

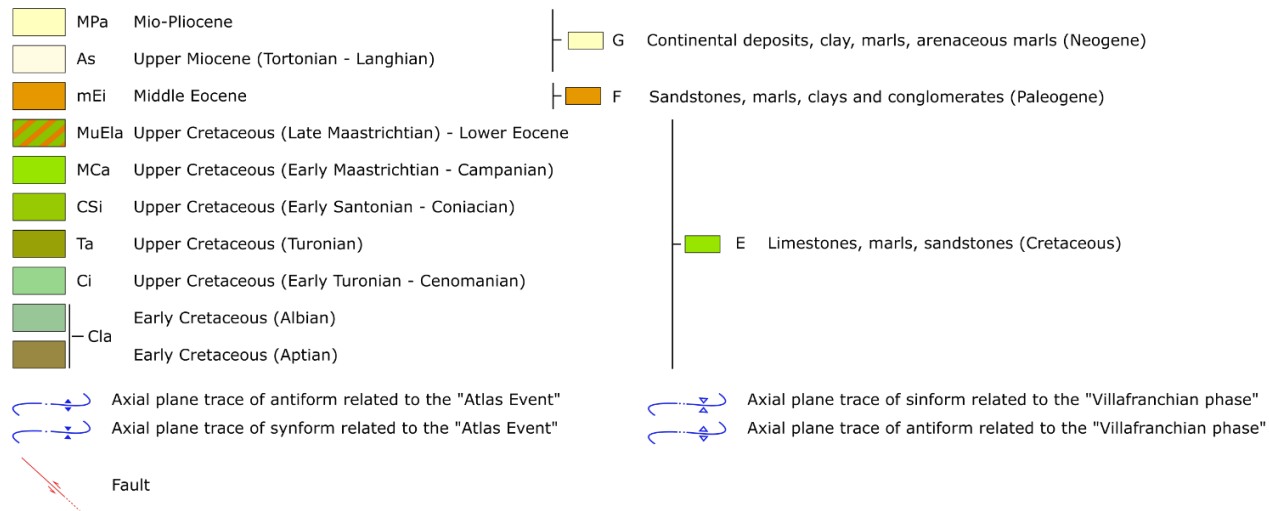
 Fault

Fig.

# Balanced geological section A-B

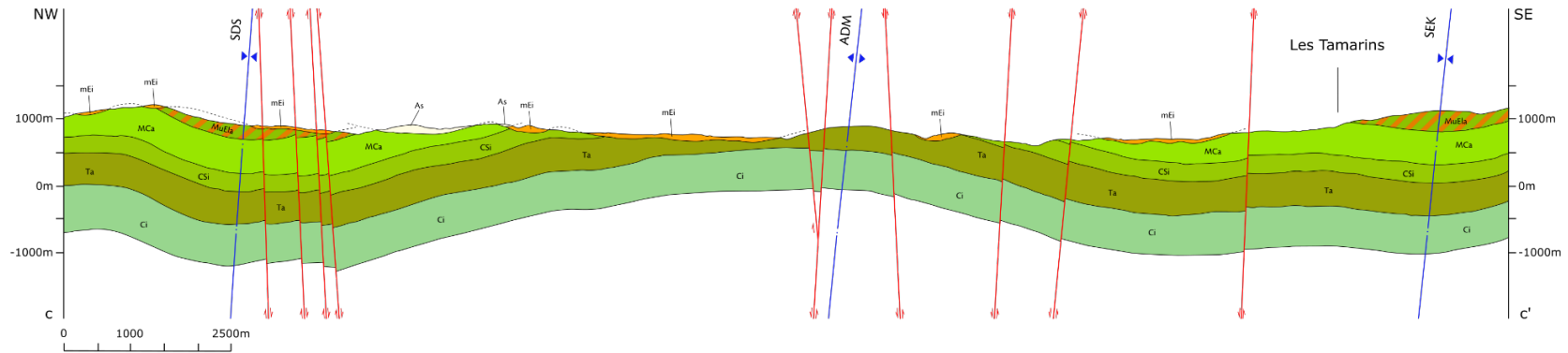


## LEGEND



Fig

# Balanced geological section c-c'



## LEGEND



















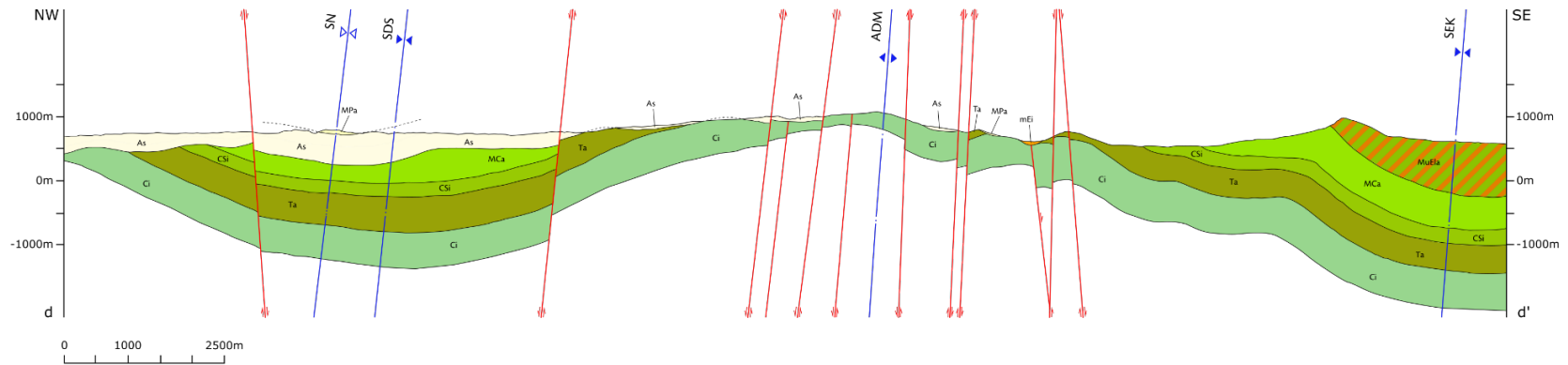
- |   |  |   |   |
|---|--|---|---|
|  MPa   | Mio-Pliocene   |  G    | Continental deposits, clay, marls, arenaceous marls (Neogene) |
|  As    | Upper Miocene (Tortonian - Langhian)                 |  F    | Sandstones, marls, clays and conglomerates (Paleogene)        |
|  mEi   | Middle Eocene  |  E | Limestones, marls, sandstones (Cretaceous)                    |
|  MuEla | Upper Cretaceous (Late Maastrichtian) - Lower Eocene |   |   |
|  MCa  | Upper Cretaceous (Early Maastrichtian - Campanian)   |   |   |
|  CSi | Upper Cretaceous (Early Santonian - Coniacian)       |   |   |
|  Ta  | Upper Cretaceous (Turonian)                          |   |   |
|  Ci  | Upper Cretaceous (Early Turonian - Cenomanian)       |   |   |
|  Cla | Early Cretaceous (Albian)                            |   |   |
|  Cla | Early Cretaceous (Aptian)                            |   |   |
- 
- |   |  |  |   |
|---|--|--|---|
|  | Axial plane trace of antiform related to the "Atlas Event" |  | Axial plane trace of sinform related to the "Villafranchian phase"  |
|  | Axial plane trace of synform related to the "Atlas Event"  |  | Axial plane trace of antiform related to the "Villafranchian phase" |
|  | Fault  |  |   |

Fig.



# Balanced geological section d-d'



## LEGEND

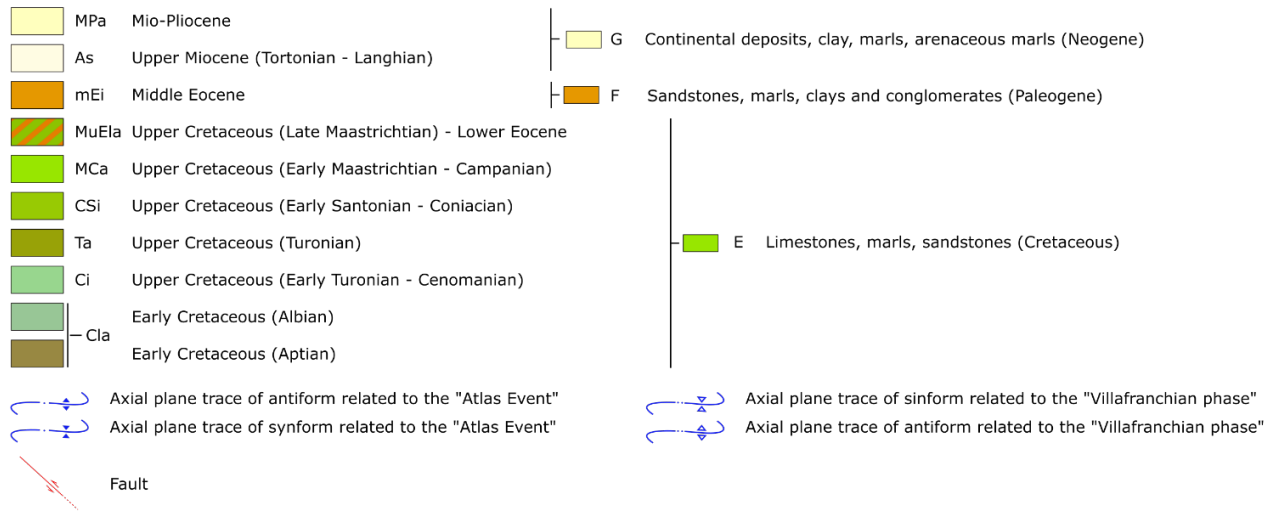
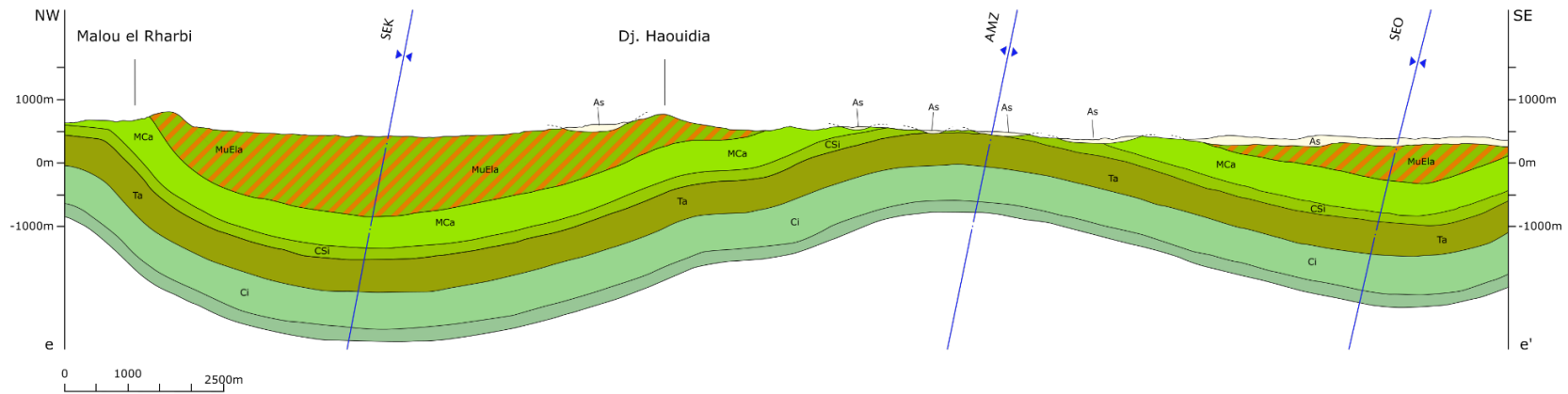


Fig.

# Balanced geological section e-e'

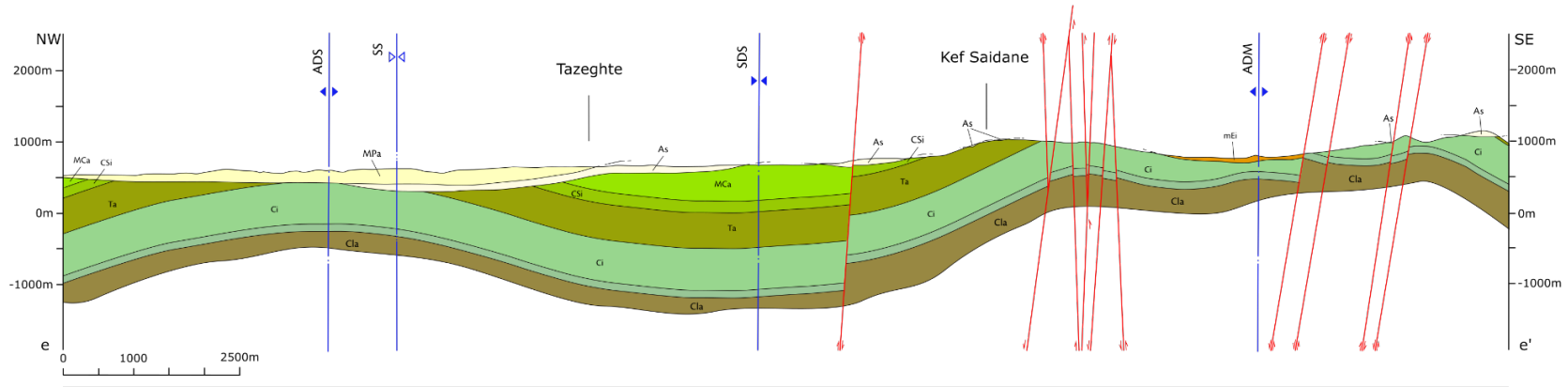


## LEGEND

- |                           |  |   |   |
|---------------------------|--|---|---|
| MPa                       | Mio-Pliocene   | G | Continental deposits, clay, marls, arenaceous marls (Neogene) |
| As                        | Upper Miocene (Tortonian - Langhian)                 | F | Sandstones, marls, clays and conglomerates (Paleogene)        |
| mEi                       | Middle Eocene  | E | Limestones, marls, sandstones (Cretaceous)                    |
| MuEla                     | Upper Cretaceous (Late Maastrichtian) - Lower Eocene |   |   |
| MCa                       | Upper Cretaceous (Early Maastrichtian - Campanian)   |   |   |
| CSi                       | Upper Cretaceous (Early Santonian - Coniacian)       |   |   |
| Ta                        | Upper Cretaceous (Turonian)                          |   |   |
| Ci                        | Upper Cretaceous (Early Turonian - Cenomanian)       |   |   |
| Cla                       | Early Cretaceous (Albian)                            |   |   |
| Early Cretaceous (Aptian) |  |   |   |
- 
- |  |  |  |   |
|--|--|--|---|
|  | Axial plane trace of antiform related to the "Atlas Event" |  | Axial plane trace of synform related to the "Villafranchian phase"  |
|  | Axial plane trace of synform related to the "Atlas Event"  |  | Axial plane trace of antiform related to the "Villafranchian phase" |
|  | Fault  |  |   |

Fig.

# Balanced geological section e-e' bis



## LEGEND


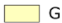
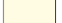















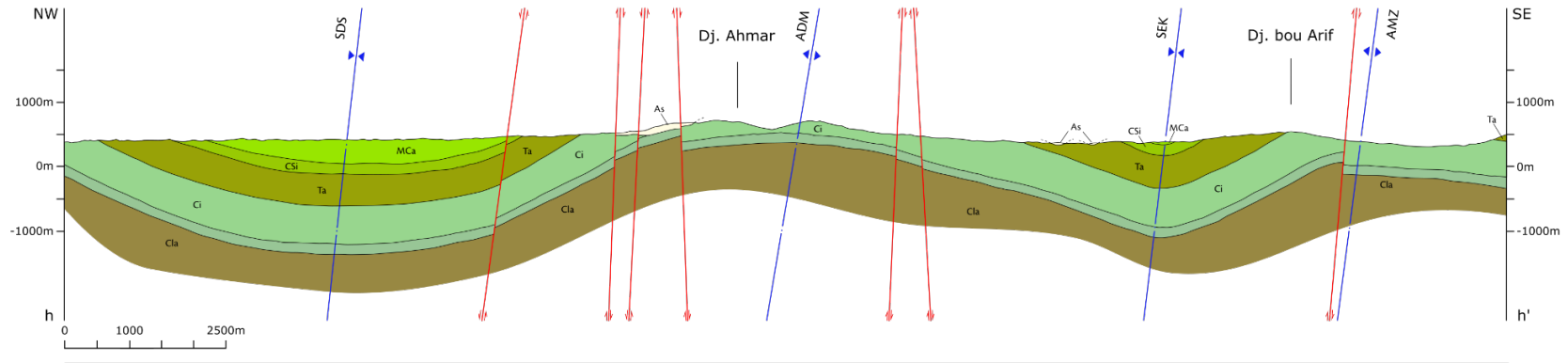
- |   |  |   |   |
|---|--|---|---|
|  MPa   | Mio-Pliocene   |  G     | Continental deposits, clay, marls, arenaceous marls (Neogene)       |
|  As    | Upper Miocene (Tortonian - Langhian)                       |  F     | Sandstones, marls, clays and conglomerates (Paleogene)              |
|  mEi   | Middle Eocene  |  E | Limestones, marls, sandstones (Cretaceous)                          |
|  MuEla | Upper Cretaceous (Late Maastrichtian) - Lower Eocene       |   |   |
|  MCa | Upper Cretaceous (Early Maastrichtian - Campanian)         |   |   |
|  CSi | Upper Cretaceous (Early Santonian - Coniacian)             |   |   |
|  Ta  | Upper Cretaceous (Turonian)                                |   |   |
|  Ci  | Upper Cretaceous (Early Turonian - Cenomanian)             |   |   |
|  Cla | Early Cretaceous (Albian)                                  |   |   |
|  Cla | Early Cretaceous (Aptian)                                  |   |   |
|      | Axial plane trace of antiform related to the "Atlas Event" |     | Axial plane trace of synform related to the "Villafranchian phase"  |
|      | Axial plane trace of synform related to the "Atlas Event"  |     | Axial plane trace of antiform related to the "Villafranchian phase" |
|      | Fault  |   |   |

Fig.

# Balanced geological section h-h'



## LEGEND

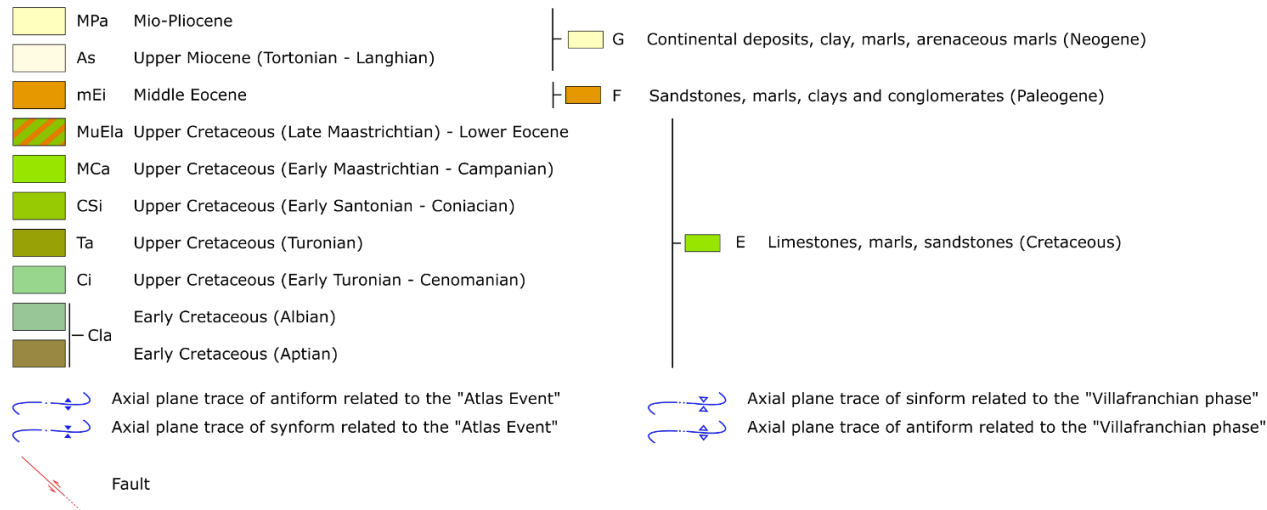
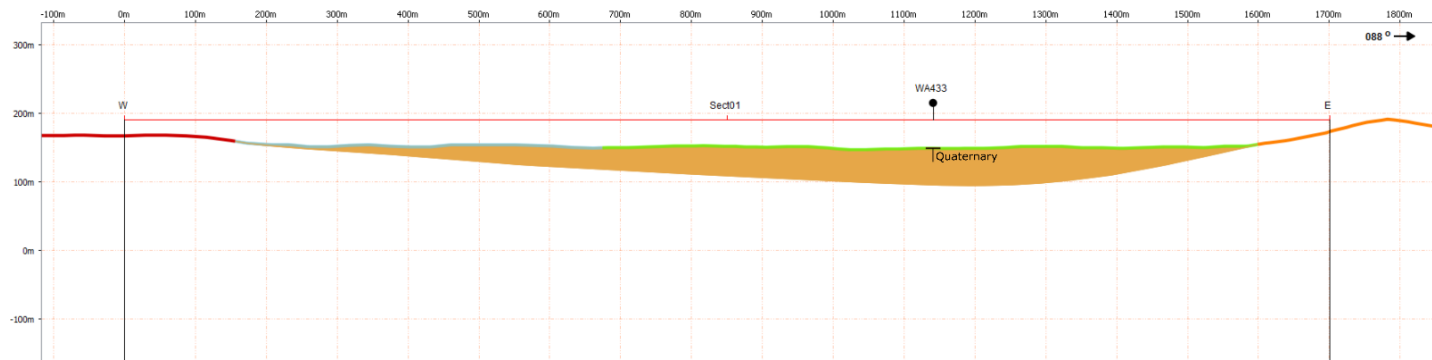


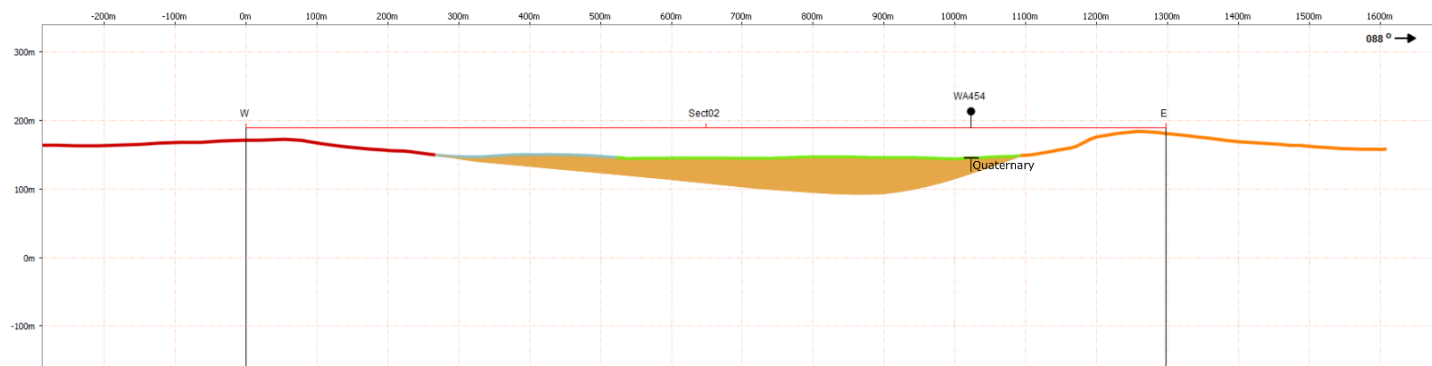
Fig.

**ANNEX B**  
LOCAL SCALE 3-D MODEL:  
Geological cross sections at 1:10.000 scale



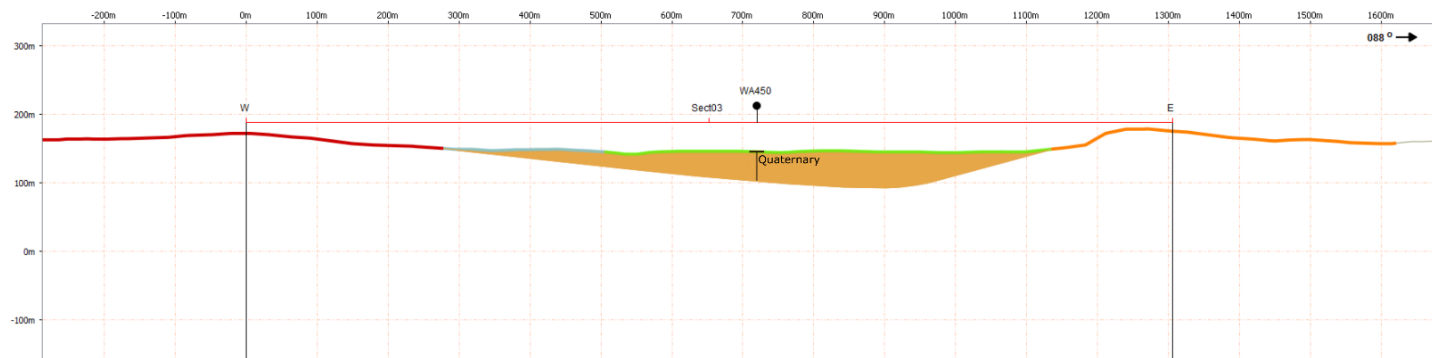
**Legend:**

- Outcropping geology projected on the SRTMGL1 DEM:  
 Quaternary (Holocene)  
 Present alluvium  
 Old and recent alluvium
- Neogene  
 Upper Pliocene: Conglomerates, marls and sandstones  
 Mio-Pliocene: Sandstones, clays and gypseous marls
- Symbology:  
 Inféro-flux aquifer (corresponding to the oued Biskra alluvium)  
 Well-log



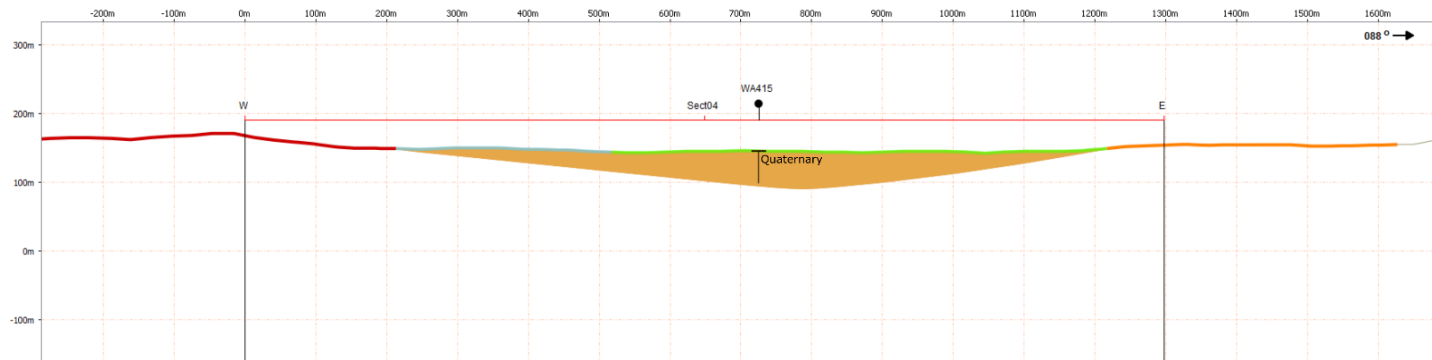
**Legend:**

- Outcropping geology projected on the SRTMGL1 DEM:  
 Quaternary (Holocene)  
 Present alluvium  
 Old and recent alluvium
- Neogene  
 Upper Pliocene: Conglomerates, marls and sandstones  
 Mio-Pliocene: Sandstones, clays and gypseous marls
- Symbology:  
 Inféro-flux aquifer (corresponding to the oued Biskra alluvium)  
 Well-log



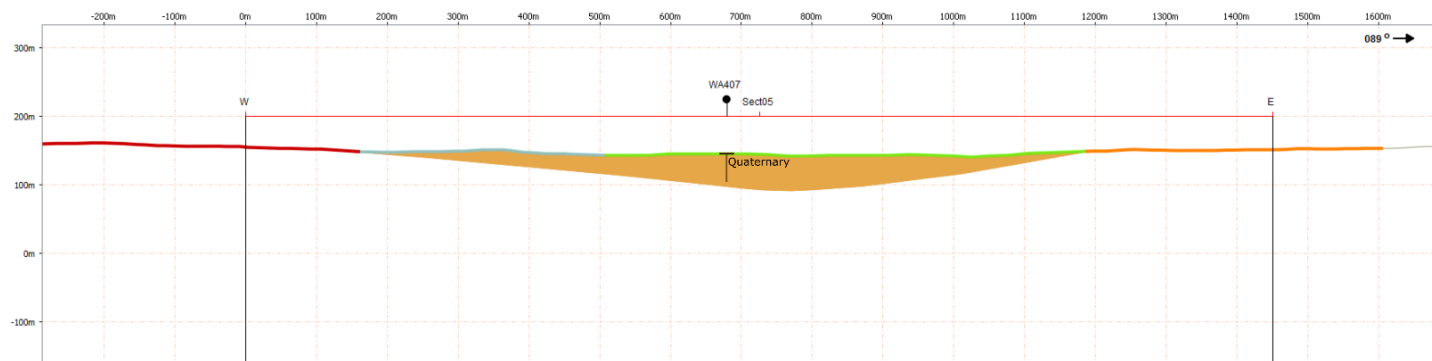
**Legend:**

- Outcropping geology projected on the SRTMGL1 DEM:  
 Quaternary (Holocene)  
 Present alluvium  
 Old and recent alluvium
- Neogene  
 Upper Pliocene: Conglomerates, marls and sandstones  
 Mio-Pliocene: Sandstones, clays and gypseous marls
- Symbology:  
 Inféro-flux aquifer (corresponding to the oued Biskra alluvium)  
 Well-log



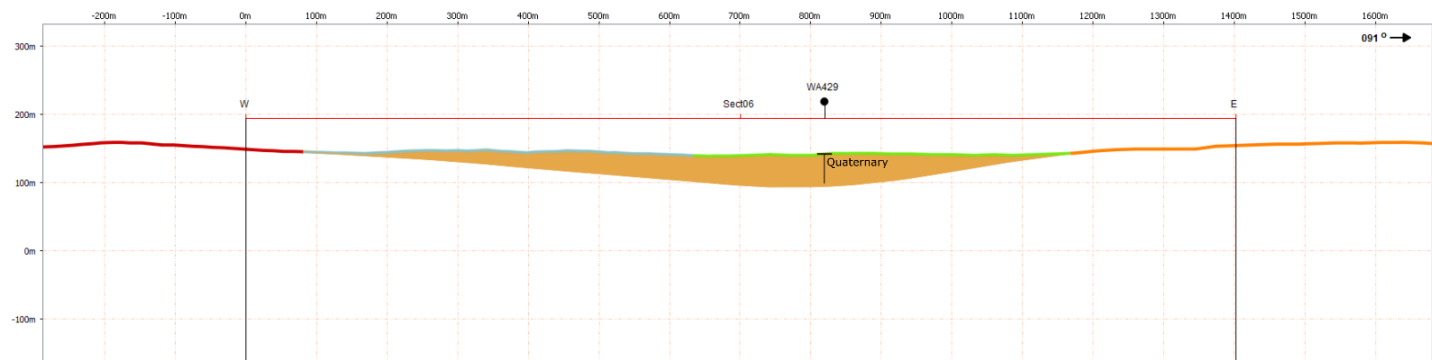
**Legend:**

- Outcropping geology projected on the SRTMGL1 DEM:  
 Quaternary (Holocene)  
 Present alluvium  
 Old and recent alluvium
- Neogene  
 Upper Pliocene: Conglomerates, marls and sandstones  
 Mio-Pliocene: Sandstones, clays and gypseous marls
- Symbology:  
 Inféro-flux aquifer (corresponding to the oued Biskra alluvium)  
 Well-log



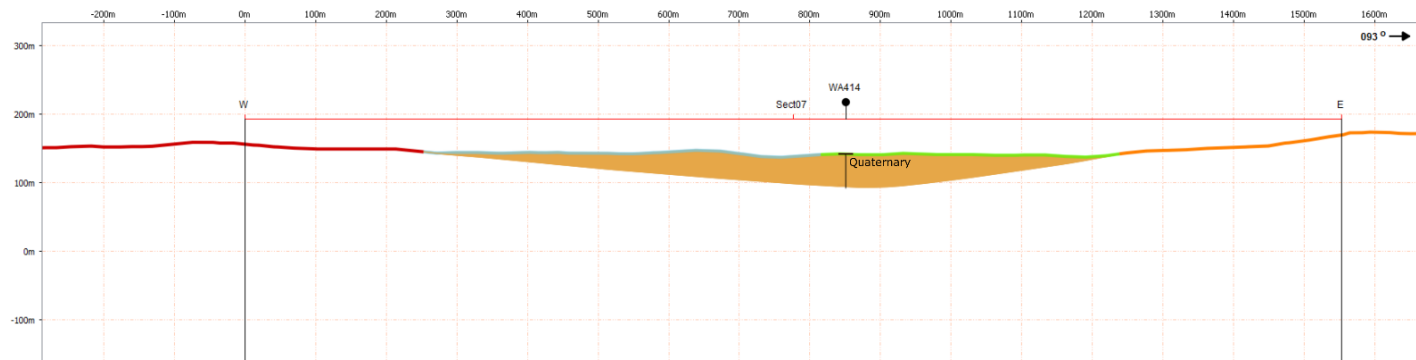
**Legend:**

- Outcropping geology projected on the SRTMGL1 DEM:  
 Quaternary (Holocene)  
 Present alluvium  
 Old and recent alluvium
- Neogene  
 Upper Pliocene: Conglomerates, marls and sandstones  
 Mio-Pliocene: Sandstones, clays and gypseous marls
- Symbology:  
 Inféro-flux aquifer (corresponding to the oued Biskra alluvium)  
 Well-log



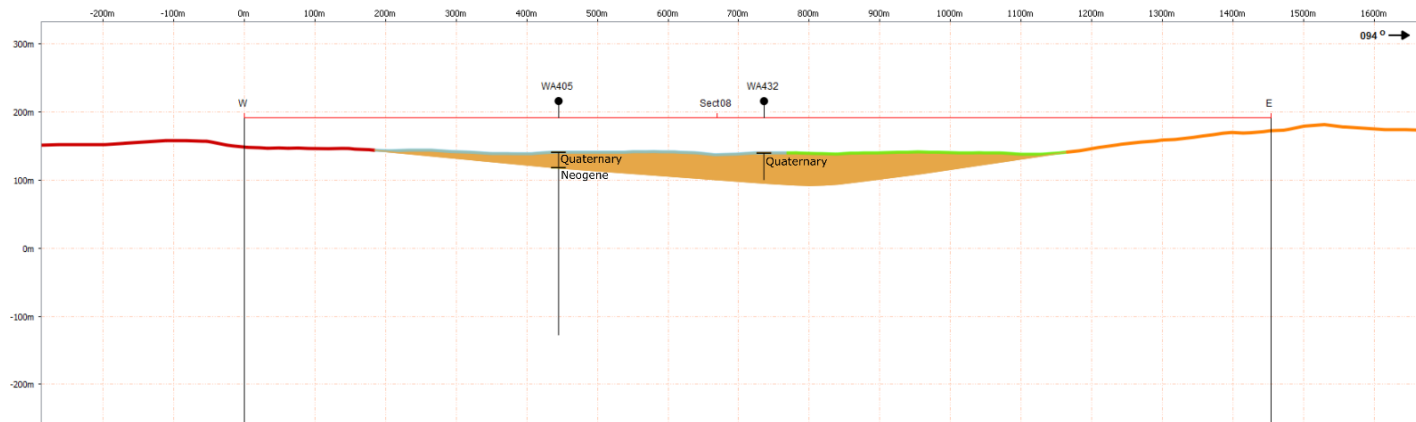
**Legend:**

- Outcropping geology projected on the SRTMGL1 DEM:  
 Quaternary (Holocene)  
 Present alluvium  
 Old and recent alluvium
- Neogene  
 Upper Pliocene: Conglomerates, marls and sandstones  
 Mio-Pliocene: Sandstones, clays and gypseous marls
- Symbology:  
 Inféro-flux aquifer (corresponding to the oued Biskra alluvium)  
 Well-log



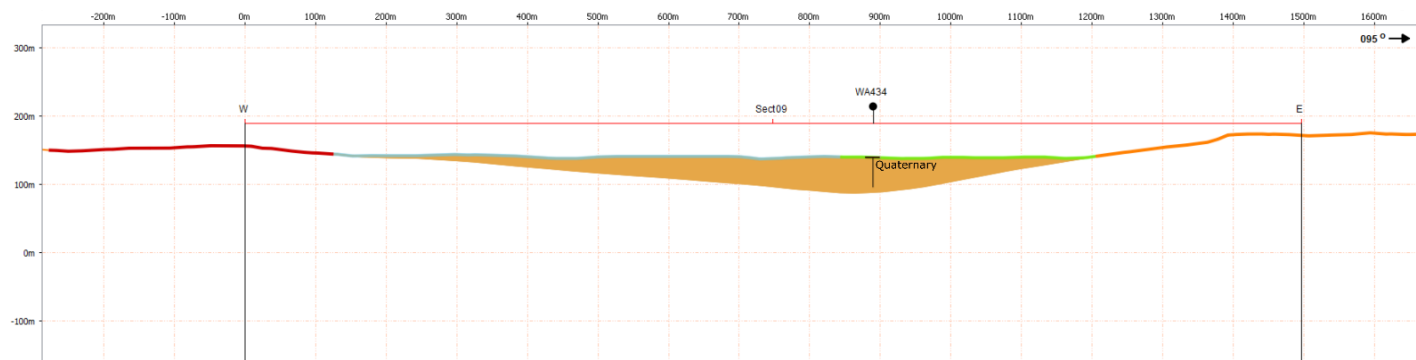
**Legend:**

- Outcropping geology projected on the SRTMGL1 DEM:  
 Quaternary (Holocene)  
 Present alluvium  
 Old and recent alluvium
- Neogene  
 Upper Pliocene: Conglomerates, marls and sandstones  
 Mio-Pliocene: Sandstones, clays and gypseous marls
- Symbology:  
 Inféro-flux aquifer (corresponding to the oued Biskra alluvium)  
 Well-log



**Legend:**

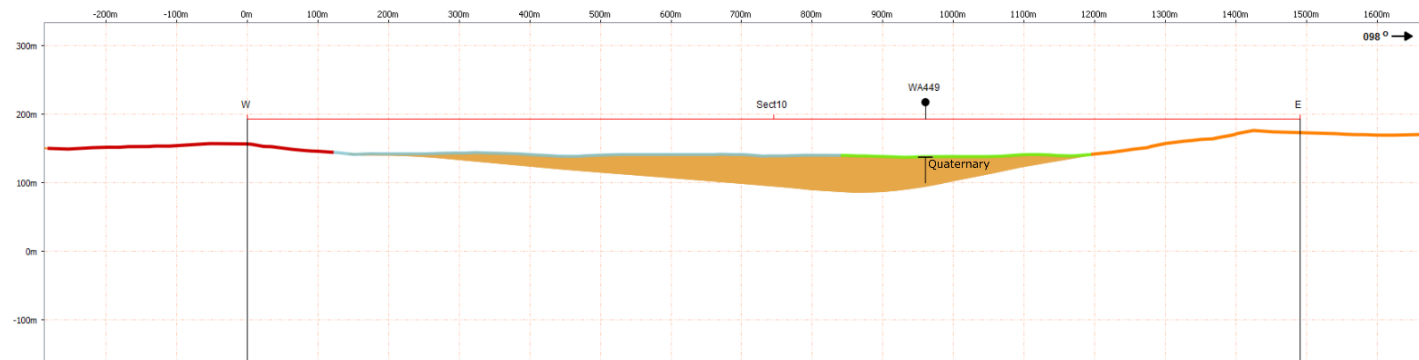
- Outcropping geology projected on the SRTMGL1 DEM:  
 Quaternary (Holocene)  
 Present alluvium  
 Old and recent alluvium
- Neogene  
 Upper Pliocene: Conglomerates, marls and sandstones  
 Mio-Pliocene: Sandstones, clays and gypseous marls
- Symbology:  
 Inféro-flux aquifer (corresponding to the oued Biskra alluvium)  
 Well-log



**Legend:**

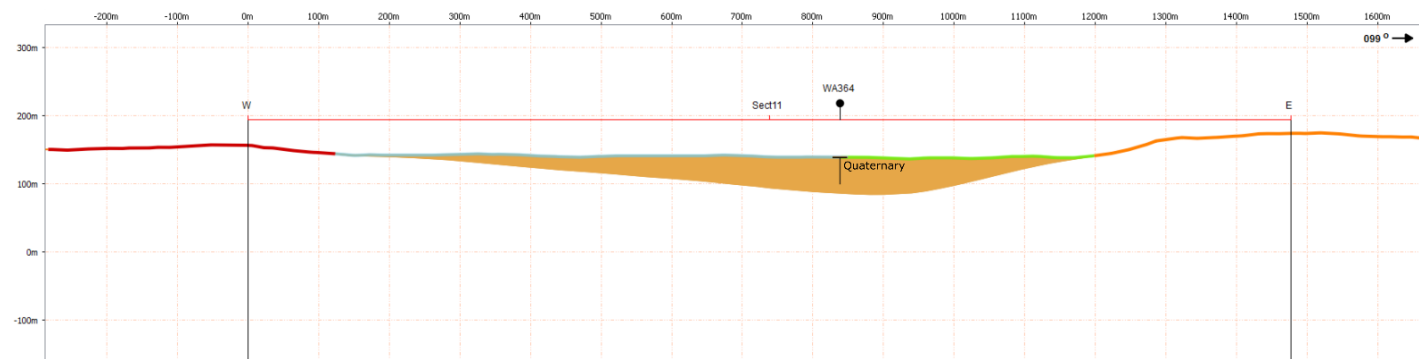
- Outcropping geology projected on the SRTMGL1 DEM:  
 Quaternary (Holocene)  
 Present alluvium  
 Old and recent alluvium
- Neogene  
 Upper Pliocene: Conglomerates, marls and sandstones  
 Mio-Pliocene: Sandstones, clays and gypseous marls
- Symbology:  
 Inféro-flux aquifer (corresponding to the oued Biskra alluvium)  
 Well-log





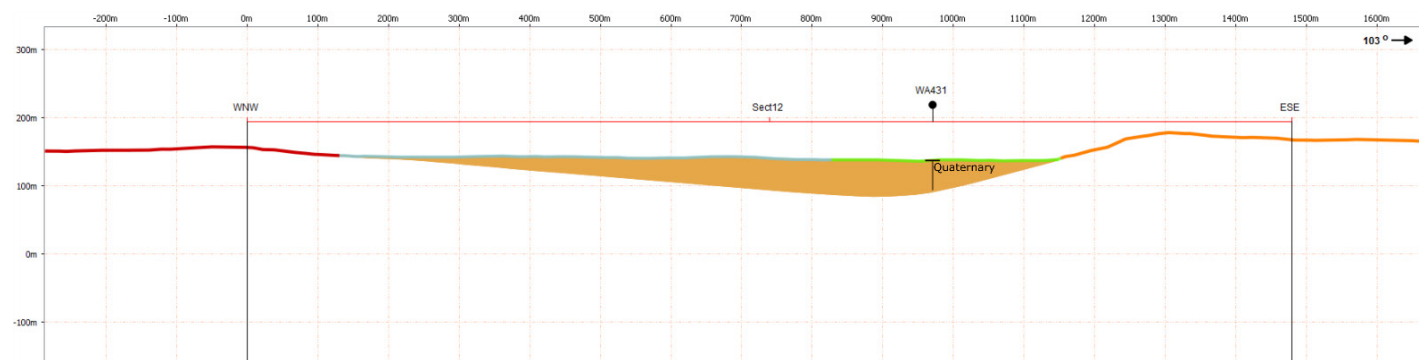
**Legend:**

- Outcropping geology projected on the SRTMGL1 DEM:  
 Quaternary (Holocene)  
 Present alluvium  
 Old and recent alluvium
- Neogene  
 Upper Pliocene: Conglomerates, marls and sandstones  
 Mio-Pliocene: Sandstones, clays and gypseous marls
- Symbology:  
 Inféro-flux aquifer (corresponding to the oued Biskra alluvium)  
 Well-log



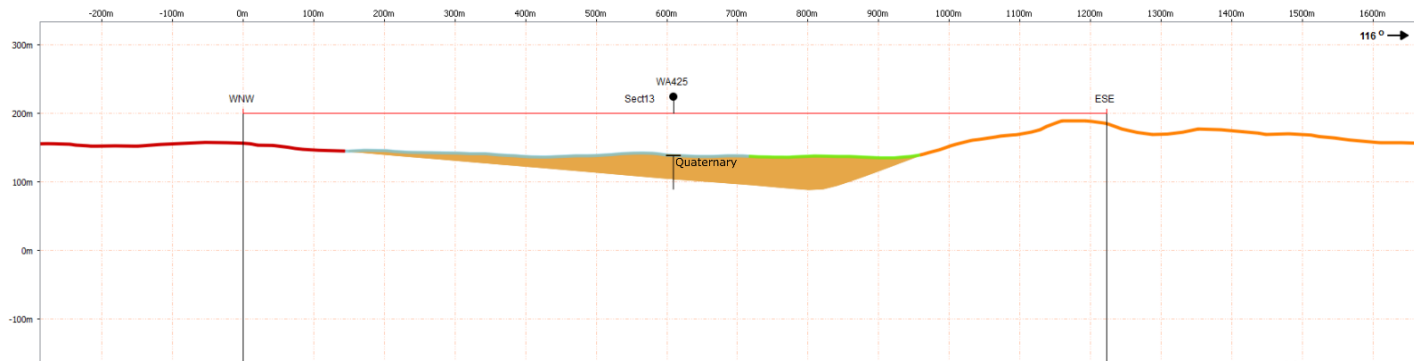
**Legend:**

- Outcropping geology projected on the SRTMGL1 DEM:  
 Quaternary (Holocene)  
 Present alluvium  
 Old and recent alluvium
- Neogene  
 Upper Pliocene: Conglomerates, marls and sandstones  
 Mio-Pliocene: Sandstones, clays and gypseous marls
- Symbology:  
 Inféro-flux aquifer (corresponding to the oued Biskra alluvium)  
 Well-log



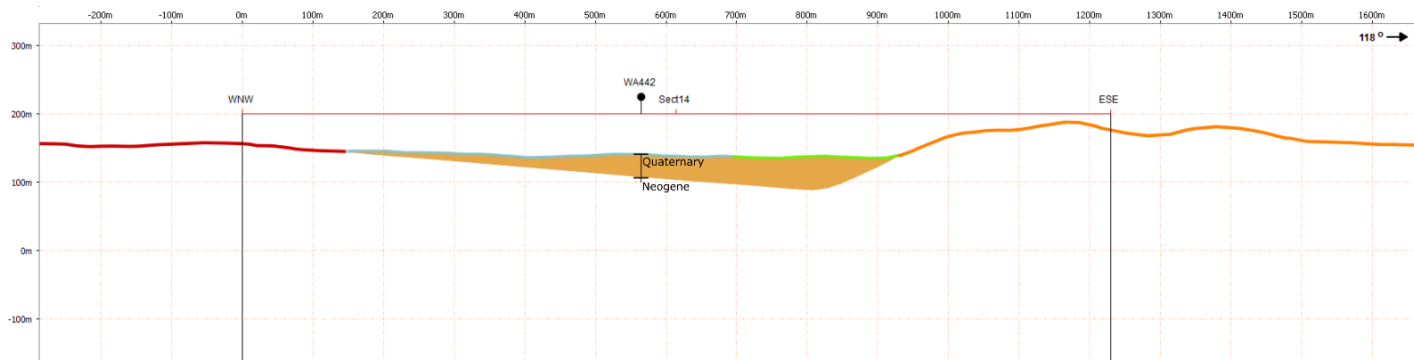
**Legend:**

- Outcropping geology projected on the SRTMGL1 DEM:  
 Quaternary (Holocene)  
 Present alluvium  
 Old and recent alluvium
- Neogene  
 Upper Pliocene: Conglomerates, marls and sandstones  
 Mio-Pliocene: Sandstones, clays and gypseous marls
- Symbology:  
 Inféro-flux aquifer (corresponding to the oued Biskra alluvium)  
 Well-log



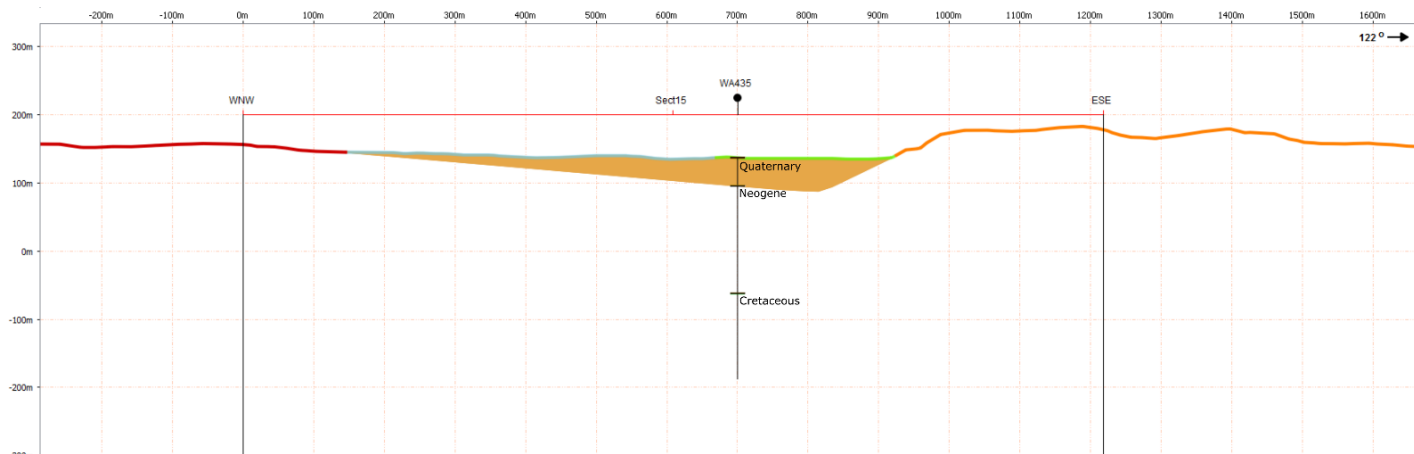
**Legend:**

- Outcropping geology projected on the SRTMGL1 DEM:  
 Quaternary (Holocene)  
 Present alluvium  
 Old and recent alluvium
- Neogene  
 Upper Pliocene: Conglomerates, marls and sandstones  
 Mio-Pliocene: Sandstones, clays and gypseous marls
- Symbology:  
 Inféro-flux aquifer (corresponding to the oued Biskra alluvium)  
 Well-log



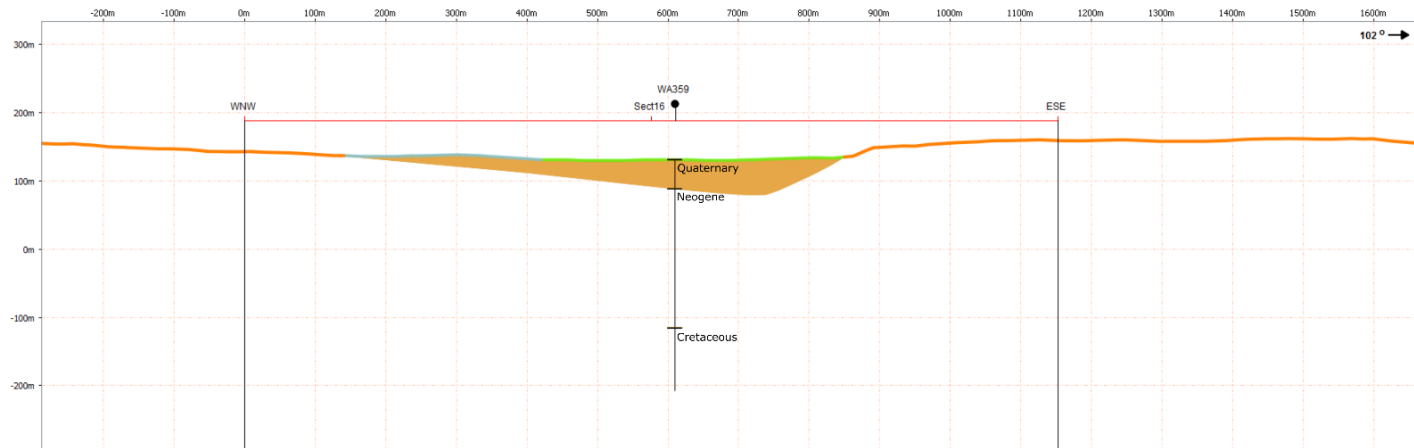
**Legend:**

- Outcropping geology projected on the SRTMGL1 DEM:  
 Quaternary (Holocene)  
 Present alluvium  
 Old and recent alluvium
- Neogene  
 Upper Pliocene: Conglomerates, marls and sandstones  
 Mio-Pliocene: Sandstones, clays and gypseous marls
- Symbology:  
 Inféro-flux aquifer (corresponding to the oued Biskra alluvium)  
 Well-log



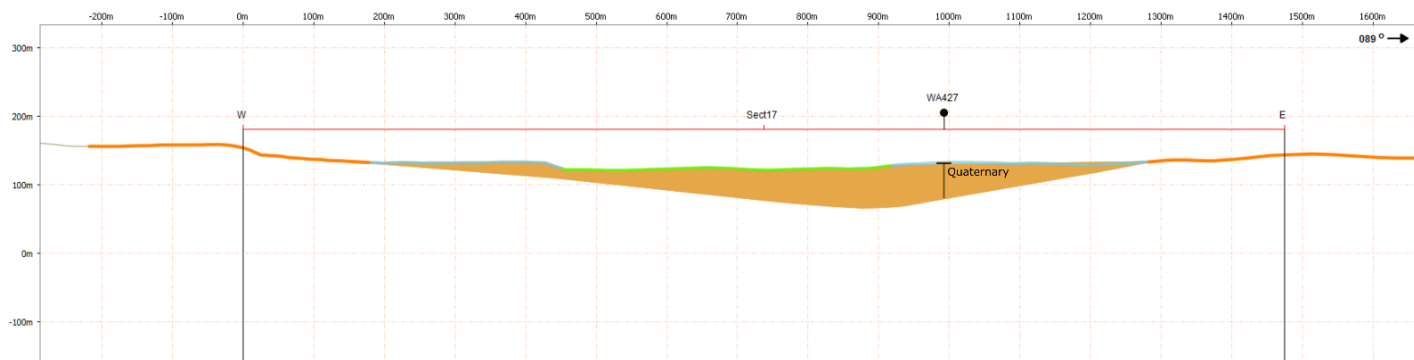
**Legend:**

- Outcropping geology projected on the SRTMGL1 DEM:  
 Quaternary (Holocene)  
 Present alluvium  
 Old and recent alluvium
- Neogene  
 Upper Pliocene: Conglomerates, marls and sandstones  
 Mio-Pliocene: Sandstones, clays and gypseous marls
- Symbology:  
 Inféro-flux aquifer (corresponding to the oued Biskra alluvium)  
 Well-log



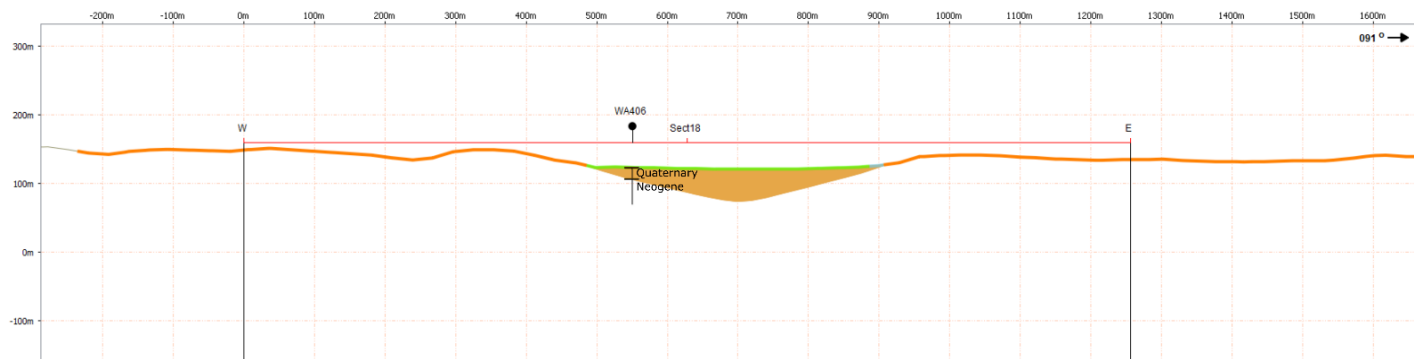
**Legend:**

- Outcropping geology projected on the SRTMGL1 DEM:  
 Quaternary (Holocene)  
 Present alluvium  
 Old and recent alluvium
- Neogene  
 Upper Pliocene: Conglomerates, marls and sandstones  
 Mio-Pliocene: Sandstones, clays and gypseous marls
- Symbology:  
 Inféro-flux aquifer (corresponding to the oued Biskra alluvium)  
 Well-log



**Legend:**

- Outcropping geology projected on the SRTMGL1 DEM:  
 Quaternary (Holocene)  
 Present alluvium  
 Old and recent alluvium
- Neogene  
 Upper Pliocene: Conglomerates, marls and sandstones  
 Mio-Pliocene: Sandstones, clays and gypseous marls
- Symbology:  
 Inféro-flux aquifer (corresponding to the oued Biskra alluvium)  
 Well-log



**Legend:**

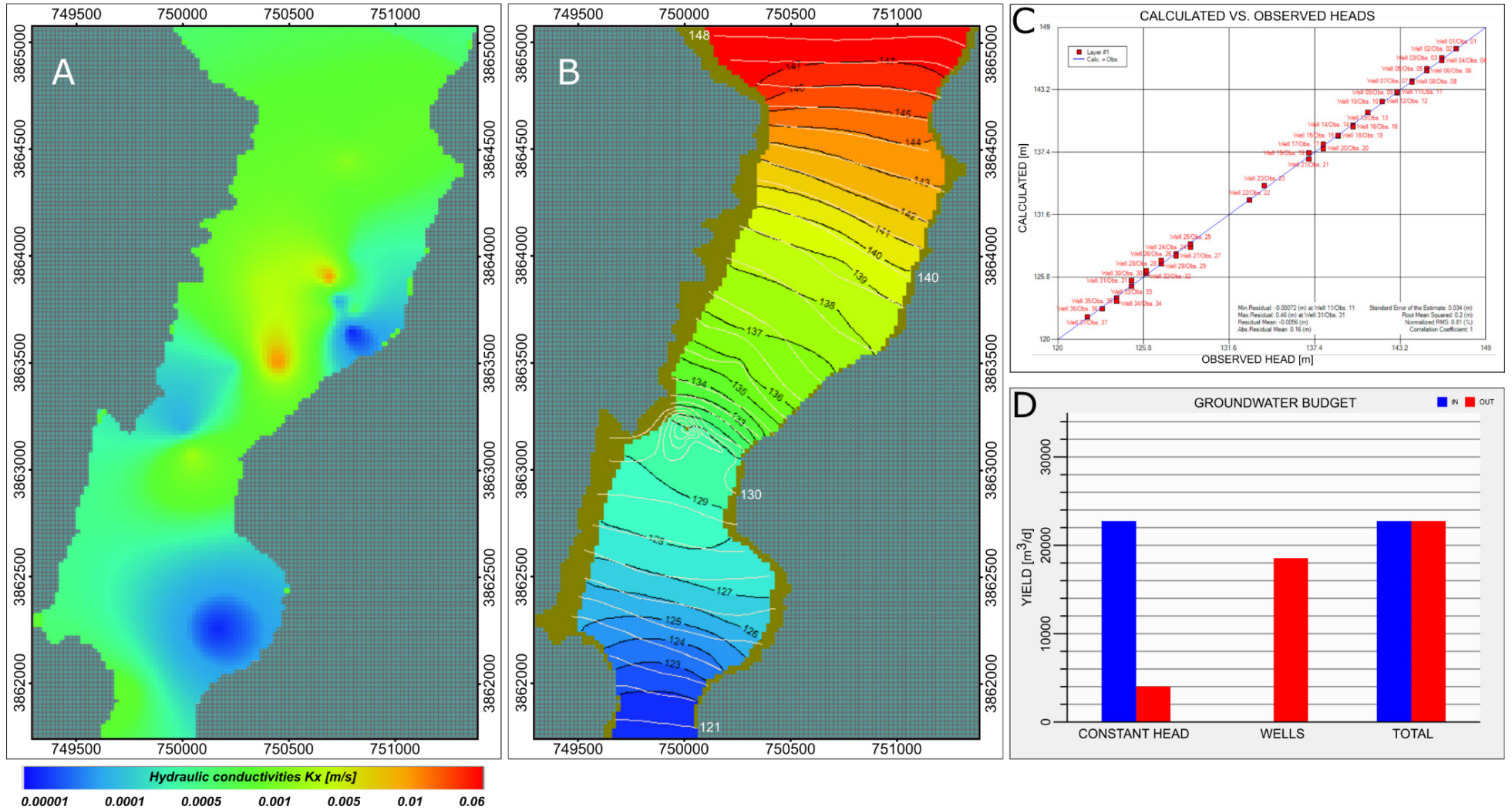
- Outcropping geology projected on the SRTMGL1 DEM:  
 Quaternary (Holocene)  
 Present alluvium  
 Old and recent alluvium
- Neogene  
 Upper Pliocene: Conglomerates, marls and sandstones  
 Mio-Pliocene: Sandstones, clays and gypseous marls
- Symbology:  
 Inféro-flux aquifer (corresponding to the oued Biskra alluvium)  
 Well-log

## **ANNEX C**

### **GROUNDWATER FLOW NUMERICAL MODEL CALIBRATION:**

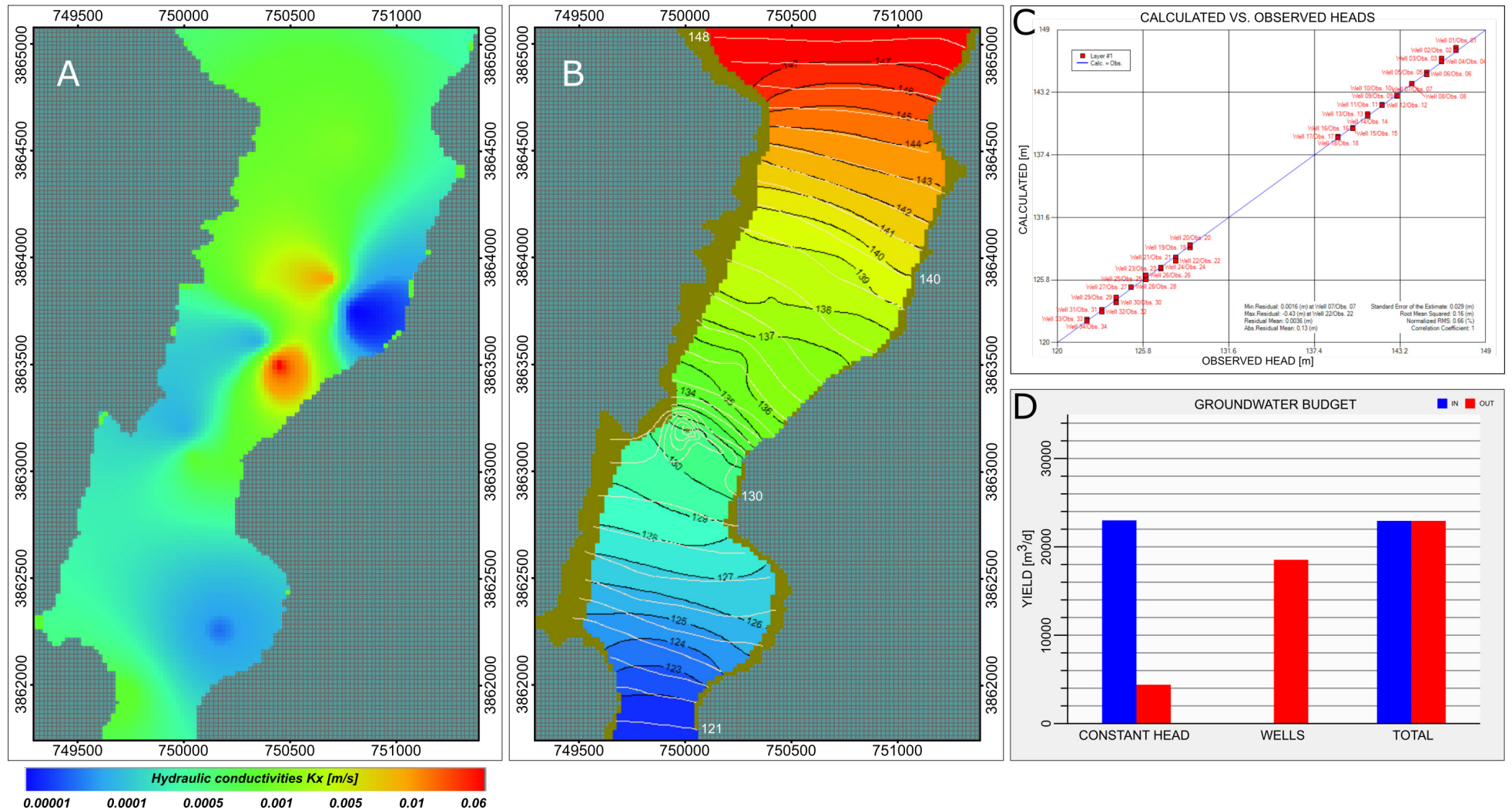
PEST execution and results of model run using the calibrated hydraulic conductivities and the hydrogeological conditions referred to the 1966 survey (SCET-COOP, 1967).

# PEST execution N.01



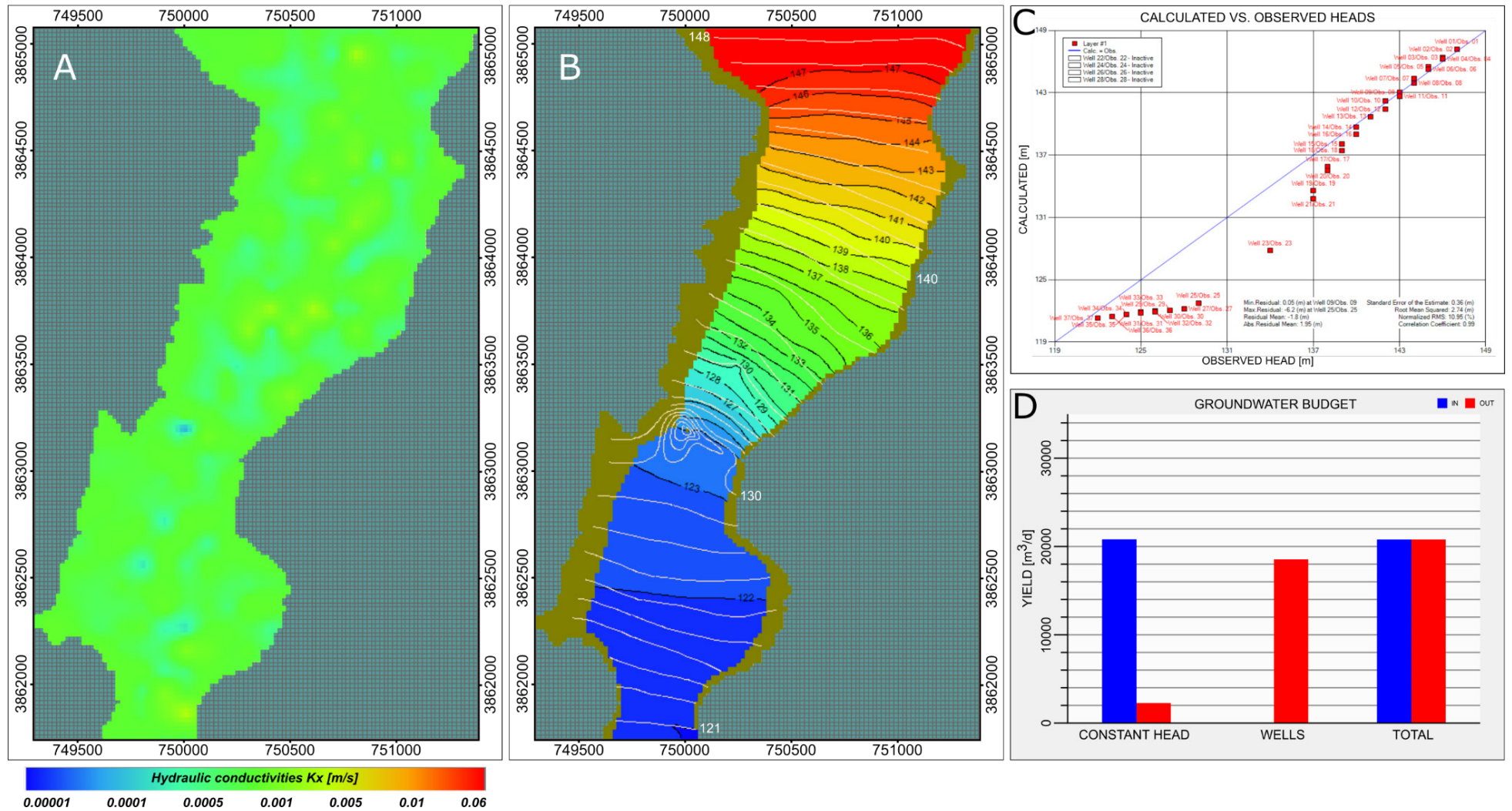
A) Distribution of the hydraulic conductivities as the result of the PEST execution n.1; B) Map view of observed (white) and simulated (black) water table (shown by contours); C) scatter plot of simulated to observed fit of water levels; D) bar histogram illustrating the groundwater budget components.

# PEST execution N.02



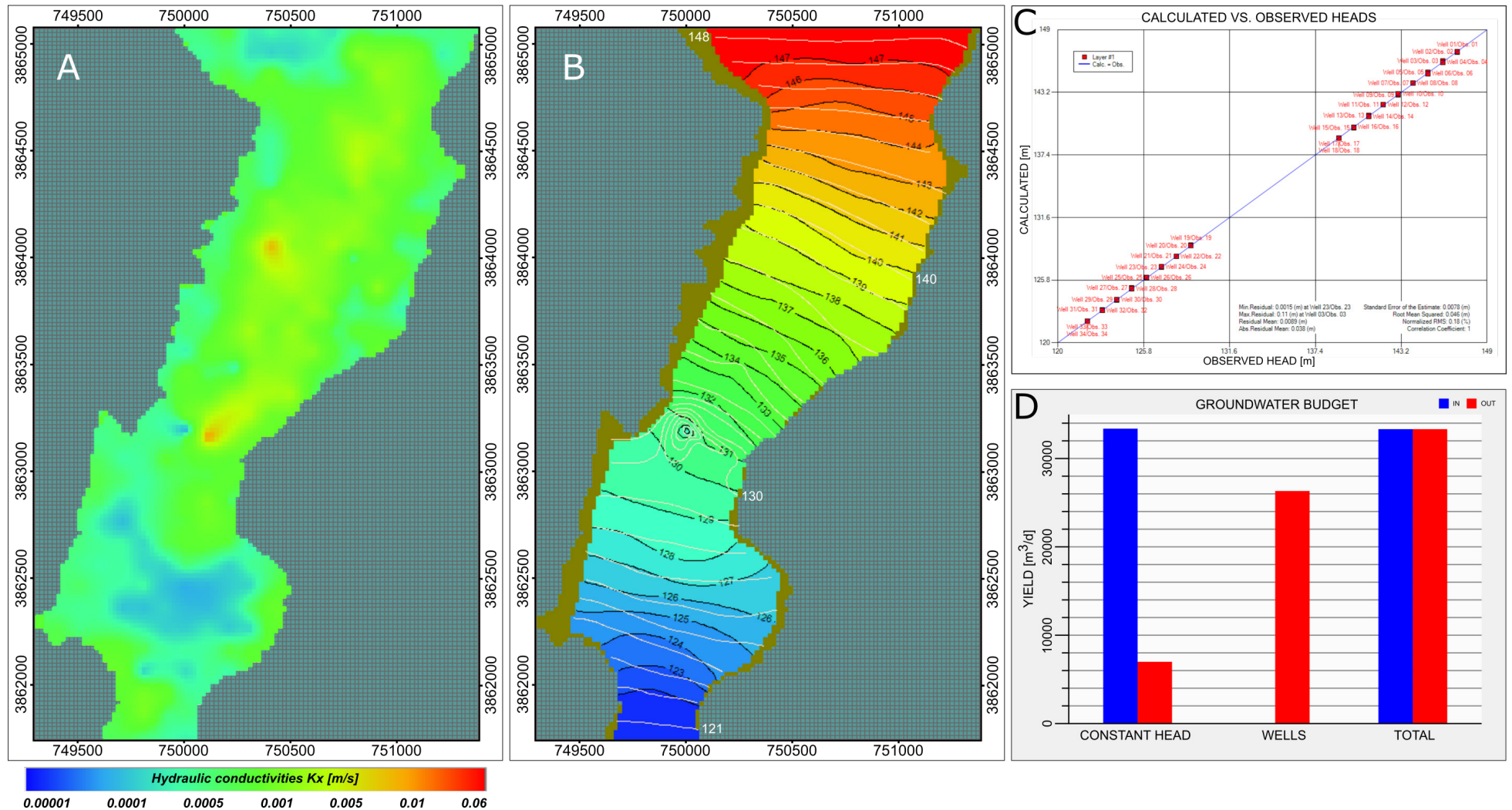
A) Distribution of the hydraulic conductivities as the result of the PEST execution n.2; B) Map view of observed (white) and simulated (black) water table (shown by contours); C) scatter plot of simulated to observed fit of water levels; D) bar histogram illustrating the groundwater budget components.

# PEST execution N.03



A) Distribution of the hydraulic conductivities as the result of the PEST execution n.3; B) Map view of observed (white) and simulated (black) water table (shown by contours); C) scatter plot of simulated to observed fit of water levels; D) bar histogram illustrating the groundwater budget components.

# PEST execution N.04



A) Distribution of the hydraulic conductivities as the result of the PEST execution n.4; B) Map view of observed (white) and simulated (black) water table (shown by contours); C) scatter plot of simulated to observed fit of water levels; D) bar histogram illustrating the groundwater budget components.